ABSTRACT

Title of Document: AEROTHERMODYNAMIC OPTIMIZATION OF EARTH ENTRY BLUNT-BODY HEAT SHIELDS FOR LUNAR AND MARS RETURN

Joshua E. Johnson
Doctor of Philosophy, 2009

Directed By: Professor Mark J. Lewis
Department of Aerospace Engineering

A differential evolutionary algorithm has been executed to optimize the hypersonic aerodynamic and stagnation-point heat transfer performance of Earth entry heat shields for Lunar and Mars return manned missions with entry velocities of 11 and 12.5 km/s respectively. The aerothermodynamic performance of heat shield geometries with lift-to-drag ratios up to 1.0 is studied. Each considered heat shield geometry is composed of an axial profile tailored to fit a base cross section. Axial profiles consist of spherical segments, spherically blunted cones, and power laws. Heat shield cross sections include oblate and prolate ellipses, rounded-edge parallelograms, and blendings of the two. Aerothermodynamic models are based on modified Newtonian impact theory with semi-empirical correlations for convection and radiation. Multi-objective function optimization is performed to determine

optimal trade-offs between performance parameters. Objective functions consist of minimizing heat load and heat flux and maximizing down range and cross range.

Results indicate that skipping trajectories allow for vehicles with L/D = 0.3, 0.5, and 1.0 at lunar return flight conditions to produce maximum cross ranges of 950, 1500, and 3000 km respectively before $Q_{s,tot}$ increases dramatically. Maximum cross range increases by ~20% with an increase in entry velocity from 11 to 12.5 km/s. Optimal configurations for all three lift-to-drag ratios produce down ranges up to approximately 26,000 km for both lunar and Mars return. Assuming a 10,000 kg mass and L/D = 0.27, the current Orion configuration is projected to experience a heat load of approximately 68 kJ/cm^2 for Mars return flight conditions. For both L/D = 0.3 and 0.5, a 30% increase in entry vehicle mass from 10,000 kg produces a 20-30% increase in $Q_{s,tot}$. For a given L/D, highly-eccentric heat shields do not produce greater cross range or down range. With a 5 g deceleration limit and L/D = 0.3, a highly oblate cross section with an eccentricity of 0.968 produces a 35% reduction in heat load over designs with zero eccentricity due to the eccentric heat shield's greater drag area that allows the vehicle to decelerate higher in the atmosphere. In this case, the heat shield's drag area is traded off with volumetric efficiency while fulfilling the given set of mission requirements. Additionally, the high radius-of-curvature of the spherical segment axial profile provides the best combination of heat transfer and aerodynamic performance for both entry velocities and a 5 g deceleration limit.

AEROTHERMODYNAMIC OPTIMIZATION OF EARTH ENTRY BLUNT-BODY HEAT SHIELDS FOR LUNAR AND MARS RETURN

By

Joshua E. Johnson

Thesis submitted to the Faculty of the Graduate School of the
University of Maryland, College Park, in partial fulfillment
of the requirements for the degree of
Doctor of Philosophy
2009

Advisory Committee:
Professor Mark J. Lewis, Chair
Professor Ashwani Gupta, Dean's Representative
Associate Professor David Akin
Associate Professor James Baeder
Associate Professor Christopher Cadou

Dedication

To my parents John and Caroline, my sisters Justine and Lucia Maria,

and the Agape mission community.

Acknowledgements

I would like to express my gratitude to Dr. Mark J. Lewis for the opportunity to conduct this research, who through his achievements in the field of hypersonics, has inspired me to strive forward in my studies and aerospace career. I would like to thank Dr. Ryan Starkey for his endless patience and time given in assisting me with my research. I would also like to thank the other members of my committee Dr. David Akin, who provided good insight into space systems, Dr. James Baeder, who provided the basic theories of computation fluid dynamics, Dr. Christopher Cadou, and Dr. Ashwani Gupta.

I would like to acknowledge Dr. Roman Jits for all his insight into understanding entry corridor theory and using POST, and Dr. Mike Wright for his support throughout the years. I also would like to acknowledge the NASA funding that supported this work in its entirety. This research was supported by the Space Vehicle Technology Institute (SVTI), one of the NASA Constellation University Institute Projects (CUIP), under grant NCC3-989, with joint sponsorship from the Department of Defense. Appreciation is expressed to Dr. Darryll Pines, director of the SVT Institute at the University of Maryland, Claudia Meyer of the NASA Glenn Research Center, program manager of CUIP, and to Dr. John Schmisseur and Dr. Walter Jones of the Air Force Office of Scientific Research, the support of whom is greatly appreciated.

I would also like to thank Dr. Robert Braun of the Georgia Institute of Technology for his entry vehicle system and trajectory insight. Finally, I would like to thank my fellow SVTI and rotorcraft graduate students, who have given me friendship and support throughout this backbreaking process, and especially to Falcon Rankins for software training and support of his code UPTOP that has been utilized for the optimization. He has spent countless hours teaching and troubleshooting with me. Without the availability of his code, this project would have become greatly different and possibly not as high quality.

Table of Contents

List of Tables

List of Figures

List of Symbols

A	=	Coefficient of power law
A_b	=	Area of the base (m^2)
A_p	=	Planform area (m^2)
AFE	=	Aeroassist Flight Experiment
a	=	Speed of sound (m/s)
a_1	=	Semimajor axis length of a superellipse (m)
a_2	=	Semimajor axis length of a blunt body (m)
BC	=	Ballistic coefficient (kg/m^2)
b	=	Exponent of power law
b_1	=	Semiminor axis length of a superellipse (m)
b_2	=	Semiminor axis length of a blunt body (m)
C	=	Aerodynamic coefficient
CEV	=	Crew Exploration Vehicle
CFD	=	Computational fluid dynamics
CM	=	Command Module, refers to Project Apollo unless noted otherwise
D	=	Drag (N)
DOT	=	Design Optimization Tools
d	=	Diameter (m)
d_1, d_2	=	Distances from mesh point to point as indicated in the text
$d_{(j,k),(j+1,k)}$	=	Distance from mesh point (j,k) to point ($j+1,k$)
dA	=	Differential surface area
dA_p	=	Differential planform area
dr	=	Differential distance from mesh point to origin
dV	=	Differential volume
$d\theta$	=	Differential theta
$d\phi$	=	Differential sweep angle
E	=	Search direction for optimization,
	=	Total emitted power density, ($J/(m^3 s)$)
EI	=	Entry interface
EV	=	Entry vehicle
e	=	Eccentricity
FIRE	=	Flight Investigation of the Reentry Environment
F	=	Integration of f with respect to x
$\vec{F}_b$	=	External body force vector
f	=	Function of x
f_{HS}	=	Ratio of V_{HS} to V_{EV}
f_{PR}	=	Ratio of V_{PR} to V_{EV}
$\vec{G}$	=	Optimization constraints vector
G_q	=	q^{th} constraint
$\vec{g}$	=	Gravity vector (m/s^2)

g_1, g_2, g_3	=	Radiation correlation parameters
g_w	=	Ratio of wall enthalpy to total enthalpy
H	=	Correlation exponent
h	=	Step size,
	=	Length along the y-direction (m)
h_t	=	Altitude (m)
J	=	Vehicle inertia matrix
j	=	Mesh point index in ϕ-direction,
	=	Semimajor axis length of a blunt body (m)
j_{max}	=	Maximum mesh points in ϕ-direction
k	=	Mesh point index in x-direction
	=	Semiminor axis length of a blunt body (m)
k_{max}	=	Maximum mesh points in x-direction
L	=	Lift (N)
l	=	Length of heat shield from nose to base (m)
	=	Length along x-direction (m)
l_b	=	Length from differential surface to base (m)
l_M	=	Length of the semimajor axis of the cross-section
L/D	=	Lift-to-drag ratio
MMFD	=	Modified Method of Feasible Directions
M_∞	=	Freestream Mach number
m	=	Mass (kg)
m_1	=	Number of sides of the superellipse in the superformula
N	=	Total number of sections in which to divide the conical base
NCON	=	Number of constraints
NDV	=	Number of design variables
n	=	Number of the section of the conical base
n_1, n_2, n_3	=	Superelliptic parameters
n_{crew}	=	Crew number (person)
n_{max}	=	Peak deceleration load (Earth g = 9.81 m/s^2)
$\hat{n}$	=	Outward normal of a surface
OBJ	=	Objective function
$O(\vec{X})$	=	Objective function as a function of $\vec{X}$
$o_i(\vec{X})$	=	i^{th} objective in overall objective function
PL	=	Power law
$\vec{p}$	=	Position vector, range (m)
p	=	Index corresponding to a specific design variable X_p
p_{dwn}	=	Down range (km)
p_{xrs}	=	Cross range (km)
$Q(\vec{X})$	=	Quadratic Taylor series expansion of $O(\vec{X})$
Q_s	=	Stagnation-point heat load (J/cm^2)
q	=	Index corresponding to a specific constraint G_q
q_∞	=	Freestream dynamic pressure (Pa)
$\dot{q}_s$	=	Stagnation-point heat flux (W/cm^2)
$\vec{q}_t$	=	Quaternion vector

RCS	=	Reaction control system
r	=	Base radius (m)
r_c	=	Corner radius (m)
r_{eff}	=	Effective radius of curvature for radiative heat transfer (m)
r_n	=	Nose radius for spherically-blunted cone axial shape (m)
r_s	=	Radius-of-curvature for spherical-segment axial shape (m)
r_{st}	=	Length from the central axis to the stagnation point (m)
r_{sh}	=	Radius of curvature for the spherical shock (m)
S	=	Area of base cross-section (m^2)
S_{hs}	=	Surface area of heat shield without base area (m^2)
S_{veh}	=	Surface area of vehicle (m^2)
S_{EV}	=	Linear slope factor for V_{EV}
SCRAMP	=	Slotted Compression Ramp
SC	=	Spherically-blunted cone axial profile
SS	=	Spherical segment
TPS	=	Thermal Protection System
$\vec{T}_b$	=	Torque vector from body axis to the inertial frame (N-m)
t	=	Time (s)
u	=	Iteration number
V_∞	=	Freestream velocity magnitude (m/s)
V_{hs}	=	Volume of heat shield (m^3)
V_x, V_y, V_z	=	Freestream velocity components normalized by V_∞
v	=	Exponent of superellipse equation
WT	=	Wind tunnel
W	=	Weighting factor
w	=	Distance from point (j,k) to x-axis
w_v	=	Wind angle
$\vec{X}$	=	Vector of design variables X_p, in which p = 1 to NDV
X_p	=	p^{th} design variable
x, y, z	=	Coordinate directions
x_s	=	The streamwise distance from the apex of the shock to the point on the shock at distance y_* from the central axis
y_*	=	The normal distance from the axis of symmetry to the sonic point on the body (m)
α	=	Angle-of-attack (deg)
α^*	=	Scalar parameter for optimization
β	=	Sideslip angle (deg)
γ	=	Ratio of specific heats
Δ_{so}	=	Shock-standoff distance (m)
Δ_*	=	The shock-standoff distance at the sonic point (m)
ε	=	Inclination on forward body surface at the tangent point with corner radius, also mentioned as the edge tangency angle
η_v	=	Volumetric efficiency (surface area comparison)
θ_c	=	Half-cone angle (deg)
θ_s	=	Half-spherical-segment angle (deg)

θ_*	=	Shock surface inclination at a point opposite of the sonic point on a body with respect to a plane normal to the freestream direction
θ_{*o}	=	Shock surface inclination at a point opposite of the sonic point on a flat disk
λ	=	Lagrange multiplier
ρ	=	Density (kg/m^3)
Φ_*	=	Sonic angle of a blunt body, which is the body surface inclination of a blunt body at the sonic point with respect to a plane normal to freestream direction
Φ_{*1},	=	Sonic angle of a sphere
ϕ	=	Sweep angle (rad)
	=	Azimuth angle
ϕ_b	=	Bank angle (deg)
Ω_b	=	Vehicle rotation rate matrix
Ω_q	=	Vehicle tracking standard update matrix
$\bar{\omega}_b$	=	Design variables vector
ω	=	Angle from *x*-axis and in the *xy* plane (rad)

Subscripts

0	=	Location at tip of nose, stagnation point, moments normalized by base diameter *d*
1	=	Before the normal shock
2	=	After the normal shock
75	=	75% of value assuming uniform density
A	=	Axial force
cg	=	Center of gravity
conv	=	Convective
cp	=	Location of center of pressure
D	=	Drag
d	=	Mission duration (day)
E	=	Entry interface (km) (h_t = 122 km)
EV	=	Entry Vehicle
eff	=	Effective
f	=	Final
H	=	Horizontal component in the aerodynamic reference frame
HS	=	Heat shield
j	=	*xy*-plane index
L	=	Lift
l	=	Rolling moment
lower	=	Lower constraint value
m	=	Pitching moment
max	=	Point of maximum heat transfer
N	=	Normal force
nd	=	Non-dimensionalized vector
n	=	Yawing moment
R	=	Resultant

rad	=	Radiative
sl	=	Sea level
tot	=	Total
UD	=	Uniform density
upper	=	Upper constraint value
V	=	Vertical component in the aerodynamic reference frame
Y	=	Side force
α	=	Derivative with respect to angle-of-attack (per rad)
β	=	Derivative with respect to sideslip angle (per rad)
∞	=	Freestream conditions

Chapter 1. Introduction

1.1. Motivation

Returning to Earth from other planetary bodies entails surviving an extreme hypersonic environment during atmospheric entry. This involves entering Earth's atmosphere at high velocities ranging from 10 km/s to 15 km/s with corresponding Mach numbers from thirty to fifty,[1] while withstanding 3000+ K temperatures at and near the stagnation points. The heat shield, which faces the freestream flow and protects the entry vehicle (EV), is the primary source of the vehicle's hypersonic aerothermodynamic performance, i.e., the aerodynamic forces, moments, and heat transfer.[2] The rest of the vehicle is secondary since it is covered with regions of extremely low pressure, due to flow separation, and since it experiences significantly lower heat fluxes.

Optimizing aerodynamic and heat transfer performance are conflicting objectives. To reduce surface heating and maximize thermal energy transferred to the surrounding environment, entry vehicle heat shields have typically been blunt-body designs, limiting entry aerodynamic performance.[3] Consequently, an aerothermodynamic balance must be achieved to satisfy mission requirements without exceeding material technology constraints.

This work questions the assumption that the classic spherical segment[4] and spherically blunted cone[5,6] geometries with circular base cross sections provide optimal aerothermodynamic performance. Although they have been utilized over the past forty years, it is unknown whether either provides optimal aerothermodynamic

performance for lunar and Mars return missions. In this work, aerothermodynamic performance translates into cross range and down range capabilities and stagnation-point heat transfer. Cross range capability enables missions that require inclination changes from the initial plane of entry. Both cross range and down range allow an entry vehicle to execute course corrections to counter off-nominal atmospheric conditions and switch landing sites.[7] Stagnation-point heat transfer, though it may not be the point of maximum heating, is an accurate measure of the expected high heating generated along the heat shield. From an overall perspective, cross range, down range, and heat transfer performance are directly associated with mission requirements and material constraints; this work seeks to find optimal blunt-body heat shield designs from these standpoints. Properly broadening the design space would allow the optimizer to determine which geometric features improve performance. With the greater computational power available today, it is possible to perform multi-objective optimization on a wide range of entry heat shield designs with entry trajectory analysis.

1.2. Previous Work

1.2.1. Heat Shield Geometries

The two primary classes of shapes that have been developed by NASA are the spherical-segment and the spherically-blunted cone, shown in Figure 1.1(a) and (b) respectively. Extensive research on spherical-segments led to its use as the heat shield for human reentry space capsules including the NASA Gemini and Apollo missions. The spherical-segment is described by a spherical radius r_s and maximum spherical-

segment angle θ_s measured from the central axis. The Project Gemini Reentry Module[8,9] included a 38° spherical-segment heat shield (θ_s = 19°) with r_s = 3.712 m, and a base diameter of 2.32 m. The Project Apollo Command Module (CM) had a 50° spherical-segment (θ_s = 25°) with r_s = 4.694 m, and a base diameter of 3.912 m.

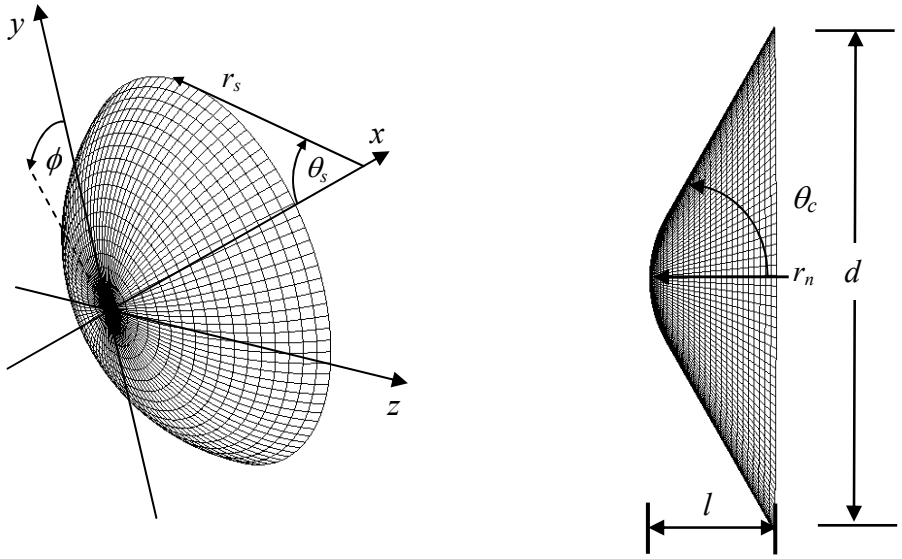

a) Spherical-segment heat shield, θ_s = 60°. **b) Spherically-blunted cone heat shield, r_n/d = 0.25, θ_c = 60°.**

Figure 1.1. The two most familiar heat shield geometries.

Specific Apollo mission aerodynamic flight data is provided for Apollo mission AS-202 and Apollo 4 in Ref. [10] and Ref. [11] respectively. The Command Module (CM) in AS-202 reentered Earth's atmosphere at 8.23 km/s (27,000 ft/s) to produce planetary entry conditions that occur when entering from satellite orbit. The unmanned Apollo 4 (AS-501) was the first mission to use the Saturn V launch vehicle. It was an unmanned mission with an instrumented Command Module. The main objective of Apollo 4 was to show the structural and thermal integrity of the Apollo CM at lunar return flight conditions. Apollo 4 utilized CM-017; it was instrumented with calorimeters and radiometers to measure the performance of the

TPS. At the apogee of CM-017's orbit, the service propulsion system (SPS) engines were fired to produce lunar return flight conditions, The Apollo 4 (AS-501) followed an elliptical orbit around Earth that produced the expected re-entry velocity from lunar return of 10.7 km/s (35,100 ft/s). Rather than passing by the Moon, Apollo 4 had a second Service Module Propulsion System (SPS) burn at the apogee of CM-017's orbit, shown as trajectory location 13 in Figure 1.2, to produce lunar return flight conditions. The total mission time was 8.5 hours rather than six days required to go to the Moon and back. Hillje[11] provided Apollo flight data which was used for code validation in Chapter 7. Note that most of the aerodynamic data from the Apollo flights can be reproduced accurately by this work, except for the normal coefficient C_N which can have up to 40% difference compared to the available flight-derived data.

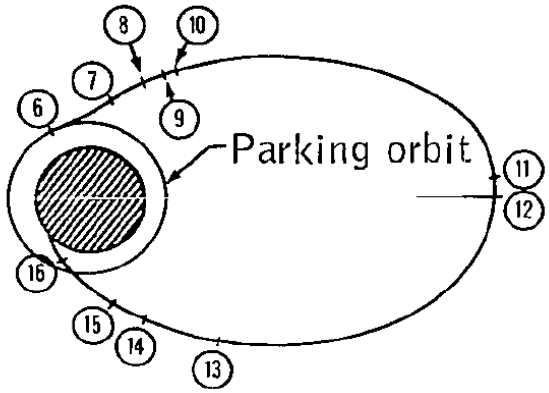

Figure 1.2. Apollo 4 Trajectory from Ref. [11].

Moseley analyzed the aerodynamic stability characteristics of the Apollo Command Module in Refs. [12] and [13]. Both of these NASA Technical Notes provide aerodynamic, static and dynamic stability wind tunnel data on several Command Module configurations with their schematics and relative dimensions. From this set, only two figures are dedicated to rolling moment stability in Ref. [12],

and so a discussion of the Command Module's roll static stability is provided in Chapter 3. DeRose[14] provides an analysis of the center-of-gravity offset from the central axis of the vehicle and also discusses the proper way to compare wind tunnel measurements of a non-ablative model to a flight vehicle with an ablative heat shield. Horstman[15] compares the Apollo and Gemini wind tunnel models with center-of-gravity offsets.

The spherically-blunted cone is another commonly-used blunt-body space capsule configuration, as shown in Figure 1.1(b). It is defined by half-cone angle θ_c, the nose radius r_n, and base diameter d. It is common to see the ratio r_n/d as a listed characteristic. Because convective heat transfer increases while radiative heat transfer decreases with a reduction in radius for a blunt-body, there is an optimum r_n that minimizes the heat transfer to the vehicle. The advantage of this configuration is that it can offer designs with the same base radius as a spherical segment without constraining the nose radius. If the optimal heat shield design for a given set of mission requirements has a smaller nose radius than can be offered by a spherical-segment with base radius r, then that nose radius could be generated with a spherically-blunted cone configuration. Also, the equations that render the spherically-blunted cone can be setup to account for the entire spherical-segment regime.

Chrusciel[6] provides a method for calculating the aerodynamic characteristics of spherically-blunted cones. Chrusciel provides the change in the center-of-pressure location with an increase in nose radius and was used in this work to determine a reasonable range of center-of-pressure locations. A discussion on the

misunderstanding present in several sources concerning the calculation of the center-of-pressure location is included in Chapter 3 and those sources are mentioned later in this section.

Jones[16] has completed a wind tunnel investigation on model comparison of the pressure distributions on sharp-nosed and spherically-blunted cones with large cone angles θ_c at hypersonic speeds in air (M_∞ = 7.9), helium (M_∞ = 20.3), and tetrafluoromethane CF_4 (M_∞ = 6.2). The pressure distributions from the three different gases for the tested configurations almost always overlap each other at $\alpha = 0^o$. These results are also compared to theoretical methods including Newtonian theory and concluded that the Newtonian theory does not predict the surface pressure distribution properly near the edges of the configuration. It also shows that there are significant differences in the actual distribution and the one rendered by Newtonian theory. It is shown in this work that although this may be true, Newtonian theory can predict the aerodynamic forces and moments of the Apollo Command Module (spherical-segment) within 15% and the trim angle-of-attack within 1.2^o. Additional work on spherically blunted cones has been completed by Tauber[17] and Bernot.[18]

The spherically-blunted cone configuration was used on the Viking[5,19] and Pathfinder[20,21,22] missions to Mars. Two Viking missions consisted of an orbiter and a lander. The orbiter mapped the surface of Mars, and the landers of the Viking I and II missions had the first successful Mars landings in 1976. The Viking space capsule,[23] shown in Figure 1.3, housed the lander and had a superlight ablative (SLA) heat shield of dimensions $\theta_c = 70^o$, $r_n/d = 0.25$, and $d = 3.505$ m.

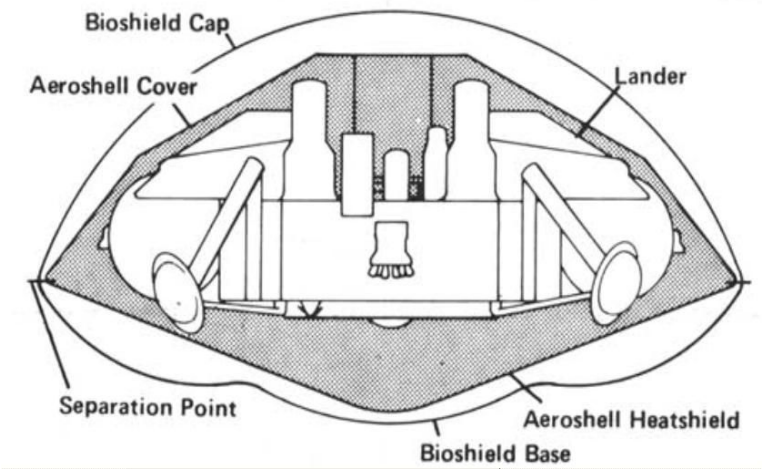

Figure 1.3. Viking Landing Capsule System from Ref. [23].

In 1997, the Mars Pathfinder mission had a Mars rover that was thermally protected during planetary entry by an aeroshell thermal protection system (TPS). Once on the surface, the Pathfinder rover would photograph the immediate vicinity and acquire data that would be sent back to Earth for analysis. Although higher heat fluxes were expected during planetary entry, the Pathfinder mission had a heat shield with the same θ_c and r_n/d as the Viking capsules.

More recent heat shield designs include the raked cone, the biconic and bent biconic cones, the parashield, and the flare-skirt aft-body. The raked cone geometry[24,25] is a spherically-blunted cone raked at an angle as shown in Figure 1.4.

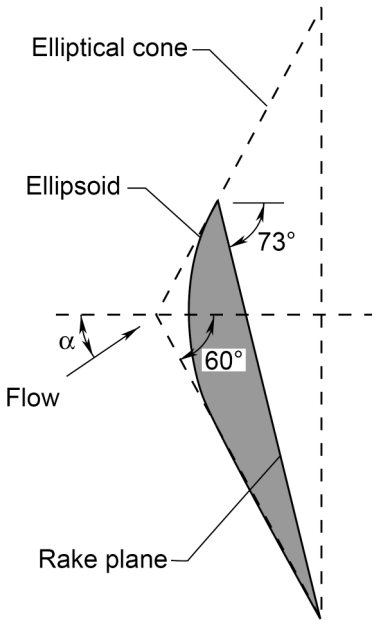

Figure 1.4. Raked cone from Ref. [25].

This geometry offers a way to produce positive lift at zero angle-of-attack. Since the bottom surface of the heat shield has greater surface area than the upper half by design, the flow accelerates more over the bottom surface. This produces positive lift because a larger portion of the surface pressure contributes to lift from the bottom surface than the top surface. The raked cone geometry can be designed to render higher *L/D* at negative angles-of attack than its axisymmetric analogue.

An example of the raked cone geometry is the Aeroassist Flight Experiment (AFE) that NASA worked on and cancelled in the early 1990s. It had a 14 ft diameter and was planned to participate in ten Shuttle-launched experiments. Figure 1.4 shows a few of the dimensions of the AFE's heat shield geometry. It has a 60^o half-cone angle and a 73^o cone rake angle. One additional feature of the AFE's rendition of the raked cone is its ellipsoid nose with an ellipticity equal to 2. The AFE geometry is shown in Figure 1.5.

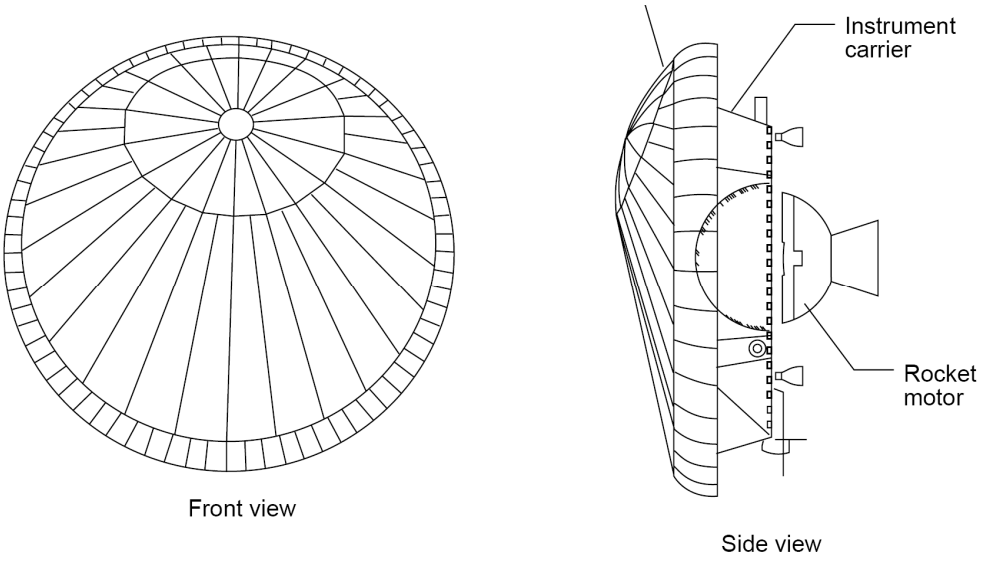

Figure 1.5. AFE flight vehicle configuration from Ref. [25].

At zero angle-of-attack, the *L/D* is approximately 0.30 while it is approximately 0.43 at $\alpha = -10^{o}$.[26] Wells presents the aerodynamic performance and shock shapes of the AFE from wind tunnel results in Ref. [26]. Micol gives the wind tunnel results for its hypersonic lateral and directional stability in Ref. [25] and discusses a simulation of real gas effects on the AFE in Ref. [27].

The biconic and bent biconic bodies have been looked at for an aero-assisted orbital-transfer vehicle application, but it can be argued that they can be used for planetary entry vehicle applications as well. The biconic heat shield is a spherically-blunted cone with an additional conical frustum that has a smaller half-cone angle. The bent biconic heat shield[28,29] has this conical frustum tilted at an angle with the spherically-blunted cone as shown in Figure 1.6(a). Davies and Park[28] present the aerodynamics characteristics of a bent biconic with a fore half-cone angle of 12.84^{o} and an aft half-cone angle of 7^{o} tilted at 7^{o}. This configuration enables a blunt-nosed body to have $L/D > 1$ at positive angle-of-attack as shown in Figure 1.6(b). Because

of its slenderness due to its low half-cone angle, it can be argued that this is an atypical example of a blunt-body.

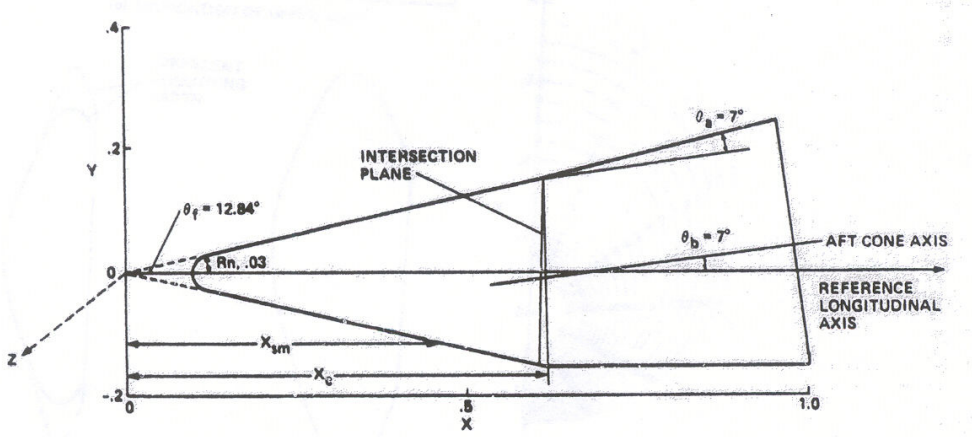

a) Bent biconic geometry

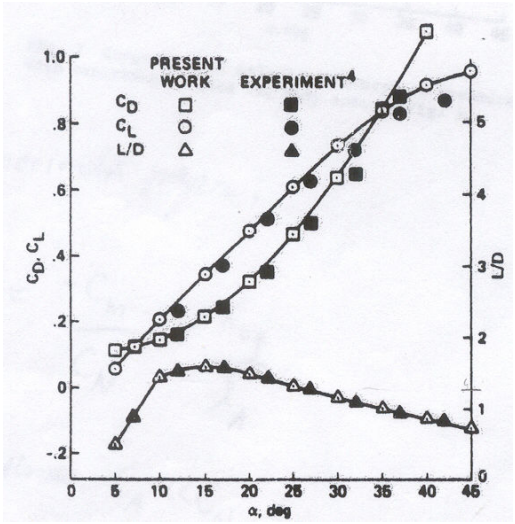

b) Aerodynamic characteristics

Figure 1.6. Bent biconic configuration from Ref. [28].

The common blunt-body produces positive *L/D* at negative angle-of-attack. Davies and Park acknowledge that a half-cone angle larger than 45^o is required to produces positive lift values at negative angle-of-attack for an axisymmetric spherically-blunted cone. The reason for this is that at negative angle-of-attack, the axial force has a larger contribution to lift than the normal force. The axial force's contribution is positive while the normal force's is negative, thereby rendering

positive lift. Slender designs are usually not considered for planetary entry because they produce higher heat transfer rates at the leading edges than blunter designs. Although the presented bent biconic configuration is slender, it will become a feasible design when more advanced high temperature materials are available. In fact, one could argue that this configuration could be feasible today if an ablative material is applied and if the nose radius-of-curvature is larger than that of the edge of the Apollo CM's heat shield, which was the location of highest heat transfer (not the stagnation point). Either way, its fore body half-cone angle can be easily modified for planetary entry applications.

Other more recent vehicle geometries are the parashield and the Slotted Compression RAMP probe. The parashield is a flexible, umbrella-like planetary entry, aerobrake, or aeroassist vehicle.[30] Magazu, Lewis, and Akin completed an analysis of a parashield with a ballistic coefficient of 181 Pa composed of twelve radial spars for LEO re-entry. This configuration has a mass of 150 kg and could be scaled by at least a factor of ten if desired. They determined that this parashield has a hypersonic *L/D* of 0.18 at $\alpha = 15^{o}$ and that there is increased pressure at each spar whether or not concavity exists.[30] The portability of this geometry in closed configuration is a feature unique to parashield and inflatable ballute geometries.

Murbach[31] has examined the Slotted Compression RAMP (SCRAMP) probe, which has undergone several sub-orbital test flights under his supervision. This geometry has a long cylindrical fore body with a hemispherical nose and an aft flare of high half-cone angle ($\approx 70^{o}$) attached to the rear of the vehicle. The aft flare creates most of the drag on the vehicle but also produces a compression ramp leading to flow

recirculation. As a result, several slots are placed where the aft flare meets the cylindrical fore body to minimize the flow recirculation and thereby increase vehicle drag.

The payload in the SCRAMP probe is located inside the front of the cylindrical fore body in order to place the center of gravity far forward. Since the aft flare produces most of the drag on the vehicle, the location of the center of pressure is far behind this center of gravity, rendering a negative $C_{m,cg,\alpha}$. Murbach observed that by increasing the slot size, the maximum pressure on the aft shield is increased. This configuration has a negative $C_{m,cg,\alpha}$ which is considerably better than the Apollo CM's value of -0.143/rad,[13] rendering an outstanding, longitudinally stable entry vehicle. Note that the described configuration does not produce significant lift but may be designed to in future flight tests.

Several of the classic and more recent design configurations were analyzed as lunar-return planetary entry applications in the work of Whitmore.[32] Whitmore's computational results for aerodynamics and stability are consistent with the results presented in this thesis. Bertin[2] provides a thorough overview and several correlations concerning hypersonic aerothermodynamics, and Rasmussen[33] provides an in-depth look at hypersonic aerodynamics.

1.2.2. Heat Transfer

Extremely high heat transfer rates may be experienced during planetary entry. Since the EV undergoes high heat transfer rates for several minutes, the heat transfer load is equally important.

In this section general references for planetary entry heat transfer are first mentioned. Since the heat transfer results of this work consist of stagnation-point heat fluxes, the corresponding references are mentioned and referred to throughout the text. For calculating the heat flux, there are more sources and emphasis in this work given to radiation than convection because radiation is an ongoing research topic. The drawback of this work is that the heat load is not determined, but it is mentioned as an important topic for future work.

In recent analyses, Park[34] and Rochelle[35] discuss the aerothermodynamic environments for Mars entry and return, as well as lunar return. Park presents an analysis of two human missions (one is 330 days and the other is 436 days) to Mars and notes that the existence of an optimum nose radius for the tradeoff between convective and radiative heat transfer. Rochelle analyzes several capsule geometries including the biconic and modified AFE aeroshell capsules for Mars entry and notes that with an increase in entry velocity from 10 km/s to 12 km/s, the radiative heat flux goes from 13% to 42% of the total heat flux.

Two classic references from Rose[36] and Kemp[37] at the Avco-Everett Research Laboratory give a general overview of stagnation-point and laminar heat transfer in dissociate air. Kemp notes that the maximum heat transfer flux can be larger than the stagnation-point heat flux, as is the case for a flat-nosed body in which the convective heat transfer flux is approximately 30% larger at the corner than that at the stagnation-point. This is noticed in the wind tunnel results for the Apollo CM presented by Lee,[38] in which the corner has a heat flux that is 80% larger than at the stagnation-point at $\alpha = 33^{o}$ at $M_{\infty} = 9.07$. The main Apollo missions that included the

astronauts did not re-enter at 33^{o}, and so the maximum heating rate was lower. This wind tunnel test was completed to find out the worst-case scenario with the crew compartment (aft body) being tangent with the freestream flow. Lee also offers a thorough explanation of the convection and radiative heat transfer and gives the heat flux and pressure distributions about the heat shield. Note that the radiative heat flux correlation is analyzed in Chapter 7, but is not recommended for use since there are simpler correlations that follow the Apollo flight data better.

Two Apollo CMs were instrumented for aerothermodynamic analysis. Lee[39] compares the flight results from superorbital entry, as is the case in lunar return, with predictions (note that Ref. [38] was written before the Apollo missions were completed). Lee also gives an aerothermodynamic evaluation in Ref. [40] that presents the highlights of the re-entry aerodynamics and heat transfer for the Apollo missions.

The heat shield of the Apollo CM is the main part of the Apollo's Thermal Protection System (TPS). Pavlosky[41] details the history of designing the Apollo TPS and the manufacturing process. Also, he includes a summary of the predicted maximum heat transfer rates and loads for Apollo missions 8 and 10-16. Park and Tauber[42] provide a current review of heat shielding problems experienced by the Apollo 4, 6, Pioneer-Venus, and Galileo Probe missions. Also, Scotti[43] presents a compilation of TPS technologies that were current in 1992 including the shuttle tiles, a TPS design for the cancelled NASA Aeroassist Flight Experiment (AFE), and proposed future materials.

The amount of stagnation-point heat transfer is one of the main aerothermodynamic benchmarks for comparing the capability of one entry vehicle to another. The stagnation-point heat transfer is not necessarily analogous with the point of maximum heat transfer, as was the case for the Apollo CM and the flat-nosed body. As a result, a more appropriate benchmark would be to compare the point of maximum heat transfer. Because this requires a more computationally expensive process that is beyond the focus of this thesis, previous work concerning the convective and radiative heat transfer at the stagnation-point has been acquired.

Lovelace[44] provides correlations for both convective and radiative heat transfer at the stagnation point; it will be shown in Chapter 7 that the radiative heat transfer correlation is one of two that matches the Apollo flight data the closest.

For convective heat transfer, Tauber[45] provides the stagnation-point, laminar and turbulent flat plate correlations that he validates against the US Space Shuttle heating rates. Tauber applies the well-known Fay and Riddell[46] relation that assumes that convection is inversely proportional to the square root of the nose radius. This would suggest that the convective heat transfer approaches zero as the nose radius is increased, but Zoby[47] notices that blunt bodies have more enthalpy than expected by this theory. Zoby shows that an adjustment that is based on the change in the velocity gradient from that of a hemisphere can produce an effective radius that can be applied to improve the theory's accuracy.

For radiative heat transfer, Tauber[48] also provides the stagnation-point correlations for Earth and Mars entries. This is one of the two correlations that match the Apollo flight data the closest. Originally, Tauber's correlations were not meant to

be applied to the entire altitude regime on Earth, but this thesis will show that there is not much difference from Lovelace's correlation[44] when following the Apollo 4 trajectory. A review of the stagnation-point radiation from the Apollo 4 is available by Park.[49]

Cauchon[50] provides the radiative heating results from the Second Flight Investigation of the Reentry Environment (FIRE II) experiment at the superorbital entry velocity of 11.4 km/s (37,400 ft/s), which is slightly larger than the fastest Apollo entry at 10.7 km/s (35,000 ft/s) for Apollo 4.[11] Cauchon compares the theory to the few flight test data points. The FIRE II had three spherical-segment heat shields layered over each other. After initiating planetary entry, heat transfer data is obtained for the first heat shield. Then it is jettisoned from the entry vehicle at a chosen point in the trajectory, leaving the second heat shield surface to face the freestream flow. Data is obtained for the second heat shield, and then it is jettisoned, leaving the third heat shield surface to protect the vehicle for the remainder of the trajectory. The three heat shields had different nose radii: 0.935 m, 0.805 m, and 0.702 m for the first through third heat shields respectively. Cauchon shows that the theory is closer to the FIRE II calorimeter data by accounting for radiation cooling and coupling; otherwise, the theory overshoots the calorimeter data by 30%.

Ried[51] compares the flight measurements and engineering predictions on the Apollo CM for mission four. Ried also provides a computational approximation of the total radiative heating rate near the stagnation point including ultraviolet lines and continuum, which were not measured by the radiometers on the heat shield of Apollo 4. The shock-standoff distance over the time of maximum radiative heat transfer is

also provided. A correlation that closely matches the behavior of how the stagnation-point shock standoff distance varies with normal-shock density ratio is included and could be used along with Lovelace's[44] or Tauber's[48] correlations to calculate stagnation-point heat transfer fluxes. For planetary entry at velocities larger than that of the Apollo missions, curve fits of inviscid heating rates and cooling factors have been produced by Suttles.[52] It is recommended that these curve fits be validated before use in future work.

Determining how the stagnation-point radiative heat transfer rate varies as a function of angle of attack for the Apollo CM is investigated by Walters.[53] By accounting for the stagnation-point shock-standoff distance, Walters is able to approximate this behavior, although the wind tunnel data is noticeably scattered. Additionally, he applies Kaattari's correlation[54] to produce an outstanding match of the Apollo CM's experimental shadowgraph of the shockwave shape at Mach 19.5 and 31.5^{o} angle of attack.

The Kaattari method approximates the shock-standoff distance of a blunt-body at zero angle of attack[55] and the shock envelope of spherical-segment blunt-bodies at large angles of attack.[54] This highly empirical method uses the normal shock density ratio to approximate the location of the sonic line on the body as well as the shock and body surface inclinations at the sonic point along with theory to determine the ratio of the shock-standoff distance to the nose radius. Since a planetary entry vehicle enters the atmosphere at high velocities, high temperatures are produced in front of the heat shield, and so high temperature gas correlations from Srinivasan[56] (an updated version of the Tannehill[57] correlations) can be used to determine the

effective specific heat ratio to determine the normal-shock density ratio. This thesis work applies the Kaattari method, with its implementation described in Chapter 3, to apply Lovelace's[44] and Tauber's[48] radiative heat flux correlations to blunt-bodies at any angle of attack.

1.2.3. Entry Trajectory

The entry phase of the trajectory begins as the entry vehicle crosses the Earth's entry interface (EI), commonly assumed at an altitude of 122 km. The entry trajectory ends when the descent phase is initiated. Figure 1.7 provides the entry trajectory for the Apollo 4 (AS-501) mission.[11] At the beginning of the entry trajectory at h_t = 122 km ≈ 400,000 ft, the altitude map in Figure 1.7(a) shows a relatively steady drop until ground time 30,030 s. The CM reaches a trough in the trajectory at h_t = 55 km and slowly increases in altitude up to 73 km and descends. The velocity distribution is given in Figure 1.7(b). The reaction control system (RCS) is the only way to control the capsule during the entry phase. Each Apollo CM had a fixed, trim α, usually between -17^o and -25^o, and so bank angle modulation was the primary means of controlling the vehicle's flight path during entry. The RCS includes roll thrusters that could bank the lift vector a full 360^o. The Command Module's computer had a predictor-corrector algorithm to provide adequate guidance, navigation, and control (GNC) during entry. Figure 1.7(c) shows the resulting bank angle history generated by use of the RCS controlled by the GNC subsystem. It indicates that a full 180^o, which corresponds to the lift down position, was required for 25 s of the trajectory, suggesting that the vehicle would have bounced out of the

atmosphere without bank angle modulation. Figure 1.7(d) shows that a maximum deceleration of 7.25 *g* occurs right before the CM completes the dip at 55 km.

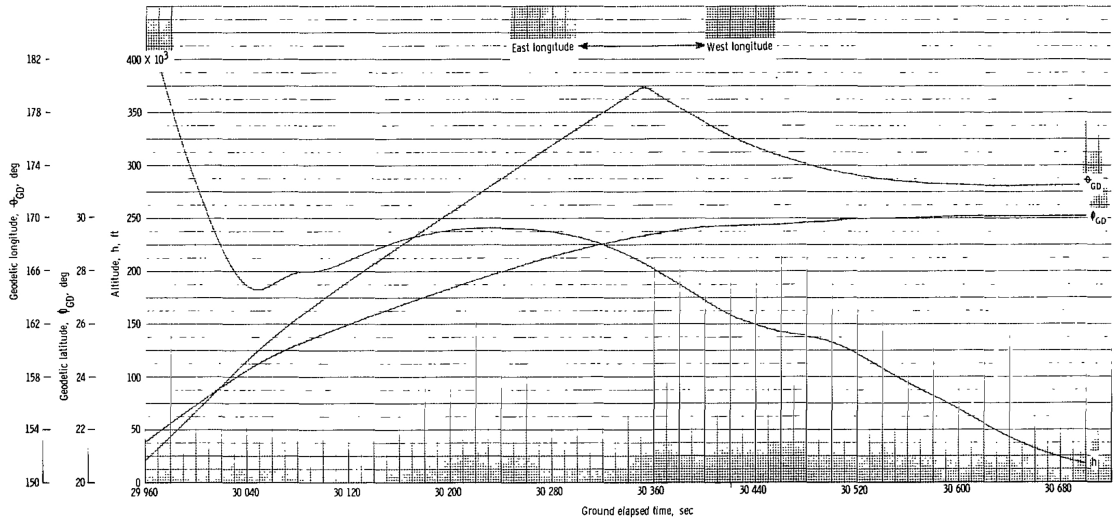

a) Altitude profile

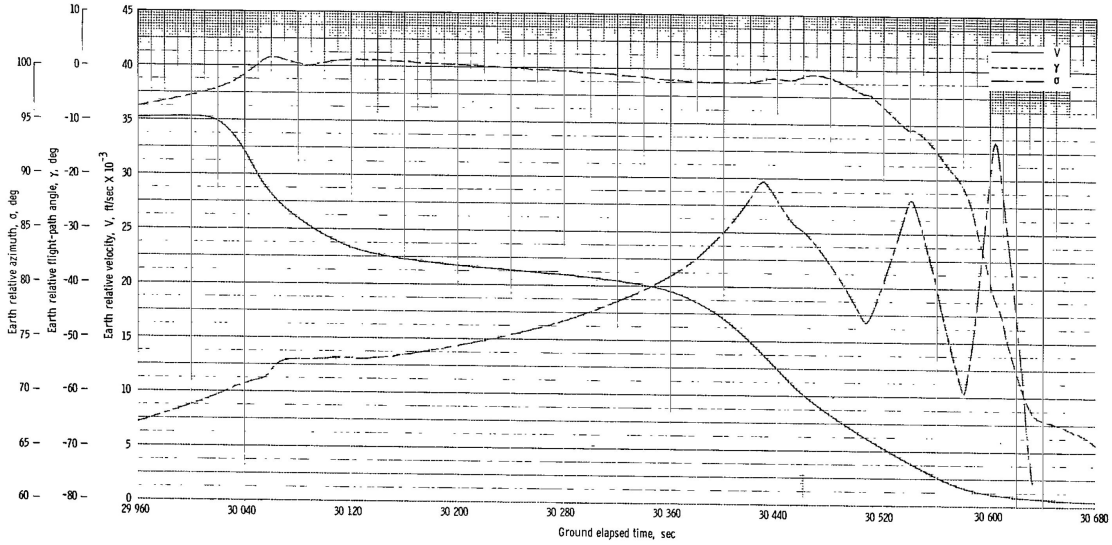

b) Velocity profile

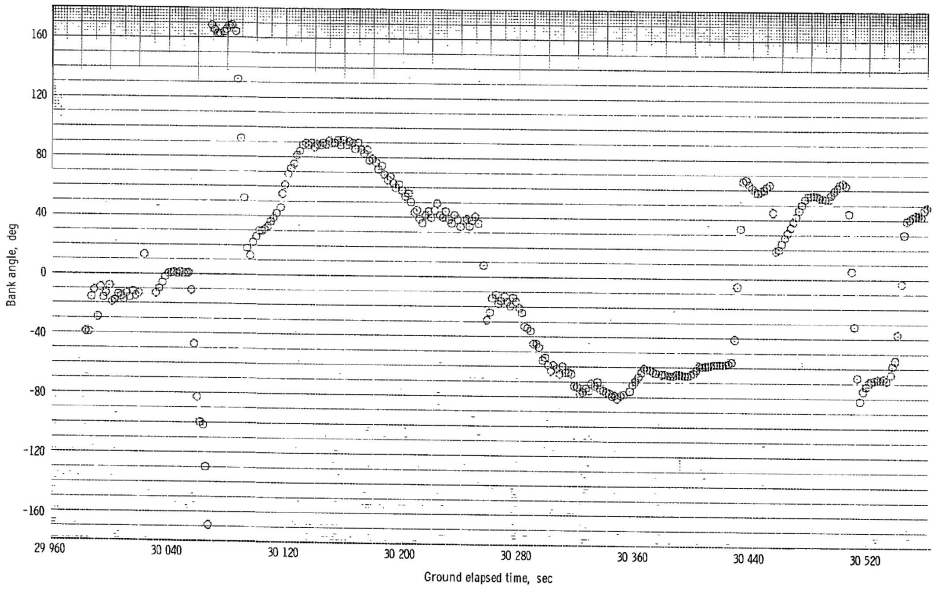

c) Bank angle profile

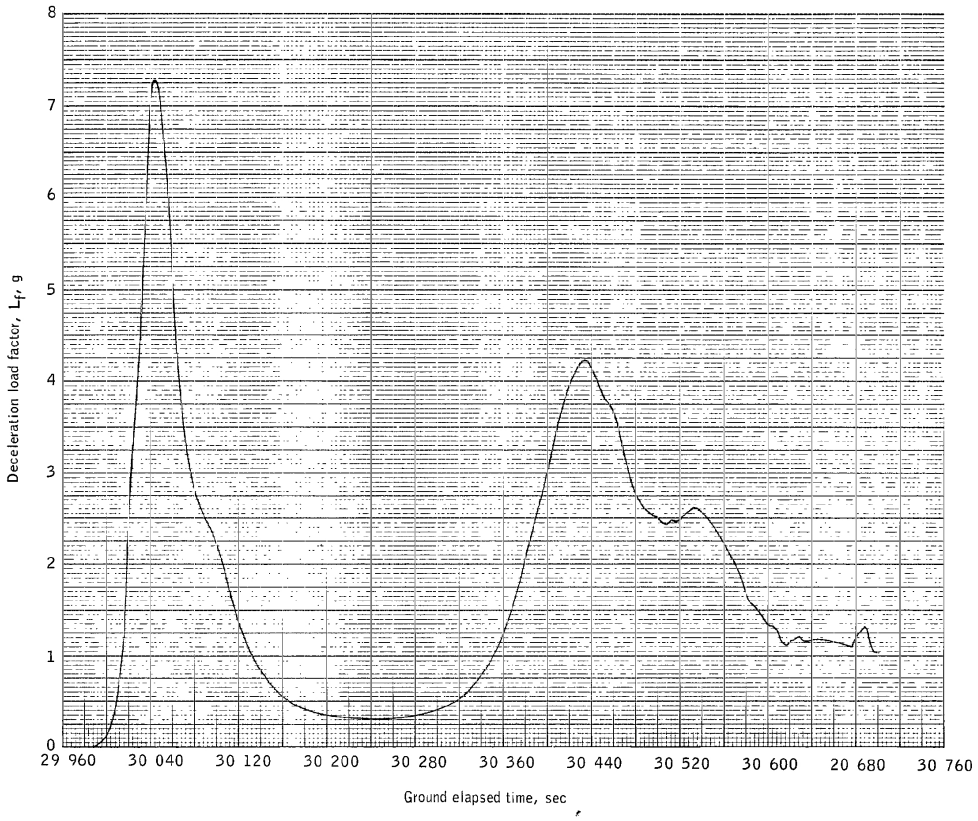

d) Deceleration load profile

Figure 1.7. Apollo 4 CM reentry trajectory from Ref. [11].

NASA has several computer-based simulated trajectory software packages that solve the equations of motion and account for the high detail needed to properly model ascent, interplanetary, and planetary entry trajectories for actual missions. The Program to Optimize Simulated Trajectories (POST) is one such benchmark trajectory software package.[58,59] POST includes highly-detailed models for in-atmosphere trajectory modeling. Initially written for the US Space Shuttle program, it utilizes a projected gradient method that allows for complex vehicle ascents and entry trajectory optimization. Another benchmark program Optimal Trajectories by Implicit Simulation (OTIS) provides similar functionality but allows also the ability to solve the equations of motion implicitly.[60] Both provide 3DOF and 6DOF simulation modes.

Much trajectory simulation research has been completed for both Earth entry and Mars entry. Braun[61,62] has completed trajectory optimization utilizing bank angle control for both manned Mars aerobraking and for Mars return. He has shown that performing bank angle modulation with guidance allows for a reduction in deceleration loads by 40%, as shown in Figure 1.8. Using bank angle modulation also increases the entry corridor width, which is the difference between the greatest and smallest flight-path-angles at the EI. A large enough corridor width is necessary to account for flight and instrument uncertainties in order to maintain mission requirements. A comparison between the constant bank angle flyable corridor and the bank angle modulation entry corridor is given in Figure 1.9.

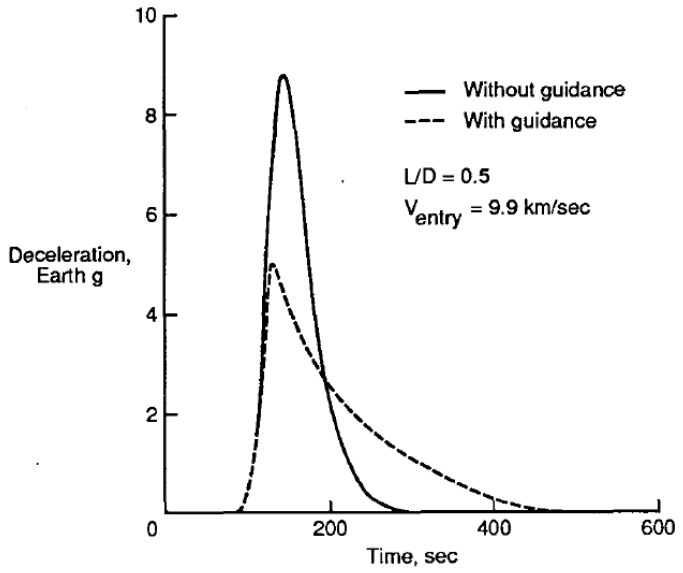

Figure 1.8. Comparison of Mars aerobraking with and without guidance from Ref. [61].

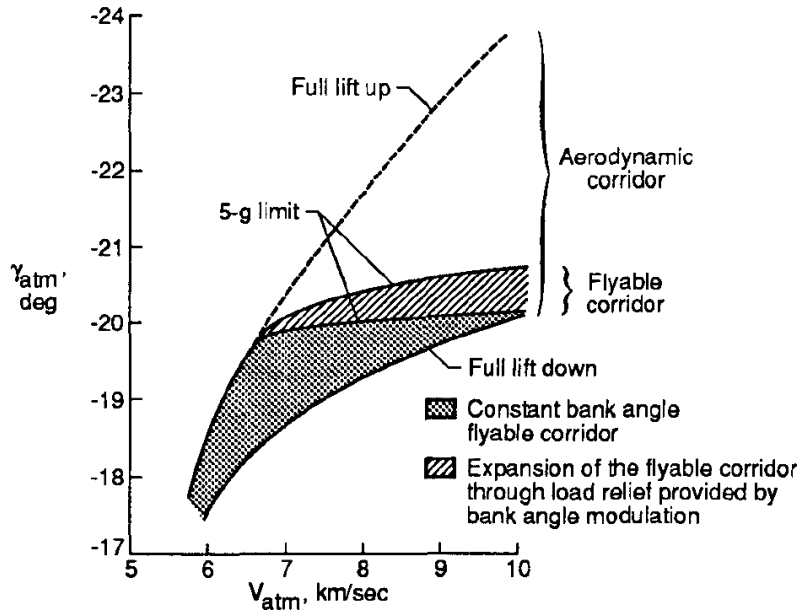

Figure 1.9. Comparison of Mars entry corridors for *L/D* = 0.5 based on atmospheric exit into a 1 Sol parking orbit from Ref. [61].

Since trajectory optimization and guidance law implementation were the primary foci, a given mass and ballistic coefficient would be assumed, along with a set of lift-to-drag ratios to complete the analysis. For human return from Moon and

Mars, Putnam and Braun[63] have studied direct entry trajectories (no entry skips) with linear feedback control. Figure 1.10(a) shows the required *L/D* for direct entry with a given *g*-limit. Putnam suggests a 0.4-deg or greater entry corridor width. With a 5 *g* deceleration limit, the direct entry corridor widths for different combinations *L/D* and *BC* are provided in Figure 1.10(b). In all of this entry trajectory work, the focus was not on the effects of different heat shield geometries at desired values of *L/D*.

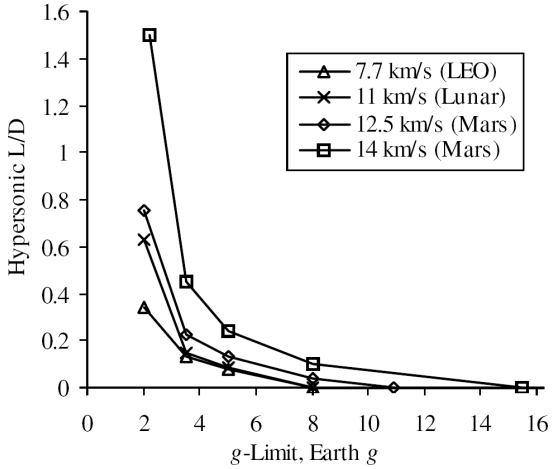

a) Required *L/D* for direct Earth entry for a given maximum *g* limit

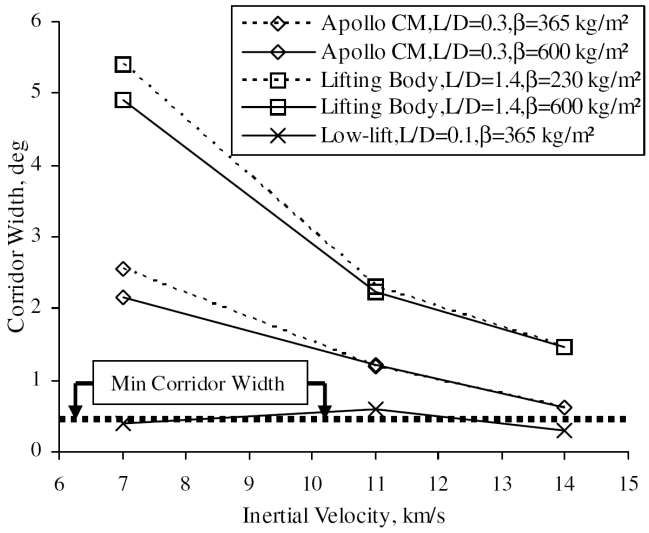

b) Direct-entry corridor width for several vehicles

Figure 1.10. Direct Earth entry results from Ref. [63].

1.2.4. Misconceptions

Misunderstandings and discrepancies in publications have been noticed throughout the literature survey. The most common misunderstanding is the theory behind calculating the *x*-location of the center of pressure of a blunt body. This location is dependent on both the axial force and normal force's contributions to the pitching moment; neither can be ignored. However, several references calculate the *x*-location by assuming the axial force's contribution to the pitching moment is negligible. This thesis explains in Chapter 3 that the axial force's contribution to the pitching moment is at least the same order of magnitude as the normal force's contribution and thereby must be accounted for in the case of a blunt body. From here, it is possible to match the Apollo CM's pitching moment wind tunnel data as will be shown in Chapter 3.

Bertin,[2] Rasmussen,[33] and Regan[64] have textbooks that assume the axial force's contribution to the pitching moment is negligible in sections concerning blunt bodies. However, Bertin's textbook[2] also has the correct derivation, and the example in which the assumption is made in the first edition of Regan's textbook[64] has been removed from Regan's second edition.

Figure 9 in the work of Levine[65] provided the *x*-location of the center of pressure of several spherical and blunt cone geometries. However, they are different from the values of this thesis by one order of magnitude except for one case. Because the work of this thesis was able to match the aerodynamic and stability results of the Apollo wind tunnel and flight test data and basic conical shapes, the use of Levine's values of the *x*-location is not recommended.

Arora[66] maximizes the center of pressure's *x*-location for a spherically-blunted cone-flare configuration. However, Arora's work assumes that the axial force's contribution to the pitching moment is negligible. As a result, the optimized *x*-location value is infeasible. Because the *x*-location is incorrect, it is not possible to find the correct pitching moment value about the blunt-body's center of gravity. An active researcher concerned with the aerodynamic performance and the stability of blunt-body planetary entry geometries should be attentive to this issue.

Papadopoulos[67,68] has figures that are mislabeled as trajectories for Apollo missions AS-201, 4, and 6. The only relations between the figures and the Apollo missions are the mentioned missions' entry flight-path angles. The plots are meant to show code output according to a particular Apollo mission's entry flight-path angle. Because several plots on a single page have legends with Apollo mission numbers, it is easy for one to assume that these must be the flight velocities, decelerations, and Reynolds numbers experienced by the Apollo missions listed. This is a simple miscommunication and not suggesting that Papadopoulos's results are not accurate; he has validated his results with POST.

Several sources that are not suggested for estimating the radiative heat transfer at the stagnation-point for an Apollo-like capsule include Barter[69] and Gupta.[70] It is possible that both sources have typographical errors in the equations, but this is not certain. However, it is shown in Chapter 7 that the implementations of these equations do not match the behavior of flight test data from Apollo 4. There are other correlations that were found to match the flight test data closely.

1.3. Research Objectives

Several entry trajectory optimizations with bank angle modulation have been completed without considering the effects of different geometric features of the heat shield, the primary reason being that those studies focused on trajectory optimization with guidance. They would assume effective radii for convection and radiation based on previous work. The primary objective of this research is to determine which geometric features of an Earth entry vehicle heat shield advance the state-of-the-art in hypersonic aerothermodynamic performance.

Since cross range, down range, and heat transfer performance are directly associated with mission requirements and material constraints; this work seeks to find optimal blunt-body heat shield designs from these standpoints. A high-order trajectory model in conjunction with low-order aerothermodynamic models is applied to balance the need for fidelity with the desire to have practical computational times, allowing the optimizer to consider a wide range of heat shield geometries. Contributions of viscous shear forces and turbulence are not considered.

As this is also a systems study, a secondary objective is to produce optimal tradeoff relationships between performance parameters. This work utilizes a population-based, multi-objective optimization scheme, in which a differential evolutionary algorithm is employed to optimize two objectives simultaneously. Focus is centered on maximizing down range or cross range while simultaneously minimizing stagnation-point heat load or heat flux. Although guidance is not incorporated into the trajectory analysis, bank angle modulation is applied and sufficient for determining which geometric features are advantageous and which are

unfavorable. Another secondary objective is to utilize trajectories that indicate the aerothermodynamic performance that would be expected for an actual mission. This is accomplished by utilizing bank angle modulation similar to that applied in the Apollo missions[11] to rotate the lift vector, and by incorporating an entry corridor methodology to focus on that specific part of the trajectory design space that would be similar to the expected design space for an actual mission.

This work fulfills these objectives for both lunar and Mars return flight conditions and decelerations requirements. Although the Apollo heat shield design was successful for returning astronauts back to Earth, it is not necessarily the optimal design from an aerothermodynamic standpoint. The final secondary objective is to compare the optimal heat shield geometries for these two cases. For lunar return at 11 km/s, the convective heat load is usually greater than the radiative heat load while the radiative heat load is greater for Mars return, assuming 12.5+ km/s. As a result, it is unknown a priori whether a heat shield optimal for lunar return is optimal for Mars return.

1.4. Thesis Overview

This thesis is organized into fifteen chapters. The investigated blunt-body geometries are introduced in Chapter 2. Then Chapter 3 provides the Newtonian aerodynamic theory and a method for approximating the shock-standoff distance from the stagnation point of a blunt-body. It also includes the equations for determining the static stability of a given heat shield geometry and provides explanations for a couple misinterpretations of basic theory. Chapter 4 includes the main assumptions and

correlations for convective and radiative heat transfer at the stagnation point. Chapter 5 provides the method for scaling the heat shield based on the mission profile, making it possible to do a mass estimate of the corresponding entry vehicle. The fundamentals of planetary entry trajectories and the entry corridor methodology are included in Chapter 6. A description of the aerothermodynamic low order code is provided in Chapter 7. Note that the geometric design space and aerothermodynamics code setup is based on the author's M.S. research in Ref [71]. The high-order trajectory code is described and validated in Chapter 8. Chapter 9 provides a general overview of the optimization theory and parametric study of the optimization parameters. Chapter 10 includes the initial results for lunar and Mars return optimization before the entry corridor analysis is applied and with more relaxed maximum deceleration limits. Chapter 11 provides a detailed optimization setup for the finalized lunar and Mars return results, including the application of the entry corridor analysis. Chapter 12 includes the lunar return results while the Mars return results are provided in Chapter 13. The final results from lunar and Mars are compared in Chapter 14, and the final conclusions of this dissertation along with suggested future work are detailed in Chapter 15.

Chapter 2. Blunt-Body Heat Shield Geometries

Each heat shield in this work is defined by two geometries: the base cross-section of the heat shield and the axial shape that is swept about the central axis and modified to match the base cross-section. The coordinate system for this work is included in Figure 2.1 with the sweep angle ω and conventional directions for positive moments. One change from convention that is not shown occurs when the vertical lift coefficient $C_{L,V} < 0$, in which the direction of the positive rolling moment switches in order for a negative $C_{l,\beta}$ to still indicate a statically roll stable shape. An explanation of the sign reversal is included in the stability section of Chapter 3.

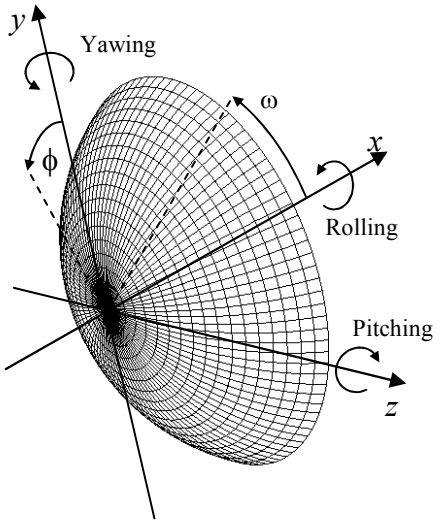

Figure 2.1. Fixed-body coordinate system, spherical-segment, $\omega = 30^o$, $\theta_s = 60^o$, $n_2 = n_3 = 2$.

2.1. Axial Shapes

The shape of the heat shield that protrudes from the base is called the axial shape in order to easily differentiate the protruded shape from the cross-section. The axial shape of the heat shield by itself represents the shield's profile if its base cross-

section were to be circular. If the base cross-section is not circular, then the axial shape is at least the top half of the shields profile at sweep angle $\phi = 0^o$. Then the axial shape is modified to follow the outline of the base cross-section. Three axial shapes: the spherical-segment, the spherically-blunted cone, and the power law are applied in this work and described in the following sections along with how they are generated.

Raked-off geometries including the raked cone Figure 1.5 are not considered in the present work for two reasons. First, the combinations of axial profiles and base cross sections in the present work already provide a wide range of lift-to-drag ratios up to 2.14 with power law axial profiles.[105] There is no evidence that a raked-off geometry would provide significantly greater *L/D*. Additionally, in maximizing overall aerothermodynamic performance, *L/D* will be traded off with $Q_{s,tot}$; and *L/D* is commonly below 1.0. Second, this work is investigating the performance of new designs, and this new design space is sufficiently large without the raked-off geometries.

2.1.1. Spherical-segment

A general spherical-segment is a region of a sphere that is left after the sphere is cut by two parallel planes. A closed spherical-segment is a region of a sphere encompassed by spherical-segment angle θ_s, in which $\omega = 90^o - \theta_s$, in which only one plane, parallel to the *yz*-plane divides the sphere. A closed spherical-segment, one shown in Figure 2.1, is also known as a spherical cap and is the type that is applied to previous and present heat shield design.

For this work, only the profile of the spherical-segment is utilized by using the following equations for the *xy*-plane at zero sweep angle:

$$r_{max} = x_{max}/(1\text{-}\cos(\theta_s)), \tag{2.1}$$

$$x_k = r_{max}(1\text{-}\cos(\theta_k)), \tag{2.2}$$

$$y_k = r_{max}\sin(\theta_k), \tag{2.3}$$

in which $x_{max} = 1$ in order to normalize the geometry to the length of the heat shield $l = x_{max}$. This set of equations produces the axial shapes shown in Figure 2.2 (a) for the Apollo CM ($\theta_s = 25^o$) and a hemisphere ($\theta_s = 90^o$). The corresponding spherical heat shields, which have circular cross-sections, are shown in Figure 2.2 (b) and (c).

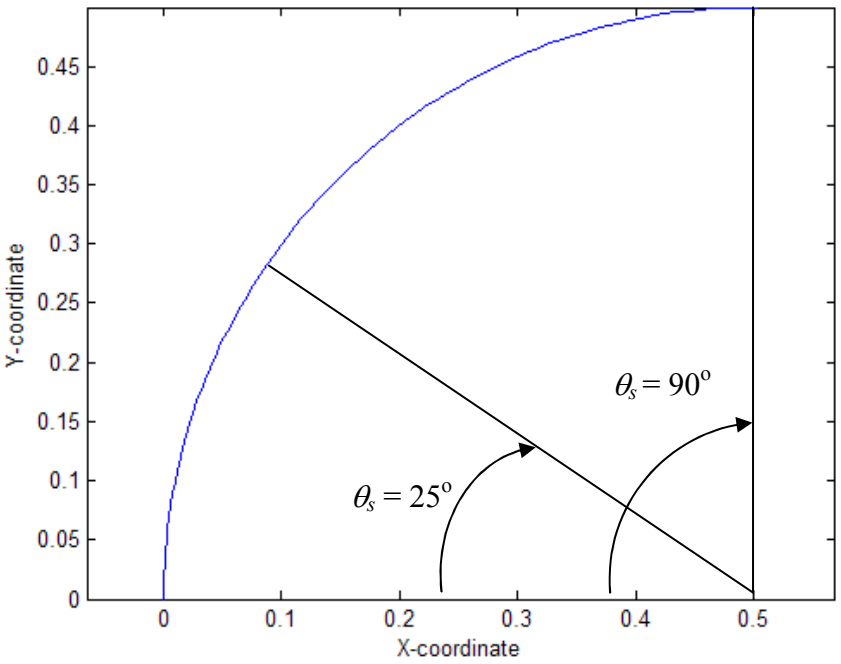

a) Spherical-segment axial profiles at $\phi = 0^o$.

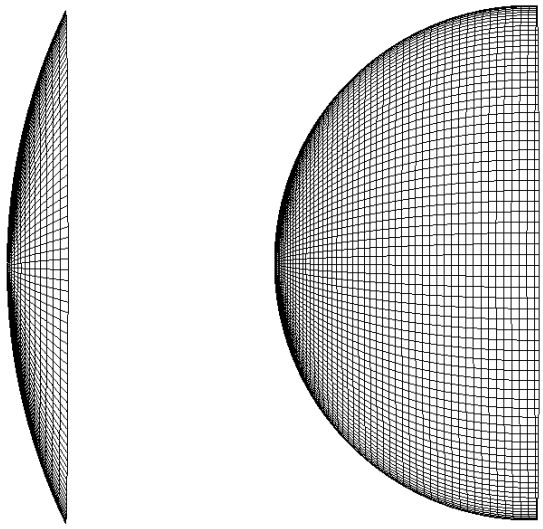

(b) Spherical heat shield, $\theta_s = 25^o$. **(c) Spherical heat shield, $\theta_s = 90^o$.**

Figure 2.2. Spherical axial profiles and heat shields.

2.1.2. Spherically-blunted Cone

The spherically-blunted cone's geometric parameters have been introduced in the previous work section of Chapter 1. Figure 1.1(b) is an example of the spherically-blunted cone heat shield. Its axial profile has two parts, a spherical nose and the conical body. The spherical nose is generated by producing a spherical-segment with $\theta_s = \pi/2\text{-}\theta_c$ to provide slope continuity from the spherical nose to the conical body. If the conical base is divided into N vertical sections that are equally spaced along the x-direction, then the spherically-blunted cone profile in the xy-plane is generated with the system of equations

$$x = \begin{cases} r_n(1-\cos\omega), & 0 \le \omega < \theta_s \\ r_n(1-\cos\omega-\sin\omega) + y/\tan\theta_c & \omega = \theta_s, \end{cases} \tag{2.4}$$

$$y = \begin{cases} r_n \sin\omega & 0 \le \omega < \theta_s \\ r_n \sin\omega + \dfrac{\frac{1}{2}d - r_n \sin\omega}{N} n & \omega = \theta_s, 0 \le n \le N. \end{cases} \tag{2.5}$$

Also, the spherical-segment can be produced using only the first equation for both x and y over the range $0 \le \omega \le \theta_s$.

2.1.3. Power Law

The power law offers axial shapes with a wide range of bluntness controlled by coefficient A and exponent b with the equation

$$y = Ax^b. \tag{2.6}$$

The effects of varying these two parameters are shown in Figure 2.3. For a fixed value of b, increasing the slenderness ratio A increases the bluntness of the shape. As a result, the effects of increasing the slenderness ratio should be similar to those of decreasing the spherical-segment angle θ_s or increasing the spherically-blunted cone angle θ_c.

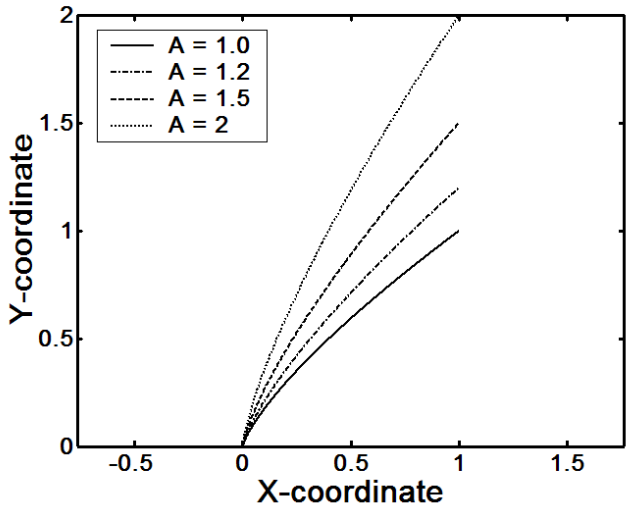

(a) Axial profile varying *A*, *b* = *0.75*.

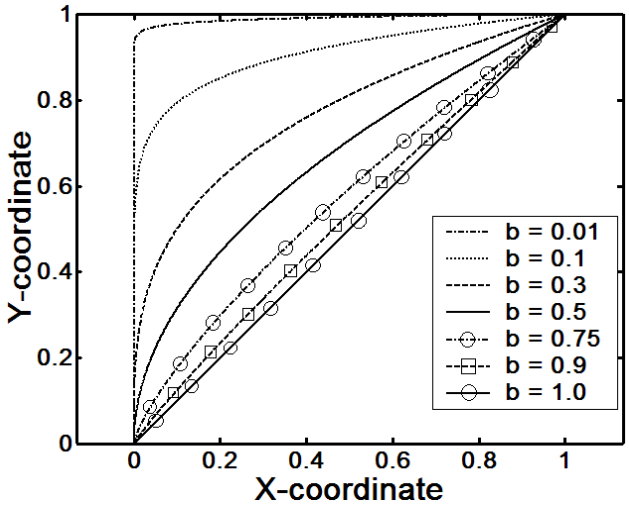

(b) Axial profile varying *b*, *A* = 1.

Figure 2.3. Power law axial shape.

For a fixed value of A, increasing the value of exponent b from 0.01 to 1.0 transforms the axial shape from a flat nosed body to a sharp cone respectively. As a result, a power law with $b = 1.0$ is equal to a sharp cone with a corresponding angle θ_c. The power law can also nearly match the spherical segment for a given set of A and b or it could produce profiles that are different from these two classic shapes.

Rasmussen[33] mentions that two minimum drag power-law bodies have exponent values of two-thirds and three-fourths based on Newton-Busemann and Newtonian surface pressure models.

When calculating the shock-standoff distance, special cases account for this heat shield shape having a discontinuity at the tip ($x = 0$) and are discussed in Chapter 3. Varying the power law's slenderness ratio and exponent should render a wide range of aerodynamic performance and stability characteristics.

2.2. *Cross-section Shapes*

The cross-section shape is the geometry of the heat shield's base. The base cross-section is usually chosen to be circular although there have been a couple cases of slightly elliptic cross-section including the AFE.[26] For optimization, it would be ideal to have a base cross-section equation that can generate a wide-range of shapes. In order to produce eccentric base cross-sections, the equation of the ellipse can be applied. To produce shapes that range from a parallelogram to an ellipse, Sabean[72] uses the following Cartesian equation for a typical superellipse curve:

$$\left|\frac{x}{a_1}\right|^{v} + \left|\frac{y}{b_1}\right|^{v} = 1, \tag{2.7}$$

By varying v from 1 to 2, the superellipse can transform from a parallelogram to an ellipse.

In 2003, Gielis[73] published a more generalized superellipse equation called the superformula; it can transform a polygon into an ellipse and then into a rounded-edge concave polygon. It defines the cross-section radius for $0 \le \phi \le 2\pi$:

$$r(\phi) = \left[\left|\frac{\cos\left(\frac{1}{4}m_1\phi\right)}{a_1}\right|^{n_2} + \left|\frac{\sin\left(\frac{1}{4}m_1\phi\right)}{b_1}\right|^{n_3}\right]^{-1/n_1}, \tag{2.8}$$

in which m_1 corresponds to the number of sides of a polygon, n_1 and n_2 are modifiers, and n_3 is set equal to n_2 to produce sharp or rounded-edge polygons. In the present work, n_2 was set to 1, and then values of n_1 that produced sharp-edged, non-concave polygons were determined. Corresponding values of n_2 for rounded-edge polygons were then determined. Because of the increased heat transfer that would be produced on sharp edges, zero radius-of-curvature polygons were not considered. Setting $n_2 = 2$

produces an ellipse; increasing n_2 beyond 2 will produce concavity in the shape. Table 2.1 presents the values for m_1, n_1, n_2, and n_3 to produce rounded-edge polygons, both straight and concave.

Table 2.1. Superformula parameters for rounded-edge polygons ($n_3 = n_2$).

m_1	n_1	n_2
4	1.00	1.50 — 4.0
5	1.75	1.50 — 4.0
6	2.30	1.50 — 4.0
7	3.20	1.50 — 5.0
8	4.00	1.40 — 6.0
9	5.50	1.40 — 6.0
10	7.00	1.40 — 7.0

The cross-sections in this analysis include polygons ranging from four to ten sides. Once m_1 and n_1 are set, n_2 can be varied to transform a polygon into an ellipse and then into a concave polygons, in which $n_3 = n_2$. With the parameters in Table 2.1, the cross-sections in Figure 2.4 can be constructed. If a rounded-edge pentagon is constructed, as shown in Figure 2.4(d), then n_2 can be increased to 2 in order to produce the corresponding ellipse in Figure 2.4(b), and then n_2 can be increased to 4 to produce the rounded-edge concave pentagon in Figure 2.4(e).

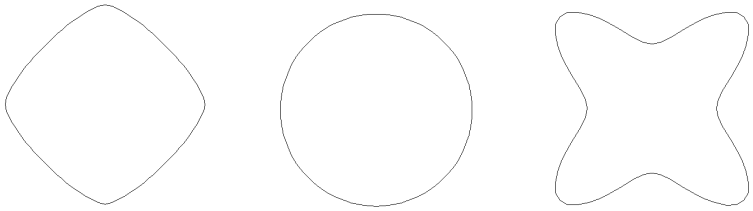

a) $m_1 = 4$, $n_2 = 1.5$. **b) $n_2 = 2.0$.** **c) $m_1 = 4$, $n_2 = 4.0$.**

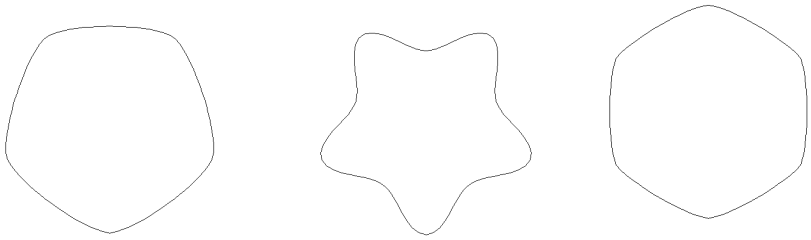

d) $m_1 = 5$, $n_2 = 1.5$. **e) $m_1 = 5$, $n_2 = 4.0$.** **f) $m_1 = 6$, $n_2 = 1.5$.**

Figure 2.4. Cross-section shapes produced using parameters from Table 2.1.

If $a_1 = b_1 = 1$, the cross-section will have no eccentricity, and so $n_2 = 2$ will produce a circular cross-section. Because a_1 and b_1 in Eqn. (2.8) relate differently to eccentricity than they do in Eqn. (2.7) for $v = 1$, it was concluded that it is easier to produce an eccentric heat shield by multiplying either a_1 or b_1 by the cross-section radius r when generating the blunt body as described in the next section.

2.3. *Generating Blunt-Bodies*

Once the axial shape at $\phi = 0^o$ is rendered, it is swept about the central body axis (the x-axis) according to the chosen base cross-section with Eqn. (2.8) according to the following three-dimensional equation set

$$\begin{cases} x_{j,k} = x_k \\ y_{j,k} = a_2 r_{j,k} \cos(\phi_j) \\ z_{j,k} = b_2 r_{j,k} \sin(\phi_j), \end{cases} \tag{2.9}$$

in which j and k are indices, r is the radius at a given j,k location, and a_2 and b_2 are the lengths of the semimajor and semiminor axes of the generated blunt body. In this work, eccentricity e has a range in-between –1 and 1, in which $e < 0$ corresponds to oblate geometries and $e > 0$ corresponds to prolate geometries. The semimajor and semiminor axes are determined from the following equation sets

$$a_2 = \begin{cases} b_2\left(1-e^2\right)^{\frac{1}{2}} & -1 < e < 0, \\ 1 & 0 \le e < 1, \end{cases} \tag{2.10}$$

$$b_2 = \begin{cases} 1 & -1 < e < 0, \\ a_2\left(1-e^2\right)^{\frac{1}{2}} & 0 \le e < 1. \end{cases} \tag{2.11}$$

The superformula cross-section equation reflects the shapes made by $n_2 > 2$ about the horizontal axis. As a result, to keep consistency when varying n_2, the reflection was removed by setting $y_{j,k} = - y_{j,k}$ and $z_{j,k} = -z_{j,k}$.

Examples of generated blunt bodies are included to show the variety of shapes that can be created from this set of axial and cross-section shapes. Figure 2.5 shows a prolate (approximately 4:1 axes length ratio) spherically-blunted cone blunt body. Figure 2.6 shows an oblate (approximately 3:1 axes length ratio) 12-sided polygon blunt body with a spherical-segment axial profile. Figure 2.7 shows a slightly prolate, concave rounded-edge pentagon with a power law axial profile. Note that the angled views do not correspond to any specific orientation.

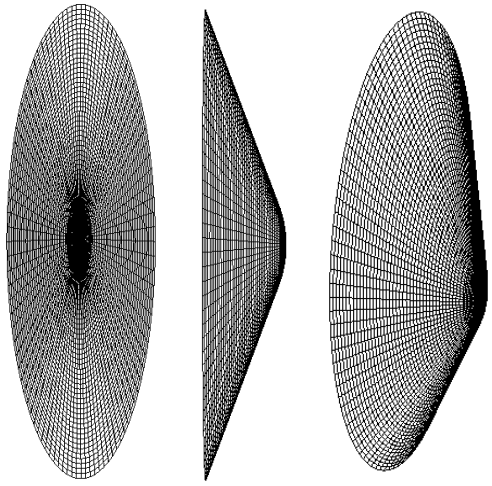

a) Front view. b) Side view. c) Angled view.

Figure 2.5. Spherically-blunted cone, $r_n/d = 0.25$, $\theta_c = 70^o$, $e = 0.95$, $m_1 = 5$, $n_1 = 1.75$, $n_2 = 2$.

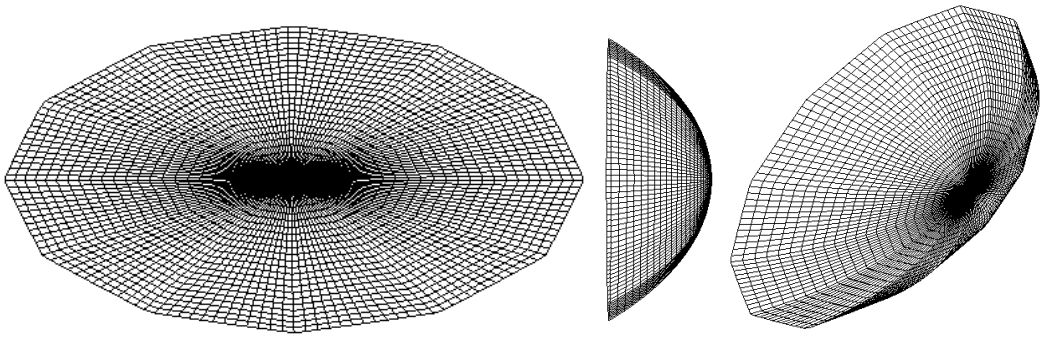

a) Front view. **b) Side view.** **c) Angled view.**

Figure 2.6. Spherical-segment, $\theta_s = 40^o$, $e = -0.85$, $m_1 = 12$, $n_1 = 10.75$, $n_2 = 1$.

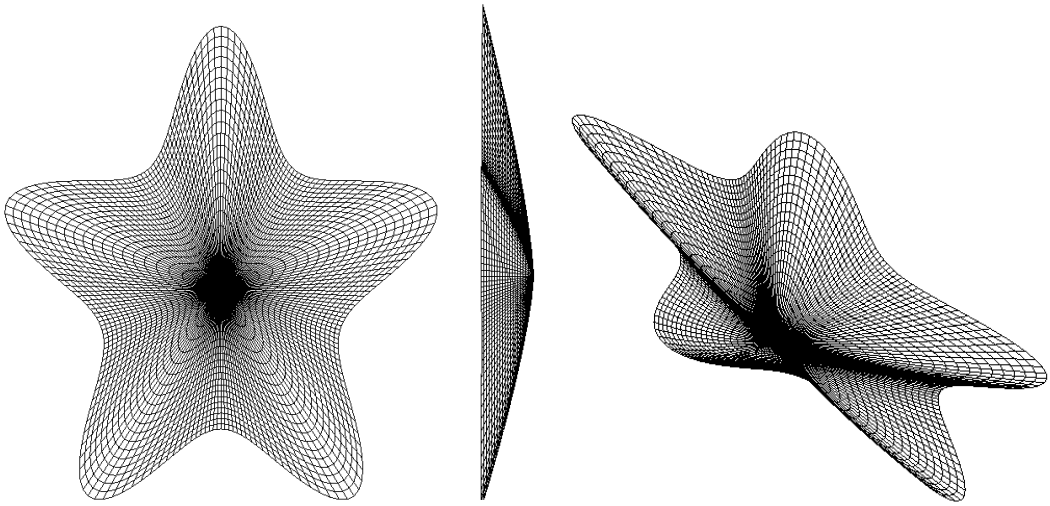

a) Front view. **b) Side view.** **c) Angled view.**

Figure 2.7. Power law, $A = 3$, $b = 0.75$, $e = 0.5$, $m_1 = 5$, $n_1 = 1.75$, $n_2 = 5$.

2.4. Geometric Properties

The main geometric properties calculated in this work are the surface and planform areas, the volume, the volumetric efficiency of the heat shield, and the location of the center of gravity. The following is a description of how the areas and volume are determined. Each point (j,k) is a part of a quadrilateral with four points (j,k), ($j-1,k$), ($j,k-1$), and ($j-1,k-1$). The distance between points (j,k) and ($j-1,k$) is indicated by $d_{1,a}$,

$$d_{1,a} = \sqrt{\left(x_{j,k} - x_{j-1,k}\right)^2 + \left(y_{j,k} - y_{j-1,k}\right)^2 + \left(z_{j,k} - z_{j-1,k}\right)^2}, \tag{2.12}$$

and the distance between points (*j,k-1*) and (*j-1,k-1*) is $d_{1,b}$. These two distances are then averaged to produce d_1. The distance between points (*j,k*), and (*j,k-1*) is $d_{2,\mathrm{a}}$, and the distance between points (*j-1,k*) and (*j-1,k-1*) is $d_{2,b}$. Likewise, they are averaged to produce d_2.

The product of d_1 and d_2 is the differential surface area *dA*. All the differential surface area components are summed to produce surface area S_{hs}, which is a term in determining the volumetric efficiency described later in this section. The differential planform area dA_p is the product of w_1 and w_2, which are the distances from and to the same point-locations as d_1 and d_2 if they were assumed to have equal *x*-components. In other words, the planform area dA_p, which is equal to part of the heat shield's base area, depends only on the area projected onto the *yz*-plane, in which

$$w_{1,a} = \sqrt{\left(y_{j,k} - y_{j-1,k}\right)^2 + \left(z_{j,k} - z_{j-1,k}\right)^2}, \tag{2.13}$$

and likewise for $w_{1,b}$, $w_{2,a}$, and $w_{2,b}$. Then the sum of the differential planform areas is equal to the heat shield's base area. The planform area is used in part to non-dimensionalize the aerodynamic forces and moments.

The differential volume is the product of the differential planform area and the distance from the differential surface to the shields base written as l_b

$$l_b = x_{\max} - \left(\frac{x_{j,k} + x_{j,k-1} + x_{j-1,k} + x_{j-1,k-1}}{4}\right). \tag{2.14}$$

Then a summation of all the differential volumes produces the volume of the heat shield V_{hs}.

The volumetric efficiency is one way to benchmark how much volume is available for a given amount of surface area. In the case of a heat shield shape, which is not a closed-shape, the volumetric efficiency is normalized to a hemisphere

$$\eta_{v,HS} = \frac{(18\pi)^{1/3} V_{hs}^{2/3}}{S_{hs}}. \tag{2.15}$$

As a result, the most volumetrically efficient shape is the hemisphere, which is defined by the terms of this work as a non-eccentric spherical-segment with $\theta_s = 90^o$.

In comparing an entire entry vehicle to another, the volumetric efficiency is normalized to a sphere

$$\eta_v = \frac{(36\pi)^{1/3} V_{veh}^{2/3}}{S_{veh}}. \tag{2.16}$$

This allows the sphere, which is the most volumetrically efficient shape for a given amount of surface area, to have $\eta_v = 100\%$.

The following equations calculate the location of the center of gravity of a uniform density body

$$\{X_{cg}, Y_{cg}, Z_{cg}\} = \left\{ \frac{\rho \iiint x dV}{\iiint dV}, \frac{\rho \iiint y dV}{\iiint dV}, \frac{\rho \iiint z dV}{\iiint dV} \right\}. \tag{2.17}$$

This equation is applied to a 3D mesh through numerical integration. One numerical integration method is Simpson's rule,[74]

$$F(x) = \int_{x_1}^{x_{2n+1}} f(x) dx \tag{2.18}$$

$$\approx \frac{h}{3}\left(f_1 + 4\left(f_2 + f_4 + \ldots + f_{2n}\right) + 2\left(f_3 + f_5 + \ldots + f_{2n-1}\right) + f_{2n+1}\right),$$

which is third-order accurate in h. For this work, h is a space step size. Additionally, this method requires an odd number of points to be integrated, and so the final point in the mesh is represented by the index $2n$+1. Because the space step h may not necessarily be the same for each pair of points, this work applies a modified version of Simpson's Rule that uses individual step sizes.

$$F(x) = \int_{x_1}^{x_{2n+1}} f(x)dx \tag{2.19}$$

$$\approx \frac{1}{3}\left(h_1 f_1 + 4\left(h_2 f_2 + h_4 f_4 + \ldots + h_{2n} f_{2n}\right) + 2\left(h_3 f_3 + h_5 f_5 + \ldots + h_{2n-1} f_{2n-1}\right) + h_{2n+1} f_{2n+1}\right).$$

It is likely that more than one integration is required to determine each term of the center-of-gravity location since the triple integrals indicate a three-dimensional shape that requires integration in three directions. It is easier to use the polar coordinate system in Figure 1.1(a). This allows one to conduct two integrations instead of three.

The method applied in this work for determining the center of gravity's location with numerical integration is detailed in this section. In the applied form, the general equation that is equal to Eqn. (2.17) is

$$\left\{X_{cg}, Y_{cg}, Z_{cg}\right\} = \left\{\frac{f_{x,3}}{NVol}, \frac{f_{y,3}}{NVol}, \frac{f_{z,3}}{NVol}\right\}. \tag{2.20}$$

The term *NVol* is a volume-related term, but it is not necessarily equal to the volume of the heat shield. For the spherical-segment axial shape, *NVol* is equal to V_{hs}, but for the spherically-blunted cone and power law axial shapes, *NVol* is equal to the terms

that are not cancelled out from being common to the numerator and denominator of Eqn. (2.17). *NVol* is defined as

$$NVol = \sum_{k=1}^{k\max} \sum_{j=1}^{j\max} dNVol_{j,k}, \tag{2.21}$$

in which $dNVol_{j,k}$ is the differential volume-related term defined as

$$dNVol_{j,k} = \begin{cases} \dfrac{w_{j,k}^2}{2} d\phi_{j,k} dr_{j,k} \cos\left(\dfrac{\pi}{2} - \theta_k\right), & \text{Spherical - segment} \\ \dfrac{w_{j,k}^2}{2} d\phi_{j,k} dr_{j,k}, & \text{Spherically - blunted cone} \\ \dfrac{w_{j,k}^2}{2} d\phi_{j,k} dr_{j,k}, & \text{Power law,} \end{cases} \tag{2.22}$$

in which spherical-segment angle θ_k only varies with x-location, $d\phi_{j,k}$ is the differential sweep angle in the *yz*-plane. This differential angle is determined from the law of cosines

$$d\phi_{j,k} = \operatorname{acos}\left(\frac{w_{j,k}^2 + w_{j+1,k}^2 - d_{(j+1,k),(j,k)}^2}{2 w_{j,k} w_{j+1,k}} \right), \tag{2.23}$$

and $dr_{j,k}$ is the average of the distances between the points (*j+1,k*) and (*j+1,k-1*) and the points (*j,k*) and (*j,k-1*), which is the numerical analogue to a differential length,

$$dr_{j,k} = \frac{1}{2}\left(d_{(j+1,k),(j+1,k-1)} + d_{(j,k),(j,k-1)} \right). \tag{2.24}$$

Since there are two differentials in *dNVol,* it is noted that it will be integrated twice to produce the denominators of Eqn. (2.20). With these equations, the denominator is fully defined. For the numerator, the subscript letter on the function *f* corresponds to

the *x, y,* and *z*-components, and the subscript number *3* corresponds to the result after the two integrations. The subscript number 2 corresponds to the result after one integration, and the subscript number 1 corresponds to the initial case before integration. The initial variables $f_{x,y,z,1}$ that are integrated twice to produce $f_{x,y,z,3}$ are defined as

$$\left\{f_{x,1}, f_{y,1}, f_{z,1}\right\} = \left\{x_{j,k}\, dNVol_{j,k}, y_{j,k}\, dNVol_{j,k}, z_{j,k}\, dNVol_{j,k}\right\}. \tag{2.25}$$

These are integrated first with respect to ϕ, and there are a k_{max}-number of values for $f_{x,y,z,2}$

$$\left(f_{x,2}\right)_k = \left(\int_{x_1}^{x_{2n+1}} f_{x,1} \right)_k \tag{2.26}$$

$$\approx \left(\frac{1}{3}\left(f_{x,1,1} + 4\left(f_{x,1,2} + f_{x,1,4} + \ldots + f_{x,1,2n}\right) + 2\left(f_{x,1,3} + f_{x,1,5} + \ldots + f_{x,1,2n-1}\right) + f_{x,1,2n+1}\right)\right)_k,$$

and likewise for $f_{y,2}$ and $f_{z,2}$. Note that the $f_{x,1}$ includes the differentials $d\phi$ and dr, and thus they are not written in Eqn. (2.26) and (2.27). The $f_{x,y,z,2}$ are integrated with respect to *r*, and so there is one value for each component of f_3

$$f_{x,3} = \int_{x_1}^{x_{2n+1}} f_{x,2} \tag{2.27}$$

$$\approx \frac{1}{3}\left(f_{x,2,1} + 4\left(f_{x,2,2} + f_{x,2,4} + \ldots + f_{x,2,2n}\right) + 2\left(f_{x,2,3} + f_{x,2,5} + \ldots + f_{x,2,2n-1}\right) + f_{x,2,2n+1}\right),$$

and likewise for $f_{y,3}$ and $f_{z,3}$. With these definitions, the location of the center of gravity of a given three-dimensional shape can be determined.

Chapter 3. Aerodynamics and Static Stability

The theory behind the aerodynamics and the static stability is presented in this section. The aerodynamic characteristics are then transformed into the quantities that are applied in the code of this work. The method for determining the shock-standoff distance to the stagnation point is introduced also, and modifications to the method to account for angle of attack are stated. Then this chapter finishes with a couple corrected misinterpretations of general aerodynamic theory.

Two coordinate systems applied in this work are the freestream coordinate system shown in Figure 3.1(a) with the positive angle of attack and sideslip angle conventions, and the fixed coordinate system shown in Figure 3.1(b), which is slightly different from Figure 2.1.

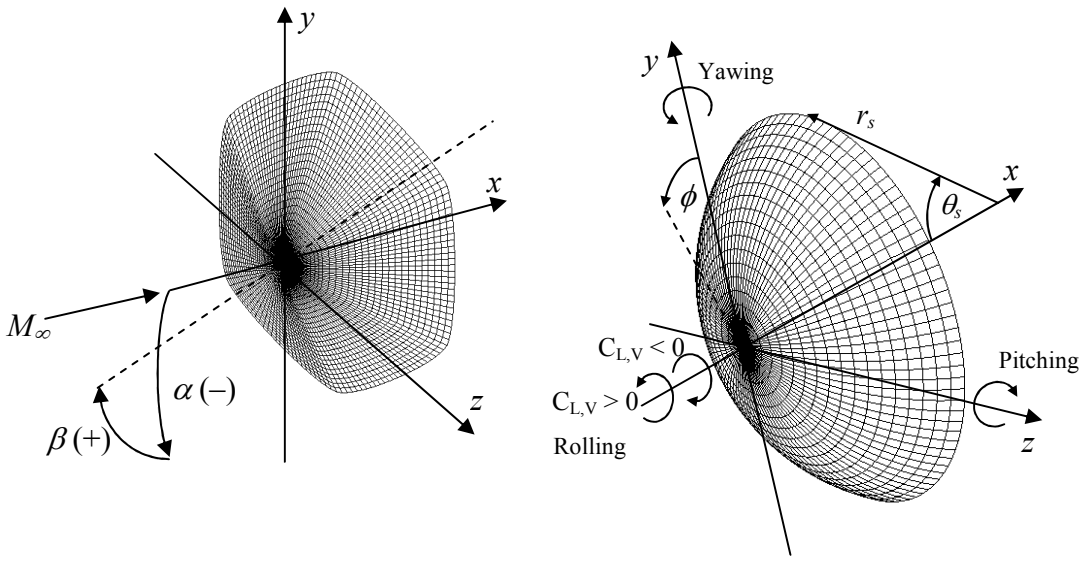

a) Freestream coordinate system with α and β. **b) Fixed coordinate system with aerodynamic moment conventions.**

Figure 3.1. Coordinate systems with positive α and β and moment conventions.

3.1. *Modified Newtonian Impact Theory*

After the heat shield geometry is generated, its aerodynamic characteristics are calculated based on a modified Newtonian surface pressure distribution. Simple Newtonian theory is equivalent to the limit of exact oblique shock theory as M_∞ approaches infinity and γ approaches one.[3] This work is currently being applied to Earth atmospheric entry by assuming $\gamma = 1.4$, and a similar analysis can be applied to a Martian atmosphere of CO_2 by assuming $\gamma = 1.3$. However, when calculating the shock-standoff distance, the effective specific heat ratio after the blunt-body shock is determined using the empirical correlations of high temperature air from Tannehill,[57] as explained in Section 3.2 on shock-standoff distance.

Because Newtonian theory allows aerodynamic performance to be determined within a fraction of a second of computation time, it has been chosen over more complicated, time-intensive methods for optimization reasons. Results from the code that apply modified Newtonian theory are compared to wind tunnel and flight test data from Apollo Command Module (CM) in Chapter 7.

The pressure coefficient, which is the pressure difference normalized by the dynamic pressure, is given by the equation

$$C_p = \frac{p - p_\infty}{q_\infty} = \frac{p - p_\infty}{\frac{1}{2}\rho_\infty V_\infty^2} = \frac{2}{\gamma M_\infty^2}\left(\frac{p}{p_\infty} - 1\right). \tag{3.1}$$

Newtonian theory assumes that the component of a particle's momentum that is normal to the surface is destroyed when impinging on the face of the blunt body while its tangential momentum is conserved.[2,33,64] The Newtonian model is

$$C_p = C_{p,\max}\left(\frac{\vec{V}_\infty \cdot \hat{n}}{V_\infty}\right)^2 \tag{3.2}$$

for $\vec{V}_\infty \cdot \hat{n} < 0$. The surface is in the aerodynamic shadow region when $\vec{V}_\infty \cdot \hat{n} \geq 0$, resulting in $C_p = 0$.

For simple Newtonian, the maximum value of the pressure coefficient is assumed equal to two. Modified Newtonian theory accounts for the maximum value $C_{p,max}$, according to the Rayleigh Pitot tube formula[75] that gives the ratio of the stagnation pressure after the shock to the freestream pressure

$$\frac{p_{0,2}}{p_\infty} = \left(\frac{1-\gamma+2\gamma M_\infty^2}{\gamma+1}\right)\left(\frac{(\gamma+1)^2 M_\infty^2}{4\gamma M_\infty^2 - 2(\gamma-1)}\right)^{\gamma/\gamma-1}. \tag{3.3}$$

This produces the following relation for $C_{p,max}$

$$C_{p,\max} = \frac{2}{\gamma M_\infty^2}\left(\frac{p_{0,2}}{p_\infty} - 1\right). \tag{3.4}$$

The velocity is modeled as a function of the angles of attack and sideslip

$$\frac{\vec{V}_\infty}{V_\infty} = \{V_x, V_y, V_z\} = \{\cos(\alpha)\cos(\beta), \sin(\alpha)\cos(\beta), \sin(\beta)\}, \tag{3.5}$$

and the local normal vector is approximated by setting it equal to the cross product of two local vectors on the differential surface *dA*. Two local vectors are formed by subtracting the values of the *x*, *y*, and *z*-locations at point (*j-1,k*) from those at point (*j,k*) and likewise for points (*j,k-1*) and (*j,k*). The cross product of the two newly-formed vectors in terms of the *x, y,* and *z* values at points (*j,k*), (*j-1,k*), and (*j,k-1*) is the numerator of local normal vector and written as

$$
\begin{aligned}
n_{v,x} &= \left(y_{j,k} - y_{j-1,k}\right)\left(z_{j,k} - z_{j,k-1}\right) - \left(y_{j,k} - y_{j,k-1}\right)\left(z_{j,k} - z_{j-1,k}\right) \\
n_{v,y} &= \left(z_{j,k} - z_{j-1,k}\right)\left(x_{j,k} - x_{j,k-1}\right) - \left(x_{j,k} - x_{j-1,k}\right)\left(z_{j,k} - z_{j,k-1}\right) \\
n_{v,z} &= \left(x_{j,k} - x_{j-1,k}\right)\left(y_{j,k} - y_{j,k-1}\right) - \left(x_{j,k} - x_{j,k-1}\right)\left(y_{j,k} - y_{j-1,k}\right).
\end{aligned} \tag{3.6}
$$

This formulation will work for points with $j \neq 1$ and $k \neq 1$ and at the base of the heat shield geometry for $k = k_{max}$ also. For points with $j = 1$, the vector formed by points (j,k) and $(j\text{-}1,k)$ is replaced by $(j+1,k)$ and (j,k), and then the numerator of the local normal vector is formed. For points with $k = 1$, which is at the tip of the nose of the vehicle, it is assumed that $n_x = -1$, and the other components are zero. The magnitude of vector n_v is then calculated to produce the normal vector

$$
\begin{aligned}
\left\|\hat{n}_v\right\| &= \sqrt{\left(n_{v,x}\right)^2 + \left(n_{v,y}\right)^2 + \left(n_{v,z}\right)^2} \\
\hat{n} &= \left\{n_x, n_y, n_z\right\} = \left\{\frac{n_{v,x}}{\left\|\hat{n}_v\right\|}, \frac{n_{v,y}}{\left\|\hat{n}_v\right\|}, \frac{n_{v,z}}{\left\|\hat{n}_v\right\|}\right\},
\end{aligned} \tag{3.7}
$$

and Eqn. (3.2) becomes

$$
C_p = C_{p,\max}\left(V_x n_x + V_y n_y + V_z n_z\right)^2. \tag{3.8}
$$

These equations calculate the pressure coefficient for a general blunt-body geometry given in the form of a three-dimensional structured mesh, with each x, y, and z surface location determined by sweep angle location j and x-section location k.

All the aerodynamic forces and moments are calculated as non-dimensional terms. The forces looked at in this analysis are the normal, axial, and side forces with coefficients C_N, C_A, and C_Y respectively. The coefficients are defined as

$$
C_N = \frac{-1}{A_p}\iint_S n_y C_p \, dA, \qquad f_{x,1} = n_{y,(j,k)} C_{p,(j,k)} dA_{(j,k)}, \tag{3.9}
$$

$$C_A = \frac{-1}{A_p}\iint_S n_x C_p dA, \qquad f_{y,1} = n_{x,(j,k)} C_{p,(j,k)} dA_{(j,k)}, \tag{3.10}$$

$$C_Y = \frac{1}{A_p}\iint_S n_z C_p dA, \qquad f_{z,1} = n_{z,(j,k)} C_{p,(j,k)} dA_{(j,k)}, \tag{3.11}$$

in which $dA_{j,k}$ is the differential surface area defined as

$$dA_{j,k} = w_{j,k} dr_{j,k} d\phi_{j,k}, \tag{3.12}$$

Using the written equations for $f_{x,1}$ that correspond to each of the force coefficients, numerical integration is completed using Simpson's rule with the process detailed in Chapter 2. Then the force coefficients become

$$\{C_N, C_A, C_Y\} = \left\{\frac{-1}{A_p} f_{x,3}, \frac{-1}{A_p} f_{y,3}, \frac{-1}{A_p} f_{z,3}\right\}. \tag{3.13}$$

The lift and drag coefficients can be determined after the normal, axial, and side force coefficients are calculated. For the Apollo CM, Hillje[10,11] divides the lift coefficient into a vertical lift coefficient $C_{L,V}$ and a horizontal lift coefficient $C_{L,H}$. This work uses the following definitions for the lift and drag coefficients

$$C_{L,V} = C_N \cos(\alpha) - C_A \sin(\alpha), \tag{3.14}$$

$$C_{L,H} = C_Y \cos(\beta) - C_A \cos(\alpha)\sin(\beta), \tag{3.15}$$

$$C_L = \sqrt{(C_{L,V})^2 + (C_{L,H})^2}, \tag{3.16}$$

$$C_D = C_N \sin(\alpha) + C_Y \sin(\beta) + C_A \cos(w_V), \tag{3.17}$$

in which w_V is the wind angle, or the magnitude of the angle from the velocity vector to the central-body axis,

$$w_V = \text{atan}\left(\frac{\sqrt{(V_y)^2 + (V_z)^2}}{V_x}\right). \tag{3.18}$$

The resulting lift-to-drag ratio equations are

$$\frac{L}{D} = \frac{C_L}{C_D}, \quad \frac{L_V}{D} = \frac{C_{L,V}}{C_D}, \quad \frac{L_H}{D} = \frac{C_{L,H}}{C_D}. \tag{3.19}$$

The aerodynamic moments about the nose that are considered in this analysis are the pitching, yawing, and rolling moments with coefficients $C_{m,0}$, $C_{n,0}$, and $C_{l,0}$. The equation for the coefficient of the pitching moment about the nose is

$$C_{m,0} = -C_N \frac{X_{cp}}{d} + C_A \frac{Y_{cp}}{d}, \tag{3.20}$$

$$\text{in which } C_{m,N,0} = -C_N \frac{X_{cp}}{d} = \frac{1}{2A_p r}\iint_S x n_y C_p \, dA, \qquad f_{x,1} = x_{j,k} n_{y,(j,k)} C_{p,(j,k)} dA_{(j,k)}, \tag{3.21}$$

$$\text{and } C_{m,A,0} = C_A \frac{Y_{cp}}{d} = \frac{1}{2A_p r}\iint_S \left(-y n_x C_p\right) dA, \qquad f_{y,1} = -y_{j,k} n_{x,(j,k)} C_{p,(j,k)} dA_{(j,k)}. \tag{3.22}$$

$C_{m,N,0}$ is the normal force's contribution to the pitching moment, and $C_{m,A,0}$ is the axial force's contribution. Similar to integrating $f_{x,1}$ to determine the force coefficients, the $f_{x,1}$ and $f_{y,1}$ of each moment coefficient can be integrated separately in order to find $f_{x,3}$

and $f_{y,3}$. Those are used to determine the location of the center of pressure after are calculated. The equation for the coefficient of the yawing moment about the nose is

$$C_{n,0} = -C_A \frac{Z_{cp}}{d} + C_Y \frac{X_{cp}}{d}, \tag{3.23}$$

$$\text{in which} \quad C_{n,A,0} = -C_A \frac{Z_{cp}}{d} = \frac{1}{2A_p r} \iint_S z n_x C_p dA, \qquad f_{x,1} = z_{j,k} n_{x,(j,k)} C_{p,(j,k)} dA_{(j,k)}, \tag{3.24}$$

$$\text{and} \quad C_{n,Y,0} = C_Y \frac{X_{cp}}{d} = \frac{1}{2A_p r} \iint_S \left(-x n_z C_p\right) dA, \qquad f_{y,1} = -x_{j,k} n_{z,(j,k)} C_{p,(j,k)} dA_{(j,k)}. \tag{3.25}$$

$C_{n,A,0}$ is the axial force's contribution to the yawing moment, and $C_{n,Y,0}$ is the side force's contribution. The equation for the coefficient of the rolling moment about the nose is

$$C_{l,0} = -C_Y \frac{Y_{cp}}{d} + C_N \frac{Z_{cp}}{d}, \tag{3.26}$$

$$\text{in which} \quad C_{l,Y,0} = -C_Y \frac{Y_{cp}}{d} = \frac{1}{2A_p r} \iint_S y n_z C_p dA, \qquad f_{x,1} = y_{j,k} n_{z,(j,k)} C_{p,(j,k)} dA_{(j,k)}, \tag{3.27}$$

$$\text{and} \quad C_{l,N,0} = C_N \frac{Z_{cp}}{d} = \frac{1}{2A_p r} \iint_S \left(-z n_y C_p\right) dA, \qquad f_{y,1} = -z_{j,k} n_{y,(j,k)} C_{p,(j,k)} dA_{(j,k)}. \tag{3.28}$$

$C_{l,Y,0}$ is the side force's contribution to the rolling moment, and $C_{l,N,0}$ is the normal force's contribution. After $f_{x,3}$ and $f_{y,3}$ are determined for each coefficient, the moment coefficients become

$$\{C_{m,0}, C_{n,0}, C_{l,0}\} = \left\{ \frac{1}{2A_p l_M}\left(f_{x,3} + f_{y,3}\right)_m, \frac{1}{2A_p l_M}\left(f_{x,3} + f_{y,3}\right)_n, \frac{1}{2A_p l_M}\left(f_{x,3} + f_{y,3}\right)_l \right\}. \quad (3.29)$$

Note that all moment coefficients are defined as the ratio of the moment to $q_\infty S l_M$, in which l_M is defined as the length of the semimajor axis. This definition of l_M makes it possible for the yawing moment coefficient $C_{n,0}$ at a given sideslip angle (the condition $\beta_1 \neq 0$, $\alpha_1 = 0$) for a prolate shape $e_1 > 0$ to be equivalent to the pitching moment coefficient $C_{m,0}$ for an oblate shape at a given angle-of-attack (the condition $\alpha_2 = \beta_1$, $\beta_2 = 0$, $e_2 = -e_1$). This definition was chosen over defining l_M as the span of the heat shield.

In validation, it is shown that the rolling moment calculations rendered a z-location of the center of pressure, Z_{cp}, that is inconsistent with the calculations of the other two moments, and so the yawing moment coefficient was used to calculate Z_{cp}. One observation is that the components of $C_{l,0}$ are of such small magnitude that the values may have numerical error on the same order, thereby producing inconsistent values for Z_{cp}. One reason for this may be that Simpson's rule has difficulty integrating numbers that have values near zero. Since the value of $C_{l,0}$ is orders of magnitude lower than the pitching and yawing moment coefficients, it is possible that Simpson's rule reached its limit around the value of $C_{l,0}$ without affecting $C_{m,0}$ and $C_{n,0}$.

3.2. *Shock-standoff Distance: Kaattari's method*

Kaattari's method for calculating the shock-standoff distance to the stagnation point is semi-empirical.[54,55] Kaattari's method assumes that the shock shape is

spherical with radius r_{sh}. There are several curves that relate the normal shock density ratio ρ_2/ρ_1 to characteristics empirically derived, including the shock-standoff distance at the sonic point for several shapes such as a cone, paraboloid, and sphere. Then there are several aerodynamic and geometric theory-based equations applied in determining the shock-standoff distance from the chosen geometry. Kaattari's method is not completely explained in this work because it is well detailed for the general blunt-body case at zero angle of attack in Ref. (55) and for a spherical-segment blunt-body at large angles of attack in Ref. (54). To introduce the method, this section does include the main equations. Then a description of how this method is implemented on the computer is included since it was originally an iterative process completed by hand. Afterwards, modifications to the method accounting for angle of attack in Ref. (54) are included to estimate the shock-standoff distance for the general blunt-body case.

3.2.1. Method Implementation

Kaattari gives two similar methods for determining the shock-standoff distance, one for conic-section bodies and the other for non-conic-section bodies. Kaattari recommends using the conic-section shock equations with ellipsoids and the non-conic-section shock equations with the spherically-blunted cone. For this work, the non-conic-section shock equations were chosen to be used for all three axial shapes because they account for edge bluntness while the conic-section equations do not. Also, for the spherical-segment blunt-bodies, it was noticed that the conic section equations and non-conic section equations produced similar results for a spherical

body. Additionally, ellipsoid relations assume a complete ellipsoid is present rather than a segment of an ellipsoid, and this may become problematic at angles of attack.

Kaattari originally calculated the shock characteristics of axisymmetric shapes by hand using plots of several geometric and aerodynamic characteristics that varied with the normal-shock density ratio. He needed to iterate his solution until the method found a converged value of the shock-standoff distance. This work uses the computer to automate Kaattari's process. Part of this is accomplished by curve-fitting the necessary semi-empirical plots. This section supplies the curve-fit equations that were generated for this work. Note that all the given digits are required in order for the curve-fits to register the corresponding norm of the residuals or R^2 values (which is given for most of the curve-fit equations). Also, even though all these digits are required to have an accurate curve-fit, this does not mean that the resulting value has a correspondingly large number of significant digits. It is suggested that the calculated results of the given curve-fits do not have more than three significant digits. As noted previously, this section does not detail the entire Kaattari method; it only includes the main modifications and additions to the method including curve-fit equations.

This section also refers to figures that are not included in this work, but the reference numbers are given. The *G* function relates the ratio of the shock-standoff distance to the shock radius, Δ_o/r_{sh}, to the blunt-body's radius of curvature at the nose

$$G = \left(1 + \frac{\Delta_o}{r_n}\right)\frac{\Delta_o}{r_{sh}} = \left(1 + \frac{\Delta_o r_{sh}}{r_n r_{sh}}\right)\frac{\Delta_o}{r_{sh}}, \tag{3.30}$$

which can be manipulated to become

$$\frac{\Delta_o}{r_{sh}} = \frac{\sqrt{1+4G\left(\frac{r_{sh}}{r_n}\right)}-1}{2\left(\frac{r_{sh}}{r_n}\right)}. \tag{3.31}$$

These relations[55] are based on a given normal-shock density ratio. Figure 1 from Ref. [55] provides a relation for the G function to the normal-shock density ratio for γ-values of 1.0 and 1.4

$$G = \begin{cases} -2.2378\left(\frac{\rho_1}{\rho_2}\right)^4 + 2.9402\left(\frac{\rho_1}{\rho_2}\right)^3 - 1.4354\left(\frac{\rho_1}{\rho_2}\right)^2 + \\ \quad + 0.81267\left(\frac{\rho_1}{\rho_2}\right) - 0.00024476, \\ \text{Norm of residuals: } 0.0033845, \qquad \gamma = 1, \\ \\ 2.4242\left(\frac{\rho_1}{\rho_2}\right)^4 - 1.4794\left(\frac{\rho_1}{\rho_2}\right)^3 - 0.047552\left(\frac{\rho_1}{\rho_2}\right)^2 \\ \quad + 0.69906\left(\frac{\rho_1}{\rho_2}\right) + 0.00062937, \qquad \gamma = 1.4. \\ \text{Norm of residuals: } 0.0025566, \end{cases} \tag{3.32}$$

If $\rho_1/\rho_2 < 0.15$, then the two curves converge and the curve-fit equation for $\gamma = 1.0$ must be used. Otherwise, interpolation between the two curves can be completed for $0.15 < \rho_1/\rho_2 < 0.45$. The shock-standoff distance at the sonic point Δ_* is non-dimensionalized by y_*, which is the normal distance from the axis of symmetry to the sonic point on the body. Figure 2 of Ref. [55] relates the Δ_*/y_* to the ρ_1/ρ_2 for two specific heat ratio values for $0.01 < \rho_1/\rho_2 < 0.45$,

$$\frac{\Delta_*}{y_*} = \begin{cases} 6.418\left(\frac{\rho_1}{\rho_2}\right)^3 - 4.3473\left(\frac{\rho_1}{\rho_2}\right)^2 \\ \quad + 2.7174\left(\frac{\rho_1}{\rho_2}\right) + 0.0018741, \\ \text{Norm of residuals: } 0.0087586, \qquad \gamma = 1, \\ \\ 1.4064\left(\frac{\rho_1}{\rho_2}\right)^3 - 0.80536\left(\frac{\rho_1}{\rho_2}\right)^2 \\ \quad + 1.9834\left(\frac{\rho_1}{\rho_2}\right) + 0.00052448, \quad \gamma = 1.4. \\ \text{Norm of residuals: } 0.0076548, \end{cases} \tag{3.33}$$

Kaattari validates these curve-fits with experimental data for spherical, disk, and cone shapes, as well as with theoretical results for spherical and parabolic shapes for zero angle of attack. From these two equations, the shock surface inclination at a point opposite the sonic point on a flat disk θ_{*o} can be determined

$$\theta_{*o} = \text{atan}\left(\frac{G}{\Delta_* / y_*}\right). \tag{3.34}$$

The sonic angle for a sphere Φ_{*1} is defined as the body surface inclination of a sphere at the sonic point, with respect to a plane normal to the freestream direction. The variation of the sonic angle for a sphere Φ_{*1} with ρ_1/ρ_2 is given in Figure 4 from Ref. [55] for $0.025 < \rho_1/\rho_2 < 0.45$,

$$\Phi_{*1}(\text{deg}) = \begin{cases} -797.1\left(\frac{\rho_1}{\rho_2}\right)^4 + 908.77\left(\frac{\rho_1}{\rho_2}\right)^3 - 380.2\left(\frac{\rho_1}{\rho_2}\right)^2 \\ \quad + 80.348\left(\frac{\rho_1}{\rho_2}\right) + 33.383, & \gamma = 1, \\ 104.8\left(\frac{\rho_1}{\rho_2}\right)^4 - 7.2046\left(\frac{\rho_1}{\rho_2}\right)^3 - 99.371\left(\frac{\rho_1}{\rho_2}\right)^2 \\ \quad + 61.984\left(\frac{\rho_1}{\rho_2}\right) + 32.589, & \gamma = 1.4. \end{cases} \tag{3.35}$$

If $\rho_1/\rho_2 < 0.15$, then the curve-fit equation for $\gamma = 1.0$ must be used. Otherwise, interpolation between the two curves can be completed for $0.15 < \rho_1/\rho_2 < 0.45$. The sonic angle for a rounded-corner blunt-body Φ_* varies with r_c/r

$$\frac{\sin(\Phi_*)}{\sin(\Phi_{*1})} = \begin{cases} 20\frac{r_c}{r}, & 0.00 < \frac{r_c}{r} \le 0.01, \\ -18.35253948\left(\frac{r_c}{r}\right)^2 + 5.31156637\left(\frac{r_c}{r}\right) \\ \quad + 0.15140845, & 0.01 < \frac{r_c}{r} \le 0.10, \\ 0.2159\ln\left(\frac{r_c}{r}\right) + 1.01, & 0.10 < \frac{r_c}{r} \le 1.00. \end{cases} \tag{3.36}$$

For each axial shape, ε, which is the inclination on the forward body surface at the point tangent with the corner radius, is given by the following set of equations. From these, the sonic angle Φ_* can be determined. For the spherical-segment and power law axial shapes,

$$\varepsilon = \begin{cases} \operatorname{asin}\left(\dfrac{\dfrac{r}{r_n}\left(1-\dfrac{r_c}{r}\right)}{1-\dfrac{r_c}{r_n}} \right), & \text{Spherical - segment,} \\ \dfrac{\pi}{2} - \left| \operatorname{atan}\left(\dfrac{y_{1,k\,\max} - y_{1,k\,\max-1}}{x_{1,k\_\max} - x_{1,k\_\max-1}} \right) \right|, & \text{Power law.} \end{cases} \tag{3.37}$$

For the power law axial shape, the term subtracted from $\pi/2$ can be defined as an effective local half-cone angle. There are two cases for the spherically-blunted cone: one in which the spherical-segment is the dominant shape, in which the r_n/d is large, and the other in which the cone shape dominates. This is described by the following equation set for the spherically-blunted cone

$$\varepsilon = \begin{cases} \dfrac{\pi}{2} - \theta_c, & 0 < \dfrac{r_n}{d} \le \dfrac{1}{2}\sin\left(\dfrac{\pi}{2} - \theta_c\right), \\ \dfrac{\pi}{2} - \left| \operatorname{atan}\left(\dfrac{y_{1,k\max} - y_{1,k\max-1}}{x_{1,k\_\max} - x_{1,k\_\max-1}} \right) \right|, & \dfrac{1}{2}\sin\left(\dfrac{\pi}{2} - \theta_c\right) < \dfrac{r_n}{d}. \end{cases} \tag{3.38}$$

Note that if $\varepsilon > 37^o$, then ε is set equal to 37^o since that is the limit of Kaattari's dataset. The spherically-blunted cone does not approach this limit since it would require a half-cone angle $\theta_c < 53^o$, and the limit for the half-cone angle in the optimizer is set at 55^o. Kaattari's method also notes that if the sonic angle $\Phi_* < \varepsilon$, then the sonic point is assumed to be taken at the tangency angle ε, and so Φ_* is set equal to ε for this case. To determine θ_*, Kaattari supplies Figure 6(b) from Ref. [55] that relates the difference $\theta_* - \theta_{*_o}$ as a function of Φ_*. This relation varies with the normal-shock density ratio, and their corresponding curve-fit equations with Φ_* limits are included in Appendix A.1.

The main non-conic-section body shock equation relates the shock radius r_{sh} to the stagnation shock-standoff distance, the corner radius, sonic shock-standoff distance and the tangency angle

$$\frac{r_{sh}}{y_*}\left(\frac{\Delta_o}{r_{sh}}\right) = \frac{x_s}{y_*} + \left[\frac{\Delta_*}{y_*} - \frac{\tan(\varepsilon) + \frac{r_n}{r}\left(\frac{\cos(\varepsilon)-1}{\cos(\varepsilon)}\right) + \frac{r_c}{r}\left(\frac{1-\sin(\varepsilon)}{\cos(\varepsilon)} - \cos(\Phi_*)\right)}{1-\frac{r_c}{r}(1-\sin(\Phi_*))}\right], \quad (3.39)$$

in which x_s is the streamwise distance from the apex of the shock to the point on the shock at distance y_* from the central axis. This relation along with the shock solution nomograph equation,

$$B_s \frac{x_s}{y_*} = \left(\frac{r_{sh}}{y_*} - \frac{1}{\tan(\theta_*)}\right), \quad (3.40)$$

and the initial value of Δ_o/r_{sh} set equal to G, determine the values of B_s, y_*/r, r_{sh}/r, and Δ_o/r,

$$B_s = \left(\frac{r_{sh}}{y_*}\right)^2 - \frac{1}{\tan^2(\theta_*)}, \quad (3.41)$$

$$\frac{y_*}{r} = 1 - \frac{r_c}{r}(1-\sin(\Phi_*)), \quad (3.42)$$

$$\frac{r_{sh}}{r} = \frac{r_{sh}}{y_*}\frac{y_*}{r}, \quad (3.43)$$

$$\frac{r_{sh}}{r_n} = \frac{r_{sh}}{y_*}\frac{y_*}{r}\frac{r}{r_n}, \quad (3.44)$$

$$\frac{\Delta_o}{r} = \frac{\Delta_o}{r_{sh}}\frac{r_{sh}}{r}. \quad (3.45)$$

From here, the value of Δ_o/r_{sh} based on Eqn. (3.31) is calculated and the process is repeated. Once the value of Δ_o/r_{sh} converges within 0.001, the iterative process has been completed, and the shock properties of the blunt-body have been determined for zero angle of attack. The main output variable is Δ_o/r_n. The complete process with referenced figures and examples is included in Ref. (55).

3.2.2. Accounting for Nonaxisymmetric Shapes & Angle of Attack

Kaattari[54] offers a way to account for angle of attack for spherical-segment axisymmetric blunt bodies. In this section, a basic method is described for determining how Δ_o/r_n changes both for a nonaxisymmetric blunt body and with angle of attack based on Kaattari's method. It also has been modified to account for the spherically-blunted cone and power law axial shapes. These modifications are meant to produce results that follow expected trends only. Although there is confidence in the expected trends, the results should not be accepted as unequivocal since several of the more exotic shapes have not been studied before from a re-entry heat transfer standpoint. The expectation is that these modifications produce shock-standoff distances for nonaxisymmetric geometries within the proper order of magnitude. The reason for using this method is to approximate the stagnation-point radiative heat flux, and Chapter 4 explains how it can be approximated for a blunt body using the shock-standoff distance.

For an axisymmetric spherical-segment geometry, Kaattari provides the process for estimating the shock-standoff distance in Ref. (54), and the equation

$$\frac{\Delta_\alpha}{d} = \frac{\Delta_o}{d} - \left(c_1 \frac{r_{st}}{r_{\max}} + c_3 \left(\frac{r_{st}}{r_{\max}} \right)^3 \right) \cos(\phi) \sin(\alpha) \tag{3.46}$$

relates the shock-standoff distance at angle of attack to that at zero angle of attack. Note that for this work, the angle of the azimuth ϕ is assumed equal to zero. To determine how the value of Δ_o/r_n varies with angle of attack, semi-empirical data of shock correlation functions from Kaattari in Ref. (54) have been curve-fit. Applying these curve-fits is described in the next section, including the modifications required to use Kaattari's method to approximate how the shock-standoff distance changes with angle of attack. Figure 9(a) from Ref. [54] shows how the shock correlation coefficient c_1 varies with the normal-shock density ratio and the tangency angle ε. It is curve-fitted (input ε in degrees) with limits of applicability in Appendix A.2. Interpolation for cases with normal-shock density ratios in-between the given curve fits has been tested and is completely feasible. The correlation constant c_3 is also supplied in Figure 9(b) from Ref. [54], and the curve-fit equations (input ε in degrees) are listed in Appendix A.3. With all of these equations, it is possible to approximate the shock-standoff distance. This is the full extent of Kaattari's method.

To account for nonaxisymmetric geometries, it is assumed that the change in the shock-standoff distance for shape variance and an angle of attack is dependent on eccentricity and the axial shape of the upper half at $\phi = 0^o$ (j = 1) and the lower half at $\phi = 180^o$ (j = ($jmax$-1)/2). An example geometry is shown in Figure 3.2 to show how Kaattari's method is applied.

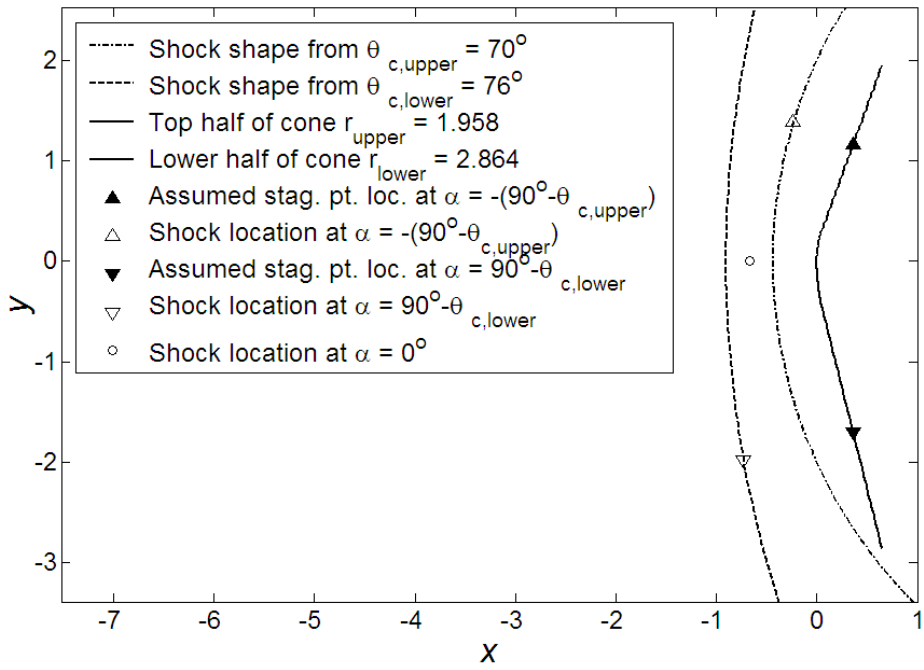

Figure 3.2. Spherically-blunted cone profile shock-standoff distance variance.

Kaattari's method is applied to determine the radii of the shock for the upper profile $r_{sh,upper}$ = 4.827 and the lower profile $r_{sh,lower}$ = 11.30 separately. This is accomplished by accounting for the different half-cone angles for the upper and lower surfaces, $\theta_{c,upper}$ = 70° and $\theta_{c,lower}$ = 76° respectively. Also the different upper and lower base radii, r_{upper} = 1.958 m, and r_{lower} = 2.864 m respectively are accounted for and added together to produce the base diameter. The shock-standoff distances for each case is calculated $\Delta_{o,upper}$ = 0.4175 m and $\Delta_{o,lower}$ = 0.9215 m. After the shock-standoff distances are determined this work assumes that this cone shape must have a zero angle of attack shock-standoff distance Δ_o that is in-between the two calculated shock-standoff values. It is assumed that each has equal effect on Δ_o, and so it is set equal to the average of the two and produces the open circle in Figure 3.2 corresponding to Δ_o = 0.6695 m.

Originally, to account for angle of attack, Kaattari's Eqn. (3.47) was applied, but for the case of Figure 3.2, $\Delta_{\alpha<0} > \Delta_{\alpha>0}$, which does not follow the most probable trend. At $\alpha<0$, the upper profile faced the freestream more than the lower profile, and so it should have more effect on Δ_α than the lower profile. Because $r_{sh,lower} > r_{sh,upper}$, it is expected that $\Delta_{\alpha=-(90-\theta)} < \Delta_{\alpha=90-\theta}$, which is the opposite of the trend produced by Eqn. (3.47). As a result, the following basic method is applied to guarantee that this trend is held.

This work assumes that the shock-standoff distance at $\alpha = 90^o - \theta_{c,lower}$, which is $\alpha>0^o$, can be approximated by the distance from the lower shock with radius $r_{sh,lower}$ that is perpendicular to the lower face. This distance is the length between the two inverted triangles shown in Figure 3.2. For $\alpha < 0$, the shock-standoff distance at $\alpha = -(90^o - \theta_{c,upper})$, can be approximate by the distance from the upper shock with $r_{sh,upper}$ that is perpendicular to the upper face. This distance is the length between the two triangles shown in Figure 3.2. As a result, this also means that if $r_{sh,lower} < r_{sh,upper}$, then $\Delta_{\alpha=-(90-\theta)} > \Delta_{\alpha=90-\theta}$, thus this method accounts for either case. Linear interpolation between Δ_o and Δ_α is applied once the endpoints $\Delta_{\alpha=-(90-\theta,upper)}$ and $\Delta_{\alpha=90-\theta,lower}$ are determined. This simple method is implemented only so that the shock-standoff distance is varied and follows an expected trend.

To account for eccentricity, the average base radius is determined; then it is divided by the maximum base radius to produce the non-dimensional average base radius $r_{avg,nd}$. This term is then used to calculate the upper and lower shock radii

$$r_{sh,upper} = \begin{cases} \dfrac{r_{sh,upper}}{r_n}\dfrac{r_n}{r_{upper}} r_{upper} r_{avg,nd}, & e \geq 0, \\ \dfrac{r_{sh,upper}}{r_n}\dfrac{r_n}{r_{upper}}\dfrac{r_{upper}}{r_{avg,nd}}, & e < 0, \end{cases} \tag{3.47}$$

$$\text{and } r_{sh,lower} = \begin{cases} \dfrac{r_{sh,lower}}{r_n}\dfrac{r_n}{r_{lower}} r_{lower} r_{avg,nd}. & e \geq 0, \\ \dfrac{r_{sh,lower}}{r_n}\dfrac{r_n}{r_{lower}}\dfrac{r_{lower}}{r_{avg,nd}}, & e < 0. \end{cases} \tag{3.48}$$

Eccentricity is accounted for through this approach so that the calculated shock radii of a prolate shape with eccentricity e at α and those of an oblate shape with the same eccentricity are affected equally. This is one way of producing consistency throughout the results. Note that this addition does not provide true consistency when calculating the radiative heat transfer, as the value of q_{rad} varies up to 33% at eccentricity $|e| > +/- 0.9$ and up to 20% at $|e| > +/- 0.8$. As a result, any calculations for highly eccentric shapes should be seen only as approximate solutions.

For rounded-edge concave shapes such as that shown in Figure 2.7, the profile could look similar to an inverted Figure 3.2. In this case, it is assumed that only the surface with the larger r (in the case of Figure 2.7 it would be r_{upper}) is applied rather than using the average of shock-standoff distances because the surface with the larger r represents the primary radius of the shock-shape. This is assumed for the rounded-edge concave shapes since they have not been investigated experimentally or through computational fluid dynamics (CFD). It should be noted that the shock shape about rounded-edge concave shapes may have a radius that varies with sweep angle, and so only basic assumptions can be made at the level of this work's analysis.

3.3. Static Stability

The stability of a planetary entry vehicle is one of the main factors that determines whether a particular design is feasible. If the EV requires quasi-steady flow in order for it to follow the designed trajectory, then the vehicle must be able to remain or return to the designed trim angle of attack α_{trim} after encountering flow disturbances. This can be determined by looking at the static and dynamic stability of the vehicle. This work analyzes the heat shields' static stability only for a first-look analysis. An in-depth, full vehicle analysis would require the study of both the static and dynamic stability since it is possible for a statically stable vehicle to be dynamically unstable. If a vehicle is statically stable, then it possesses the aerodynamic moments required to restore the vehicle to an equilibrium state after encountering a flow disturbance.[76]

One way to measure a vehicle's static stability is to analyze its aerodynamic moments about the vehicle's center of gravity. In this work, the aerodynamic moment coefficients $C_{m,0}$, $C_{n,0}$, and $C_{l,0}$ about the nose of the vehicle and the force coefficients C_N, C_A, and C_Y are calculated using modified Newtonian Impact Theory. Then the center of pressure location is determined from this information as previously explained. The center of pressure is the location at which the aerodynamic forces are applied. As a result, the aerodynamic moments, which are produced by the aerodynamic forces, are zero about the center of pressure. Once a center of gravity location is either chosen or calculated, moments produced by the aerodynamic forces about the center of gravity are calculated.

For a fixed body-axis moment with conventions for positive moments given in Figure 3.1(b), there are twelve possible center of pressure positions, with respect to the vehicle's center of gravity and the central axis. For example, in longitudinal stability, the contributions of the normal and axial forces to the pitching moment about the center of gravity are determined. If the center of gravity is below the central axis, then the center of pressure can be below the center of gravity, above the center of gravity in the same quadrant (below the central axis), or above the center of gravity in a different quadrant (above the central axis). In each of these cases, the center of pressure could be in front of, aligned with, or behind the center of gravity. If the aligned case is grouped with either the in front or behind cases, then there are six different geometric cases. The other six cases correspond to the inverted case in which the center of gravity is above the central axis, thereby producing a total of twelve cases.

After deriving each of the twelve cases for the pitching, yawing, and rolling moments about the center of gravity, it was observed that all twelve cases for each moment could be reduced into one equation, producing the following three equations

$$C_{m,cg} = C_N\left(\frac{X_{cg} - X_{cp}}{d}\right) + C_A\left(\frac{Y_{cp} - Y_{cg}}{d}\right), \tag{3.49}$$

$$C_{n,cg} = C_Y\left(\frac{X_{cp} - X_{cg}}{d}\right) + C_A\left(\frac{Z_{cg} - Z_{cp}}{d}\right), \tag{3.50}$$

$$C_{l,cg} = \begin{cases} C_N\left(\dfrac{Z_{cp} - Z_{cg}}{d}\right) + C_Y\left(\dfrac{Y_{cg} - Y_{cp}}{d}\right), & C_{L,V} \geq 0, \\ -\left(C_N\left(\dfrac{Z_{cp} - Z_{cg}}{d}\right) + C_Y\left(\dfrac{Y_{cg} - Y_{cp}}{d}\right)\right), & C_{L,V} < 0. \end{cases} \tag{3.51}$$

In order for the definition of rolling moment static stability to remain constant, the rolling moment $C_{l,cg}$ equation accounts for the change in positive moment convention that occurs when the vertical component of the lift coefficient becomes negative. The explanation for this is included in the next section, which comments on two misinterpretations of basic aerodynamic and stability theory.

With the moments about the vehicle's center of gravity determined, its static stability can be determined through an analysis of its moment derivatives with respect to angle of attack and sideslip angle. These derivatives $C_{m,cg\alpha}$, $C_{n,cg\beta}$, and $C_{l,cg\beta}$ are known as the static stability derivatives. For longitudinal stability, the derivative of the pitching moment with respect to angle of attack must be negative. For yaw stability, the derivative of the yawing moment with respect to sideslip angle must be positive. For roll stability, the derivative of the rolling moment with respect to sideslip angle must be negative. If the positive moment convention for $C_{l,cg}$ were kept constant for positive and negative lift, then roll stability requires the rolling moment derivative to be positive for negative lift.

To calculate the stability derivatives numerically, the code determines the $C_{m,cg}$, $C_{n,cg}$, and $C_{l,cg}$ at α - 0.25°, α + 0.25°, β - 0.5°, β + 0.5° in order to use the following finite-differencing approximate of the first derivative

$$C_{m,cg,\alpha} = \frac{dC_{m,cg}}{d\alpha} = \frac{C_{m,cg,\alpha+0.25^o} - C_{m,cg,\alpha-0.25^o}}{\Delta\alpha}, \tag{3.52}$$

$$C_{n,cg,\beta} = \frac{dC_{n,cg}}{d\beta} = \frac{C_{n,cg,\beta+0.5^o} - C_{n,cg,\beta-0.5^o}}{\Delta\beta}, \tag{3.53}$$

$$C_{l,cg,\beta} = \frac{dC_{l,cg}}{d\beta} = \frac{C_{l,cg,\beta+0.5^o} - C_{l,cg,\beta-0.5^o}}{\Delta\beta}. \tag{3.54}$$

These numerical approximations are second-order accurate in space. With the static stability derivatives calculated, an analysis of the vehicle's static stability can be completed.

3.4. Modified Uniform Density Assumption

This work uses a modified center of gravity location based on uniform density. The uniform density's center of gravity location is calculated according to section 2.4. While Y_{cg} and Z_{cg} are equal to their uniform density values, the prescribed $X_{cg}$is modified to equal 75% of the uniform density value. Bringing the X_{cg} forward increases the feasible design space by allowing more slender blunt-bodies with higher *L/D* to be longitudinally statically stable. For example, with the high eccentricity of e=−0.95, shown in Figure 3.3, comes the unstable pitching moment derivative $C_{m,\mathrm{cg},\alpha}$ =0.0566/rad if a uniform density heat shield is assumed.

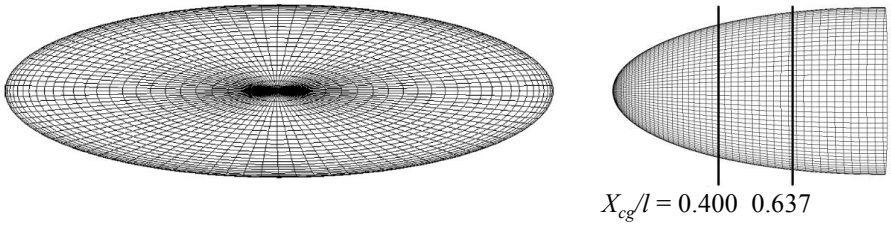

a) Front view **b) Side view**

Figure 3.3. Spherical segment $\theta_s = 90^o$ and e = -0.95.

However, if the uniform density value X_{cg}/l =0.635 is switched to X_{cg}/l =0.400, then the pitching moment becomes stable with $C_{m,\mathrm{cg},\alpha}$ =−0.099/rad. Note that the center of gravity location required for α_{trim} and the feasibility of that location is not determined in this work. Heat shields that required α_{trim} > ~20^o may require a center of gravity location that a more detailed analysis could determine is infeasible.

3.5. *Correcting Misinterpretations*

Two common misconceptions are detailed in this section to emphasize the importance of understanding these basic aerodynamic concepts. The first concerns the static roll stability requirement on a given aerodynamic vehicle. The second involves calculating the location of the center of pressure on a passive aerodynamic vehicle.

3.5.1. Static Roll Stability Requirement

When either a disturbance in the flow or a control input generates a rolling moment about the center of gravity of a lift-generating vehicle, the direction of the lift vector relative to the horizon is no longer perpendicular, causing the vehicle to sideslip. In general, a lift-generating vehicle sideslips as it rolls, and general stability theory concludes that there is a coupled effect that can be related to the vehicle's roll angle and the freestream sideslip angle. To make a lift-generating vehicle statically stable when it encounters a flow disturbance that brings the vehicle away from its desired orientation and path, the vehicle must be able to produce a counter-moment to bring it to its initial orientation (usually zero-roll angle or the designed trim position).

Aircraft stability assumes that the lift vector is always positive for an aircraft in wings-level attitude; this leads to the standard convention that a positive rolling moment renders a positive change in sideslip. As a result, the rolling stability derivative $C_{l,\beta}$ is required to be negative for static stability to counter flow disturbances.[76]

Spacecraft stability must also account for the possibility that the vehicle may be designed to produce negative lift during a portion of its trajectory. If the lift vector

is negative, then a positive rolling moment renders a negative change in sideslip, producing the reverse relationship between roll angle and sideslip angle, in which a positive roll angle produces a negative sideslip angle. In this case, the rolling stability derivative $C_{l,\beta}$ is required to be positive for static roll stability. Since a negative $C_{l,\beta}$ is commonly associated with a statically roll stable vehicle, this convention is maintained in this work by reversing the direction of the positive rolling moment convention when the vehicle produces negative lift as shown in Figure 3.1(b). The sign reversal of the positive rolling moment produces the discontinuity shown in Figure 3.4 in order for all roll stable configurations to have $C_{l,\beta} < 0$.

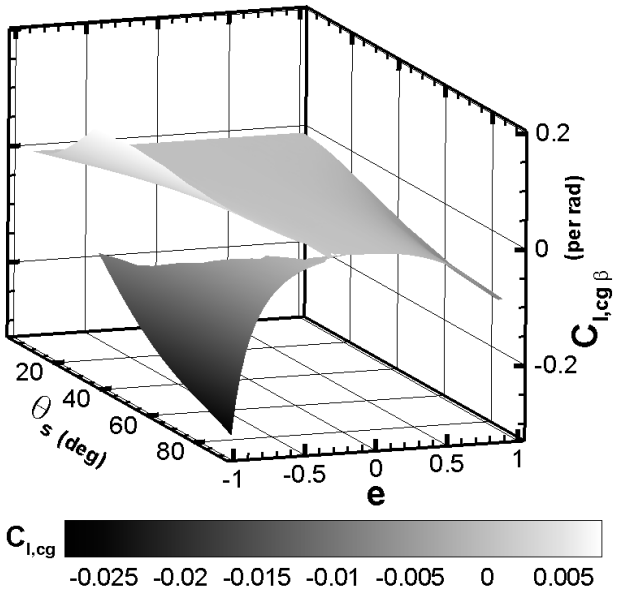

Figure 3.4. $C_{l,cg,\beta}$ distribution for spherical-segment, elliptical base ($n_2 = 2$), varying e and θ_s, $\alpha = 20^o$, $\beta = 5^o$.

As a result, if the positive rolling moment direction were kept constant, then there would be stable configurations with $C_{l,\beta} > 0$, and there would not be a discontinuity. With the sign reversal, Figure 3.4 clearly divides the stable and

unstable oblate geometries. Phillips[77] includes a good discussion on roll stability in his flight mechanics textbook.

3.5.2. *Determining the Location of the Center of Pressure*

One of the assumptions of aircraft stability, $C_L >> C_D$, cannot be followed in a blunt-body analysis since blunt bodies usually have an $L/D < 1$. The assumption of $C_L >> C_D$ leads to the conclusion that the center of gravity must lie in front of the aircraft's neutral point (or the vehicle's center of pressure) to satisfy the requirement of $C_{m,cg,\alpha} < 0$ for longitudinal static stability.[31] Since this assumption does not apply to blunt-bodies, it may be possible to produce longitudinal static stability with the center of pressure in front of the center of gravity. From modified Newtonian results for $C_{m,cg}$ shown in Figure 3.5 for $-30^o \le \alpha \le 0^o$, it is determined that the $X_{cp}/l = 0.6556$ and Y_{cp}/l varied from 0.0000 to 0.5530 for a spherical-segment of $\theta_s = 25^o$ with a non-eccentric base. As a result, the code suggests that the Apollo CM with a $X_{cg}/l = 2.171$ is one successful example of maintaining longitudinal static stability with the center of pressure in front of the center of gravity.

Similar to X_{cp}/l being constant over a range of α for a spherical-segment $e = 0$, $\theta_s = 25^o$, it has been proven that $X_{cp}/l = 0.6667$ for a sharp cone in a Newtonian surface pressure field, suggesting that X_{cp}/l is independent of half-cone angle θ_c.[2] Note that not all spherical-segments have $X_{cp}/l = 0.6556$, but at least one does with $\theta_s = 25^o$, $e = 0$ including the Apollo CM. The general pitching moment equations that relate X_{cp} and Y_{cp} to $C_{m,0}$ are given as Eqns. (3.20-3.22). These equations follow the coordinate system shown in Figure 3.1(b) that has a positive C_m corresponding to a

nose-up moment. Bertin[2] notes that the axial force's contribution to the pitching moment is commonly neglected in the definition of the center of pressure location at and near zero angle-of-attack. However, this assumption does not apply to blunt-body aerodynamics because $C_{m,A,0}$ is commonly the dominant term for a blunt-body.

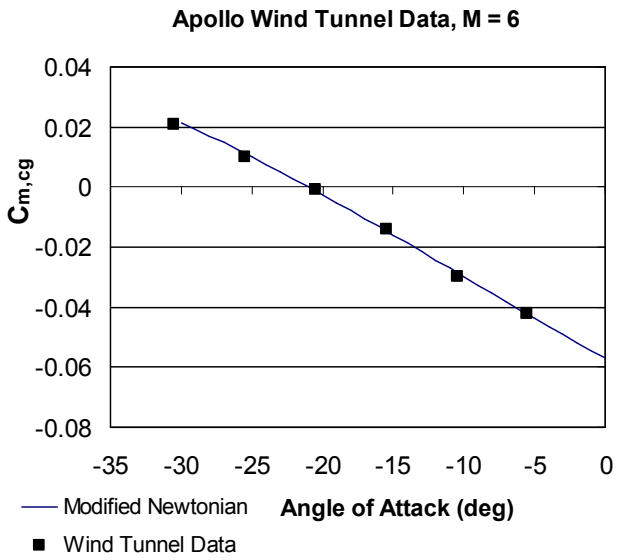

Figure 3.5. Variation in $C_{m,cg}$ with angle of attack.

$C_{m,N,0}$ is not usually the dominating term for slender bodies, in which case the resulting formula[2,33,64] for a circular cone at zero angle-of-attack $X_{cp}/l = 2/(3\cos^2\theta_c)$ can be used, but this equation complicates the analysis since X_{cp}/l is constant at 0.6667 without the assumption. When this assumption is applied to a blunt circular cone with $\theta_c = 70^\circ$, then $X_{cp}/l = 5.7$, which is not close to the actual $X_{cp}/l = 0.6667$. This assumption is only close to the exact solution for small θ_c, but a blunt-body cone does not have a small θ_c. For a general blunt-body shape, the following relation does not determine the x-location of the center of pressure

$$\frac{X_{cp}}{d} \neq -\frac{C_{m,0}}{C_N}. \tag{3.55}$$

Instead, X_{cp}/l for a given blunt-body shape can be determined from the normal force's contribution to the pitching moment $C_{m,N,0}$ as shown in Eqn. (3.21).

Arora's 2003 aerodynamic shape optimization work[66] maximizes X_{cp}. Unfortunately, he equates X_{cp} to $C_{m,0}/C_N$, which contradicts Eqn. (3.60). Since he does not account for the axial force's contribution to the pitching moment, his work is an example of recent research that has made this incorrect assumption on basic blunt-body aerodynamics, rendering the published optimization results unusable. His conclusion is that the optimized X_{cp} value is 1.213 m, but a quick analysis of the geometry he chose accounting for the axial force's contribution to the pitching moment suggests that the actual X_{cp} is less than approximately 1.1 m, suggesting that his optimization results are within an infeasible region of x-locations due to the incorrect definition of X_{cp}. Additionally, his optimization results could be significantly different when accounting for the general relation of X_{cp} and $C_{m,0}$ given by Eqn. (3.20). Note that the incorrect definition of X_{cp} for a blunt body is included in Regan's first edition[64] and Rasmussen.[33] These are all examples of published work that show what Bertin[2] mentions is the conventional definition of X_{cp}, not the true definition of X_{cp} that is required to complete an aerodynamic analysis of blunt-bodies.

Chapter 4. Heat Transfer

The primary physical mechanisms that contribute to the hypersonic aerothermodynamics, i.e., the aerodynamic forces, moments, and heat transfer,[2] in this work consist of (1) the surface pressure distribution, (2) the velocity gradient along the heat shield, and (3) the radiating shock layer. The local bow shock strength, imposed on the vehicle by freestream conditions, strongly affects both the surface pressure distribution and the resulting heat transfer along the heat shield. The surface pressure distribution has been approximated with modified Newtonian theory, as described in the previous chapter. This chapter describes how the latter two are taken into account. Conduction through the shock layer is negligible; thus, two heat transfer modes convection and radiation are considered in this work. Convective heat transfer occurs at the surface based on the surface pressure distribution that imposes a velocity gradient along the heat shield, which sets the velocity at the edge of the boundary layer. The thickness of the high temperature shock layer influences the thermal radiative heat flux.

The two arguably most important heat transfer characteristics are the heat flux and the heat load. The heat flux is power density in the form of heat per unit area. The heat load is equal to the heat flux integrated over the trajectory in time. It is common in the first analysis of a vehicle to look at the heat fluxes and heat loads at the stagnation point because they have been shown to correlate with TPS mass.[1]

The Apollo CM reentered at an angle of attack that brought the stagnation point near the corner radius. In such cases, as noticed in Ref. (38), the heat transfer is

higher at the edge of the heat shield than at the stagnation point. In fact, the Apollo Command Module at $\alpha = \pm 33^{o}$ had a heat transfer flux at the edge that is 92% larger than that at the stagnation point corresponding to $\alpha = 0^{o}$, according to wind tunnel results,[38] but the actual CMs did not necessarily travel trajectories that required this high an angle of attack. The most likely reason that this was one of the highest angles of attack tested is because the conical shaped crew compartment that connected to the heat shield was at a 33^{o} angle with the horizontal. As a result, the flow would pass by the crew compartment flush at $\alpha = \pm 33^{o}$. The Apollo 4 CM traveled with a maximum angle of attack of $\pm 25^{o}$, in which the heat transfer at the edge is around 60% higher than at the stagnation point corresponding to $\alpha = 0^{o}$, according to other wind tunnel results.[39] In both the cases of $\alpha = \pm 25$ and $\pm 33^{o}$, the stagnation-point heat flux is approximately 15% larger than it would be at $\alpha = 0^{o}$.[38,39] As a result, the heat flux is higher at the edge of the heat shield than that at the stagnation-point of the Apollo CM.

Both the heat flux and heat load are equally important. This chapter explains the correlations applied in this work and their assumptions. The correlations were originally designed to calculate the stagnation-point heat flux on a sphere. Applying these correlations allows for the heat flux to vary with the radius of curvature of a given blunt body. Explanations on how these correlations are applied to blunt-bodies are included in the following sections. These correlations also vary with altitude through a freestream density factor and with speed through a freestream velocity factor. For this work the ARDC 1959 Model[78] and US Standard Atmosphere of 1976[79] have been applied. The 1976 standard atmosphere is applied for results, but

the 1959 model atmosphere is used as noted throughout the text for the application of older correlations and code validation of results that used standard atmospheres before 1976.

4.1. Convection

The properties of the high temperature shock layer affect both convection and radiation due to the presence of dissociated and partially-ionized air. Additionally, the heat shield geometry directly affects the surface pressure distribution, and thus, the velocity gradient along the heat shield, at the edge of the boundary layer. A smaller local radius-of-curvature increases the velocity gradient, thereby increasing the local convective heat flux.[3] Low-order correlations based on empirical data account for these upstream effects with a local radius-of-curvature term. The stagnation-point convective heat transfer correlation of Tauber[45] is applied in this work. Tauber assumes equilibrium flow conditions and a flight regime where boundary-layer theory is valid. Tauber produces a specific equation for planetary entry from satellite speed, but it is the objective of this work to approximate the heat transfer flux for planetary entry from both satellite and superorbital entry speeds. To account for this, the general form of his correlations, which is given as Eqn. (4) of his article[45], is applied to produce the following correlation for the stagnation-point convective heat flux

$$q_{s,conv} = \left(1.83\times10^{-8}\right) r_n^{-0.5}(1-g_w)\rho_\infty^{0.5}V_\infty^3, \tag{4.1}$$

in which g_w is the ratio of wall enthalpy to total enthalpy. It is assumed that $g_w << 1$, and so g_w is zero in this work. This correlation assumes a fully catalytic surface, which makes Eq. (4.1) a conservative estimate since this makes the convective heat

flux independent of material choice as the recombination rate is infinitely large. Bertin[2] indicates that the fully catalytic wall boundary condition produces results that approach the equilibrium flow solution (Figure 5.12 of Ref. [2]). This correlation also holds true to the Fay and Riddell[46] derivation that states the $q_{s,conv}$ is inversely proportional to the square root of the nose radius. Zoby[47] presents evidence that this relation breaks down for blunt bodies with ratio values of base radius r to nose radius r_n less than 0.6, in which $r_n > r$. He suggests that this is due to the velocity gradient being higher than would be otherwise expected by the deriving $q_{s,conv} \propto r_n^{-0.5}$. If possible, this would be a good addition for future work. This is only one example that these heat transfer derivations are not accepted as fact in their application to blunt bodies, but they generate trends that are accepted as generally true for stagnation-point heat transfer.

The form of the correlation shown in Eqn. (4.1) was originally designed for calculating stagnation-point heat flux on a sphere. Since the stagnation-point convective heat flux relies mainly on the geometry nearby the stagnation-point, as opposed to the full body shape and size, it can be approximated by setting the radius of curvature equal to the nose radius. The nose radius is the term that relates the heat flux to the geometry in Eqn. (4.1). For the spherical-segment and spherically-blunted cone axial shapes, determining r_n is a trivial calculation. For the power law axial shape, the slope of the shape at the tip of the nose may not necessarily be continuous, as in the case of setting $b = 1$, in which a sharp cone axial shape is generated.

As a result, the blunt-bodies with a power law axial shape must have an equivalent nose radius term produced. This equivalent nose radius is only an

approximation and should not be accepted as a complete model for power law shapes. First, it is assumed that the power law shape's nose tip is blunted if its slope is discontinuous. Then the profile of the power law shape is examined; for this analysis, a line that is normal to the power law profile and that produces a 15^o angle with the horizontal is generated. A segment of that line that begins at the line's intersection with the power law profile and ends at its intersection with the horizontal central axis is produced. The effective radius is assumed to be equal to the average of the length of that line segment and the distance to the nose from the end point of that line segment on the horizontal axis. If the normal line intersects the power law curve beyond the base of the geometry (the intersection occurs outside of the heat shield shape), then the geometry's curvature is assumed sharp and given an effective radius value of 0.001 m. To produce a true method for determining the effective radius of the general power law shape for convective heat transfer is a research topic in itself.

4.2. Radiation

Since radiation over a blunt-body can be primarily modeled as an elliptic problem, the radiation at the stagnation point depends on the body of the vehicle in addition to the nose radius. For a given set of freestream conditions and a shock layer with emitted power density E, $q_{s,rad}$ will be greater for the heat shield with the larger Δ_{so}.[3] Also, the radiative heat flux is significantly more sensitive to the angle-of-attack of the blunt body than the convective heat flux. In this work, all these effects are incorporated into the term called the effective radius. In order to apply $q_{s,rad}$ correlations for spheres to non-spherical blunt-bodies, the effective

radius in this work is directly related to the spherical radius for a given set of freestream conditions. This is accomplished by estimating the shock-standoff distance Δ_{so} across from the stagnation point at a given normal shock density ratio ρ_2/ρ_1 of the blunt body.

To calculate the normal shock density ratio ρ_2/ρ_1, high temperature properties of air must be determined in order to calculate an effective specific heat ratio after the normal shock $\gamma_{eff,2}$. Tannehill[57] supplies high temperature air correlations for this work, and they are also located in Chapter 11 of Anderson.[3] The effective specific heat ratio after the normal shock is determined through an iterative process. First, a test variable for $\gamma_{eff,2}$ is called $\gamma_{test,2}$ and set equal to 1.4 as an initial condition. Then the corresponding pressure p_2 and density ρ_2 after the normal shock are calculated based on $\gamma_{test,2}$

$$p_2 = p_1\left(1+\frac{2\gamma_{test,2}}{\gamma_{test,2}+1}\left(M_1^2-1\right)\right), \tag{4.2}$$

$$\rho_2 = \rho_1\left(\frac{\left(\gamma_{test,2}+1\right)M_1^2}{\left(\gamma_{test,2}-1\right)M_1^2+2}\right), \tag{4.3}$$

and these two variables are entered into Tannehill's Fortran code that returns the corresponding enthalpy h_2 and $\gamma_{eff,2}$

$$h_2 = \frac{p_2}{\rho_2}\left(\frac{\gamma_{eff,2}}{\gamma_{eff,2}-1}\right), \tag{4.4}$$

$$\gamma_{eff,2} = c_1 + c_2Y + c_3Z + c_4YZ + \frac{c_5 + c_6Y + c_7Z + c_8YZ +}{1+\exp\left(c_9\left(X + c_{10}Y + c_{11}\right)\right)}, \tag{4.5}$$

$$\text{in which } X = \log_{10}\left(\frac{p_2}{1.292}\right),\ Y = \log_{10}\left(\frac{\rho_2}{1.013\times10^5}\right),\ Z = X - Y, \tag{4.6}$$

and coefficients c_1 through c_{11} are curve-fit values tabulated in Tannehill.[57] For this work, only the $\gamma_{eff,2}$ is used. The value of $\gamma_{eff,2}$ is compared to $\gamma_{test,2}$; then $\gamma_{test,2}$ is set equal to the calculated $\gamma_{eff,2}$, and the process is iterated until the absolute value $|\gamma_{eff,2} - \gamma_{test,2}|$ is less than 0.01. Once a converged value of $\gamma_{eff,2}$ is determined, then the corresponding normal shock density ratio ρ_2/ρ_1 has been calculated and could be used in Kaattari's method described in Chapter 3 to approximate the shock-standoff distance.

It is assumed that the effective nose radius for stagnation-point radiative heat transfer, r_{eff}, for a given blunt body is equal to the radius of a particular sphere that maintains an equal shock-standoff distance. After calculating the normal shock-standoff distance, the corresponding spherical radius still would have to be determined.

According to wind tunnel results shown in Figure 4.1, the ratio of the normal shock-standoff distance to a sphere of radius r_{eff} is constant for a given normal-shock density ratio.

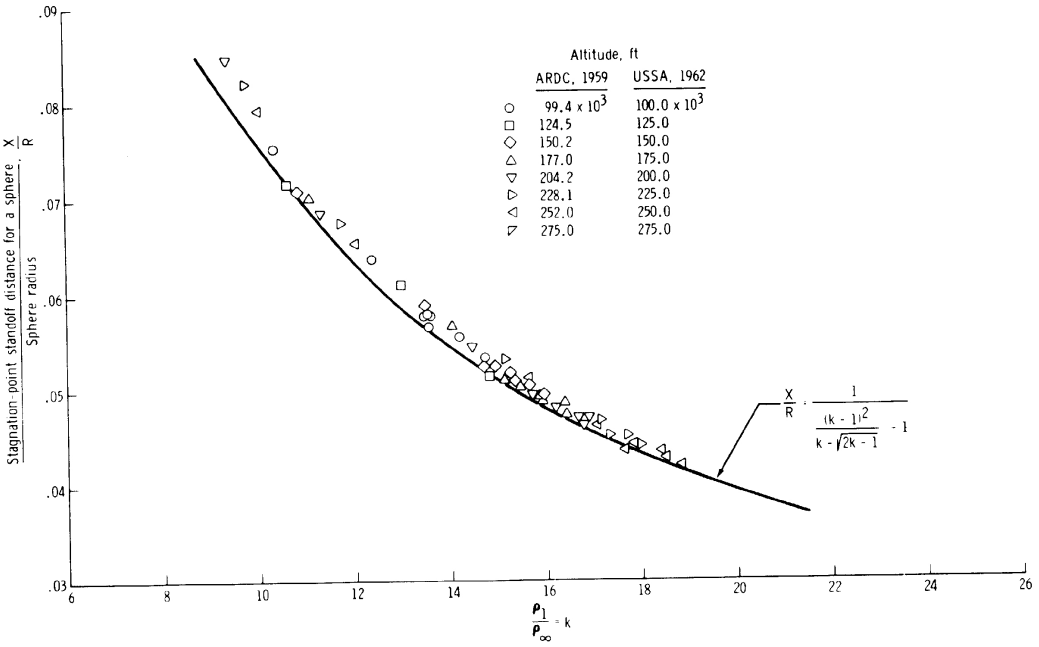

Figure 4.1. Stagnation-point Δ_{so} wind tunnel data with empirical curve-fit, Ref. [51].

Ried[51] offers an empirical curve-fit that renders an acceptable approximation, also shown in Figure 4.1:

$$\Delta_{so}/r_{eff} = \left(\frac{\left(\frac{\rho_2}{\rho_1} - 1\right)^2}{\frac{\rho_2}{\rho_1} - \sqrt{\frac{2\rho_2}{\rho_1} - 1}} - 1 \right)^{-1} . \tag{4.7}$$

Then the r_{eff} from this equation replaces the sphere's radius in the stagnation-point radiative heat flux correlations. Two $q_{s,rad}$ correlations are applied over a range of freestream velocities. For $V_\infty < 9000$ m/s, the correlation applies the following form

$$q_{s,rad} = r_{eff}\, g_1 \left(3.28084 \times 10^{-4} V_\infty\right)^{g_2} \left(\frac{\rho_\infty}{\rho_{sl}}\right)^{g_3}, \tag{4.8}$$

in which $g_1 = 372.6$, $g_2 = 8.5$, and $g_3 = 1.6$ from Ref. [2] for $V_\infty < 7620$ m/s, and $g_1 = 25.34$, $g_2 = 12.5$, $g_3 = 1.78$ from Ref. [44] for velocities 7620 to 9000 m/s. For velocities above 9000 m/s, Tauber and Sutton[48] apply

$$q_{s,rad} = 4.736 \times 10^4 \, r_{eff}^{H} \rho_{\infty}^{1.22} f(V_{\infty}), \tag{4.9}$$

$$\text{in which } H = 1.072 \times 10^6 V_{\infty}^{-1.88} \rho_{\infty}^{-0.325},$$

$$\text{and } f(V_{\infty}) = \begin{cases} -3.93206793 \times 10^{-12} V_{\infty}^4 + 1.61370008 \times 10^{-7} V_{\infty}^3 - 2.43598601 \times 10^{-3} V_{\infty}^2 \\ +16.107869 V_{\infty} - 39494.8753 \end{cases} \quad 9000 \le V_{\infty} \le 11500 \, m/s$$

$$\begin{cases} -1.00233100 \times 10^{-12} V_{\infty}^4 + 4.89774670 \times 10^{-8} V_{\infty}^3 - 8.42982517 \times 10^{-4} V_{\infty}^2 \\ +6.25525796 V_{\infty} - 17168.3333. \end{cases} \quad 11500 < V_{\infty} \le 16000 \, m/s$$

Thermochemical equilibrium is assumed. The curve-fit equation for $f(V_\infty)$ has a high number of significant figures in order to have < 2% error with the published tabulated values.[48] It is suggested that all of these digits are maintained; if they are not, the values of $f(V)$ may go below zero for low V_∞ or produce extremely large values for high V_∞, either case producing erroneous results. The high number of digits does not correspond to the number of significant figures from this correlation. It is suggested that no more than three digits should be specified as significant for all three radiation correlations.

Chapter 5. Mission Profile & Entry Vehicle Scaling

The mission profiles and entry vehicle scaling evolved throughout this work. The results in Chapter 10 apply the first set. The second set applies to Chapter 11–Chapter 14; it is based on the first set with some modifications to produce more practical design conditions. The first set of mission profiles and entry vehicle scaling is first detailed and then the modifications made for the second set are then provided.

5.1. Initial mission profile and entry vehicle scaling set

5.1.1. Mission profile

To simulate Earth entry for lunar return, an initial entry velocity of 11 km/s is applied.[32] For Mars return, a fast 180-day return renders entry velocities up to 14.7 km/s,[80] and an initial entry velocity of 15 km/s is applied. Although the hypersonic aerodynamics at these two velocities are similar for a given heat shield design, their heat transfer environments are greatly different. While convection typically dominates for a vehicle entering at 11 km/s, radiation is projected to be the primary heat transfer mode for 15 km/s.

The mission profile for the Orion Crew Exploration Vehicle (CEV) with an overall duration of 18 days, a crew of four, and a pressurized volume of 5 m^3/person is applied.[81] The Earth entry simulation begins at the atmospheric interface, at an altitude of 122 km, and terminates after the freestream Mach number becomes less than five, account for the hypersonic aerodynamics only. For blunt-bodied capsules

(low L/D), whether the trajectory ends at $M_\infty < 5$ does not strongly affect the values of the three optimization parameters in this analysis: cross range p_{xrs}, peak stagnation-point heat flux $q_{s,max}$, and total stagnation-point heat load $Q_{s,tot}$. This profile is utilized for both lunar and Mars return.

5.1.2. Entry vehicle mass estimation and scaling

Mass estimation and scaling of the entry vehicle is based on the mission profile, heat shield geometry, and dimension requirements for incorporating the crew or payload. The scaled vehicle must satisfy required crew seating dimensions. These sizing constraints may require the vehicle to be increased in size, in which case the crew number may be increased. The assumed seat dimensions required for suited astronauts include an upright front-to-back depth lp_1 = 1.1 m, an upright width wp_1 = 0.7 m, an upright top-to-bottom height hp_1 = 1.4 m, a reclined depth $lp_2 = hp_1$, and a reclined height $hp_2 = lp_1$. In this analysis, upright corresponds to a seat back positioned parallel the z-axis while reclined refers to a seat back positioned parallel to the x-axis. This allows the seat to be positioned against the base of the heat shield for (1) highly blunt configurations (Apollo CM) in which the vehicle's base is parallel to the z-axis and (2) for slender configurations (low θ_c) in which the base is more aligned with the x-axis.

Vehicle scaling is necessary due to the wide range of heat shields in the design space. High θ_s, for example, can allow the heat shield to encompass part of or the entire pressurized volume. If the entry vehicle geometry is assumed to have the same top–to-bottom base height of 5 m as Orion, then heat shields with high eccentricity would have over 15 times Orion's volume. Other designs may have smaller volumes

than the Orion's. To scale the entry vehicle, a heat shield is categorized into one of four cases based on l_{HS}. This differentiates the procedures applied for estimating the pressurized volume based on the heat shield's geometry. As a result, each heat shield is categorized into one of four cases to size the vehicle:

(1) $l_{HS} \leq l_{Orion}$, $l_{Orion} = 0.55$ m

(2) $l_{Orion} < l_{HS} \leq l_{R1}$, in which $l_{R1} = b_t l_{p1} + l_{Orion} = 2.2$ m,

(3) $l_{R1} < l_{HS} \leq l_{R2}$, in which $l_{R2} = b_t l_{p2} + l_{Orion} = 2.65$ m,

(4) $l_{R2} < l_{HS}$.

The value for factor b_t is 1.5 to account for the surrounding structure, in order for the seat dimensions to fit within the heat shield's dimensions for all cases. For case 1, the heat shield has a shorter length l_{HS} than the Orion's. For this case, a volume equal to $\frac{1}{4}\pi ab(l_{Orion} - l_{HS})$ is added to the calculated heat shield volume as a conservative estimate for the required thickness of the heat shield for storage of non-pressurized vehicle systems. The ratio f_{HS} of the heat shield volume to the entry vehicle volume is utilized to determine the resulting volume of the entry vehicle V_{EV}. For cases 1, $f_{HS} = f_{HS,Orion} \approx 17.7\%$. For all cases, it is assumed that the ratio f_{PR} of the pressurized volume V_{PR} to the entry vehicle volume V_{EV} is equal to that of Orion, $f_{PR} = f_{PR,Orion} \approx 63\%$. The crew number n_{crew} is determined based on V_{PR} and the pressurized volume requirement.

Once the pressurized volume is closely matched and seat dimensions are satisfied, the entry vehicle mass is estimated based on the following empirical correlation[82]

$$m_{EV} = 592\left(n_{crew} t_d V_{PR}\right)^{0.346}. \tag{5.1}$$

Based on the mission profile, Orion's estimated mass of 7340 kg is precisely the reported landing mass of Orion.[81] The entry vehicle masses for this analysis are nearly constant since heat shield scaling is designed to render a pressurized volume that meets the mission requirements as closely as possible. For the Apollo mission profile[82] of n_{crew} = 3 crew, t_f = 10 days, $V_{PR} \approx 9.2\text{m}^3$, d = 3.9 m the calculated m_{EV} is within 30% of 5800 kg, and so it is suggested to adjust Eq (5.1) by a factor of 1.3 accordingly when applying the Apollo mission profile. For case 2, a portion of the heat shield's volume can be utilized for seat locations. When $l_{HS} = l_{R1}$, the heat shield has sufficient dimensions to fit the entire crew. To approximate the amount of heat shield volume that is allocated as pressurized volume, a linear curve is designed to join the two end-states of this range, $l_{HS} = l_{Orion}$ and $l_{HS} = l_{R1}$, resulting in this function of entry vehicle volume

$$V_{EV} = \frac{V_{HS}}{S_{EV} f_{HS,Orion}}, \tag{5.2}$$

$$\text{in which } S_{EV} = \left(\frac{1 - \frac{1}{f_{HS,Orion}}}{l_{R1} - l_{Orion}} \right) (l_{HS} - l_{R1}) + 1, \tag{5.3}$$

and S_{EV} = 1 for case 1. For cases 3 and 4, the entire pressurized volume fits inside the heat shield geometry. Case 3 represents highly blunt configurations, and thus, the seats are placed in an upright position. Case 4 represents slender configurations. Since the seats are placed in a reclined or horizontal position, the height requirement for case 4 is reduced to $b_t h_{p2}$ = 1.6 m. Once the available pressurized volume is determined, the crew number is calculated based on pressurized volume requirements.

If the crew number is greater than four, then an iterative process proceeds to scale down the vehicle until either $n_{crew} = 4$ or the seat dimensions limit is met. Then Eq. (5.1) is applied to determine the final mass of the entry vehicle. For this analysis, the aim is to bring the entry vehicle's mass towards the projected mass of Orion.

This mass estimate is independent of heat load, which determines the heat shield material's thickness in a detailed design analysis. Several new heat shield designs are considered, and thus, the heat load for a given vehicle and flight path is unknown a priori. The required iterative process, which would increase the computation time by a few factors, has not been integrated into the optimization setup. Uniform density is assumed to calculate the center of gravity location of the heat shield, and the prescribed X_{cg} is modified to equal 75% of the uniform density value. Bringing the X_{cg} forward increases the feasible design space by allowing more slender blunt-bodies with higher *L/D* to be longitudinally statically stable.

5.2. Modifications to initial set

5.2.1. Mission profile

The mission profile for lunar return mostly remains the same. To simulate Earth entry for Mars return, an initial entry velocity has been changed from 15 km/s to 12.5 km/s. The required inertial Mars return velocity is a function of the year of transit and the return transit time. A fast 180-day transit[80] to Earth produces entry velocities up to 14.7 km/s. Braun[83] indicates that a 14 km/s entry may produce heat loads as high as 95 kJ/cm^2 for a vehicle with a 3-m nose radius and ballistic coefficient of 310 kg/m^2. This heat load is nearly halved at 50 kJ/cm^2 by reducing V_E

to 12.5 km/s. Recent work[1] indicates heat loads near 120 kJ/cm^2 and 65 kJ/cm^2 are produced at 14 and 12.5 km/s respectively for BC = 350 kg/m^2. The entry velocity 12.5 km/s covers ~40% of the years of transit for a 180-day return to Earth.[1] It accommodates ~80% of the years of transit for 230 to 270-day returns, and ~100% thereafter. The manned Apollo missions experienced heat loads[41] of ~31 kJ/cm^2 with V_E = 11 km/s. As a result, the expectation on TPS design to accommodate a ~100 kJ/cm^2 heat load with V_E = 14 km/s, which will greatly challenge the current capabilities of several other subsystems, may be unnecessary and impractical for the first manned Mars return missions. The Earth entry simulation terminates at M_∞ = 2, at which drogue parachutes would be deployed. This is different from the initial setup and allows for more realistic end constraints on the entry trajectory.

5.2.2. Entry vehicle mass estimation and scaling

The projected mass of Orion is currently ~10,000 kg. The initial mass estimation method was based on Orion's projected mass of 7340 kg. As a result the empirical correlation in Eq. (5.1) underestimates the Orion mass by 30-40%, as it does for the Apollo Command Module. This method is extended in the current work by modifying the heat shield mass based on surface area and heat load comparisons with Orion. Since the Apollo heat shield comprised of 13% of the Command Module's mass,[21] it is assumed that the heat shield mass is 15% of Orion's total mass, assumed to be 10000 kg, and that the remaining 8500 kg is fixed. After surface area is accounted for in the heat shield mass, two mass estimations are produced based on heat load. The first mass estimation assumes that the additional heat load does not augment the mass of the heat shield. Evidence of this being possible for vehicles with

$L/D \leq 0.5$ is given in Fig. 11 of Ref. [1], in which TPS thickness only slightly increases with V_E increasing from 11 to 14 km/s, although the heat load significantly increases. The second mass estimation provides an upper-end conservative value that assumes that the mass of the heat shield is increased by a factor of three. Preliminary results indicated that a heat load three times the $Q_{s,tot}$ at lunar return conditions (~20 kJ/cm^2) is produced at Mars return conditions. The factor of three assumes that if the heat load is three times the heat load at lunar return conditions, then the heat shield has three times the thickness. Ultimately, the heat shield thickness will be trajectory dependent. By incorporating both upper and lower mass estimations, a sensitivity of mass on $Q_{s,tot}$ is conducted concurrently with the results, and a range of heat loads for optimal geometries for both mass estimates are given. Uniform density is assumed to calculate the center of gravity location of the heat shield, and the prescribed X_{cg} is modified to equal 75% of the uniform density value. Bringing the X_{cg} forward increases the feasible design space by allowing more slender blunt-bodies with higher L/D to be longitudinally statically stable.

5.3. *Mass and geometric trends of entry vehicles*

Manned space capsule geometries have been approximated using a generic space capsule model, shown in Figure 5.1, to determine any trends between the masses and the geometries of previous work as well as the current estimates for the Orion CEV. The generic space capsule model is composed three sections: the spherical-segment heat shield, the conical frustum crew compartment, and an end cylinder.

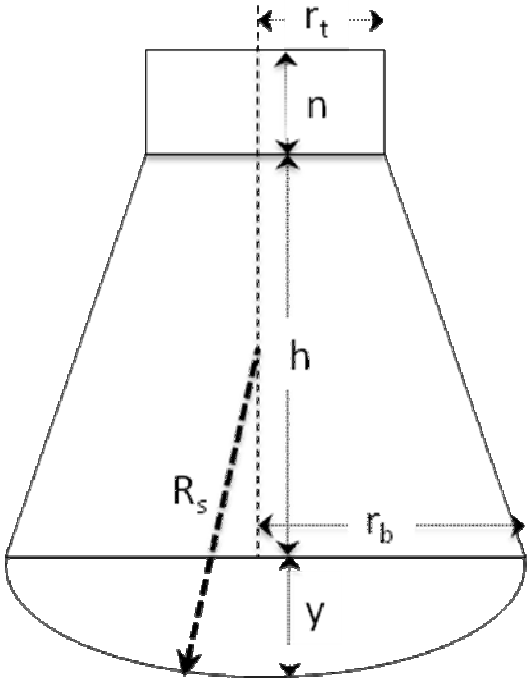

Figure 5.1. Generic space capsule model.

Note that y is related to r_b and R_s as

$$R_s = \frac{r_b^2 + y^2}{2y} \tag{5.4}$$

$$\text{such that } y = R_s\left[1 - \sqrt{1 - \left[r_b / R_s\right]^2}\right].$$

The surface area is the sum of the three section areas, in which the heat shield area is

$$A_1 = 2\pi R_s^2\left\{1 - \sqrt{1 - \left[r_b / R_s\right]^2}\right\}, \tag{5.5}$$

the conical frustum area is

$$A_2 = \pi\left(r_b + r_t\right)\sqrt{h^2 + \left[r_b - r_t\right]^2}, \tag{5.6}$$

and the end cylindrical area is

$$A_3 = \pi\left(r_t^2 + 2r_t n\right). \tag{5.7}$$

The total surface area of the generic space capsule model is

$$A_{tot} = \pi\left\{2R_s^2\left(1-\sqrt{1-\left[r_b/R_s\right]^2}\right)+\left(r_b+r_t\right)\sqrt{h^2+\left[r_b-r_t\right]^2}+\left(r_t^2+2r_t n\right)\right\}. \quad (5.8)$$

The volume is the sum of the three section volumes, in which the heat shield volume is

$$\begin{aligned} V_1 &= \frac{1}{6}\pi y\left(3r_b^2+y^2\right) \\ &= \frac{1}{6}\pi R_s\left[1-\sqrt{1-\left[r_b/R_s\right]^2}\right]\left(3r_b^2+R_s^2\left[1-\sqrt{1-\left[r_b/R_s\right]^2}\right]^2\right), \end{aligned} \quad (5.9)$$

the conical frustum volume is

$$V_2 = \frac{1}{3}\pi h\left(r_b^2+r_t^2+r_t r_b\right), \quad (5.10)$$

and the end cylindrical volume is

$$V_3 = \pi r_t^2 n. \quad (5.11)$$

The total volume of the generic space capsule model is

$$V_{tot} = \pi\left\{\tfrac{1}{6}R_s\left[1-\sqrt{1-\left[r_b/R_s\right]^2}\right]\left(3r_b^2+R_s^2\left[1-\sqrt{1-\left[r_b/R_s\right]^2}\right]^2\right)+\tfrac{1}{3}h\left(r_b^2+r_t^2+r_t r_b\right)+r_t^2 n\right\}. \quad (5.12)$$

This model has been applied to the Mercury, Gemini, Apollo, and Orion atmospheric entry spacecrafts. Dimensions and masses of the spacecraft, listed in Table 5.1, have been gathered from Refs. [84], [85], [86], [87], and [88].

Table 5.1. Mass and dimensions of manned spacecraft.

Spacecraft	Shield radius R_s (m)	Base radius r_b (m)	Top radius r_t (m)	Shield height y (m)	Cone height h (m)	Nose height n (m)	Overall height (m)	Total mass m_{EV} (kg)
Mercury	3.2	0.95	0.41	0.14	0.91	1.15	2.21	1360
Gemini	3.7	1.14	0.49	0.18	1.61	1.52	3.32	3190
Apollo	4.6	1.96	0.64	0.44	2.45	0.00	2.89	5800
Orion CEV (projected)	6.0	2.52	0.76	0.55	2.75	0.00	3.30	9700

The calculated volumes and areas are provided in Table 5.2.

Table 5.2. Area and volume characteristics of manned spacecraft.

Spacecraft	Shield area A_1 (m^2)	Cone area A_2 (m^2)	Nose area A_3 (m^2)	Base cross sectional area A_{xrs} (m^2)	Total surface area A_{tot} (m^2)	Shield volume V_1 (m^3)	Cone volume V_2 (m^3)	Nose volume V_3 (m^3)	Total volume V_{tot} (m^3)	Volumetric efficiency, η_v Eq. (2.16)
Mercury	2.88	4.49	3.46	2.81	10.83	0.21	1.37	0.60	2.18	74.9%
Gemini	4.21	8.91	5.46	4.10	18.58	0.38	3.55	1.15	5.08	76.9%
Apollo	12.62	22.68	1.30	12.02	36.60	2.67	14.09	0.00	16.76	86.5%
Orion CEV	20.83	33.58	1.83	19.87	56.24	5.58	25.42	0.00	31.00	84.8%

In addition to manned spacecraft, the X-20 Dyna-Soar (Dynamic Soarer)[89,90] and ASV-3 ASSET (Aerothermodynamic Elastic Structural Systems Environmental Tests)[91,92] have been incorporated into this analysis although they do not follow the generic capsule model. The X-20, shown in Figure 5.2, as a lifting body with a high $L/D \approx 1.4$, was a United States Air Force entry vehicle project that was cancelled in 1963 near the beginning of its construction. This high L/D allows a vehicle to have greater cross range capability and maneuverability than typical space capsule designs. The ASV-3 ASSET program was part of the Dyna-Soar project; shown in Figure 5.3, it also was a lifting body with $L/D \approx 1.1$. The ASV-3 was tested unmanned and successfully to acquire aerothermodynamics data.

For this analysis, previous manned spacecraft provide entry vehicle characteristics for $L/D < 0.4$, and the X-20 and ASV-3 provide entry vehicle characteristics for $L/D = 1.0 - 1.5$. Their surface areas and volumes were deduced from Figure 5.2 and Figure 5.3, and their characteristics are listed in Table 5.3. Note that the base radius is derived from the planform area and corresponds to the radius for a circular cross section that has an area equal to the listed planform area. The planform area will be utilized in the base cross sectional area comparison.

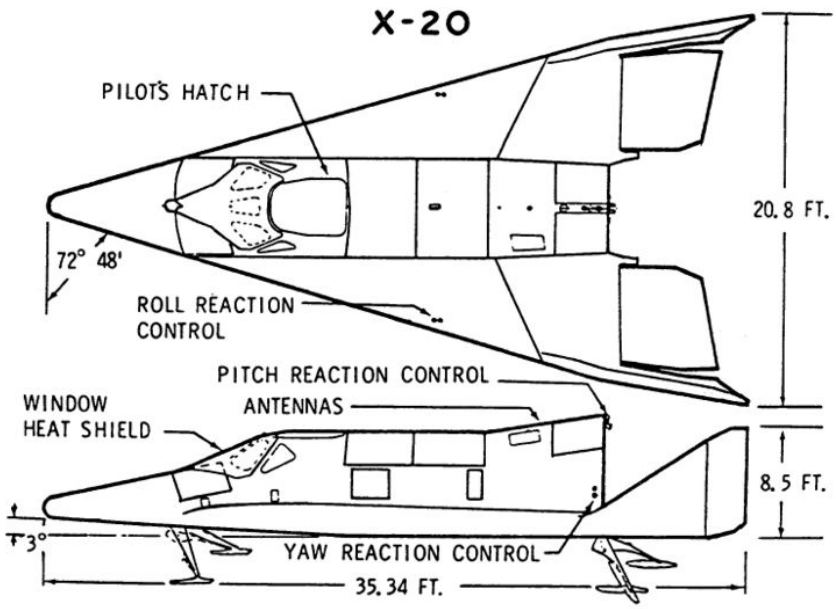

a) Top and side view from Ref. [90]

b) Front view from Ref. [89]

Figure 5.2. X-20 Dyna-Soar.

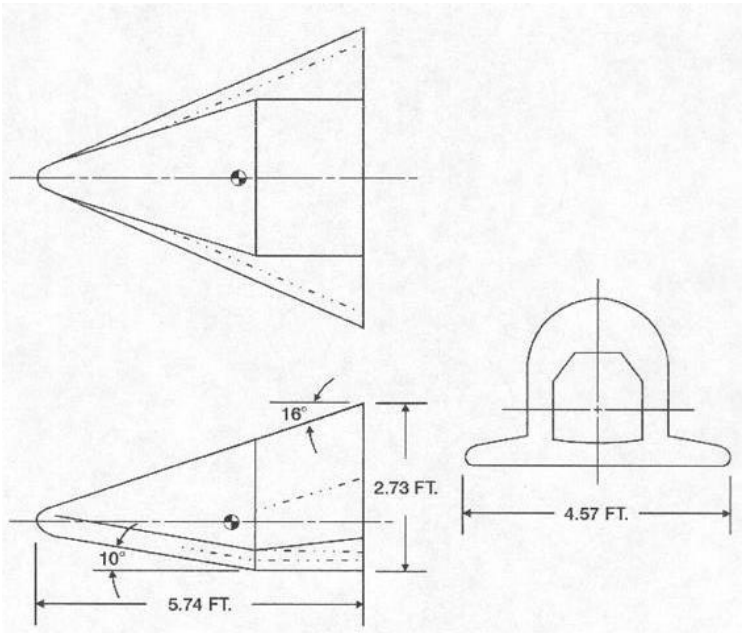

Figure 5.3. ASV-3 ASSET drawing from Ref. [92].

Table 5.3. Characteristics of Dyna-Soar and ASSET.

Spacecraft	Base radius r_b (m)	Base area A_{tot} (m^2)	Planform area (m^2)	Total surface area A_{tot} (m^2)	Total volume V_{tot} (m^3)	Volumetric efficiency, η_v Eq. (2.16)	Total mass m_{EV} (kg)
Dyna-Soar	1.21	4.57	32.00	89.77	38.01	60.9%	5160
ASSET	0.41	0.53	1.32	4.02	0.56	81.9%	540

Trends in surface area, base cross sectional area, and volumetric with respect to entry vehicle mass are given in Figure 5.4, Figure 5.5, and Figure 5.6.

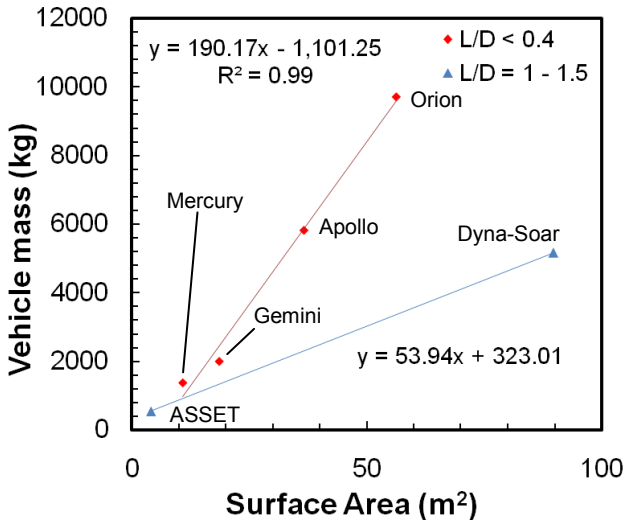

Figure 5.4. Surface area effects on vehicle mass.

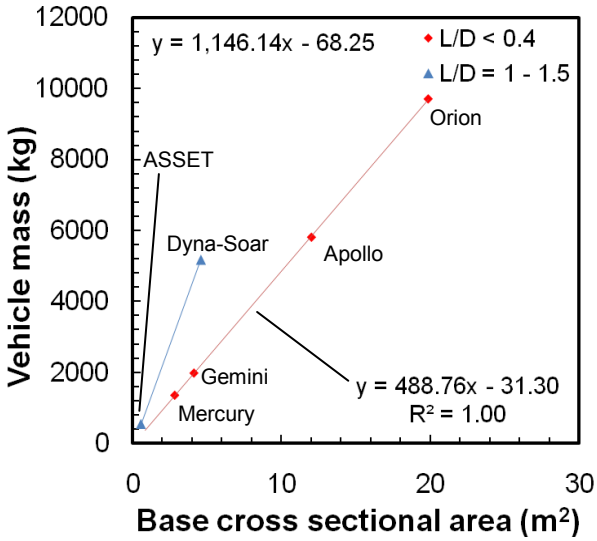

Figure 5.5. Base cross sectional area effects on vehicle mass.

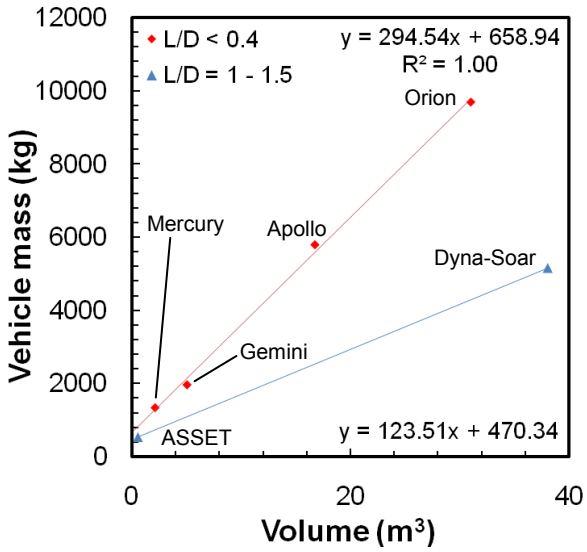

Figure 5.6. Volume effects on vehicle mass.

Linear regression curves have been supplied to illustrate the trends for both $L/D < 0.4$ and also a first idea of how higher L/D geometries compare to $L/D < 0.4$ configurations for this vehicle mass range. These trends indicate that the masses of previous spacecraft scale best with base cross sectional area, though there are so few data points that no concrete trends for entry vehicles in general could be concluded. More specifically, the $L/D < 0.4$ spacecraft scale precisely with $r_b^{2.04}$

$$1470.64\, r_b^{2.04} + 41.42, \tag{5.13}$$

in which $R^2 = 1.00$.

The regression curves for $L/D < 0.4$ come near ASSET with its $m_{EV} = 540$ kg in Figure 5.5 and Figure 5.6, indicating that at similarly small volumes and base cross sectional area, these two cases have similar m_{EV}. The characteristics for Mercury and Gemini are similar since Gemini was primarily a scaled-up geometry of Mercury, accommodating two astronauts instead of one. The Orion CEV is currently expected to have a 67.2% greater mass than the Apollo CM with similar outer mold lines to the

Apollo's and a 53.7% increase in surface area. Applying the relation in the following form,

$$\left(\frac{d_{new}}{d_{ref}}\right)^{x} = \frac{m_{EV,new}}{m_{EV,ref}}, \tag{5.14}$$

it has been determined that $x = 2.045$ with Apollo as the reference case and Orion as the new case. Thus, the Apollo spacecraft shape scales closely with base cross sectional area. This result is consistent with the $L/D < 0.4$ linear regression curve in Eq. (5.13). Assuming that the purpose for the entry vehicle is reasonably constant between missions and that the shape is held constant, this result indicates that scaling the Apollo entry vehicle will not produce any significant advantage with respect to ballistic coefficient. No decrease would be expected since Orion's greater mass cancels out the advantage of its greater drag area.

ASSET has a volumetric efficiency of 81% in-between the values for Gemini and Apollo; it is an example of a $L/D = 1$ class vehicle that has a volumetric efficiency similar to the space capsules' value. With a 22.6% greater volume than Orion and a 46.8% lower mass, the Dyna-Soar has a 108% increase in surface area and thus, ~26% lower volumetric efficiency than the space capsules. With its $L/D = 1$, it exemplifies the trade-off between volumetric efficiency and greater aerodynamic performance at m_{EV} that are representative of manned spacecraft. Note that Orion and Dyna-Soar were designed for greatly different missions; thus, any overall, concrete conclusions regarding different L/D class vehicles and mass are not made.

Chapter 6. Planetary Entry Trajectory Fundamentals

Several fundamental concepts regarding entry trajectory formulation have been applied, and a brief summary of them is provided in this chapter including descriptions of the equations of motion, the ballistic coefficient, and entry corridor.

6.1. Equations of motion

A three degrees-of-freedom set of the equations of motion is applied for this work. This analysis assumes that the vehicles designs are dynamically stable, and to determine whether they actually are dynamically stable would require a six degrees-of-freedom set of the equations of motion to be applied in future work. The point-mass equations of motion for rigid-body flight in a vertical plane given by[93,94,95]

$$\frac{d\vec{p}}{dt} = \vec{V}, \tag{6.1}$$

$$\frac{d\vec{V}}{dt} = \frac{B}{m}\vec{F}_b + \vec{g}, \tag{6.2}$$

$$\frac{d\vec{\omega}_b}{dt} = \left(-J^{-1}\Omega_b J\right)\vec{\omega}_b + J^{-1}\vec{T}_b, \tag{6.3}$$

$$\frac{dm}{dt} = -\left(\frac{dm}{dt}\right)_{fl}, \tag{6.4}$$

$$\frac{d\vec{q}_t}{dt} = -\frac{1}{2}\Omega_q \vec{q}_t, \tag{6.5}$$

in which p, V, and g are specified in an inertial reference frame while the vehicle rotation rates ω are defined in the local vehicle coordinate system.

6.2. *Ballistic coefficient BC and drag area D/q_∞*

The ballistic coefficient is commonly described as the ratio of the entry vehicle mass to the product of the drag coefficient and reference area, usually the base cross section. The produce of the drag coefficient and reference area is called the drag area = $C_D S$. The main advantage to this form is that it allows for the designer to analyze the effect of scaling a given vehicle design on the ballistic coefficient by varying the reference area. In this optimization work, the optimizer may choose from a wide range of vehicle designs. As a result, neither the drag coefficient nor the reference area is assumed constant. This work applies the ballistic coefficient equation in the form

$$BC = \frac{m_{EV}}{D/q_\infty}. \tag{6.6}$$

With this form of the equation, one vehicle's D/q_∞ can be compared to another's D/q_∞ rather than drag coefficient or reference area. The drag area is $D/q_\infty = C_D S$. From a physical standpoint, the drag area is the amount of resistant aerodynamic force produced along the direction of the velocity vector for a given amount freestream dynamic pressure. As a result, a higher drag area allows an entry vehicle to decelerate higher in the atmosphere. For a given mass m_{EV}, this allows the peak deceleration loads and heat fluxes to be experienced higher in the atmosphere and thus, allows the peak heat fluxes to be lower than they would be with a lower drag area. As a result, it is advantageous to reducing the ballistic coefficient to reduce both the peak heat flux and total heat load. For lifting entry, the flight path is a strong function of *L/D* and

BC. They are incorporated into a single metric called the lift parameter. The lift parameter is equal to the ballistic coefficient divided by *L/D*.[3] The lift area would be $C_L S = L/q_\infty$. The *BC* and *L/D* have traditionally been looked at separated rather than as a single metric, and they are likewise treated in this work.

The ballistic coefficient is assumed to be an independent variable to the extent that m_{EV} is a function of mission profile variables (mission duration and pressurized volume requirement) and D/q_∞ is a function of geometry and α. The ballistic coefficient is indirectly restricted based on vehicle sizing requirements detailed in sections 5.1.2 and 5.2.2. Part of the geometric sizing is based on volume and dimension requirements for the seated astronauts. As a result, it is not possible for all of the required pressurized volume to be distributed through a thin heat shield volume, as such heat shields would fit under categories 1 or 2 in section 5.1.2 which assume a complete crew compartment is added after the heat shield.

6.3. Entry corridor

The entry corridor is the allowable region of γ_E that is deemed flyable based on the mission requirements. It is a function of entry velocity, lift-to-drag ratio, and ballistic coefficient. It is a stronger function of the two former. For a given entry velocity, the entry corridor width will vary with m_{EV}, D/q_∞ , and L/q_∞. Note that $L/q_\infty = C_L S$ for a given entry vehicle.

The entry corridor width defines the flyable space. It must be sufficiently large such that all possible uncertainties that may occur during a given trajectory do not lead to a loss in control of the vehicle. These primarily include uncertainties in

atmospheric conditions, and the guidance, navigation, and control subsystems. Putnam and Braun[1] suggest that a corridor width of 0.4-deg is sufficient, stating that this is much larger than the entry corridor widths of 0.16-deg the successful re-entries from the Stardust and Genesis missions.[1] Human missions may need larger corridor widths than these two missions' since there will be stricter *g*-load requirements and longer duration trajectories, giving more time for both expected and unexpected events to affect the vehicle. Uncertainties become more prevalent as entry velocity increases and *L/D* decreases, which corresponds to a reduction in control authority and thus, a smaller entry corridor width. This work assumes that an entry corridor of 0.4-deg is sufficient.

The boundaries of the entry corridor are known as the overshoot (upper boundary, shallowest γ_E) and undershoot (lower boundary, steepest γ_E) trajectories. These boundaries represent the limits to the vehicle's control capability. The overshoot experiences the largest heat load and lowest heat flux and is achieved by flying a lift-down orientation. The undershoot experiences the smallest heat load and greatest heat flux by flying a lift-up orientation and a -90^o flight path angle, representing a vertical dive. The operational entry corridor includes a modified undershoot trajectory that has a greatly reduced γ_E that satisfies the required peak deceleration limit. The operational entry corridor is also based on the set of flight controls available for a given vehicle configuration. This work assumes a reaction control system (RCS) provides control authority over banking the vehicle. This allows the vehicle to rotate to a desired bank angle ϕ_b to rotate the lift vector.

Chapter 7. Aerothermodynamics Code

All of the presented theory in Chapters 2 – 5 has been implemented into a low-order aerothermodynamics code written in FORTRAN 95 for this work. This chapter presents the layout of the code and validation of the low-order methods.

7.1. Code Description

The aerothermodynamics code determines the aerothermodynamic characteristics of a chosen blunt-body shape at given freestream conditions. A single call of the aerothermodynamics code for a given α and β results in running through the code at five different conditions in order to calculate $C_{m,cg,\alpha}$, $C_{l,cg,\beta}$, and $C_{n,cg,\beta}$, which require the values of $C_{m,cg}$, $C_{l,cg}$, and $C_{n,cg}$ at four neighboring conditions (α+0.5^o, β), (α-0.5^o, β), (α, β+0.5^o), and (α, β-0.5^o) for the second-order accurate finite-difference scheme mentioned in Chapter 3.

The aerothermodynamics code has five objectives: to generate the blunt-body geometry, to scale it to fulfill the necessary pressurized volume mission requirements, estimate the resulting entry vehicle mass, determine the heat shield's geometric properties, and to calculate the aerodynamics, static stability, and the stagnation-point heat transfer. A diagram of the analysis code is given in Figure 7.1. Given the geometric parameters of a chosen base and axial shape, the shape generator produces a 3D mesh of the heat shield geometry. Then the entry vehicle sizing and mass estimation is executed. The aerodynamics calculator determines the aerodynamic characteristics of a given shape based on modified Newtonian surface pressure

distribution at a given angle-of-attack, sideslip angle, and Mach number. The primary variables that are calculated in the aerodynamics code are M_∞, α, C_L, C_D, L/D, C_N, C_A, $C_{m,0}$, $C_{l,0}$, $C_{n,0}$, X_{cp}/L, Y_{cp}/L, Z_{cp}/L.

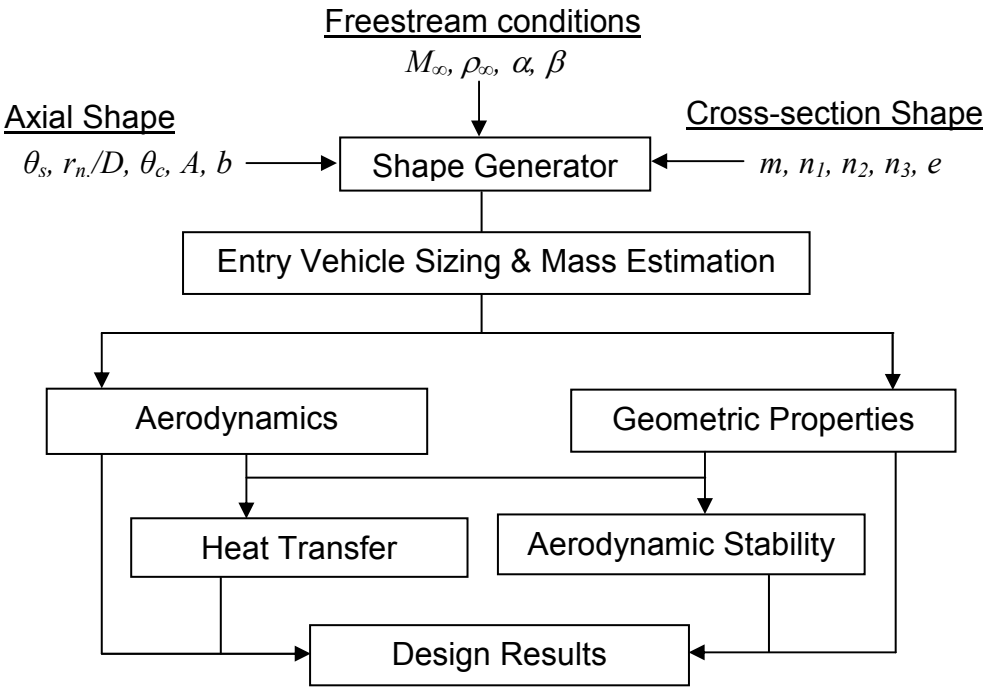

Figure 7.1. Diagram of Analysis Code.

The aerodynamics calculator is acceptable for determining blunt-body shape hypersonic aerodynamics at fine mesh sizes with extremely low run times (usually a fraction of a second for a j_{max} = 121, k_{max} = 203 mesh). Additionally, the aerodynamics code uses Tannehill's code[57] to determine $\gamma_{\text{eff},2}$ and ρ_2/ρ_1, and it uses Kaattari's method[54,55] to determine the shock-standoff distance Δ_{so} to the stagnation-point that are used in the heat transfer portion of the code. The primary output of the heat transfer portion of the code are r_{eff}, $\dot{q}_{s,conv}$, and $\dot{q}_{s,rad}$.

The analysis code applies a third-order accurate Simpson's Rule integration method to determine the aerodynamic characteristics and center of gravity location. The center of pressure location is then determined. Geometric properties such as the

volume, surface area, and planform area are calculated in the analysis code. Additionally, a center of gravity can be either chosen or calculated assuming a uniform density volume. The static stability calculator uses the aerodynamics in conjunction with the location of the center of gravity to determine the moment coefficients about the center of gravity and the pitch, yaw, and roll stability derivatives. Note that the analysis code requires two atmospheric models and Tannehill's high temperature air code. Two atmospheric models, the ARDC 1959 Model Atmosphere[96,97] and the US 1976 Standard Atmosphere,[98] are integrated in order to use the older atmospheric model for part of the validation process of the heat transfer correlations and use the newer for the optimization.

7.2. Code Validation

To validate the design code, and the corresponding implemented theories, results of the design code are compared to data from the Apollo and FIRE II missions. The results are divided into two areas: (1) aerodynamic performance and static stability and (2) stagnation-point heat transfer. The first section notes that the aerodynamic coefficients and stability derivatives match the Apollo data within 15%. The second section observes that the maximum heat transfer heat flux and heat load is within 15% of actual predictions after the stagnation-point heat transfer heat flux is related to the maximum heat flux according to wind tunnel data.

7.2.1. Aerodynamics and Static Stability

The aerodynamic performance and static stability are compared to both Apollo wind tunnel data and Apollo flight test data. There is more certainty in the

Apollo wind tunnel data than in the Apollo flight test data, and most of the wind tunnel data is for $M_\infty = 6$ while the flight test data is for $M_\infty = 36$. To convert from the listed angle of attack value of the NASA Apollo reports to the angle of attack value used in this work, defined in Figure 3.1(a), subtract 180^o from the NASA reported value. This should usually convert the NASA reported value to a negative angle of attack. Note that there is not any truly acceptable experimental data on the rolling moment stability coefficient, but predictions are compared to Whitmore's recent computational work.[32]

7.2.1.1. Comparison with Apollo Wind Tunnel Data

Results from the code based on modified Newtonian theory, have been compared to wind tunnel[12,13] data of the Apollo Command Module (CM). The center of gravity is offset from the central body axis in order to trim the Apollo CM at a specific angle-of-attack during re-entry.[14] Different center of gravity locations were considered in the wind tunnel models during the design of the CM.[12,13,15] In Figure 7.2, the center of gravity location is $X_{cg}/l = 2.171$, $Y_{cg}/l = 0.3158$, and $Z_{cg}/l = 0.0$ according to the body-fixed coordinate system in Figure 3.1(b).

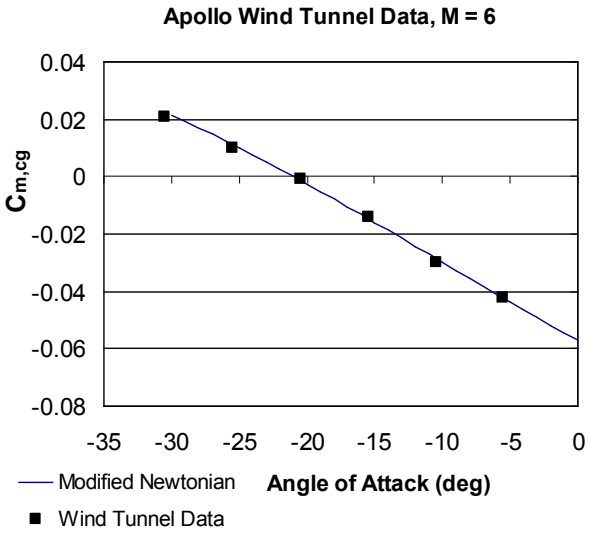

Figure 7.2. $C_{m,cg}$ comparison between modified Newtonian and wind tunnel data, Ref. [12].

Additionally, because $X_{cg}/l > 1$, the center of gravity location of the CM is past the heat shield. The Newtonian results for the pitching moment $C_{m,cg}$ at $M_\infty = 6$ in Fig. 5 produce $C_{m,cg,\alpha} = -0.16$/rad; the modified Newtonian results follow the behavior and closely agree with the values of the Apollo wind tunnel (WT) data.[12] As a result, this is evidence that the modified Newtonian results can match the pitching moment closely and thus predict α_{trim}, and it is well-known to match the lift-to-drag ratio for a blunt body better than the lift or drag coefficients.

The wind tunnel data for the rolling moment C_l was scattered near zero and has values that are two orders of magnitude smaller than those measured for C_m. Although the data accuracy of C_l and C_m is not reported for this wind tunnel data, the scattering and smaller values of the C_l data points in Fig. 6 suggest that the measurement instruments did not have the precision required to obtain a clear data set of the CM's rolling moment behavior.

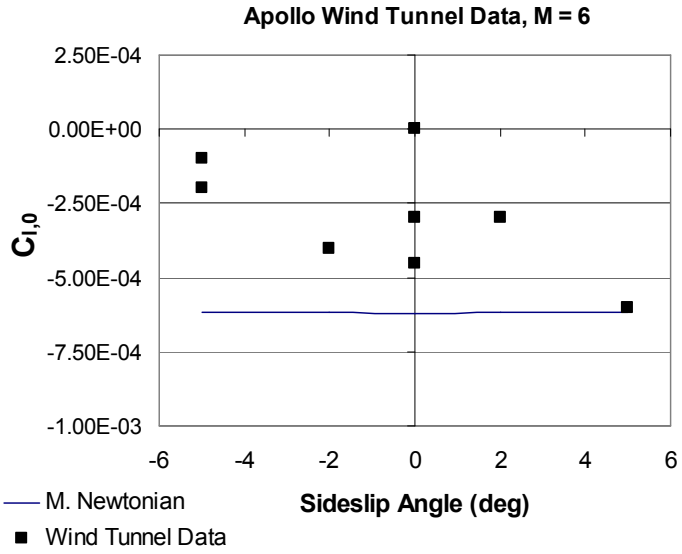

Figure 7.3. $C_{l,0}$ comparison between modified Newtonian and wind tunnel data, Ref. [12].

The wind tunnel data suggest a neutrally stable spherical-segment at -20° angle-of-attack, and the modified Newtonian results agree. A mesh with j_{max} = 203 and k_{max} = 121 has been chosen based on a grid convergence study. Since the Apollo CM is axisymmetric, the yawing moment coefficient $C_{n,0}$ at a given sideslip angle (the condition $\beta_1 \neq 0$, $\alpha_1 = 0$) would be equivalent to the pitching moment coefficient $C_{m,0}$ at a given angle-of-attack (the condition $\alpha_2 = \beta_1$, $\beta_2 = 0$). This is one reason that no specific $C_{n,0}$ data exists in the references.

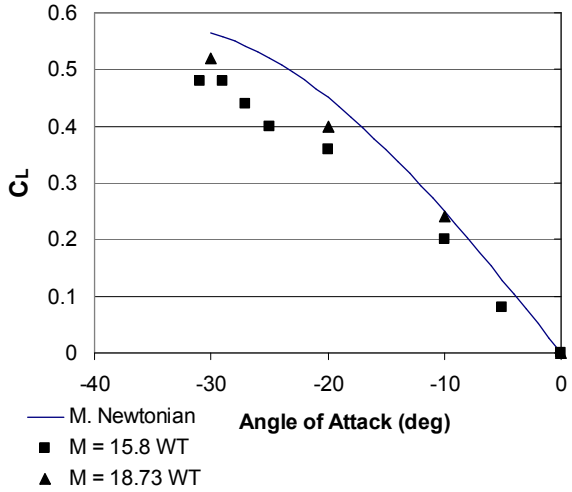

a) Validation of C_L results.

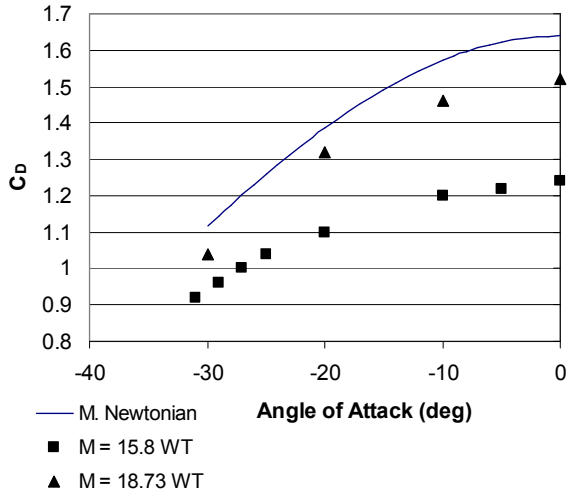

b) Validation of C_D results.

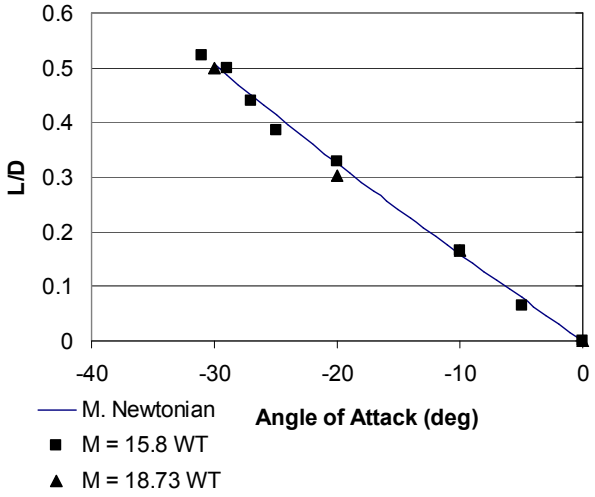

c) Validation of *L/D* results.

Figure 7.4. Aerodynamic force comparisons between modified Newtonian and wind tunnel data, Ref. [12].

The modified Newtonian results in Figure 7.4 were calculated at $M_\infty = 18.73$, but the difference between these results and those at $M_\infty = 15.8$ is negligible (0.05% difference at $\alpha = -20^o$). Modified Newtonian results for the lift and drag coefficients are larger than values from both datasets shown in Figure 7.4(a) and (b). However, the increase in lift and drag with an increase in Mach number in the wind tunnel data is more significant than expected; this may suggest the presence of significant wind tunnel effects. At M_∞=18.73, C_L and C_D from Newtonian theory are at most 9.6% and

7.2% larger than the wind tunnel data respectively, and they are within the uncertainty of the wind tunnel data of ±0.114 for C_L and ± 0.10 for C_D.[12] *L/D* Newtonian results shown in Figure 7.4(c) agree very well with the wind tunnel data (better than for the individual C_L and C_D as expected).

At lower freestream Mach numbers, such as M_∞=9, the errors are larger than 10% for the lift coefficient as shown in Table 7.1. While the data presented for M_∞=15.8 and 18.73 are based on Apollo CM models with r_c/d of approximately 0.1, the data in Table 7.1 corresponds to r_c/d = 0.0. Moseley conducted a survey of the effect of increasing r_c/d, and his wind tunnel results for M_∞=9 at r_c/d = 0.1 would increase the errors from those values in Table 7.1, for C_L to approximately 22% and C_D to approximately 13% while the error in *L/D* was constant at 8% at α = -15°.

Table 7.1. Percentage error of Newtonian computations compared to wind tunnel data in Ref. [13], M_∞ = 9, α = -25°.

	Wind Tunnel Value	Modified Newtonian Value	Percentage Error
C_L	0.45	0.534	18.6%
C_D	1.25	1.296	3.70%
L/D	0.37	0.412	11.3%

As the code used in this work does not account for corner radius in determining the surface pressure distribution, this is one reason for the increase in error. The Newtonian surface pressure distribution is known to become more accurate with an increase in Mach number, and the validation results are consistent with this understanding. However, it is shown in the next section that comparisons with the flight test data from Apollo AS-202 result in an amount of error similar to that for M_∞=9. Overall, the modified Newtonian results are within 10% of the wind tunnel data with corner radius for $M_\infty \geq$ 18.73, within 15% of the wind tunnel data without

corner radius for $M_\infty \geq 9$, and within 25% of wind tunnel data with corner radius for $M_\infty \leq 18.73$.

7.2.1.2. Comparison with Apollo Flight Test Data

Results from the code have been compared to flight test[10,11] data for the Apollo Command Module (CM) for mission AS-202 and Apollo 4 (also known as AS-501). The CM in AS-202 re-entered Earth's atmosphere at satellite orbit speed 8.23 km/s (27,000 ft/s) while the Apollo 4 CM produced the expected re-entry velocity from lunar return of 10.7 km/s (35,000 ft/s).

The uncertainty in the flight data varies throughout the trajectory, and so the more steady aerodynamic data was identified and utilized. Of the two datasets, the flight data from AS-202 had the smaller uncertainty in the flight coefficient data of ±9% at 4900 s into the mission. The coefficients of the normal force, lift, and lift-to-drag ratio have percentage errors around this error. However, the coefficients of the axial force and drag have higher errors around 17%. The Newtonian results are compared to the AS-202 flight data in Table 7.2.

Table 7.2. Comparison of Apollo AS-201 Data and Computations, $M_\infty = 14$, $\alpha = -16.5^o$ at 4900 s.

	AS-201 [ref. 10]	Mod. Newtonian	% Error
C_N	-0.05	-0.0454	-9.2%
C_A	1.34	1.56	16.2%
C_L	0.37	0.399	7.8%
C_D	1.28	1.51	17.6%
L/D	0.289	0.265	-8.4%

The trend in the percentage error being higher for C_L than C_D seen in the wind tunnel data comparison is the opposite for AS-201. Because the corner radius is not accounted for, it is expected that the error in L/D to stay constant at 8%, for C_L,

according to wind tunnel results, to have approximately 22% error instead of 7.8% and C_D to have approximately 13% instead of 17.6%. Note that these percentage errors are nearly constant, at least over the range of angle of attack values from -30^o to 0^o. It is completely feasible for C_D to have a difference in error of 4.6% since the uncertainty is a higher percentage, and so the only surprising trend is that the lift coefficient has 14% less error than expected.

From the wind tunnel data, it is suggested that the corner radius affects the lift and drag coefficients less at higher freestream Mach numbers, but this is countered with the higher errors present in the AS-201 flight test data. In fact, wind tunnel effects could be changing the trends also, and so it is apparent that there is not consistency throughout this wind tunnel and flight test data to the resolution required to reason for the different percentage errors. Therefore, no conclusions could be made concerning whether the modified Newtonian results are less than 18±9% accurate.

Compared to flight data for Apollo 4 at $M_\infty = 30$, Newtonian theory produces a C_D that is 3.7% larger and a C_L that is 18.6% larger as shown in Table 2.[11] According to Hillje, the best flight-derived data for C_N (near maximum freestream dynamic pressure) has an uncertainty of ±0.048.[11] Because the normal force coefficient has a small magnitude, small precision errors in C_N strongly affect the calculation of C_L. The contribution of C_N to C_L is one order of magnitude less than the contribution of C_A to C_L. However, the contribution of C_N to C_D is two orders of magnitude less than the contribution of C_A to C_D, and so an error in C_N will not affect C_D as much as C_L. This produces significant increase in accuracy of the Newtonian results for C_D at 3.7% compared to C_L at 18.6%.

Table 7.3. Comparison of Apollo 4 Data and Computations, $M_\infty = 30$, $\alpha = -25^o$ at 30040 s.

	Apollo 4 [ref. 11]	Mod. Newtonian	% Error
C_N	-0.11	-0.06387	-41.9%
C_A	1.32	1.400	6.1%
C_L	0.45	0.5337	18.6%
C_D	1.25	1.296	3.7%
L/D	0.37	0.4119	11.3%

Additionally, Newtonian theory produces results that trim the CM within 1.2^o for both Apollo missions AS-202 ($\alpha = 17.5^o \pm 0.5^o$)[10] and Apollo 4 ($\alpha = 25.5^o \pm 3^o$).[11] For all these reasons, it is concluded that the C_N flight data is probably inaccurate, rendering the higher percentage errors in C_L and L/D. Since the percentage differences between Newtonian theory and the acceptable CM experimental wind tunnel and flight data is less than 15%, and since the theory follows the behavior of the wind tunnel data, modified Newtonian flow is considered acceptable for comparing the basic hypersonic aerodynamic characteristics of the investigated blunt-body heat shield shapes with low computational time. Only the rolling moment values and stability derivatives have not been completely validated since a lack of this data exists, but it is partly validated in the next section.

7.2.1.3. Comparison with Additional Sources

Whitmore[32] offers a recent analysis of the Apollo capsule as well as other human-rated lunar return vehicles such as a flattened bi-conic with trim flaps and an HL-20-derived lifting body configuration. His numerical results on the stability characteristics of the Apollo capsule closely match the results of this work's code. Whitmore also uses a modified Newtonian surface pressure distribution to determine the aerodynamics of each vehicle.

Both the results of this work and of Whitmore suggest that the Apollo capsule is slightly statically unstable in the roll direction. In this case, to be statically roll stable, the vehicle would have a negative value of $C_{l,cg,\beta}$ since vertical lift is positive at negative angles of attack for the Apollo CM. Both works indicate that the Apollo capsule would have slightly positive values for the $C_{l,cg,\beta}$, if the center of gravity is above the central axis during planetary entry.

Since the Apollo CM had a Reaction Control System (RCS) that could control the Command Module's roll angle, one guess is that the RCS may have been used once in a while to fix the CM's roll alignment. Another guess is that the $C_{l,cg,\beta}$ had a negligible value for the CM. Whitmore reports a value of $C_{l,cg,\beta}$ = 0.0065/rad while this work produces a value of $C_{l,cg,\beta}$ = 0.00541/rad at $\alpha = -16^{o}$ to produce L/D = 0.25. Since both of our works concur and Whitmore's work is the only source in the literature search that offered a value to compare, this is the extent that the $C_{l,cg,\beta}$ is validated in this work.

Magazu[30] investigated the feasibility and aerothermodynamic performance of a 12-sided parashield re-entry vehicle that has a shape similar to a 12-sided umbrella with no more than 7% concavity. The reproduction of this heat shield shape is defined as having a spherical-segment axial shape with $\theta_s \approx 45^{o}$ and a dodecagon cross-section without any concavity. The superformula of the superellipse Eqn. (2.8) can approximate a sharp dodecagon with the following parameters m = 12, n_1 = 10.75, n_2 = n_3 = 1. With these parameters, this work's code produced a lift-to-drag ratio of 0.19 compared to the reported 0.18 in Ref. [30] at $\alpha = -15^{o}$.

7.2.2. *Stagnation-Point Heat Transfer*

Validating the results of this work's stagnation-point heat transfer methods against Apollo and FIRE II experimental and flight data is completed in this section. It is shown that the methods produce results with < 15% error. Note that it is not the purpose of this work to imply from these low errors that heat transfer during planetary entry is well understood. CFD would also produce results with errors of approximately 10-15% also. Additionally, although the percentage error is low for the stagnation-point heat transfer methods of this work, the error would probably increase dramatically for entry velocities greater than 12 km/s, in which it is expected that radiation cooling and convection coupling would lower the radiative heat flux. However, it is unknown precisely how much reduction there would be since no instrumented flight tests have been completed on flights with entry speeds greater than 11.4 km/s from the FIRE II. Several questions still exist on laminar, transitional, and turbulent boundary layer heat transfer during planetary entry. As a result, experimental research in this area would be especially worthwhile as future work.

7.2.2.1. *Apollo 4*

The peak radiative heat flux for the Apollo 4 mission occurred at an altitude of approximately 200000 ft around 30030 s into the mission at which point the Command Module was moving at a speed of 34000 ft/s. For the portion of the trajectory with high radiative heat flux, Figure 7.5 shows the calculated normal-shock density ratio and corresponding specific heat ratio using Tannehill's correlation set.[57]

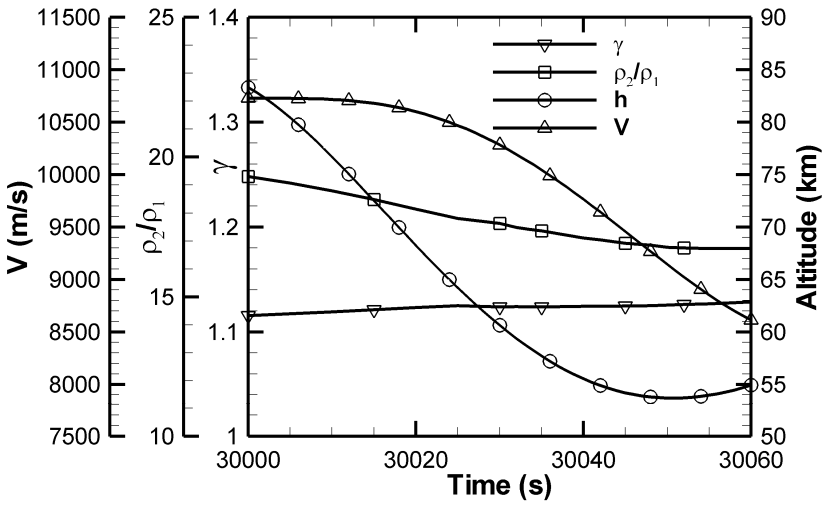

Figure 7.5. Normal-shock density and specific heat ratios for the high radiative heat flux portion of the Apollo 4 trajectory, *h* and *V* from Ref. [11].

The altitudes and velocities during this portion of the Apollo 4 trajectory are also shown in Figure 7.5. The stagnation point on a blunt-body is usually across from the part of the bow shock that is normal to the freestream. As a result, the normal-shock density ratio ρ_2/ρ_1 and corresponding effective specific heat ratio after the shock can be used to approximate the effective radius-of-curvature at the stagnation point. Kaattari's method requires ρ_2/ρ_1 and $\gamma_{eff,2}$ to determine r_{eff}. To validate the implementation of Kaattari's method in this work, in Figure 7.6 it is compared to other methods of determining the shock-standoff distance for the case of a sphere. This figure is partially a reproduction of Figure 4.1 in which the empirical curve-fit Eqn. (4.8) is compared to wind tunnel data. As a result, it can be observed that Kaattari's method in Figure 7.6 follows the experimental data closer than the empirical curve-fit at the lower values of ρ_2/ρ_1. Rasmussen[33] provided the solutions to the vorticity method and parabolic thin shock layer approximation in his textbook. The solution from the vorticity method follows the behavior of Eqn. (4.8) almost

perfectly while the parabolic thin shock layer approximation produces shock-standoff distances that are at least 25% larger than wind tunnel results.

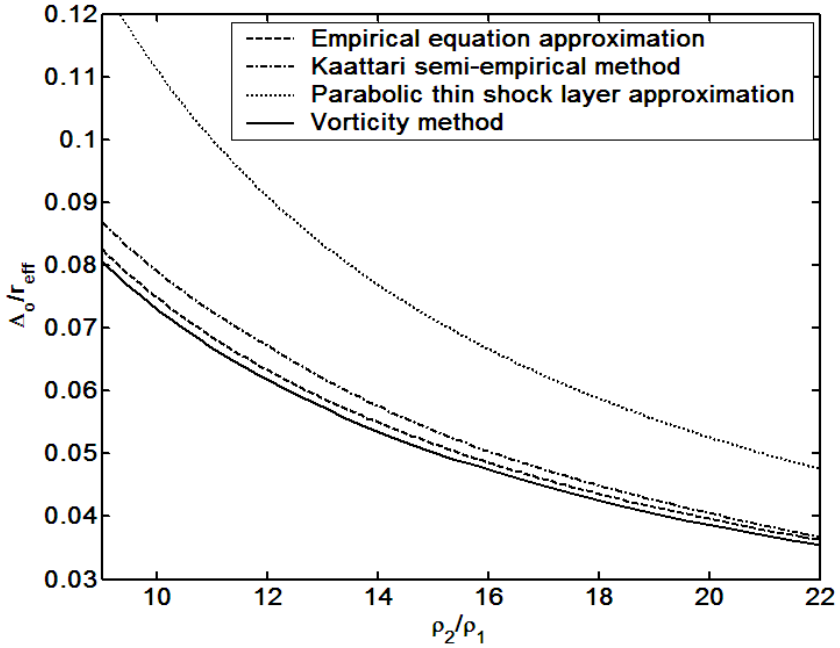

Figure 7.6. Shock-standoff distance method comparison.

It is noticed that Kaattari's method and Eqn. (4.8) bracket most of the wind tunnel results shown in Figure 4.1. After Kaattari's method determines the shock-standoff distance at zero angle of attack, the modified method for finding the shock-standoff distance at the prescribed angle of attack is accounted for through the effective radius term. For the Apollo 4, Ried[51] generated predictions with early 1970 computer technology using CFD. Ried produced an effective radius at the stagnation point that would apply for radiative heat transfer, and it is compared to the results of Kaattari's modified method in Figure 7.7.

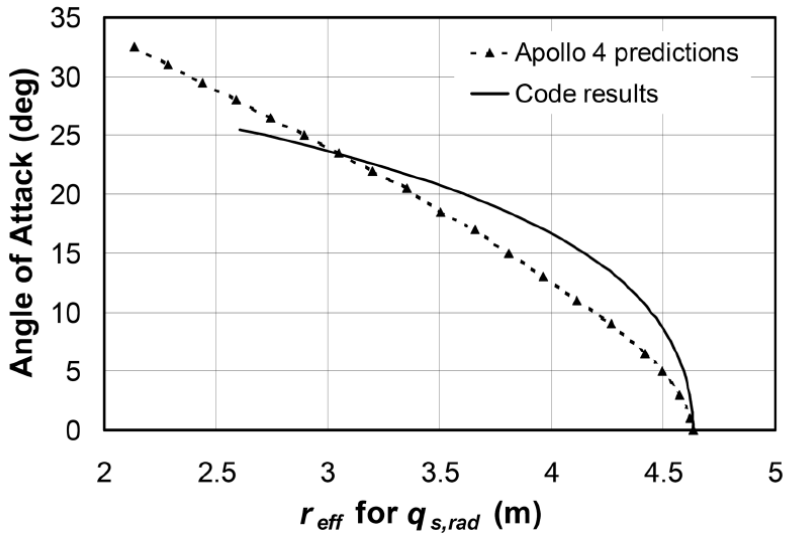

Figure 7.7. Apollo 4 r_{eff} for stagnation-point radiative heat transfer.

Kaattari's modified method varies no more than 10% from Ried's predictions. Then the r_{eff} is applied in the radiative heat flux correlation set. To determine which correlations would be best to apply for this work, a plot of the Apollo 4 mission's radiative heat flux shown in Figure 7.8 is used to compare correlations. Figure 7.8 shows these results for the portion of the Apollo 4 trajectory with radiative heat flux values greater than 50 W/cm^2. Both radiometer and calorimeter measurements were made on the Apollo 4 at the point of maximum heating and the stagnation point, although measurement uncertainties were not recorded. Ried shows that his calculations match the radiometer results that measured only the visible and infrared radiation. Ried also calculated the UV continuum and UV line radiation. It made the most sense to compare the values of the correlations to the total radiative heat flux. As a result, the total radiative heat transfer that includes the visible, infrared, UV continuum, and UV lines is shown in Figure 7.8 as the Apollo 4 predictions.

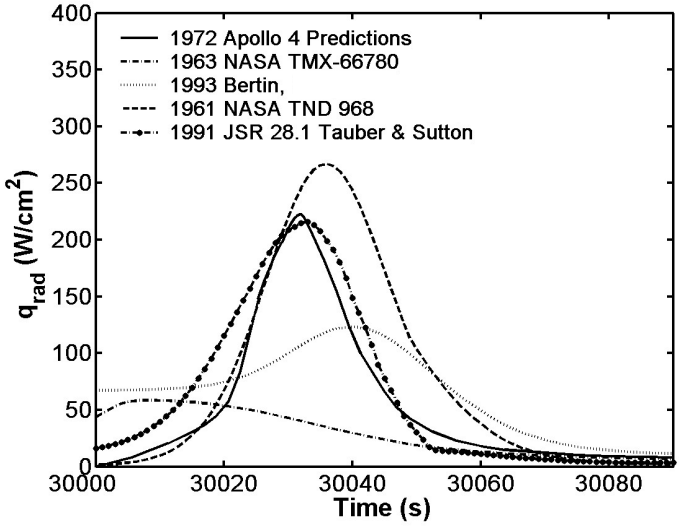

Figure 7.8. Validation of radiative heat flux correlations for Apollo 4 from Ref. [105].

The most recent correlation from Tauber and Sutton[48] matched the Apollo 4 results for most of the region. However, the results of this correlation do not match the predictions for speeds less than 9000 m/s.

In fact, both Lovelace[44] and Bertin[2] provide correlations that produce conservative results that are not far from the results for speeds less than 9000 m/s. Since the correlation from Bertin was originally designed for speeds less than 7620 m/s (25,000 ft/s), Lovelace's correlation is applied for speeds less than 9000 m/s. Along with a method to transition between the two correlations, Lovelace and Tauber's correlations are used in this code and produce the results shown in Figure 7.9. Together, these correlations produce results that are conservative but close enough for first-order optimization results.

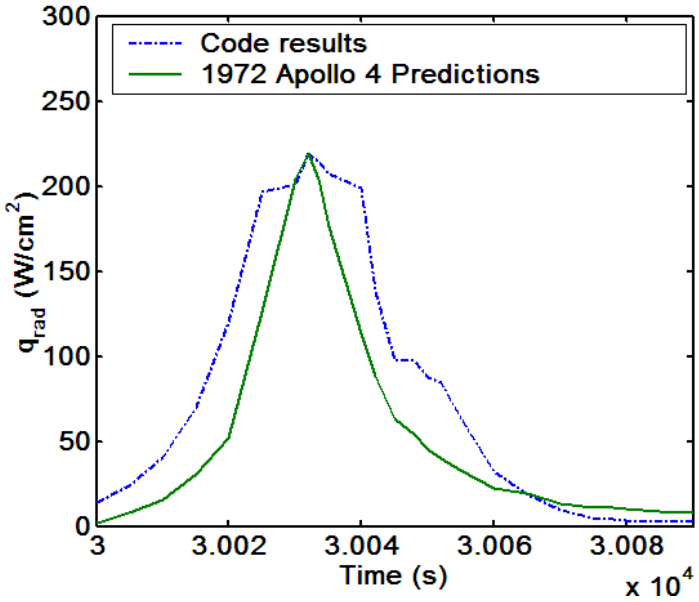

Figure 7.9. Apollo 4 radiative heat transfer code validation, predictions from Ref. [51].

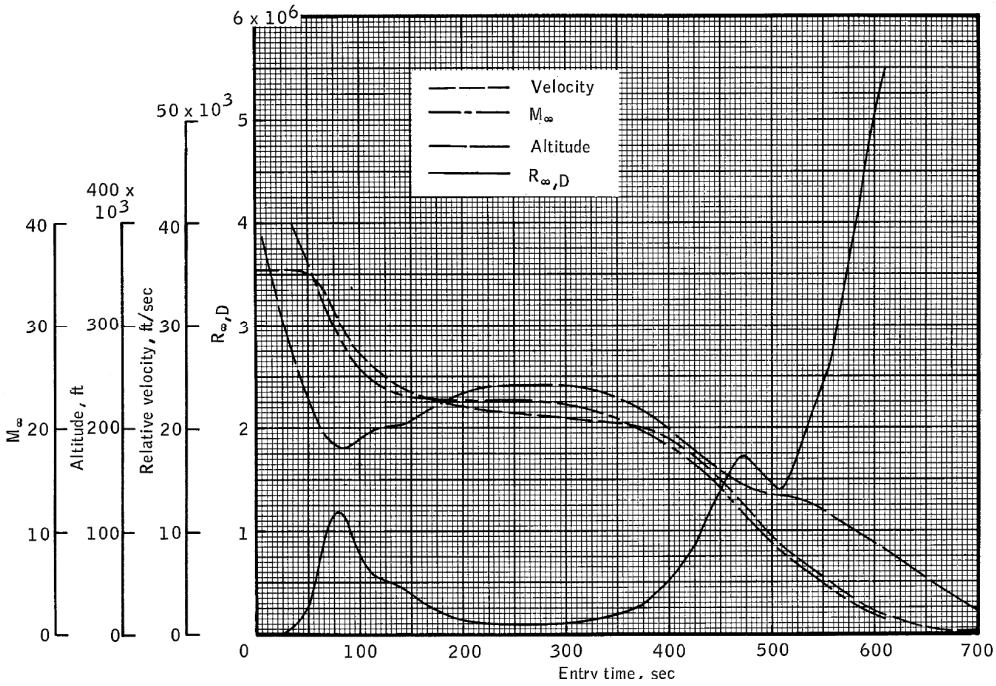

Figure 7.10. Apollo 4 Trajectory from Ref. [39].

To validate the convective heat flux, radiative heat flux, and the corresponding heat load values, results have been generated using the Apollo 4 trajectory shown in Figure 7.10. Apollo 4's maximum Mach number[11] during Earth entry was Mach 40, and because it had the highest entry velocity of all the Apollo

missions, it also had the largest heat load. The total heat flux and heat loads are calculated using both Lovelace's Eqn. (4.9) and Tauber's Eqn. (4.10), and so Table 7.4 includes two columns of results. The equations used to produce each results are listed in the title of each column. These results are within 15% of the reported values.

Table 7.4. Apollo 4 Comparison of Total Heat Transfer.

Parameter	**Apollo 4, Ref. [41]**	**Results from [1.6*1.06*Eqn. (4.1)+Eqn. (4.9)]**	**Results from [1.6*1.06*Eqn. (4.1)+Eqn. (4.10)]**
$q_{max,tot}$ (W/cm^2)	483	542 (+12%)	469 (-2.9%)
$Q_{max,tot}$ (J/cm^2)	42600	46200 (+8.5%)	38700 (-9.2%)

NASA reported the values of the heat flux and heat load at the point of maximum heating, which in the case of the Apollo CM was not at the stagnation point. Although this work calculates the stagnation-point heating only as explained in Chapter 4, these reported values can still be used for validation. As shown in Figure 7.11, the maximum convective heating for the Apollo CM at α = -25^o was 60% larger than the stagnation-point convective heat flux at zero angle of attack.

Maximum heating is located at S/R = 0.9 while the stagnation point at α = -25^o is located at S/R = 0.74. Since the stagnation point at α = -25^o has a 10% higher heat flux than that at zero angle of attack, the maximum heat flux is 45% larger than the stagnation-point heat flux at α = -25^o. Although angle of attack has been accounted for by this work's radiative heat flux calculations, it has been assumed that the convective heat flux would be kept constant at the nose.

Due to the Apollo CM's low spherical-segment angle of 25^o and corner geometry, the stagnation-point does not have the highest convective heat flux at α = 25^o. Bertin[2] notes that a correction factor of 1.06 to the correlation for a sphere can be

used to account for the change in the sonic line location from 45° to approximately 25° for the CM. As a result, after multiplying the convective heat flux by 1.06 and then 1.60 to account for the corner radius' effect that produces maximum heating, the convective heat flux can be added to the radiative heat flux to produce maximum heat flux and heat load results within 12% of the reported values.

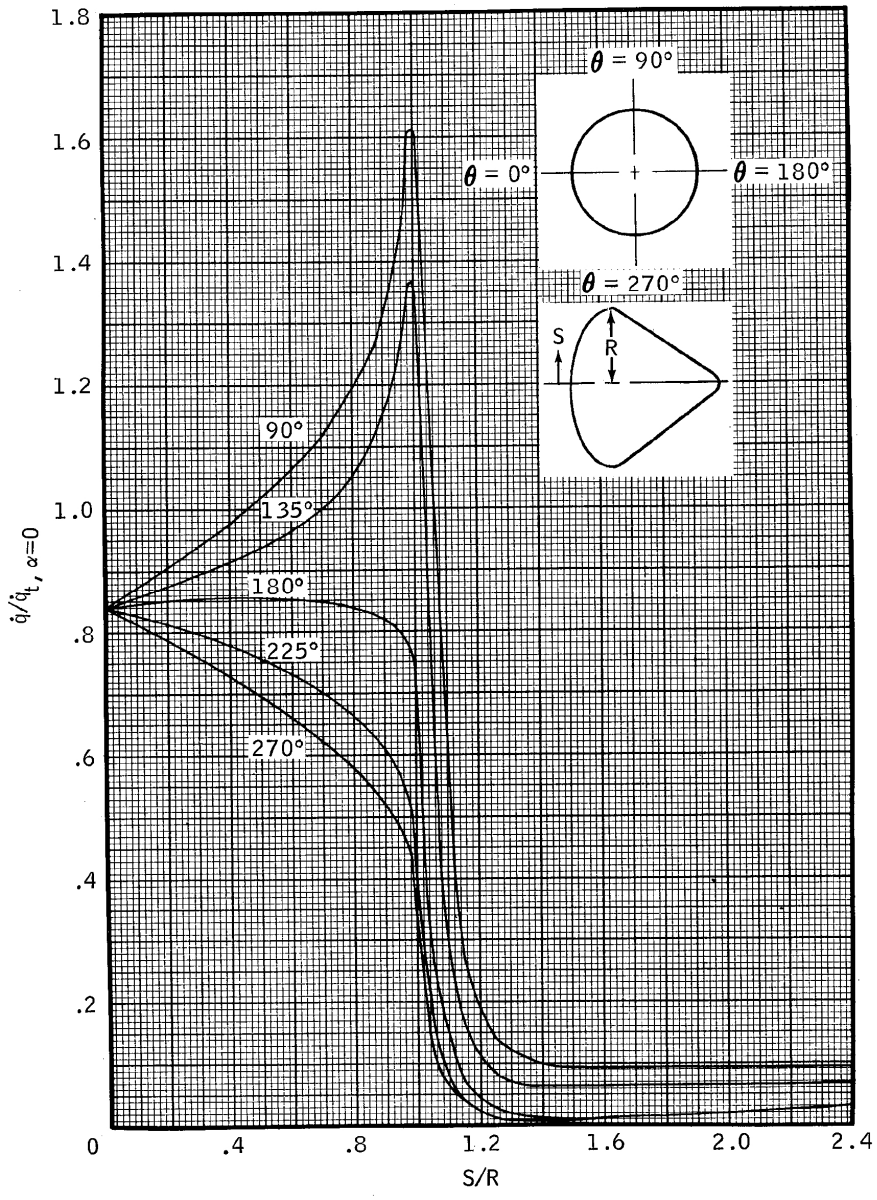

Figure 7.11. Convective heat flux distribution of Apollo Command Module at $\alpha = 25^0$ from Ref. [39].

7.2.2.2. FIRE II

In the case of the FIRE II flight, the entry vehicle's stagnation point was equal to the point of maximum heating, and it traveled mainly at zero angle of attack. As a result, it would be expected that this work would match the FIRE II data more closely than the Apollo 4 data. However, the FIRE II had an entry velocity of 11.4 km/s (37400 ft/s), which is slightly faster than the entry velocity of Apollo 4 at 10.7 km/s. Because FIRE II had an entry Mach number greater than forty, it is possible for there to be coupled effects between convection and radiation that would reduce the total heat flux. The FIRE II had three heat shields of different radii placed on top of each other. One heat shield would be jettisoned at a time to acquire heat transfer data for each heat shield. Since the heat shields have different radii, discontinuities in the flight data are expected. As shown in Figure 7.12, flight data from the calorimeter produced a noticeably smaller heat flux value than the theory that does not assume coupling.

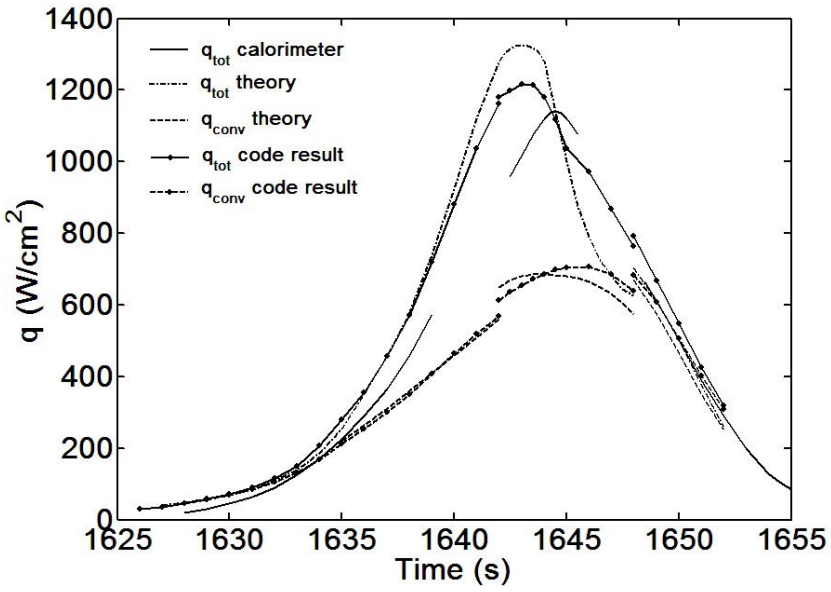

Figure 7.12. FIRE II Total heat flux comparison with flight data from Ref. [50].

The correlations of this work, which are labeled as code results, also do not assume coupling. The maximum total heat calculated by this work is 9% larger than the flight data. The interesting part is that the convective theory curve that assumes coupling and the code results nearly match perfectly for the first shield and do not vary greatly for the other two. However, it is apparent that the correlations fall approximately halfway in-between the theory that assumes no coupling and the calorimeter data. It is believed that the FIRE II had some coupling, and that this is the reason why the total heat flux theory without coupling and the code results produce a peak at a different time than the FIRE II calorimeter data. As a result, it would be expected that this work's accuracy would begin to disappear at slightly higher velocities.

One additional comparison has been completed to determine the accuracy of the convective heat transfer correlation Eq. (4.1). The stagnation-point convective heat flux for the first heat shield has been estimated in Ref. [99] by subtracting the approximated radiative heat flux from total heat flux calorimeter data. It utilizes the beginning of the Fire II entry from 1630 to 1635 s, and it has been determined that $q_{s,conv}$ is ± 20 W/cm^2 for altitudes between 71 and 85 km. From Figure 7.12, it is determined that the peak $q_{s,conv}$ is 16 W/cm^2 greater than the value from the theory. The worst point of accuracy is at an altitude of 46 km and a velocity of 9.4 km/s, at which $q_{s,conv}$ is 44 W/cm^2 greater than the value from theory. The worst under prediction for $q_{s,conv}$ is 38 W/cm^2 less than the value from theory at an altitude of 55 km and a velocity of 10.7 km/s. Since the reported maximum heat fluxes are normally between 60 and 75 km, and the worst $q_{s,conv}$ in this altitude range is at 71 km, it is assumed that the reported $q_{s,conv}$ is ± 20 W/cm^2.

7.2.2.3. Additional radiative heat flux validation

Using the multiband radiation model of Nicolet, Tauber and Sutton[48] completed validation of Eq. (4.9) against high-order models with an radiative effective radius r_{eff} = 3.0 m at altitudes of 60, 66, and 72 km and velocities of 10, 11, 12, and 14 km/s. The provided percentage difference between the high-order results and Eq. (4.9) is utilized to approximate the absolute error in the reported peak $q_{s,rad}$. In order to generate r_{eff} = 3.0 m, a spherical segment heat shield with $\theta_s = 89^o$, e = -0.001, n_2 = 2.00, and d = 8.3 m without vehicle scaling and $\alpha = -5^o$ is applied. This geometry/α combination is the most straight forward to implement.

Table 7.5 Radiative heat flux validation against high-order modeling.

Altitude, ρ (kg/m^3)	**V_∞ = 10 km/s** Form of results: $q_{s,rad}$ (W/cm^2) % error from Ref. [48], Absolute error (W/cm^2)	**V_∞ = 11 km/s**	**V_∞ = 12 km/s**	**V_∞ = 14 km/s**
72 km, 6.659×10^{-5}	28 0%, 0	107 +11%, +12	228 +18%, +41	581 +9%, +52
66 km, 1.471×10^{-4}	64 +2%, +1	250 +6%, + 15	546 +8%, +44	1442 +4%, +58
60 km, 3.059×10^{-4}	143 -7%, -10	570 -1%, -6	1271 +3%, +38	3441 +5%, +172

Most of the designs for 11 km/s entry experience the maximum heat flux at $V_\infty \approx 10.5 \pm 0.5$ km/s. Most for 12.5 km/s entry experience the maximum heat flux at $V_\infty \approx 11.5 \pm 0.5$ km/s. Most for 15 km/s entry experience the maximum heat flux at $V_\infty \approx 13.5 \pm 0.5$ km/s. Thus, the reported $q_{s,rad}$ is assumed to have an absolute error of ± 20, 35, and 60 W/cm^2 for 11, 12.5, and 15 km/s respectively. Together with $q_{s,conv}$ being ± 20 W/cm^2, the reported $q_{s,max}$ is ± 40 W/cm^2 for 11 km/s and ± 80 W/cm^2 for 15 km/s.

Chapter 8. University of Maryland Parallel Trajectory Optimization Code

The University of Maryland Parallel Trajectory Optimization Program (UPTOP) is applied to conduct a three-degrees-of-freedom entry trajectory analysis.[93,94] It utilizes a 4th-order Runge-Kutta routine to propagate the point-mass equations of motion for rigid-body flight in a vertical plane, given in Chapter 6,[93,94,95] to determine the flight path of a vehicle. Its capability is not restricted to planetary entry applications. The time step is normally set to 1 s. A rotating, ellipsoidal Earth model is applied with a second harmonic gravity model based on the WGS-84 Geocentric Equipotential Ellipsoid model.[100] The US 1976 Standard Atmosphere[79] is applied for $h_t < 85$ km, and the NRLMSISEE-00 Atmosphere[101] is applied for $h_t \geq 85$ km.

Both trajectory and vehicle optimization can be performed using either single or multiple objective functions. For single objective function optimization, several optimization techniques are available: an evolutionary, population-based algorithm, a gradient-based scheme using Design Optimization Tools (DOT),[102] and also a hybrid evolutionary/gradient-based scheme that attempts to provide the best of both worlds. After a user-specified number of generations, the gradient-based optimizer Design Optimization Tools (DOT) can be executed on the current optimal solution. In this way, the hybrid method accounts for gradient information and increases the chances of obtaining a global optimum. For optimizing multiple objective functions, the evolutionary algorithm is available. UPTOP utilizes the Message Passage Interface

(MPI) to process an optimization case using multiple processors. Descriptions of the optimization methods applied in this work are provided in Chapter 10.

Trajectories generated with UPTOP are compared to those of the benchmark Program to Optimize Simulated Trajectories (POST)[103] in Figure 8.1. UPTOP is capable of optimizing multi-stage trajectories where the vehicle may have multiple engines and fuel tanks. The benchmark case[104] for the optimal Space Shuttle transport ascent trajectory through Space Shuttle Main Engine (SSME) cutoff is provided in Figure 8.1(a) to demonstrate UPTOP's comparable optimization capability. The optimal pitch and altitude profiles generated by UPTOP closely match POST's optimal profiles. Additionally, the results from POST as calculated by UPTOP match the POST profiles. The reentry altitude and velocity profiles of an oscillating trajectory generated in UPTOP and POST are shown in Figure 8.1(b) to match for the given entry conditions. Validation for Earth entry from lunar return at V_E = 11 km/s is given in Figure 8.1(c). For the given bank angle profile, which rotates the lift vector, the skipping trajectory generated in UPTOP matched POST's and illustrates UPTOP's suitability for high-velocity entry applications.

UPTOP's flexible framework allows for an external code to provide the aerothermodynamics for a heat shield design throughout the trajectory calculation. A diagram of the overall optimization code setup is provided in Figure 8.2. In UPTOP, the optimization scheme provides different combinations design variable values to the trajectory code. The trajectory code then calls the low-order aerothermodynamic code at each calculated step in the trajectory.

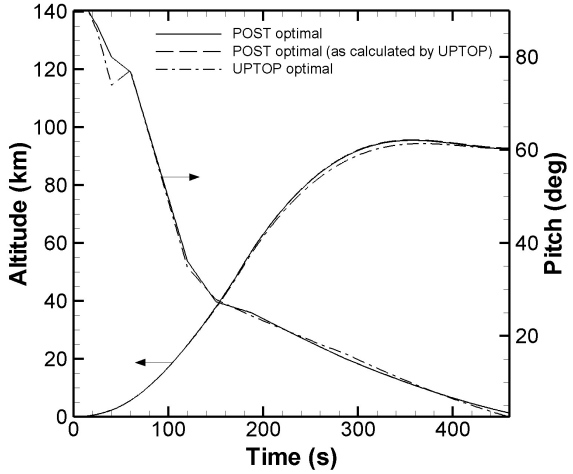

(a) Space Shuttle Transport Ascent through SSME cutoff, optimized trajectory

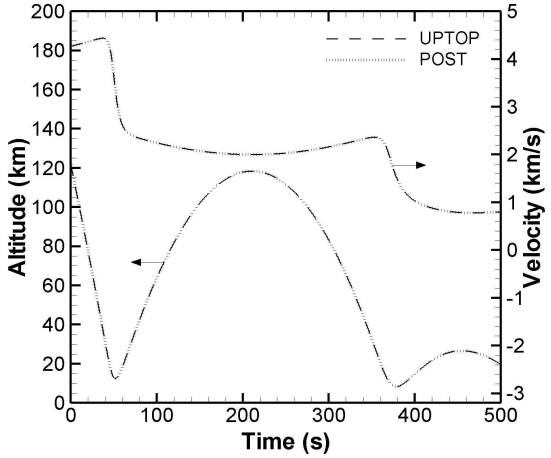

(b) Reentry body trajectory, V_E = 4267 m/s, γ_E = -30°, ϕ_b = -20°, BC_i = 11200 kg/m^2, 1.5 < L/D < 2.2

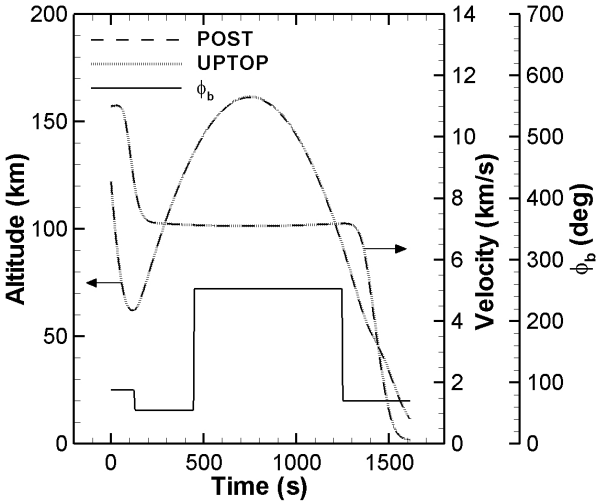

(c) Earth entry vehicle trajectory, V_E = 11 km/s, γ_E = -5.89°, BC = 218 kg/m^2, L/D = 0.33, C_D = 1.4286, S = 25.113 m^2

Figure 8.1. Trajectory validation of UPTOP results with POST.

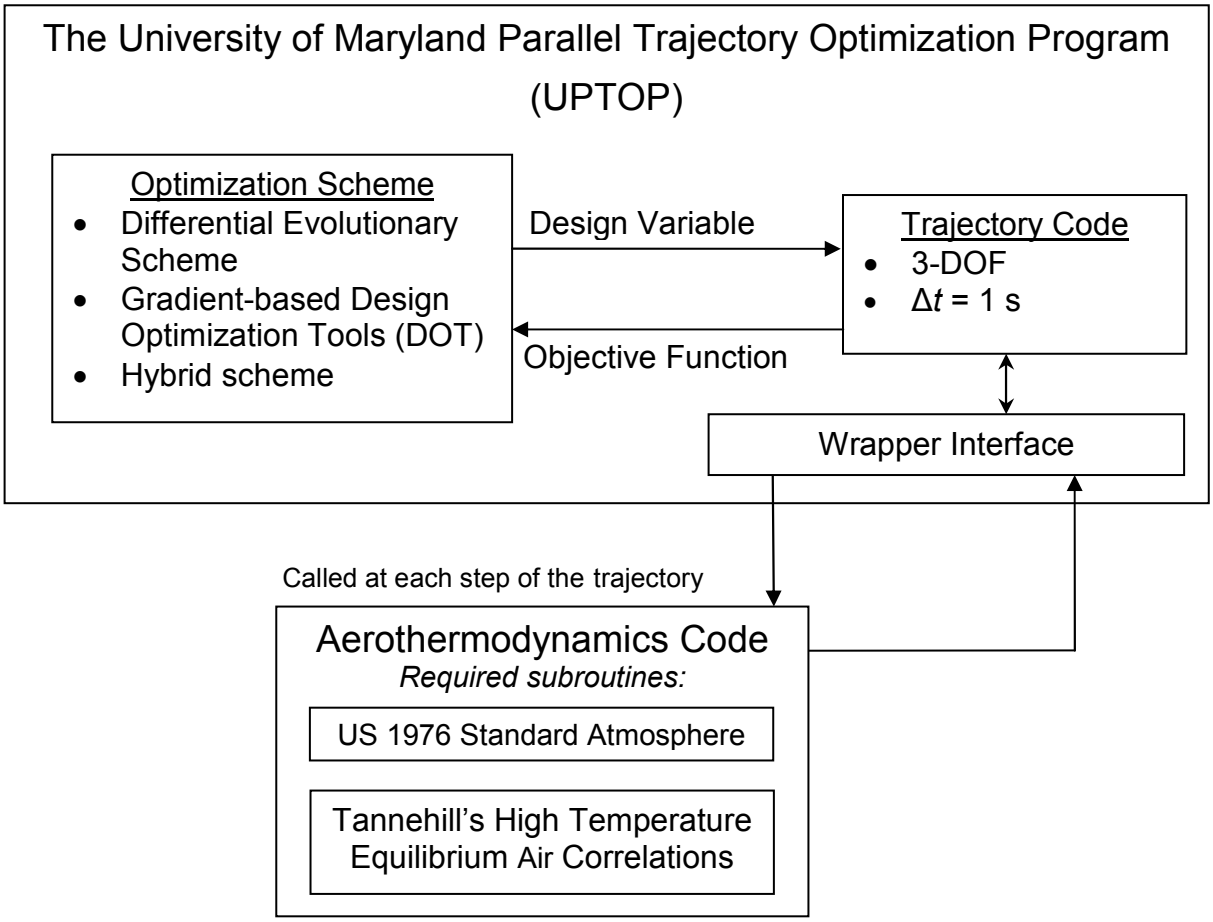

Figure 8.2. Diagram of Optimization Code Setup.

Integrating the aerothermodynamic models into the UPTOP setup to perform heat shield optimization allows for a higher fidelity model of radiative heat transfer to account for angle of attack in calculating the shock-standoff distance at each point in the trajectory to gain more accurate radiative heat flux values. With the Newtonian flow solver integrating over the surface pressure distribution for each point in the trajectory, a duration of 20 minutes on an AMD 2.2GHz Opteron 248 processor was required to complete a single run of a 2000 s trajectory. Modified Newtonian flow uses the Rayleigh Pitot tube formula[33] to account for different specific heat ratios in determining the maximum pressure coefficient. For $\gamma = 1.4$, the Rayleigh Pitot tube formula varies $C_{p,max}$ by 1.7% between freestream Mach numbers of five and fifty.

This results in nearly constant hypersonic aerodynamic coefficients for modified Newtonian flow in air and is, thus, an example of Mach number independence. To reduce the computation time, α-profiles of aerodynamic coefficients are stored in interpolation tables prior to trajectory calculation. With a range of α equal to $\pm 30^{o}$ and a data point in the interpolation table for every degree of α, the runtime for a single trajectory case of 2000 s takes approximately 10 s although both convective and radiative heat fluxes are calculated at each point. Additional runtime improvement is gained by increasing the interval to generating a data point every 3-degrees of α.

A mesh convergence study has been conducted to reduce the number of mesh points used to form the heat shield geometry. For optimization the mesh was reduced to $j_{max} = 45$, $k_{max} = 101$ while the detailed analysis uses a finer mesh of $j_{max} = 301$, $k_{max} = 401$. Figure 8.3(a) and (b) provide the aerodynamic coefficient profiles for the optimal *L/D* heat shield in Ref. [105]. This heat shield, shown in Figure 8.3(c) and (d), is located in one of the extremes of the design space and exhibits nonlinear aerodynamic behavior, thus, providing a good test case. There is considerable agreement in the aerodynamic coefficient values between the two meshes except for $C_{m,cg,\alpha}$. For the optimizer, only the sign of the static stability derivatives is accounted for. As a result, differences in values are acceptable for optimization as long as the stability derivatives are not part of the objective function. For other geometries, this may change the angle of attack at which the vehicle becomes unstable, but for the worst case this occurs at 2^{o} difference, which is not significant. The aerodynamic characteristics of the optimal designs are reported based on the refined mesh. Note that changes in heat transfer values between the two meshes are minimal.

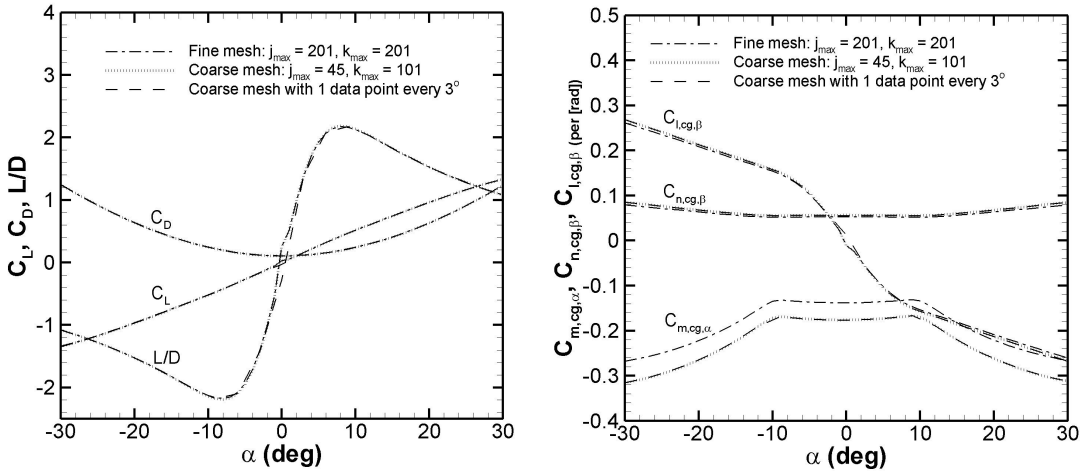

(a) Aerodynamic coefficient profiles **(b) Static stability derivative profiles**

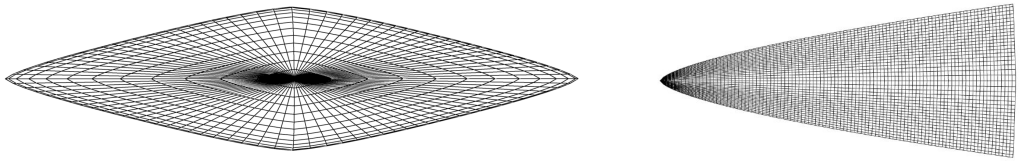

(c) Parallelogram cross section **(d) Power law axial profile**

Figure 8.3. Comparison of results from fine and coarse meshes for power law axial profile A = 0.900, b = 0.663, e = -0.968, parallelogram cross section, m_1 = 4, n_2 = 1.3.

Chapter 9. Optimization Theory

Both evolutionary, population-based optimization and gradient-based optimization algorithms are applied in this work. This chapter presents introductions to these methods, background on multi-objective function optimization, and a parametric analysis of the effect of the evolutionary optimization parameters on the results.

9.1. Gradient-based optimization algorithm

UPTOP utilizes Vanderplaats Research & Development, Inc.'s Design Optimization Tools (DOT)[102] for gradient-based optimization. DOT is professional software program that varies design variables based on a gradient-based minimization method to determine an optimum value of an objective function. DOT offers both unconstrained and constrained minimization methods. Broydon-Fletcher-Goldfarb-Shanno (BFGS) and Fletcher-Reeves (F.R.) are the two unconstrained minimization methods available in DOT. When DOT refers to unconstrained methods, it means that there are no constraints present except those on the design variables that DOT varies. The constrained methods offer the ability to restrict values on non-design variables or a combination of variables based on theory limits or other reasons. The constrained minimization methods available in DOT include the Modified Method of Feasible Directions (MMFD), Sequential Linear Programming (SLP), and Sequential Quadratic Programming (SQP).

The following optimization problem is solved by DOT: find the values of NDV design variables contained in $\vec{X}$ that will minimize or maximize $\text{OBJ} = O(\vec{X})$, in which the OBJ is the objective function, subject to constraints $G_q(\vec{X}) \leq 0$ for q = 1 to NCON, in which NCON is the number of constraints, and design variables X_p have side constraints $X_p^L \leq X_p \leq X_p^U$ for *p = 1 to* NDV*,* in which NDV is the number of design variables.[102]

For this work, DOT has been setup to use SQP to vary the design variables to find an optimum value of an objective function, in this case, an aerothermodynamic parameter or combination of parameters. SQP uses the following overall process. First, DOT creates a quadratic Taylor series approximation of the objective function and linearized Taylor series approximations of the constraints. Then a direction finding problem is formed to find a search direction E:

$$\text{Minimize } Q(E) = O^0 + \nabla O^T E + \frac{1}{2} E^T B E, \tag{9.1}$$

$$\text{Subject to } \nabla g_j^T E + E_j^0 \leq 0, \text{ j} = 1, \text{M}, \tag{9.2}$$

In which O is the original objective function and Q is the quadratic Taylor series approximation. This is solved using the Modified Method of Feasible Directions (MMFD). For MMFD, the objective function and constraints are first evaluated at the user inputted initial values of the design variables. Then the gradient of the objective function and constraints are calculated, and a search direction E is created. Then a one-dimensional search is completed to find the scalar parameter α^* that minimizes

$Q(\vec{X})$. Scalar parameter α^* is used to find a new $\vec{X}$ that is set equal to the sum of the initial $\vec{X}$ and the product of α^* and the search direction,

$$\vec{X}^u = \vec{X}^{u-1} + \alpha^* E^u, \tag{9.3}$$

in which u is the iteration number. If convergence is not satisfied, then iterations of the following process are completed until convergence requirements including the Kuhn-Tucker conditions are satisfied.[102]

The three Kuhn-Tucker conditions[102] must be satisfied for obtaining convergence. The first is that optimum design $\vec{X}^*$ must be feasible, or produce constraint values $g_q(\vec{X}^*) \leq 0$ for q = 1 to NCON. The second condition is that the product of the Lagrange multiplier λ_q and $g_q(\vec{X}^*)$ must be zero. The third condition is that the gradient of the Lagrangian becomes zero, in which the gradient of the Lagrangian is

$$\nabla Q(\vec{X}^*) + \sum_{q}^{NCON} \lambda_q \nabla g_q(\vec{X}^*) = 0. \tag{9.4}$$

Detailed descriptions of SQP and the Kuhn-Tucker conditions are included in Appendix E of Ref. [102].

9.2. Evolutionary, population-based optimization algorithm.

Previous work[105] by the authors applied the Modified Method of Feasible Directions (MMFD) gradient-based method to optimize over the geometric design space (without trajectory analysis) for a single objective. There were numerous local optima; over 200 runs were required to locate the global optima for four objective

functions. For the present work, a more robust and global search algorithm is required to account for both the additional complexity of multi-objective optimization and the broader design space with trajectory analysis. UPTOP includes a differential evolutionary scheme (DES).[93,106] As an evolutionary algorithm, DES bases its search for an optimum on nature's evolutionary principles.[107] Each heat shield design, known as an individual in a population of designs, is evolved throughout each iteration with other individuals based on mutation intensity and crossover parameters. It begins by randomly-selecting an initial population of designs, and hundreds of iterations are required to settle on an optimal solution.

A brief description of the method is given, based on Ref. [108]. Consider the set of design variable vectors $X_{j,n}$ at generation n

$$X_{j,n} = [x_{1,j,n}, x_{2,j,n}, x_{3,j,n}, \ldots, x_{D,j,n},], \tag{9.5}$$

in which $x_{i,j,n}$ corresponds to the design variable in dimension i in a D-dimensional optimization problem. The initial population is randomly chosen within the side constraints of the design variables. The mutation, recombination, cross over, and selection operators are applied to the population each generation until the optimization method is stopped. To evolve the design variable vector $X_{j,n}$, three different design variable vectors are randomly chosen, $X_{a,n}$, $X_{b,n}$, $X_{c,n}$. A trial design variable vector Y is then defined as

$$Y = X_{a,n} + R(X_{b,n} + X_{c,n}), \tag{9.6}$$

in which R is a user specified constant, $0 < R < 1$. A candidate vector for improving the current value for minimizing objective function O is defined as $Z = [z_1, z_2, z_e, \ldots, z_D]$:

$$z_i = \begin{cases} y_i & if\ r_i \le C \\ x_{i,j,n} & if\ r_i > C \end{cases} \tag{9.7}$$

in which r_i is a uniformly distributed random variable, $0 < r_i < 1$, and C is a user specified constant $0 < C < 1$. The final step in the evolution of $X_{j,n}$ involves the selection process and minimization of the objective function $O(X)$, given by

$$X_{j,n+1} = \begin{cases} Z & if\ O(Z) \le O(X_{j,n}) \\ X_{j,n} & if\ O(Z) > O(X_{j,n}). \end{cases} \tag{9.8}$$

The concepts of mutation intensity and crossover are also applied. Each design variable is given a binary string representation, called the chromosome of the design variable. Mutation intensity refers to the probability of one digit in the chromosome switching from a 0 to a 1 or vise-versa. Crossover refers to breaking strings into substrings and then interchanging some of the substrings at random. For example, two designs will randomly be chosen for crossover; they are known as parents for the crossover operation. They are the parent strings or chromosomes; they are broken into three substrings with the cross sites chosen randomly, and the middle portion is switched. The resulting designs are known as the offspring, the new designs in the current generation. Based on the design space, different values for the mutation intensity and crossover probability would produce more optimal results. Details on DES and its parameters are provided in Refs. [106], [107], [108], and [109].

9.3. Multi-objective function optimization

In single-objective optimization, the one optimal or non-dominated solution is better than all other solutions. In multi-objective optimization, two or more objective

functions are optimized simultaneously to produce a set of optimal or non-dominated solutions known as the Pareto frontier. When two objective functions are optimized simultaneously, a Pareto frontier has the form of a curve that represents the optimal trade-off between the two objectives. Shown in Figure 9.1, the results of minimizing $Q_{s,tot}$ and maximizing p_{dwn} simultaneously are given. This Pareto frontier is composed of those solutions in the feasible population that are not dominated with respect to both objective functions; each point on the frontier represents an optimal solution. In general, the Pareto frontier is a set of non-dominated solutions, in which one solution is better than another with respect to at least one objective, but not all objectives.[107]

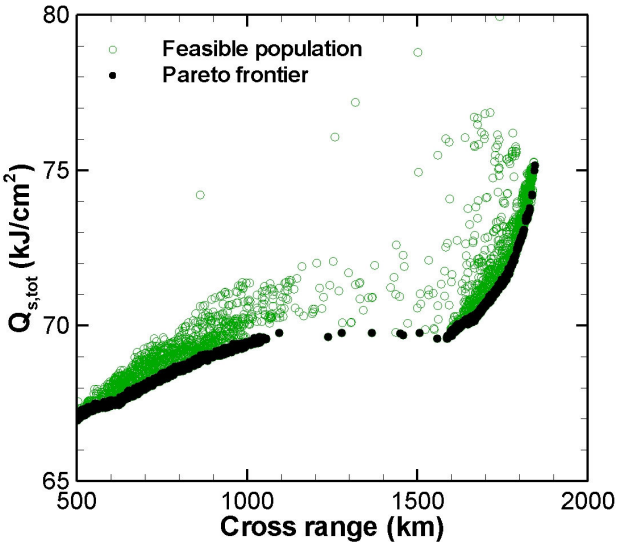

Figure 9.1. Multi-objective function population with Pareto frontier, spherical segment, *L/D* = 0.5, V_E = 12.5 km/s.

A Pareto frontier can also be generated using single-objective optimization. A single objective function can be generated using a combination of performance parameters with the weight variable W

$$O\left(\vec{X}\right) = Wo_1\left(\vec{X}\right) + (1-W)o_2\left(\vec{X}\right), \tag{9.9}$$

in which $0 \leq W \leq 1$. By incrementing the weighting variable and applying several initial conditions, a set of non-dominated solutions are obtained to produce a Pareto frontier. This objective function form is designed to provide a compromise between two performance parameters. One drawback to the single objective function approach is that there is only one solution generated on the Pareto frontier for each optimization run, totaling to an overall large computational time on the order of a week per Pareto frontier using the differential evolutionary scheme. Another drawback is that finding the specific sub-range(s) of W (within the overall range from zero to one) at which the optimization is sensitive requires several test runs. Furthermore, this method does not necessarily produce a full Pareto frontier.

Performing the optimization with a multi-objective function methodology allows for more of the Pareto frontier to be generated within a given amount of time when using the evolutionary scheme. Instead of locating a single solution that dominates the remaining 10,000+ designs, a multi-objective function optimization results in a few hundred or thousand non-dominated solutions. This allows a much greater portion of the Pareto frontier to be generated within a single run. The time required is on the order of 10 hours while using a similar population size. In this way, it is also more efficient for a given population size.

Multi-objective optimization is utilized to optimize conflicting objectives. Since an increase in cross range produces a larger heat load, maximizing cross range and minimizing heat load are conflicting objectives. Non-optimal results may produce higher heat loads than necessary for a desired cross range. Minimizing heat load and minimizing peak heat flux are also conflicting objectives. For this work, optimal

solutions are provided in the form of Pareto frontiers between two objectives to highlight performance trade-offs and provide comparisons between axial profiles.

9.4. Applying optimization methods

Primarily, the differential evolutionary scheme is applied for this work since the main results are from multi-objective optimization, in which UPTOP uses the DES. A hybrid method utilizing both SQP and DES is utilized in calculating the entry corridor boundaries and the initial feasible design within the boundary that is placed along with the initial population for the multi-objective optimization. In this case, DES is primarily utilized for finding the overshoot and undershoot, in which targeting a feasible design at a given γ_E is employed by using the single-objective optimization setup. In this part of the analysis, optimization is not focus although the objective function is heat load $Q_{s,tot}$; instead, the hybrid method is conducting a global search to locate a feasible design at a given γ_E. In this case, the DES allows the hybrid method to perform the global search, and then the gradient-based SQP method is applied to the best design after 21 iterations to determine a feasible design. Additional detail into how the entry corridor is found using UPTOP is included in Chapter 11.

9.5. DES Parameter and Population Size Analysis

A parametric study of the effects of population size, crossover probability, and mutation intensity on the Pareto frontier for maximizing p_{xrs} and minimizing $Q_{s,tot}$ is provided in this section. The ideal Pareto frontier provides a full and comprehensive profile of non-dominated solutions for a given set of performance metrics. Previous

work by the authors[110,111] used an initial population size of 130 with random values chosen for crossover probability and mutation intensity for each generation. To determine if a better Pareto frontier could be generated, an analysis on the effects of population size and DES parameters on the Pareto frontiers has been completed. The DES parameters crossover probability and mutation intensity have been applied with values of 0.2, 0.5, 0.8, and with a random value between zero and one chosen for each generation. These DES parameters were tested with initial population sizes of 130, 260, and 390. When studying the effects of crossover probability, the mutation intensity is varied randomly each generation, and vice-versa for studying the effects of mutation intensity. Each optimization runs until approximately 18,000 feasible solutions were created that improve in one objective function value over previously generated solutions. As expected, the larger population size causes an increase the runtime.

Figure 9.2 indicates that increasing the population size not only produces a fuller Pareto frontier but also improves the performance metrics. Doubling the initial population to 260 produced significant reductions in heat load for cross ranges near 1000 km. Slight improvements are noticed when increasing the population to 390, but it also produces a wider range of results with a cross range up to 2100 km.

A crossover probability of 0.2 with an initial population of 130 produced a continuous and almost linear relation between cross range and heat load, as shown in Figure 9.3. Increasing the population size to 390 greatly improves the performance metrics, though low values of crossover probability still produced sparser Pareto frontiers. A high crossover probability with a population of 130 produces step

increases in heat load at cross ranges of 1000 km and 1800 km. Increasing the population size to 390 removed them. A high crossover probability of 0.8 with a population size of 390 produced more dominant results than the random value case (R).

A low mutation intensity value of 0.2 produced a sparse Pareto frontier for cross ranges greater than 800 km, shown in Figure 9.4. Increasing the population size to 390 allowed the optimizer to widen the band of the Pareto frontier and locate designs for cross ranges less than 1000 km with a 33% decrease in heat load. Increasing mutation intensity to 0.5 and 0.8 produced smaller improvements. The random value case with a population size of 390 produced the fullest Pareto frontier.

In summary, the most comprehensive Pareto frontier for this design space is produced by a population size of 390, a crossover probability of 0.8, and a mutation intensity that is randomly varied for each generation between 0 and 1. An initial population of 390 individuals is applied since diminishing returns were observed from increasing it. These settings provide a significant gain in the optimizer's ability to locate better solutions and produce fuller Pareto frontiers. Fourteen AMD 2.2 GHz Opteron 248 processors were utilized in this analysis, and the time required per run was 8-16 hr, depending on the duration of the trajectories analyzed; optimizations that found primarily 400 s duration trajectories that satisfied the constraints and were optimal would take less time to run that optimizations that found longer 3000 s duration trajectories were necessary.

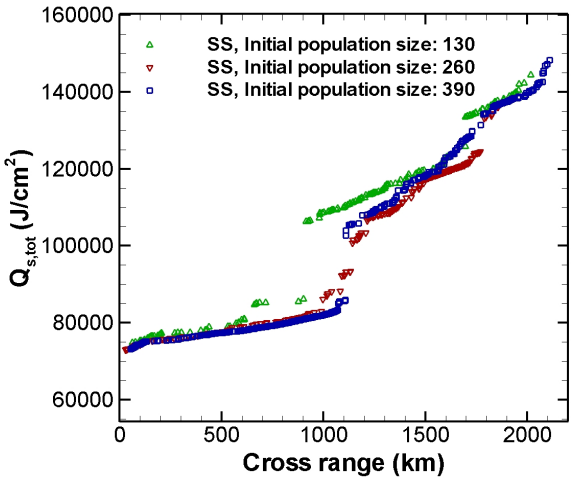

Figure 9.2. Effect of population size on the Pareto frontier.

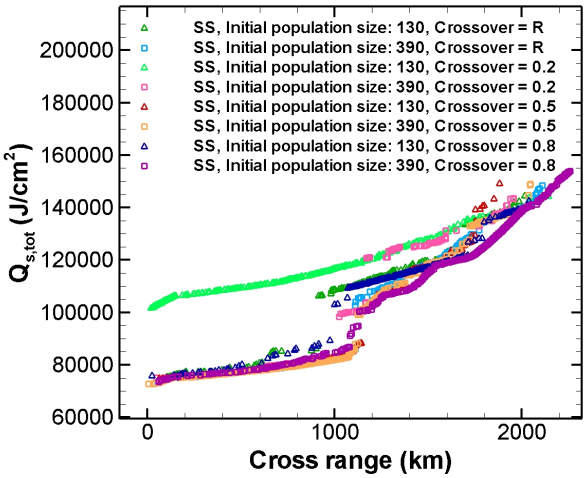

Figure 9.3 Effect of crossover probability on the Pareto frontier.

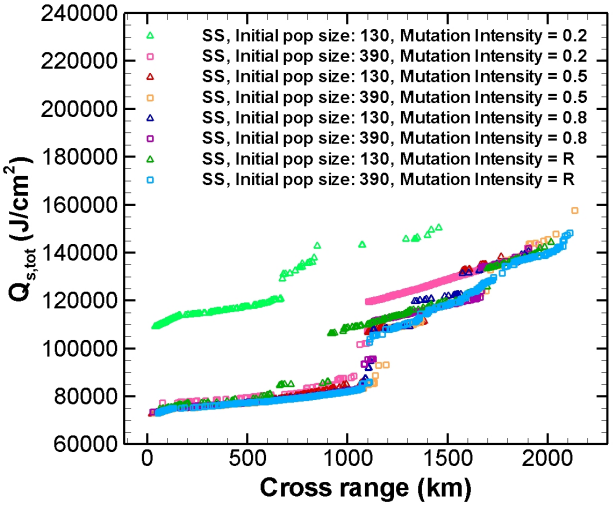

Figure 9.4 Effect of mutation intensity on the Pareto frontier.

Chapter 10. Initial Lunar and Mars Return Optimization Results

Several full sets of optimization cases had to be completed in order (1) to understand the results from the Pareto frontiers, (2) to become familiar with the design space, and (3) to understand how the optimization worked and if it is working properly. In this dissertation, two full sets of optimization cases are completed. The first set assumes relaxed constraints that were required to produce a successful optimization. These relaxed constraints would produce some heat shield/trajectory configurations that would not be survivable by astronauts. Note that several sets of optimization cases were completed before this set, and those are listed in Refs. [105], [110], [111], and [112]. This chapter provides the optimization setup description and the results for lunar and Mars return with these relaxed constraints. Once the limitations of the optimization setup and the drawbacks of the trajectory results were understood, an entry corridor methodology was implemented to produce more practical trajectories for both astronaut survivability and more realistic trajectory constraints. This second set of lunar and Mars return results is provided in Chapter 11– Chapter 14; and represents the final results of this work. The set of results in this chapter provided important groundwork for understanding the heat shield geometry and entry trajectory design space that led to producing practical final results.

10.1. Optimization Setup

UPTOP applies a differential evolutionary scheme (DES)[93,106] for this optimization. To simulate Earth entry for lunar return, an initial entry velocity of 11

km/s is applied.[32] For Mars return, a fast 180-day return renders entry velocities up to 14.7 km/s,[80] and an initial entry velocity of 15 km/s is applied. A separate optimization is performed for each axial profile: spherical segment (SS), spherically blunted cone (SC), and power law (PL).

10.1.1. Objective functions

Three objective functions are applied in the initial work: minimizing stagnation-point heat load $Q_{s,tot}$, minimizing peak stagnation-point heat flux $q_{s,max}$, and maximizing cross range p_{xrs}. These objective functions have been selected on the basis of (1) relevance to mission requirements, (2) connection to low-performing or restrictive capabilities of existing blunt-body designs, and (3) the availability of accurate physical models suitable for optimization purposes.

The peak heat flux of the trajectory determines which materials are capable of surviving the selected entry conditions. Minimizing heat load reduces the heat shield's thickness and mass indirectly. Minimizing both requires the capability to change the flight path and heat flux calculations throughout hundreds of entry trajectories. As a result, low-order computational models of the aerothermodynamics are implemented to balance the need for fidelity with the desire to have practical computational times. Heat transfer is tracked at the stagnation point. There is more confidence in well-validated stagnation-point correlations than in low-order estimates of the maximum heat flux, especially when applied to a wide range of geometries in extreme hypersonic conditions. They also cost less computational time.

Cross range capability enables missions that require immediate inclination changes, and likewise, enable more abort scenarios. Existing designs have low cross

range performance due to trajectory design and low *L/D*. For a vehicle flying a direct entry trajectory from lunar return with a hypersonic *L/D* = 0.30, the maximum cross range is limited to ≈ 200 km with a 5 *g*-limit.[1] To increase cross range capability, both skipping trajectories, which have been shown to increase cross range significantly,[7] and higher *L/D* designs are considered feasible.

10.1.2. Design variables

For each axial profile, the design variables along with their side constraints are listed in Table 10.1. For θ_s, the lower limit of 5^o provides a blunt-body that has a large but finite radius-of-curvature. For both θ_s and θ_c, the upper limit 89^o removes numerical issues present if the upper limit is set to 90^o. Additionally, zero radius-of-curvature designs are not considered since they produce high heat concentrations. The maximum eccentricity of ±0.968 was chosen to limit the axes ratio *j/k* to less than or equal to four. The angle of attack is limited to $\pm 30^o$ since manned space capsules usually enter at or below $|\alpha| = 25^o$ and also due to the fact that the heat shield may not be even half of the vehicle's shape.

Table 10.1. Design variables with side constraints for initial optimization.

Axial profile	Profile specific design variables	Common design variables	
Spherical segment	$5.0^o \le \theta_s \le 89.0^o$	$-30^o \le \alpha \le 30^o$	$-15.5^o \le \gamma_E \le -0.05^o$
Spherically-blunted cone	$55.0^o \le \theta_c \le 89.0^o$ $0.15 \le r_n/d \le 2.00$	$-0.968 \le e \le 0.968$ $1.30 \le n_2 \le 2.00$ $t_0 + 5\text{ s} \le t_1 \le 7190\text{ s}$ $t_1 + 5\text{ s} \le t_2 \le 7190\text{ s}$	$0^o \le \phi_{b,0} \le 180^o$ $0^o \le \phi_{b,1} \le 180^o$ $0^o \le \phi_{b,2} \le 180^o$ $0^o \le \phi_{b,3} \le 180^o$
Power law	$0.900 \le A \le 10.000$ $0.200 \le b \le 0.650$	$t_2 + 5\text{ s} \le t_3 \le 7190\text{ s}$	$0^o \le \phi_{b,4} \le 180^o$

If θ_s is large, then it is possible that the entire space capsule could fit within a hard or soft shell re-entry system including inflatable aeroshell devices. A non-eccentric heat shield with $\theta_c \approx 45^o$ is the interface at which the spherically-blunted cone begins to produce positive lift at negative α.[28] If $\theta_c \leq 45^o$, then negative lift is generated at negative α. The term *blunt body* for re-entry commonly refers to a vehicle that produces a bow shock with a substantial standoff distance. Since Ried[51] approximated that the shock-standoff distance of the Apollo 4 was 14 cm and this work predicts 12.4 cm ($M_\infty = 32.8$, $\alpha = 25^o$ at $h = 61$ km, at 30030 s into the mission), it was decided that the order of accuracy of Kaattari's method is approximately 2.54 cm. As a result, the characteristics of the spherically-blunted cone that has a shock-standoff distance of 2.54 cm would represent the lower limit for θ_c and r_n/d. For a non-eccentric heat shield, this work predicts a 2.54 cm shock-standoff distance for a spherically blunted cone with $\theta_c = 55^o$ and $r_n/d = 0.25$. If the shock-standoff distance at angle of attack decreases by more than 50% from the value at $\alpha = 0^o$, then the shock-standoff distance at $\alpha = 0^o$ is applied. At $\alpha = -25^o$, the Apollo CM shock-standoff distance decreases by approximately 40%, and thus, in this work, the assumed feasible limit is 50%. The lower limit on the nose radius-to-diameter ratio is not greater than 0.25 since previous work such as the Mars Viking missions included heat shields with $r_n/d = 0.25$. The chosen lower limit of 0.15 on r_n/d widens the design space. For the blunted cone, the upper limit of r_n/d of 2.0 is chosen to provide overlap and continuity between the blunted cone and spherical segment design spaces. This allows the optimizer to choose a spherical-segment over a spherically-blunted cone in the same optimization if necessary.

For the power law, Newtonian impact theory may have an accuracy issue given the quick slope changes shown in Figure 2.3(b) for $b = 0.1$ or smaller; a lower limit value of 0.2 for b has been chosen arbitrarily. Sharper-nosed power law profiles with exponent $b > 0.65$ have been removed from the design space since these shapes cannot be optimal from a convective heat transfer standpoint. In addition, the current low-order method of determining an effective nose radius for the power law profile is not accurate enough for the optimizer to remove them from the design space. The upper limit on b produces a nearly linear profile, but the code requires the slope of the power law profile to vary at least slightly to prevent derivative calculation dilemmas. Since blunt-bodies in previous work usually have $l < d$ (i.e., Apollo CM $l/d \approx 1/9$), it was decided in this work to widen the design space by including $A = (l/d)^{-1} = (10/9)^{-1}$. Then the upper limit $A = 10$, at which the power law becomes similar to the spherical-segment axial profile, was chosen since the power law profile is no longer unique. In generating the base cross section, the lower limit of n_2 produces slightly rounded-edge polygons. As n_2 is increased, the polygon's edges become more rounded, and the polygon is completely transformed into an ellipse at $n_2 = 2.0$.

A wide range of γ_E including the Apollo[41] missions' $\gamma_E \approx -6.5^o$ is allowed. To modify the vehicle's flight path through rotation of the lift vector, a bank angle profile with five control points is available. The first and last control points $t_0 = 0$ s and $t_4 = 7300$ s are fixed, and the optimizer can modify the five bank angles $\phi_{b,0}$ through $\phi_{b,4}$, as well as the three intermediate times at which the bank angles are initiated. Connecting the control points (t, ϕ_b) produces the ϕ_b-profile. A limit of 0^o to 180^o lowers the size of the design space; angles 181^o through 359^o are not necessary

since longitude and latitude constraints are not considered. A mesh convergence study, provided in Chapter 8, was implemented to reduce computational time; for optimization the geometry's mesh is $j_{max} = 45$, $k_{max} = 101$.

10.1.3. Design constraints

Boundaries for the feasible design space are provided in Table 10.2. These constraints account for trajectory design limits, theory limitations, and static longitudinal, directional, and roll stability. For blunt-bodied capsules (low *L/D*), whether the trajectory ends at $M_\infty < 5$ does not strongly affect the values of the three optimization parameters in this analysis. Since the heat shield shape is not necessarily or usually the entire vehicle shape, a limit on the angle of attack at which a given heat shield can be analyzed, must be chosen in order to maintain the assumption that the flow generally separates before passing over the aft body (crew compartment). Otherwise, the entire vehicle must be examined initially to determine the hypersonic aerodynamics since the Newtonian flow assumption $C_p = 0$ for $\vec{V}_\infty \cdot \hat{n} \geq 0$ would not apply. This is completed with the edge tangency constraint $|\alpha| \leq |\varepsilon + 1^o|$. The edge tangency constraint requires that a given heat shield must not be placed at an angle of attack more than one degree larger than the heat shield's tangency angle ε, which is

Table 10.2. Trajectory and aerodynamic constraints for initial optimization.

Optimization constraints	
Trajectory	Aerodynamic/Geometric
$t_f \leq 7200$ s	$M_{\infty,f} \leq 5$
$h_t \leq 3000$ km	$C_{m,cg,\alpha} \leq -0.001$
$h_{t,f} \leq 75$ km	$C_{n,cg,\beta} \geq 0.001$
$n_{max} \leq 6\ g$, $V_E = 11$ km/s	$\text{sign}(C_{L,V})\ C_{l,cg,\beta} \leq 0.01$
$n_{\max} \leq 12\ g$, $V_E = 15$ km/s	$\|\alpha\| \leq \|\varepsilon + 1^o\|$

the angle produced between the heat shield's edge surface and the vertical axis. In this way, at the limit the heat shield's edge is normal to the freestream flow when $\alpha = \varepsilon$, and the one-degree above ε was chosen as a small relief factor. When maximizing L_V/D, the optimizer sometimes increases α beyond ε, which leads the optimizer into a region of design space where the Newtonian flow assumption does not necessarily apply. Note that for heat shields with $\varepsilon < 15^o$, an aft-body with an angle greater than 15^o is assumed to allow heat shields with low θ_s, for example $\theta_s = 10^o$, to be feasible for $|\alpha| \leq 15^o$.

Longitudinal and yaw static stability requirements are also included; because this is a numerical analysis, the magnitude value of 0.001 is deemed significant rather than 0.000. The roll static stability requirement, but it is different from the longitudinal and yaw requirements in that it allows for slight instabilities with unstable values up to 0.01/rad in order to produce heat shields such as the Apollo CM, which is believed to have been slightly statically roll unstable with $C_{l,cg,\beta} \approx$ 0.005/rad. This keeps the design space open to successful previous work. The requirement for roll static stability changes sign when the $C_{L,V}$ changes sign as explained in Ref. [112], thus requiring a change in the constraint.

Since guidance laws are not considered in the trajectory analysis, optimal trajectories with similar entry interface characteristics but with less complex ϕ_b-profiles tend to generate longer duration trajectories. A compromise was chosen to be two hours, $t_f \leq 7200$ s, which is greater than twice the upper-limit to the estimated t_f for the Orion CEV. An arbitrary maximum altitude for skipping trajectories has been set to 3000 km. A final altitude $h_{t,f}$ no greater than 75 km has been chosen to ensure

that the vehicle's trajectory ends within the atmosphere. This allows for higher *L/D* vehicle designs to be feasible since their optimal trajectories may result in deceleration at higher altitudes in the atmosphere. For V_E = 11 km/s, a peak *g*-load of 6 *g* was chosen since it is the maximum allowable acceleration level for a deconditioned astronaut in a reclined position.[32] It is also lower than the 7 *g* that Apollo 10 experienced.[113,114] Preliminary analysis indicated that for a 15 km/s entry, this optimization setup would be over-constrained with a 6 *g* upper limit. This limit was increased to 12 *g* based on previous work that indicates a pilot can sustain 12 *g* for up to 60 s and still continue to perform the assigned tasks.[114] Though this is not expected to conform to future standards for manned Mars return, the results provide a sense of the heating environment when entering at high hyperbolic velocities. Results for V_E = 15 km/s can be applied at least towards most unmanned missions.

10.1.4. Choosing the base cross section

For the spherical-segment axial profile, it is shown in Table 10.3 that the vertical lift-to-drag ratio *L/D* is largest for the parallelogram and pentagonal cross-sections. The parallelogram cross-section (m_1 = 4) has the minimum number of sides examined and offers the maximum lift-to-drag configuration in this analysis. The optimal m_1 = 4, 5, and 6 designs are shown in Figure 10.1.

Table 10.3 Optimal designs for maximizing L_1/D with different m_1.

Spherical-segment axial profile Initial Design $\theta_s = 85.0^o$, $n_2 = 1.40$, $e = -0.900$, $\alpha = 25^o$			
Optimal Design $\theta_s = 89.0^o$, $e = -0.968$			Objective Function
m	n_2	α	L/D
4	1.30	18^o	1.10
5	1.30	24^o	0.88
6	2.60	22^o	0.75
7	1.30	20^o	0.76
8	1.30	21^o	0.82

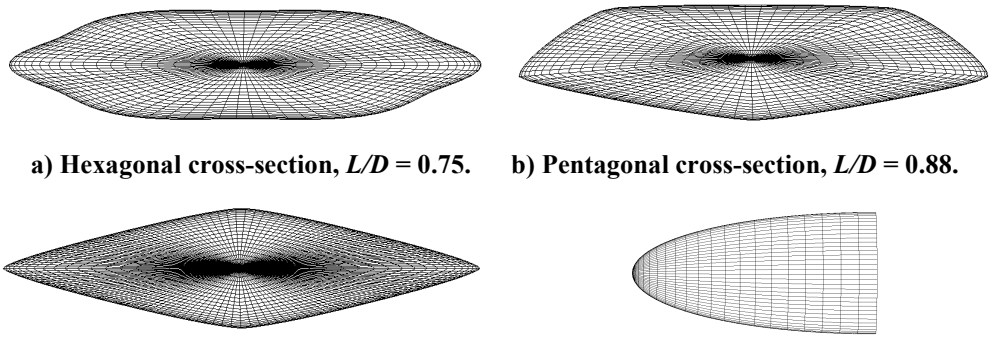

a) Hexagonal cross-section, $L/D = 0.75$. **b) Pentagonal cross-section, $L/D = 0.88$.**

c) Parallelogram cross-section, $L/D = 1.10$. **d) Spherical-segment axial profile, $\theta_s = 89.0^o$.**

Figure 10.1. Optimal geometries from Table 10.3, $e = -0.968$.

The hexagonal geometry is the only design with a rounded-edge concave base contour. In Figure 10.2 the behavior of the hexagonal cross-section with a spherically-blunted cone axial profile is compared to the parallelogram cross-section. The hexagonal design's *L/D* has a maximum magnitude of 0.61, 19% less than its spherical-segment analogue, with an oblate, rounded-edge concave cross-section. The parallelogram design's *L/D* continues to increase in magnitude at it approaches the lower endpoint, which is located in the non-concave region. As a result, varying the hexagonal design produces a different trend than one generated by varying the parallelogram design. It is only a coincidence that the n_2 value of 2.6 for the

hexagonal design in Table 10.3 is twice that of the other designs with the n_2 lower side constraint active.

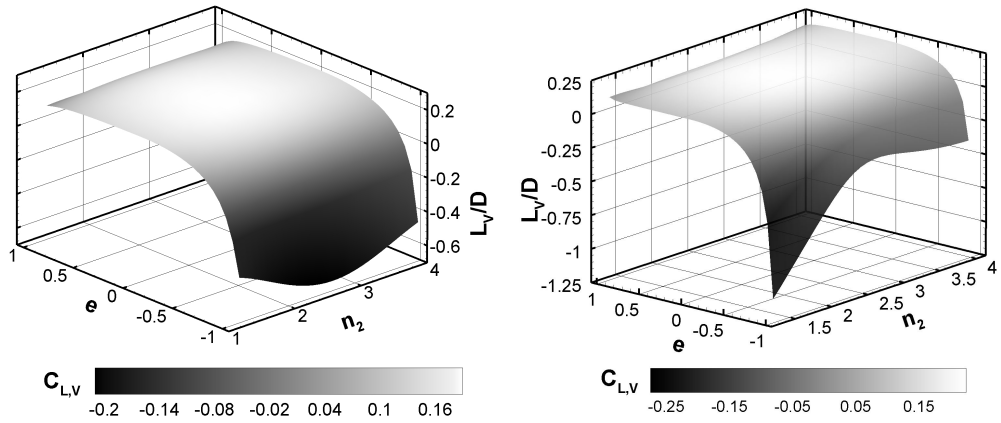

a) Hexagonal base ($m = 6$). **b) Parallelogram base ($m = 4$).**

Figure 10.2. L_V/D distribution for $m = 4$ and 6, spherically-blunted cone axial profile, $\theta_c = 55^o$, $r_n/d = 0.05$, varying e and $n_2 = 1.3$ to 4.0, $M_\infty = 32.8$, $\alpha = -20^o$.

The spherical-segment angle constraint is active for the optimal designs with $\theta_s = 89^o$. This high spherical-segment angle θ_s creates geometries that produce positive lift at positive angles of attack because each has a normal force that contributes more to the lift force than the axial force. For the classic blunt-body Apollo Command Module ($\theta_s = 25^o$), the axial force contributes more to the lift force, thereby requiring a negative angle of attack for positive lift.

Since a high L/D is desired for several reasons, such as increasing the range of available landing sites and reducing g-loads for manned missions, it is one of the most important aerodynamic characteristics of a lifting re-entry vehicle. From this point, the optimization analysis is completed with the parallelogram cross-section ($m_1 = 4$) in order to have the largest range of L/D values available for optimization.

10.2. Optimal configurations for V_E = 11 km/s

10.2.1. Minimizing $Q_{s,tot}$ and maximizing p_{xrs}

Specific designs are labeled on the Pareto frontiers and listed in Table 10.4. The lowest possible heat load is expected to increase with cross range p_{xrs} provided that down range is relatively constant or increasing. A Pareto frontier is given for each type of axial profile in Figure 10.3(a), for cross ranges up to 1500 km and heat loads from 11 to 33 kJ/cm^2. The optimizer produced similar Pareto frontiers for all three axial profiles. The power law's is expected to be the least accurate since an artificial effective nose radius is applied. All three frontiers closely match for p_{xrs} > 750 km; close inspection indicates that for this region, the spherically blunted cone and power law profiles are disguised spherical segments, including designs B and C shown in Figure 10.4 with elliptical base cross sections from Figure 10.5. Geometries with p_{xrs} < 250 km have down ranges of at least 2000 km while designs with higher p_{xrs}, including A, B, and C, have relatively constant down ranges of 10900 ± 200 km.

The design variable distribution for the spherical segment's Pareto frontier is provided in Figure 10.6. The transformation variable n_2 is nearly constant at 2.0, indicating an elliptical cross section rather than a parallelogram-form is optimal for this set of p_{xrs}. The parallelogram form would be applied to increase *L/D* beyond the capability possible with an elliptical cross section. Since the maximum *L/D* for these Pareto frontiers is 0.50, provided by design C, the parallelogram form is unnecessary. These results indicate that for low *L/D* designs, an elliptical cross section is better due to its larger drag area ($C_D S = D/q_\infty$), rendering a lower *BC* for a given m_{EV}.

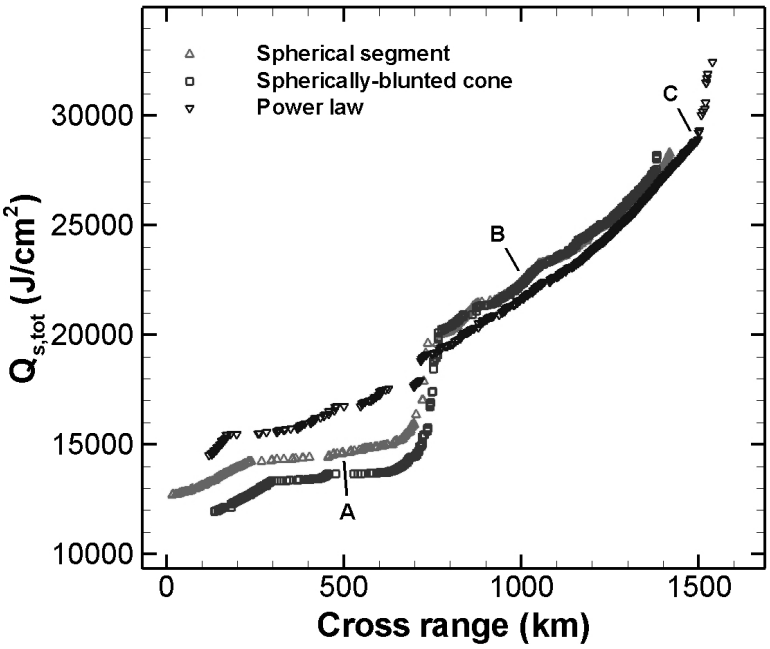

(a) Minimizing $Q_{s,tot}$ and maximizing p_{xrs}

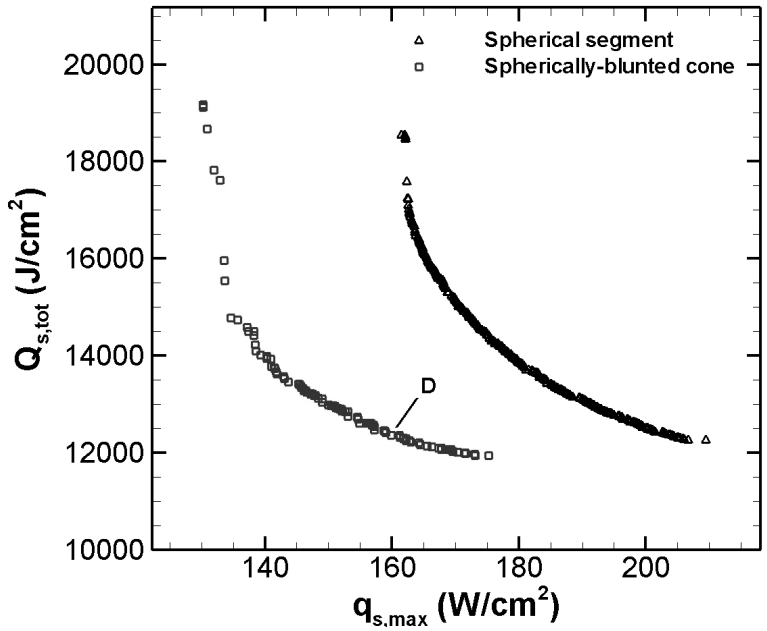

(b) Minimizing $Q_{s,tot}$ and $q_{s,max}$

Figure 10.3. Pareto frontiers for Earth entry, V_E = 11 km/s.

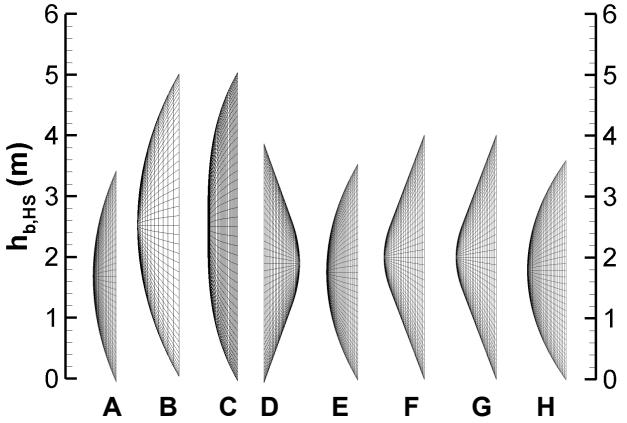

Figure 10.4. Axial profile designs from Table 10.4.

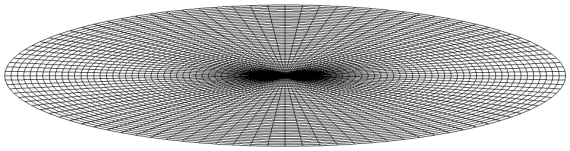

(a) Designs A, D - H, e = -0.968, $n_2 \approx 2$

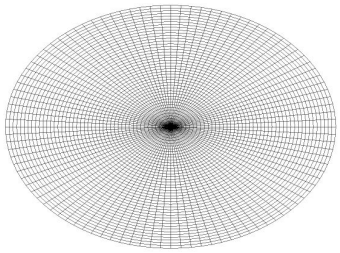

(b) Design B, e = -0.682, n_2 = 2

Figure 10.5. Specific base cross sections from Table 10.4.

Table 10.4. Optimal configurations for two multi-objective function sets, m_1 = 4.[a,b]

	Minimizing $Q_{s,tot}$ & Maximizing p_{xrs}					Minimizing $Q_{s,tot}$ & $q_{s,max}$		
	V_E = 11 km/s (Fig. 9a)			V_E = 15 km/s (Fig. 14a)		V_E = 11 km/s (Fig. 9b)	V_E = 15 km/s (Fig. 14b)	
	A	B	C	E	F	D	G	H
Design Variables	SS θ_s = 6.80° n_2 = 1.99 e = -0.968 α = -13.7°	SC θ_c = 60.4° r_n/d =1.26 n_2 = 2.00 e =-0.682 α =-23.8°	PL b = 0.34 A = 5.25 n_2 = 1.96 e = -0.003 α = 30.0°	SS θ_s = 8.1° n_2 = 1.98 e = -0.968 α = 14.8°	SC θ_c = 84.3° r_n/d =1.29 n_2 = 2.00 e = -0.968 α = -15.9°	SC θ_c = 84.4° r_n/d = 2.00 n_2 = 2.00 e = -0.968 α = -15.8°	SC θ_c = 84.3° r_n/d =1.30 n_2 = 2.00 e = -0.968 α = -15.9°	SS θ_s = 10.2° n_2 = 2.00 e = -0.968 α = 9.00°
γ_E (t_0, $\phi_{b,0}$) … (t_f, $\phi_{b,f}$)	-6.01° (0 s, 59.0°) (1440, 76.0°)	-6.14° (0 s, 75.9°) (1530, 55.1°)	-6.29° (0 s, 97.9°) (1540, 135.7°)	-6.60° (0 s, 43.7°) (248.4, 161.5°) (1450, 137.4°)	-6.44° (0 s, 143.5°) (190, 40.7°) (870, 84.5°) (1214, 85.8°)	-5.37° (0 s, 144.0°) (267, 66.1°)	-6.18° (0 s, 177.0°) (197, 84.0°)	-6.41° (0 s, 1.93°) (219, 6.14°)
Parameters								
n_{max}, g	6.0	5.9	6.0	12.0	11.8	5.9	11.7	11.9
$Q_{s,tot}$, kJ/cm^2 ($Q_{s,conv}$, $Q_{s,rad}$)	14.7 (7.1, 7.6)	22.6 (14.9, 7.7)	29.4 (19.8, 9.6)	82.4 (13.6, 68.8)	65.2 (18.5, 46.7)	12.4 (7.4, 5.0)	63.6 (16.3, 47.3)	76.7 (12.9, 63.8)
$q_{s,max}$, W/cm^2 ($q_{s,conv}$, $q_{s,rad}$)	250 (50, 200)	300 (100, 200)	380 (130, 250)	1930 (150, 1780)	1400 (200, 1200)	160 (60, 100)	1100 (180, 920)	1500 (140, 1360)
p_{xrs}, km	520	1010	1500	990	1000	120	100	10
C_D	1.62	1.32	1.17	1.57	1.56	1.57	1.56	1.60
L/D	0.22	0.36	0.50[c]	0.22[c]	0.24	0.24	0.24	0.12[c]
$C_{m,cg,\alpha}$, /rad	-0.18	-0.15	-0.10	-0.20	-0.19	-0.19	-0.20	-0.27
BC, kg/m^2	130	220	350	130	100	110	100	120
$h_{b,HS}$, m	3.4	5.0	5.0	3.5	4.0	3.8	4.0	3.6
S, m^2	36.9	27.1	19.0	38.1	49.0	45.8	49.0	41.0
$\eta_{v,HS}$	38.8%	60.6%	58.5%	43.0%	41.2%	40.5%	41.3%	49.1%

[a]Axial profiles SS: spherical segment, SC: spherically-blunted cone, PL: power law
[b]m_{EV} = 7800 kg
[c]The lift-to-drag ratio has a negative value for the reported α

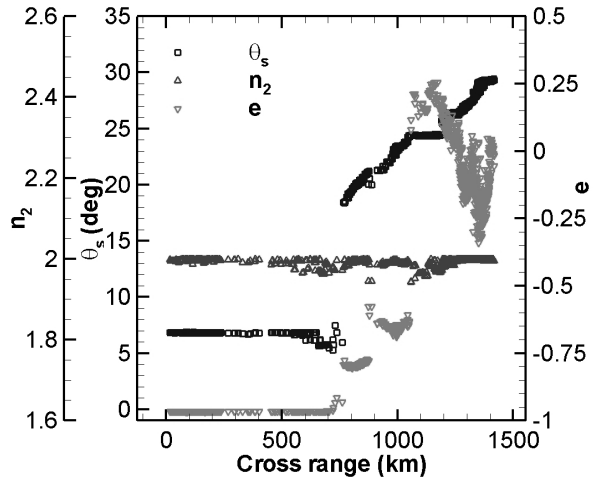

(a) Geometric variables

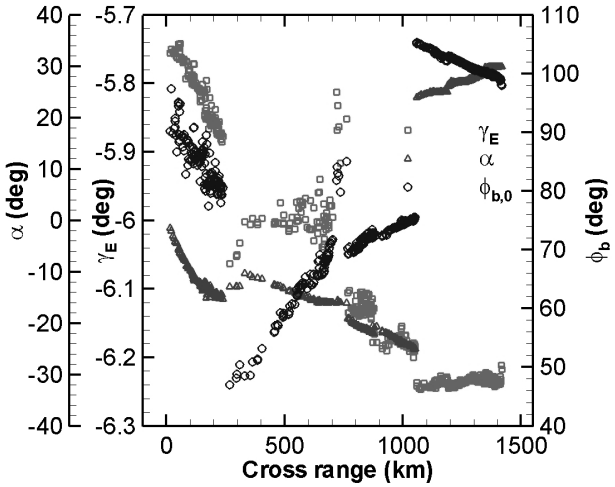

(b) Trajectory variables

Figure 10.6. Design variable distribution for spherical segment designs from Figure 10.3(a).

For $p_{xrs} \leq 700$ km, optimal designs have highly oblate $e = -0.968$, which is the lowest allowed value. With an increased heat shield radius of curvature, this design allows for less convective heat transfer. Higher e also increase the drag area, thus decreasing BC. The heat shield geometry is held constant until $p_{xrs} = 700$ km, at which point there is a strong jump in θ_s from 6.8° to 18°. In general, $|\alpha|$ is increasing throughout this portion of the Pareto frontier, indicating higher $|L/D|$ is required to produce additional cross range. At $p_{xrs} = 700$ km, $|\alpha| = 16°$, and the geometric constraint $|\alpha| \leq |\varepsilon + 1°|$ is active. A parametric analysis completed in Ref. [112]

indicates that for specific ranges of θ_s, an increase in θ_s decreases $|L/D|$ for fixed α and e, as shown in Figure 10.7.

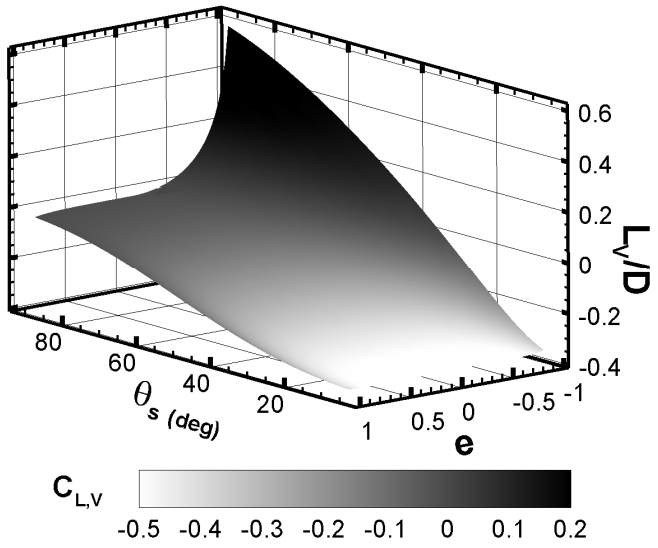

Figure 10.7. L_V/D distribution for spherical-segment: elliptical base (n_2 = 2), varying e and θ_s, α = 20°, β = 5°.

This trend applies to this case. The $|\alpha|$ is fixed at 16° until $\theta_s > 15°$, and the optimizer determines that a decrease in e along with an increase θ_s that allows for $|\alpha| > 16°$, would render a sufficient and incremental increase in $|L/D|$. The increase in θ_s to 18° limits the reduction in radius-of-curvature, thus concurrently minimizing $Q_{s,tot}$. These necessary adjustments to θ_s, e, and α produce the sudden rise in $Q_{s,tot}$ on the Pareto frontier at p_{xrs} = 700 km. Consequently, drag area is traded-off with $|L/D|$ as p_{xrs} increases. A similar explanation applies to the other axial profiles.

For $p_{xrs} \leq 250$ km, optimal solutions use direct entry trajectories. To increase p_{xrs}, the banked lift vector must turn the vehicle further. This is achieved by steepening γ_E to travel deeper in the atmosphere for a given V_∞, increasing q_∞ and thus, the lift dedicated for turning. As shown in Figure 10.6(b), $\phi_{b.0}$ is adjusted, pointing the lift vector slightly upwards, to keep the vehicle slightly higher in the

atmosphere for minimizing $Q_{s,tot}$. The change in behavior of γ_E and ϕ_b at $p_{xrs} \approx 250$ km indicates a switch from direct entry trajectories to skipping trajectories. This cross range limit for direct entry trajectories is consistent with the work of Putnam and Braun.[1] For a skipping trajectory, a steeper γ_E is utilized to dissipate sufficient energy to avoid violating trajectory constraints. Minimizing heat load restricts low $|\gamma_E|$ and trajectory duration while maximizing p_{xrs} and the deceleration limit restricts high $|\gamma_E|$. For skipping trajectories, larger p_{xrs} requires ϕ_b to approach 90^o. Since there is a smaller proportion of lift dedicated to producing the skip as ϕ_b approaches 90^o, the vehicle requires a steeper γ_E, as indicated by Figure 10.6(b).

Designs A, B, and C are optimal for p_{xrs} = 520, 1010, and 1500 km, respectively. Design A represents the spherical segment geometry applied for $p_{xrs} \leq$ 700 km. Its heat shield axial profile is provided in Figure 10.4, and its base cross section is provided in Figure 10.5(a). By utilizing design B, a 54% increase in $Q_{s,tot}$ is required to double Design A's cross range. Not only does $q_{s,max}$ affect $Q_{s,tot}$ but also does the change in individual contributions from conduction and radiation. By halving the radius-of-curvature of design B from 6.3 m, using $\theta_c = 60.4^o$, e = -0.682, r_n/d = 0.615, the $q_{s,max}$ is approximately unaffected, with $q_{s,conv}$ = 140 W/cm^2 and $q_{s,rad}$ = 160 W/cm^2. However, $Q_{s,conv}$ increases by 40% while $Q_{s,rad}$ decreases by 20%. As a result, $Q_{s,tot}$ increases by 20%. For a design similar to the Viking's spherically blunted cone, $\theta_c = 70^o$, e = -0.682, r_n/d = 0.25, $q_{s,max}$ is approximately 380 W/cm^2 and provides a 68% increase in $Q_{s,tot}$ over design B's heat shield geometry. The results in Figure 10.3 indicate that the optimal heat shield geometry for skipping trajectories at V_E = 11 km/s is the spherical segment, with non-zero eccentricity. The oblate cross

section of Design B, shown in Figure 10.5(b), illustrates the significant reduction in eccentricity that was required to increase *L/D*. By utilizing design C, $Q_{s,tot}$ is doubled to triple the p_{xrs} of Design A. Shown in Table 10.4, *BC* increases with p_{xrs}, and both $q_{s,max}$ and $Q_{s,tot}$ increase as expected.

When the peak $q_{s,conv}$ is less than the peak $q_{s,rad}$, it is possible for $Q_{s,conv} > Q_{s,rad}$. This occurs for designs B and C when minimizing $Q_{s,tot}$. Significant convective heat transfer occurs throughout the entire hypersonic trajectory while radiative heat transfer contributes significantly only at the highest velocities, for $V_\infty \geq 7600$ m/s. For designs B and C, $q_{s,rad} < 5$ W/cm^2 for $V_\infty < 7600$ m/s.

10.2.2. *Minimizing $Q_{s,tot}$ and $q_{s,max}$*

Pareto frontiers are provided in Figure 10.3(b) for $q_{s,max}$ ranging from 130 to 210 W/cm^2, producing heat loads ranging from 11.8 to 19.3 kJ/cm^2. The results for the power law form were inconclusive. The minimum $Q_{s,tot}$ decreases with increasing $q_{s,max}$. The trajectory design variable distribution for the spherically blunted cone, given in Figure 10.8, demonstrates that a shallower γ_E renders a smaller $q_{s,max}$ and larger $Q_{s,tot}$. The optimal geometric configurations are similar to those with low $Q_{s,tot}$ in Figure 10.3(a). They fly direct entry trajectories, as suggested by the shallower γ_E and higher ϕ_b than those reported in Figure 10.3(b).

Both the SS and SC geometries are relatively constant throughout the Pareto frontiers. The spherical segment geometry is $\theta_s = 6.83^o$, $n_2 = 2.00$, $e = -0.968$, $h_{b,HS} =$ 3.2 m, and the blunted cone geometry is listed in Table 10.4 as Design D. The two Pareto frontiers are within correlation error, within 35 W/cm^2 of each other.

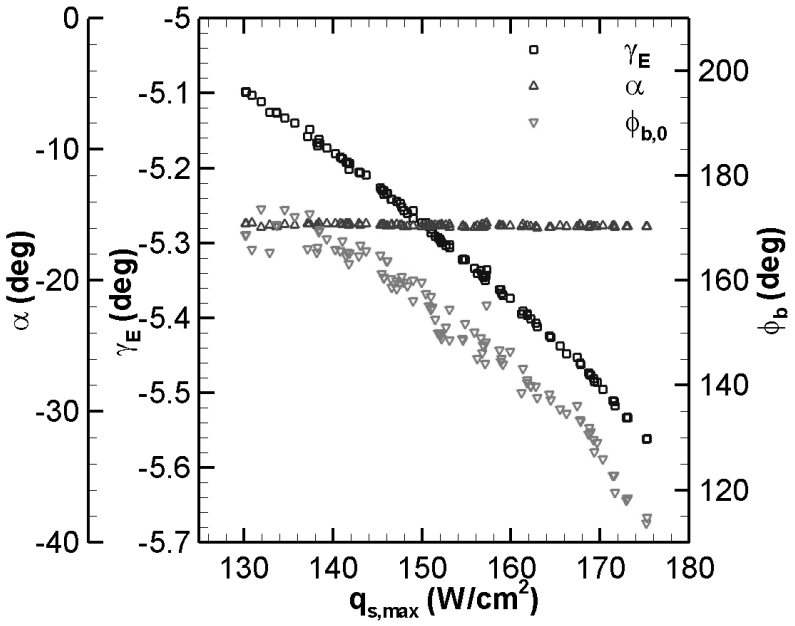

Figure 10.8. Trajectory design variable distribution for spherically blunted cone designs from Figure 10.3(b).

Both configurations are equally optimal. Comparing the two geometries at the freestream conditions of $q_{s,max}$ for design D, at h_t = 73.1 km, V_∞ = 10.5 km/s, the spherical segment would produce a different combination of heat fluxes, $q_{s,conv}$ = 40 W/cm^2 and $q_{s,rad}$ = 140 W/cm^2, but result in nearly the same $Q_{s,tot}$. The radius-of-curvature is 14.3 m for the SS and 7.5 m for SC. Rather than reducing curvature to reduce $Q_{s,conv}$, the main advantage to the highly eccentric base is the increase in drag area that reduces BC. This indirectly reduces $q_{s,max}$ and $Q_{s,tot}$ since larger drag area provides deceleration at higher altitudes for a given m_{EV}. For this range of curvatures, heat transfer is significantly interchanged between convection and radiation, rendering $Q_{s,tot}$ relatively constant for these short duration trajectories. The skipping entry of design B has a 132% increase in duration with $q_s \geq 5$ W/cm^2 over the direct entry of design D. With this and a 0.77^o steeper γ_E, radius-of-curvature becomes of greater importance.

10.3. Optimal configurations for V_E = 15 km/s

10.3.1. Minimizing $Q_{s,tot}$ and maximizing p_{xrs}

Entry at V_E = 15 km/s renders at least a factor of three increase in $Q_{s,tot}$ above that experienced at V_E = 11 km/s, caused by the conversion of 85% more kinetic energy into thermal energy during deceleration. Radiative heat transfer produces a majority of $Q_{s,tot}$ and can be minimized by decreasing the radius-of-curvature to reduce Δ_{so}, which is smaller for a SC than a SS for a given L/D_{max} design. The different thermal environment may render different optimal configurations at 15 km/s. Pareto frontiers are provided in Figure 10.9(a) for $p_{xrs} \leq 2200$ km with $Q_{s,tot}$ ranging 60 – 160 kJ/cm^2 compared to 11 – 33 kJ/cm^2 for V_E = 11 km/s. The Pareto frontier of the power law is composed of effective spherical segment forms.

The significant difference in $Q_{s,tot}$ between the SS and SC Pareto frontiers is caused primarily by differences in drag area. Spherical segment design E has a 27.8% lower drag area than blunted cone design F since the vehicle sizing routine determined that the spherical segment can maintain requirements with a smaller vehicle. This is indicated in Table 10.4 by design E having a 12.5% lower $h_{b,HS}$ than design F. Design E experiences $q_{s,max}$ at an altitude of 66.1 km, 2 km deeper than design F, and acquires a 26% larger $Q_{s,tot}$ than design F. Both designs follow similar skipping trajectories and experience $q_{s,max}$ at V_∞ = 13.5 km/s.

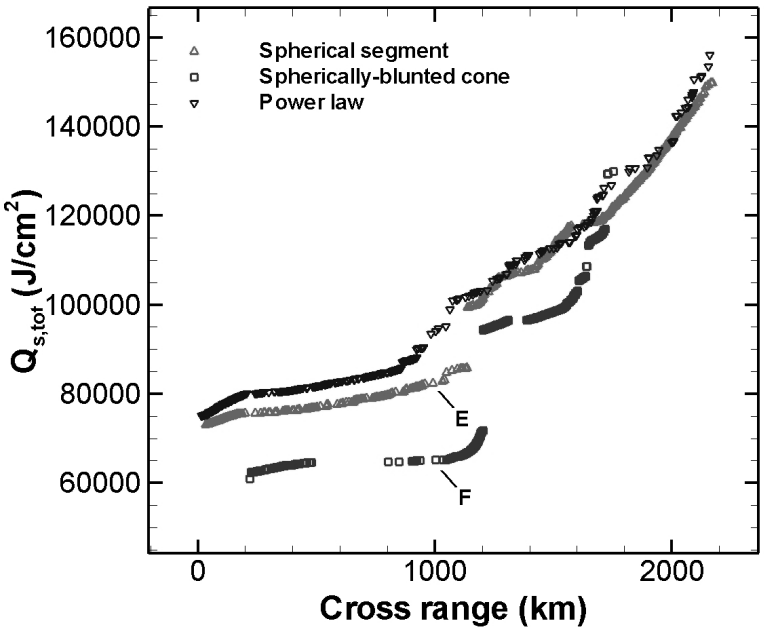

(a) Minimizing $Q_{s,tot}$ and maximizing p_{xrs}

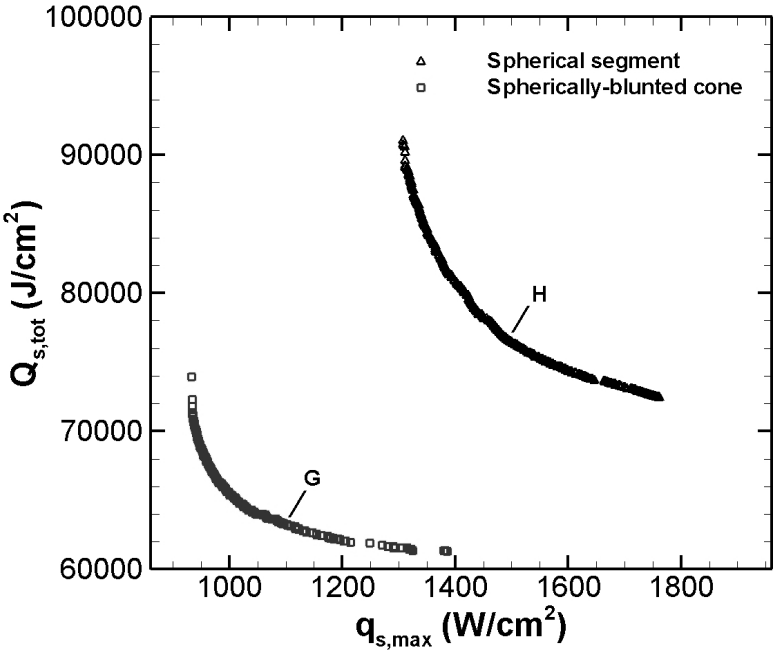

(b) Minimizing $Q_{s,tot}$ and $q_{s,max}$

Figure 10.9. Pareto frontiers for Earth entry, V_E = 15 km/s.

The trajectory of design F is provided in Figure 10.10. At 66.1 km, air density is 40% thicker. Since the normal-shock density ratio is relatively constant between the two

altitudes with the same V_∞, the Δ_{so} does not change significantly. This results in a 40% increase in E and thus, a 31% increase in $q_{s,rad}$. This demonstrates the higher sensitivity of heat transfer with altitude when traveling at hyperbolic speeds through the atmosphere.

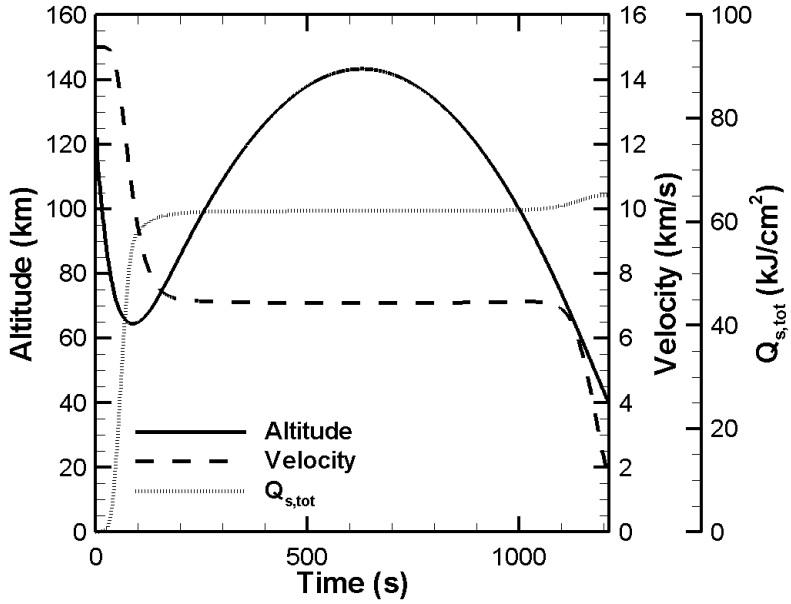

Figure 10.10. Heat shield skip trajectory of design F from Table 10.4.

A proper balance of radiative and convective heat loads is important for minimizing total heat load, but the optimal SS and SC geometries produce nearly the same minimum $Q_{s,tot}$. At the freestream conditions of design E, design F would generate $q_{s,rad}$ = 1560 W/cm^2 and $q_{s,conv}$ = 230 W/cm^2. With this 7% lower $q_{s,max}$, the resulting $Q_{s,tot}$ is still relatively the same as for design E. If design E were required to have the same $h_{b,HS}$ as design F, then Design E would have drag area similar to design F's since they have nearly the same C_D, resulting in an equivalent BC. They would then fly nearly the same trajectories. At the freestream conditions of design F and with $h_{b,HS}$ = 4.0 m, design E would generate $q_{s,rad}$ = 1460 W/cm^2 and $q_{s,conv}$ = 120 W/cm^2, producing an 8.2% larger $q_{s,max}$ than design F. The resulting $Q_{s,tot}$ would be

approximately 4% greater, suggesting that the blunted cone has a slight advantage only. At the freestream conditions of design F, a geometry similar to Viking except e = -0.968, would produce $q_{s,rad}$ = 1100 W/cm^2 and $q_{s,conv}$ = 470 W/cm^2, rendering a 32% increase in $Q_{s,tot}$. This indicates that $Q_{s,tot}$ is sensitive to different combinations of radius-of-curvature and Δ_{so}.

The design variable distributions for the blunted cone Pareto frontier are provided Figure 10.11; the trends in these distributions are consistent with those discussed for V_E = 11 km/s in Figure 10.6. Only skipping trajectories were captured for the spherically-blunted cone as its Pareto frontier begins at p_{xrs} = 200 km. The spherical segment switches from direct entry trajectories to skipping trajectories at p_{xrs} = 170 km. As cross range is increased, the sudden changes in geometry are produced to incrementally increase L/D.

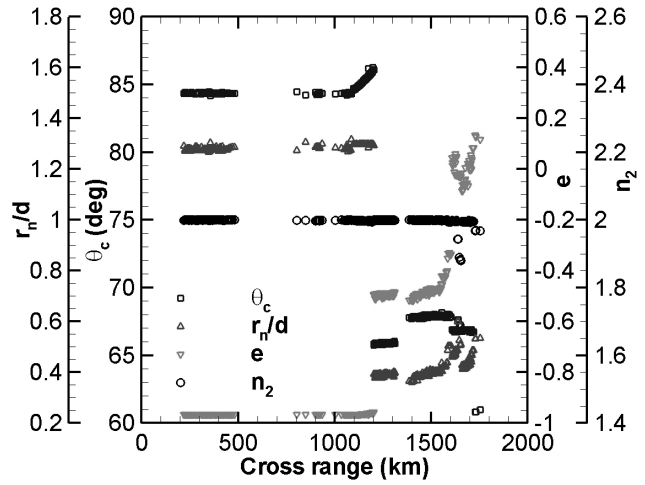

a) Geometric variables

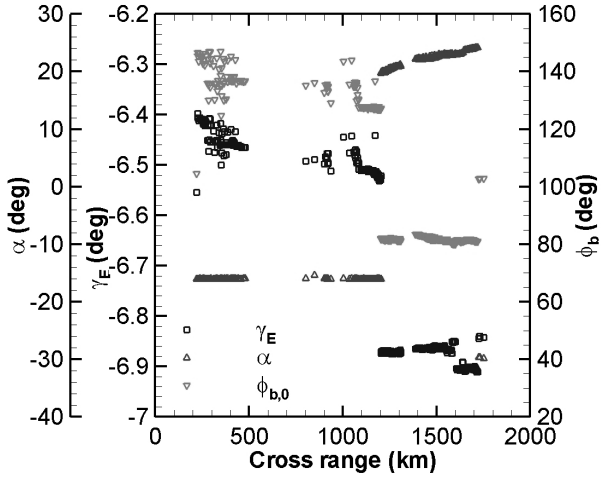

b) Trajectory variables

Figure 10.11. Design variable distribution for spherically blunted cone designs from Figure 10.9(a).

10.3.2. *Minimizing $Q_{s,tot}$ and $q_{s,max}$*

Pareto frontiers are provided in Figure 10.9(b) for the spherical segment and spherically blunted cone. The results for the power law form were inconclusive. For the two Pareto frontiers, the geometries are relatively constant, listed as designs G and H in Table 10.4. Both the spherical segment and blunted cone geometries are very similar to designs E and F respectively. Similarly, the spherical segment has a smaller $h_{b,HS}$ than the blunted cone, thus having a smaller drag area and rendering higher $Q_{s,tot}$ and $q_{s,max}$.

To isolate the effects of trajectory design and geometry, the heat fluxes for both designs are compared at each other's $q_{s,max}$ freestream conditions. Design G experiences $q_{s,max}$ at h_t = 70.4 km, V_∞ = 13.6 km/s while design H experiences $q_{s,max}$ at h_t = 68.7 km, V_∞ = 13.7 km/s. At the freestream conditions of design H, design G would generate $q_{s,rad}$ = 1180 W/cm^2 and $q_{s,conv}$ = 210 W/cm^2, a 26% increase in $q_{s,max}$; this blunted cone design produces an 8% lower $q_{s,max}$ than the spherical segment. At the freestream conditions of design G, design H would generate $q_{s,rad}$ = 1060 W/cm^2

and $q_{s,conv}$ = 130 W/cm^2, a 21% decrease in $q_{s,max}$; this spherical segment design produces an 8% higher $q_{s,max}$ than design G. As a result, the spherically blunted cone generates a lower $q_{s,max}$ for both cases. Differences in $Q_{s,tot}$ for both cases are negligible. Thus, the $q_{s,rad}$ is more sensitive than $Q_{s,tot}$ for these optimal designs. Since these geometries are similar to E and F, the importance of balancing radiative and convective heat transfer also holds.

The trajectory design variable distributions are given in Figure 10.12 for the blunted cone. For this objective function set, the aim of both α and ϕ_b is the same since p_{xrs} is not being optimized. For the blunted cone case, α is constant, and the optimizer varies ϕ_b to control how much lift is applied to counteract gravity. For the spherical segment case (not shown), $\phi_{b,0}$ is relatively constant at 0^o, and α decreases with increasing $q_{s,max}$ in order to lower the flight duration and thus, minimize $Q_{s,tot}$.

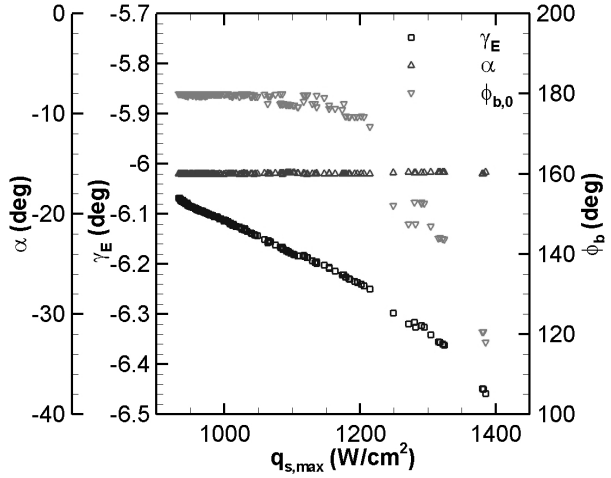

Figure 10.12. Trajectory design variable distribution for spherically blunted cone designs from Figure 10.9(b).

Chapter 11. Detailed Optimization Setup for Lunar and Mars Return

This chapter provides the detailed optimization setup for the final set of results for this work. A complete chapter is dedicated in order to detail the different optimization setup, including changes in side constraints for design variables, the choice of axial profiles, changes in trajectory and aerodynamic constraints, and the methodology for generating the entry corridors.

11.1. Mission profile modifications summary

The mission profile for lunar return mostly remains the same. To simulate Earth entry for Mars return, an initial entry velocity has been changed from 15 km/s to 12.5 km/s. a result, the expectation on TPS design to accommodate a 100+ kJ/cm^2 heat load with V_E = 15 km/s, which will greatly challenge the current capabilities of several other subsystems, may be unnecessary and impractical for the first manned Mars return missions. With the current projected mass of Orion at ~10,000 kg, the mass estimation process has been updated, along with the addition of lower and upper mass estimations that are a function of surface area and heat load. The lower mass estimation assumes that the additional heat load does not augment the mass of the heat shield. The second mass estimation provides an upper-end conservative value that assumes that the mass of the heat shield is increased by a factor of three. Details of the modifications to the mission profile for this optimization are provided in Chapter 5.

11.2. Modifications to objective functions

Three objective functions are applied in the final work: minimizing stagnation-point heat load $Q_{s,tot}$, maximizing cross range p_{xrs}, and maximizing down range p_{dwn}. The peak heat flux objective function has been replaced with down range. A greater down range enables more abort scenarios. Generating a comparison between maximizing down range and maximum cross range capabilities while minimizing heat load has been chosen to be more important than analyzing the peak heat flux for this work. The peak heat fluxes will be shown to be feasible for these entry velocities are all within the feasible bounds while depending on the cross range, down range, entry vehicle mass, and lift-to-drag, the heat load may not be feasible. Thus, heat load is more sensitive than heat flux for this analysis. Optimization is performed using two objective function sets: (1) maximizing p_{xrs} and minimizing $Q_{s,tot}$ and (2) maximizing p_{dwn} and minimizing $Q_{s,tot}$.

11.3. Design variable modifications

Several modifications have been made to the design variable set in Table 10.1 for the final set of optimization cases. First, since the spherically-blunted cone and power law optimizations generated optimal profiles similar to the spherical segment for lunar return, only the spherical segment axial profile is analyzed in the final analysis at V_E = 11 km/s. For Mars return, the Pareto frontier of the power law was composed of effective spherical segment forms. Also, the low-order method's accuracy in predicting the power law's stagnation-point heat transfer may not be sufficient for a comparison between the spherical segment and power law. For

primarily the first reason, the power law axial profile is not included in the final optimization. Since the spherically-blunted cone optimization generated different optimal profiles from the spherical segment optimization for Mars return, both the spherical segment and spherically-blunted cone axial profiles are applied in the final analysis at V_E = 12.5 km/s. The new set of design variables is listed in Table 11.1. The γ_E is no longer a design variable in order to implement the entry corridor methodology, which determines the γ_E at which the optimization is performed. Since the entry corridor is also a function of *L/D*, the optimization for each axial profile is performed at specific values of lift-to-drag: 0.3, 0.5, and 1.0. Since the results in Chapter 10 were primarily composed of $L/D < 0.4$, this methodology is also employed to facilitate in generating optimal results at higher *L/D* values.

The bank angle profile is composed differently from the initial optimization setup, in which connecting the control points (t, ϕ_b) produces the profile. A different approach has been used for the final optimization that mimics the bank angle adjustments completed for the Apollo missions. Instead of connecting the control points, the control points represent a step change in the bank angle. The bank angle

Table 11.1. Design variables with side constraints for final optimization.

L/D	V_E = 11 km/s, *L/D* specific design variables	V_E = 12.5 km/s, *L/D* specific design variables	Common design variables	
0.3, 0.5	$5.0^o \le \theta_s \le 89.0^o$ $-0.968 \le e \le 0.968$ $-30^o \le \alpha \le 30^o$	$5.0^o \le \theta_s \le 89.0^o$, *L/D* = 0.3 $20.0^o \le \theta_s \le 89.0^o$, *L/D* = 0.5 $55.0^o \le \theta_c \le 89.0^o$ $0.15 \le r_n/d \le 2.00$ $-0.968 \le e \le 0.968$ $-30^o \le \alpha \le 30^o$	$1.30 \le n_2 \le 2.00$ $5 \text{ s} \le t_1 \le 55 \text{ s}$ $t_1 + 10 \text{ s} \le t_2 \le t_1 + 55 \text{ s}$ $t_2 + 10 \text{ s} \le t_3 \le t_2 + 55 \text{ s}$ $t_3 + 10 \text{ s} \le t_4 \le t_3 + 55 \text{ s}$ $t_4 + 10 \text{ s} \le t_5 \le t_4 + 3605 \text{ s}$ $t_5 + 10 \text{ s} \le t_6 \le t_5 + 3605 \text{ s}$	$0.27 \le L/D \le 0.33$ $0.47 \le L/D \le 0.53$ $0.95 \le L/D \le 1.05$ $0^o \le \phi_{b,all} \le 180^o$ For *L/D* = 0.3 & 0.5, *all* = 0, 1, 2, … , 5, 6 For *L/D* = 1.0, *all* = 0, 1, 2, … , 10, 11
1.0	$50.0^o \le \theta_s \le 89.0^o$ $-0.968 \le e \le -0.95$ $0^o \le \alpha \le 30^o$	$50.0^o \le \theta_s \le 89.0^o$ $-0.968 \le e \le -0.95$ $0^o \le \alpha \le 30^o$		

profile is comprised of up to six step changes for L/D = 0.3 and 0.5 and up to eleven step changes for L/D = 1.0. An example of this type of bank angle profile is shown for a L/D = 0.33 trajectory in Figure 8.1(c); this bank angle profile has three step changes. The Orion CEV is currently being designed to handle bank angle adjustments through approximate step changes also. The optimizer can modify the seven bank angles $\phi_{b,0}$ through $\phi_{b,6}$, as well as the six intermediate times t_1 through t_6, at which the bank angles are stepped. A limit of 0^o to 180^o lowers the size of the design space; angles 181^o through 359^o are not necessary since longitudinal and latitudinal-related constraints are not employed. The bank angle is assumed to rotate in 5 s rather than instantaneously to render a more realistic simulation. A 5-s rotation was chosen based on the Apollo 4 rotating through 180^o in approximately 10 – 14 s and thus, serves as an approximate average of the required rotation time for the bank angles experienced during entry. A more accurate simulation would assume a nearly constant rotation rate.

11.4. Design constraint modifications

A modified set of design constraints has been applied for the final optimization setup and is provided in Table 11.2. The final trajectory duration has been reduced to 3600 s since the current upper-limit of the Orion's entry duration is approximately 2700 s (45 min). The entry corridor methodology assists in constraining the trajectory design space to the extent that it is possible to reduce the deceleration load limits. Instead of $n_{max} \leq 6\ g$ for V_E = 11 km/s and $n_{max} \leq 12\ g$ for V_E = 15 km/s, an overall peak deceleration limit of 5 g = 49.05 m/s^2 has been chosen in

Table 11.2. Trajectory and aerodynamic constraints for final optimization.

Optimization constraints	
Trajectory	Aerodynamic/Geometric
$t_f \leq 3600$ s $n_{max} \leq 5\ g$ $h_t \leq 1220$ km 10 km $\leq h_{t,f} \leq 45$ km	$M_{\infty,f} = 2$ $C_{m,cg,\alpha} \leq -0.001$ $C_{n,cg,\beta} \geq 0.001$ sign($C_{L,V}$) $C_{l,cg,\beta} \leq 0.01$ $\lvert\alpha\rvert \leq \lvert\varepsilon + 1^{o}\rvert$

order to be consistent with recent literature on manned lunar and Mars return missions.[1,62] This is lower than the 7 *g* that Apollo 10 experienced.[113,114] The maximum height of the skipping trajectory has been reduced arbitrarily from 3000 km to 1220 km to allow the entry vehicle to skip up to 10 times the height of the entry interface (122 km). The end conditions of the trajectory have been constrained to experience Mach 2 at a range of altitudes from 10 to 45 km, at which drogue parachutes would be deployed. Hypersonic aerodynamic characteristics are applied throughout the entire trajectory and thus, may be a source for uncertainty for the end of the trajectory where lower supersonic Mach numbers are experienced. This region from Mach 5 to Mach 2 does not affect the objective functions dramatically; ending the trajectory simulation at Mach 2 has been chosen in order to utilize more practical end conditions for the entry trajectory.

11.5. Lunar return operational entry corridor

Skipping trajectories, illustrated in Figure 11.1(a), are considered feasible for this work since the Apollo Command Module (CM) was capable of performing such for an off-nominal entry. Skipping also was initially selected as its nominal entry mode.[113] Previous work[110,111] by the authors would produce trajectories located on the

bounds of the feasible design space that were extremely sensitive to small deviations in bank angle. This would lead to the vehicle either bouncing out of the atmosphere or crashing into the surface, as shown in Figure 11.2. These small deviations in bank angle (less than 1-deg change) also would produce extreme *g*-loads that are not survivable. It is possible to design away from these cliffs in the trajectory design space, by locating a range of entry flight path angles, known as an entry corridor, within which the vehicle can fly to satisfy design requirements such as maximum *g*-load, maximum heat load, and landing coordinates. The entry corridor is a function of entry velocity, lift-to-drag ratio, and ballistic coefficient. For a given entry velocity, the entry corridor width will vary with m_{EV}, D/q_∞ , and L/q_∞. Note that $D/q_\infty = C_D S$, known as the drag area, and $L/q_\infty = C_L S$.

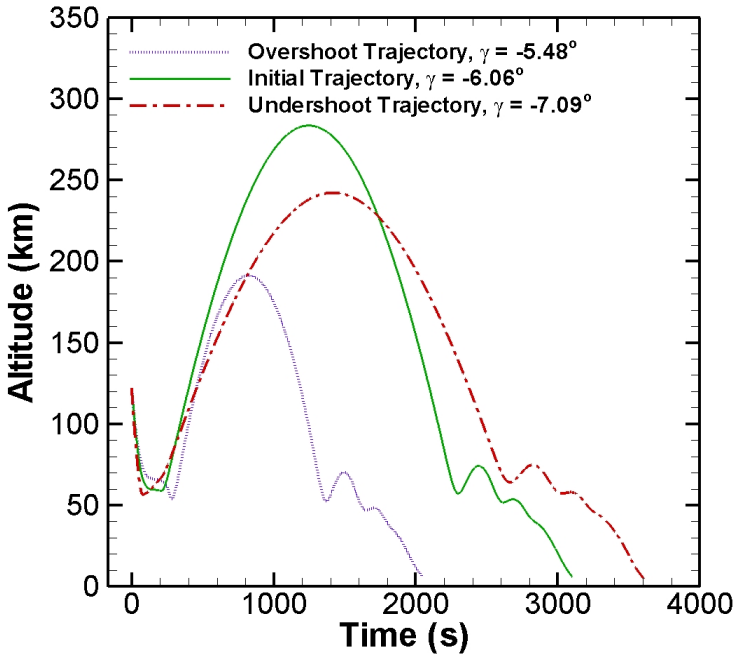

a) Altitude Profiles

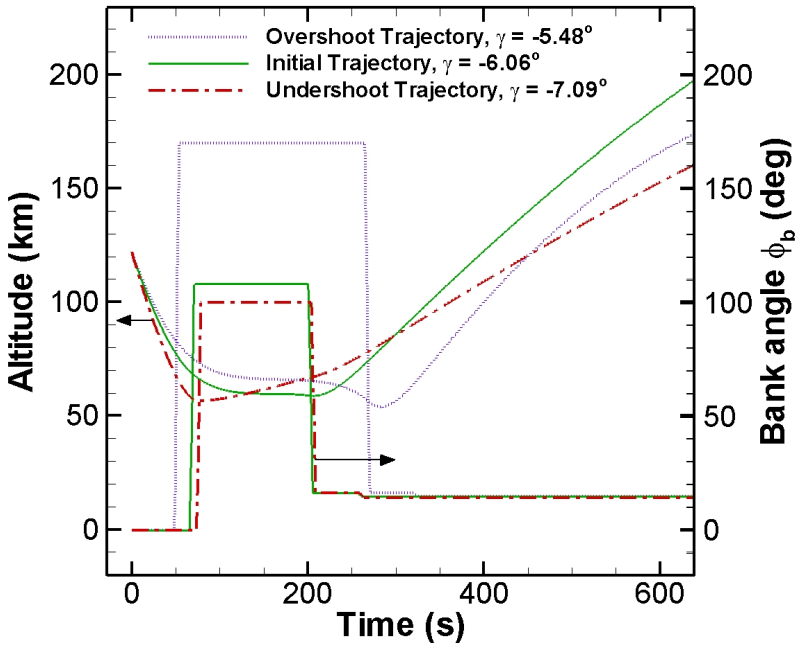

b) Bank angle Profiles

Figure 11.1. Skipping trajectories for overshoot, undershoot, and chosen initial for *L/D* = 0.6, Ref [115].

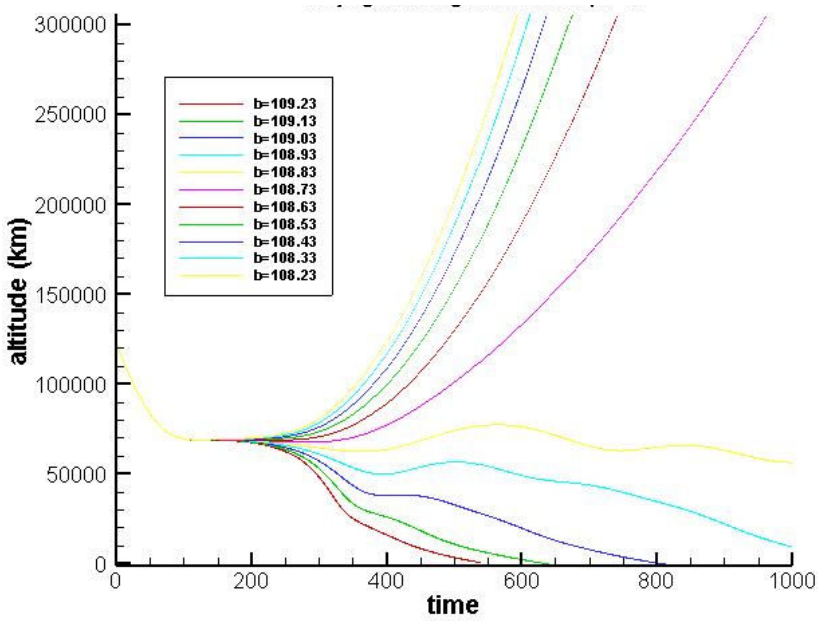

Figure 11.2. Trajectory sensitivity to $\Delta\phi_{b,2} < 1^{o}$, generated with initial optimization setup.

The operational entry corridor width defines the flyable space within the trajectory constraints of the mission, which are included in Table 11.2 for this work. It must be sufficiently large such that all possible uncertainties that may occur during

a given trajectory do not lead to a loss in vehicle control authority. These primarily consist of variations in atmospheric conditions and uncertainties related to the guidance, navigation, and control systems. Putnam and Braun[1] suggest that a corridor width of 0.4^{o} is sufficient, stating that this is much larger than the entry corridor width of 0.16^{o} for the successful Earth entries during the Stardust and Genesis missions. Manned missions may require larger corridor widths than these two missions' since there will be stricter *g*-load requirements and longer duration trajectories, giving more time for both expected and unexpected events to affect the vehicle. Uncertainties grow as entry velocity increases and *L/D* decreases, which corresponds to a reduction in control authority and thus, a smaller entry corridor width. This work assumes that an entry corridor of 0.4-deg is sufficient.

Each configuration in this work flies at a fixed-α, in which *L/D* is constant. The banking of the vehicle that is generated by the reaction control system throughout the trajectory is represented by the bank angle profile. The control inputs for the trajectory are given in a bank angle profile. For this setup, the RCS can rotate the vehicle to an initial bank angle $\phi_{b,0}$ for entry and change the bank angle six additional times, assuming a five second rotation time. Additional control authority was required for *L/D* = 1.0 case, and so the RCS can rotate the vehicle a total of twelve times instead of seven for *L/D* = 1.0 only.

Examples of overshoot, undershoot, and initial trajectories are given in Figure 11.1 for *L/D* = 0.6. In this case, the entry corridor was determined to be at least 1.61^{o}. The range of bank angle adjustments possible with the current optimization setup is exemplified in Figure 11.1(b); this also shows that small $\Delta\phi_b$ will not lead to an

immediate crash on the surface or bounce out of the atmosphere. The initial trajectory in Figure 11.1 is an example of a trajectory chosen as an design to be placed in the initial population for the optimization in order to give the optimizer a feasible design to utilize. It is located purposefully in the middle of the entry corridor at γ_E = -6.06°. The overshoot boundary is determined by executing UPTOP for a given configuration with the entire ϕ_b-profile set to 180°, reducing $|\gamma_E|$ until the vehicle bounces out of the atmosphere. The undershoot boundary is determined by utilizing UPTOP's search capabilities to locate feasible trajectories at a chosen γ_E, increasing $|\gamma_E|$ until the trajectory constraints can no longer be maintained. The entry corridors may be larger than reported since it was only necessary to find an entry corridor width of 0.4° for this analysis. Entry corridors have been determined for both lower and upper estimates of m_{EV} , described in Chapter 5. Table 11.3 provides the entry corridor widths for *L/D* = 0.3, 0.5, and 1.0, along with the corresponding heat shield configurations. All the entry corridors have a width greater than 1°. To provide a good comparison of the aerothermodynamic performance, optimization is performed at a single γ_E = -6.0° for all cases, which is close to $\gamma_E \approx$ -5.8° expected for the Orion CEV at lunar return conditions.[116] All trajectories start with a 90° initial azimuth angle of the relative velocity vector. The initial design conditions of the trajectory and characteristics of the heat shield are also included in Table 11.3. This analysis focuses optimization on base cross sections of parallelogram and elliptical forms, and blendings of the two.

Table 11.3. Operational Entry Corridors and Initial Heat Shield Designs for Optimization, V_E = 11 km/s, m_1 = 4.

	$L/D \approx 0.3$		$L/D \approx 0.5$		$L/D \approx 1.0$	
	Lower m_{EV}	Upper m_{EV}	Lower m_{EV}	Upper m_{EV}	Lower m_{EV}	Upper m_{EV}
Heat Shield Configurations	θ_s = 25.0° n_2 = 2.00 e = 0.0 α = -17.0°	θ_s = 25.0° n_2 = 2.00 e = 0.0 α = -17.0°	θ_s = 25.0° n_2 = 2.00 e = 0.0 α = -28.8°	θ_s = 25.0° n_2 = 2.00 e = 0.0 α = -28.8°	θ_s = 66.1° n_2 = 1.30 e = -0.968 α = 20.0°	θ_s = 66.1° n_2 = 1.30 e = -0.968 α = 21.5°
Entry Corridor [a]	-5.47° to -6.50°	-5.58° to -6.60°	-5.38° to –6.65°	-5.48° to –6.75°	-5.47° to –6.70°	-5.66° to -6.90°
Corridor Width [a]	1.03°	1.02°	1.27°	1.27°	1.23°	1.24°
Trajectory Design Controls γ_E (t_0, $\phi_{b,0}$) (t_1, $\phi_{b,1}$) (t_2, $\phi_{b,2}$) (t_3, $\phi_{b,3}$) (t_4, $\phi_{b,4}$) …	-6.00° (0 s, 27.2°) (28.6 s, 98.2°) (56.1 s, 84.4°) (94.7 s, 112.8°) (149.0 s, 78.0°)	-6.00° (0 s, 120.0°) (51.5 s, 97.5°) (105.1 s, 121.4°) (136.2 s, 97.9°) (179.4 s, 73.1°)	-6.00° (0 s, 60.1°) (32.8 s, 14.5°) (73.0 s, 121.2°) (125.3 s, 94.6°) (169.4 s, 75.9°)	-6.00° (0 s, 73.0°) (25.6 s, 70.0°) (54.4 s, 23.9°) (76.3 s, 140.5°) (115.0 s, 96.2°) (208.9 s, 74.6°)	-6.00° (0 s, 156.6°) (68.6 s, 98.1°) (172.1 s, 59.0°) (189.4 s, 64.1°) (292.5 s, 79.5°) (356.0 s, 148.1°) (488.9 s, 125.9°) (617.8 s, 36.3°) (634.7 s, 101.3°) (819.2 s, 89.1°) (1698.0 s, 106.0°) (2053.1 s, 72.6°)	-6.00° (0 s, 175.3°) (24.4 s, 162.9°) (93.5 s, 97.5°) (221.1 s, 81.5°) (310.2 s, 70.5°) (396.7 s, 54.8°) (576.7 s, 48.7°)
Parameters						
m_{EV}, kg	10,000	13,100	10,000	13,100	12,700	21,100
$Q_{s,tot}$, kJ/cm^2	27.1	33.1	31.3	37.2	95.5	127.0
p_{xrs}, km	200	190	440	360	1690	1090
p_{dwn}, km	2380	2410	2820	2610	18,390	3080
BC, kg/m^2	350	450	430	560	1040	1600
L/q_∞, m^2	8.7	8.7	11.3	11.3	11.9	12.5
D/q_∞, m^2	28.8	28.8	23.5	23.5	12.3	13.2
S, m^2	19.9	19.9	19.9	19.9	16.3	16.3
t_f, s	340	340	420	380	2550	600

[a] Undershoot and corridor widths may be of larger magnitude.

11.6. Mars return operational entry corridor

Developing the Mars return operational entry corridor was completed accordingly. However, once the operational entry corridor was determined to be greater than the required width of 0.4°, the search for the true undershoot boundary was ended, as determining the true undershoot boundary is not necessary for this analysis. As a result, it is likely that the entry corridors are larger than reported. Table

11.4 provides the entry corridor widths for L/D = 0.3, 0.5, and 1.0, along with the corresponding heat shield configurations. Five of the six cases have corridor widths of at least 0.65°, while the upper m_{EV}, L/D = 1.0 case has a corridor width of at least 0.51°. In comparison to the entry corridor values for lunar return, these ranges of γ_E are steeper. To provide a good comparison of the aerothermodynamic performance, optimization is performed at a single γ_E = -6.4° for all cases, which is very close to γ_E ≈ -6.5° for Project Apollo.[41] All trajectories for Mars return also start with a 90° initial azimuth angle of the relative velocity vector. The initial design conditions of the trajectory and characteristics of the vehicle are also included in Table 11.4. Figure 11.3 shows the lifting body geometry of the L/D = 1.0 design that is used to develop the entry corridor for both lunar and Mars return. From lunar return to Mars return, the $Q_{s,tot}$ increased by 100% and 124% using the lower and upper mass estimates respectively. The extremely high $Q_{s,tot}$ for both L/D = 1.0 cases indicates that these L/D = 1.0 geometries are currently impractical for Mars return with this trajectory setup. The increase in TPS mass for such high heat loads would increase the overall mass, thus increasing $Q_{s,tot}$; and this cycle would close on a vehicle mass much greater than that required for L/D = 0.3 or 0.5.

Table 11.4. Operational Entry Corridors and Initial Heat Shield Designs for Optimization, V_E = 12.5 km/s, m_1 = 4.

	$L/D \approx 0.3$		$L/D \approx 0.5$		$L/D \approx 1.0$	
	Lower m_{EV}	Upper m_{EV}	Lower m_{EV}	Upper m_{EV}	Lower m_{EV}	Upper m_{EV}
Heat Shield Configurations	$\theta_s = 25^o$ $n_2 = 2.00$ $e = 0.0$ $\alpha = -18.7^o$	$\theta_s = 25^o$ $n_2 = 2.00$ $e = 0.0$ $\alpha = -18.7^o$	$\theta_s = 25^o$ $n_2 = 2.00$ $e = 0.0$ $\alpha = -28.8^o$	$\theta_s = 25^o$ $n_2 = 2.00$ $e = 0.0$ $\alpha = -28.8^o$	$\theta_s = 66.1^o$ $n_2 = 1.30$ $e = -0.968$ $\alpha = 20.0^o$	$\theta_s = 66.1^o$ $n_2 = 1.30$ $e = -0.968$ $\alpha = 21.5^o$
Entry Corridor	-6.00° to -6.70°	-6.15° to -6.80°	-5.91° to –6.70°	-6.02° to -6.70°	-6.01° to –6.70°	-6.19° to -6.70°
Corridor Width	0.70°	0.65°	0.79°	0.68°	0.69°	0.51°
Trajectory Design Controls γ_E (t_0, $\phi_{b,0}$) (t_1, $\phi_{b,1}$) (t_2, $\phi_{b,2}$) (t_3, $\phi_{b,3}$) (t_4, $\phi_{b,4}$) …	-6.40° (0 s, 102.8°) (34.3 s, 83.4°) (73.0 s, 126.4°) (127.5 s, 110.6°) (171.5 s, 78.8°)	-6.40° (0 s, 96.8°) (29.7 s, 101.2°) (74.3 s, 131.7°) (117.7 s, 116.4°) (169.9 s, 78.8°)	-6.40° (0 s, 113.5°) (40.4 s, 81.1°) (63.8 s, 110.4°) (112.5 s, 121.3°) (143.1 s, 67.0°) (187.8 s, 32.6°) (707.6 s, 70.0°)	-6.40° (0 s, 127.3°) (16.2 s, 112.5°) (66.4 s, 108.1°) (118.8 s, 136.3°) (154.8 s, 44.8°) (2285.6 s, 67.2°)	-6.40° (0 s, 69.7°) (22.9 s, 0.0°) (60.6 s, 160.4°) (104.2 s, 102.6°) (248.2 s, 49.0°) (400.6 s, 18.9°) (521.7 s, 93.6°) (549.9 s, 50.7°) (705.8 s, 70.5°) (757.8 s, 79.6°)	-6.40° (0 s, 102.8°) (20.4 s, 0.0°) (46.5 s, 138.3°) (134.7 s, 99.8°) (256.7 s, 45.9°) (352.8 s, 143.9°) (479.7 s, 45.5°) (582.6 s, 39.8°) (697.7 s, 85.5°) (799.5 s, 2.8°)
Parameters						
m_{EV}, kg	10,000	13,100	10,000	13,100	12,700	21,100
$Q_{s,tot,}$, kJ/cm^2	64.1	80.8	74.2	93.4	191.6	284.8
p_{xrs}, km	250	260	860	280	2230	2990
p_{dwn}, km	2630	2740	18,290	20,030	5920	9230
BC, kg/m^2	350	450	430	560	1040	1600
L/q_∞, m^2	8.7	8.7	11.3	11.3	11.9	12.5
D/q_∞, m^2	28.8	28.8	23.5	23.5	12.3	13.2
S, m^2	19.9	19.9	19.9	19.9	16.3	16.3
t_f, s	350	360	2480	2910	910	1560

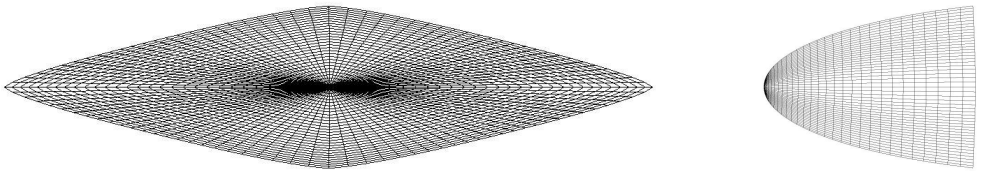

a) Front view, parallelogram cross section m_1 = 4 b) Side view, spherical segment θ_s = 66.1°

Figure 11.3. L/D = 1.0 design from Table 11.4, e = -0.968, n_2 = 1.30.

Chapter 12. Lunar Return Results

Optimization has been performed using only the spherical segment (SS) heat shield axial profiles since, as indicated in Chapter 10, it is the optimal axial profile for lunar return for this analysis. For V_E = 11 km/s and γ_E = -6.0^o, Pareto frontiers are provided for two multi-objective function sets: (1) minimizing heat load $Q_{s,tot}$ and maximizing cross range p_{xrs} in Figure 12.1, and (2) minimizing heat load $Q_{s,tot}$ and maximizing down range p_{dwn} in Figure 12.2. Results based on lower and upper mass estimates are given. The aerothermodynamic characteristics of lettered designs in Figure 12.1and Figure 12.2 are listed in Table 12.1. These lettered designs represent one point on the Pareto frontier. Both the geometric and trajectory design variables may vary along the Pareto frontier. Design variable distributions for selected Pareto frontiers are provide in Appendix B in Figure B.0.1 – Figure B.0.7. These design variable distributions provide the values of the design variables throughout the Pareto frontier.

12.1. Maximizing p_{xrs} and minimizing $Q_{s,tot}$

Figure 12.1(a) shows how cross range p_{xrs} increases with *L/D*. Designs A – D are based on lower mass estimates, and their design characteristics are listed in Table 12.1. A *L/D* = 0.3 produces a maximum $p_{xrs} \approx$ 950 km while an *L/D* of 0.5 and 1.0 produce maximum cross ranges of 1500 km and 3000 km respectively before $Q_{s,tot}$ strongly increases. Increasing mass by 30% does not strongly affect the maximum possible cross range, but it increases $Q_{s,tot}$ by at least 23%, 30.3%, and 44% for *L/D* = 0.3, 0.5, and 1.0 respectively. There is a 76% increase in $Q_{s,tot}$ from design D at *L/D* =

0.32 to design B at L/D = 0.49 for a 67% increase in p_{xrs}. There is a 380% increase in $Q_{s,tot}$ from design D at L/D = 0.32 to design A at L/D = 0.95 for a 240% increase in p_{xrs}.

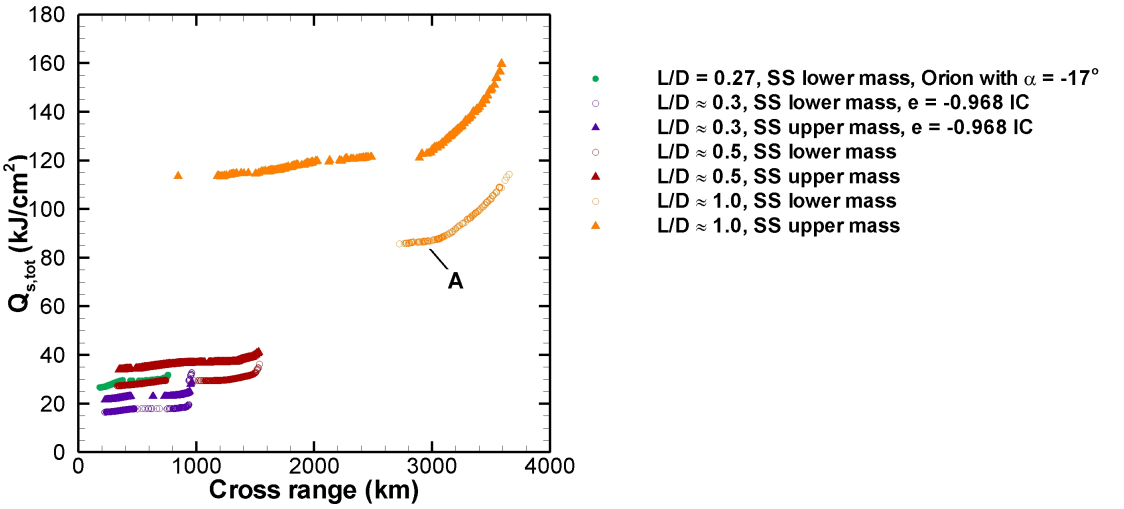

a) L/D = 0.3, 0.5, and 1.0 Pareto frontiers

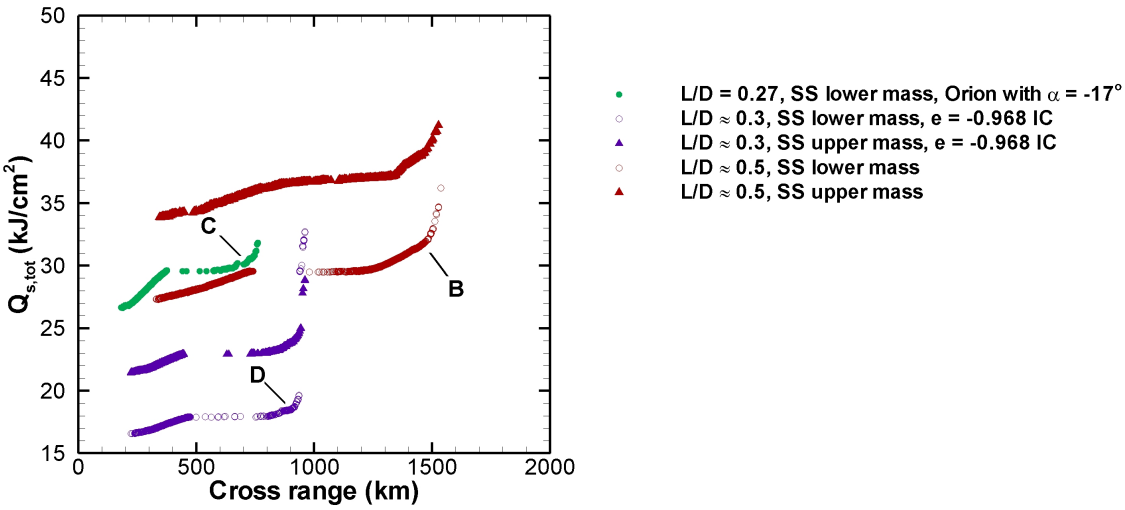

b) Close-up of L/D = 0.3 and 0.5 Pareto frontiers

Figure 12.1. Pareto frontiers for maximizing cross range and minimizing stagnation-point heat load, V_E = 11 km/s.

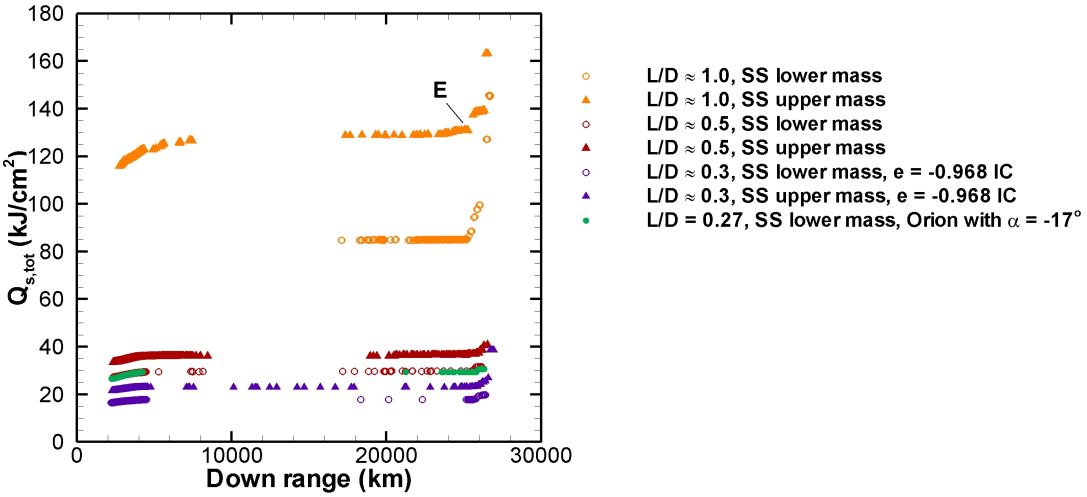

a) L/D = 0.3, 0.5, and 1.0 Pareto frontiers

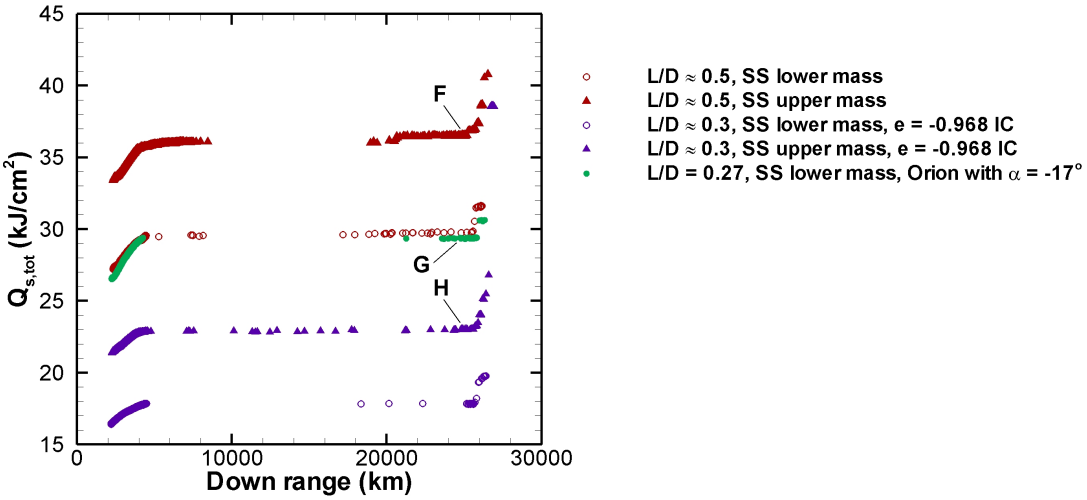

b) Close-up of L/D = 0.3 and 0.5 Pareto frontiers

Figure 12.2. Pareto frontiers for maximizing down range and minimizing stagnation-point heat load, V_E = 11 km/s.

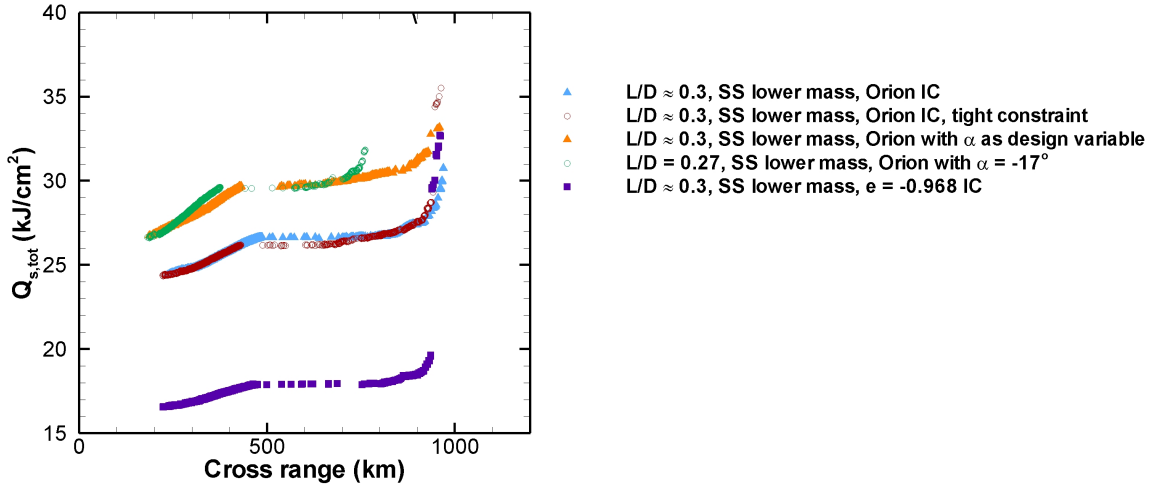

Figure 12.3. Pareto frontiers for L/D = 0.3 lower mass cases, maximizing cross range and minimizing stagnation-point heat load, V_E = 11 km/s.

Table 12.1. Optimal configurations for two multi-objective function sets for SS, V_E = 11 km/s, m_1 = 4.[a]

	Minimizing $Q_{s,tot}$ & Maximizing p_{xrs} (Fig. 9)				Minimizing $Q_{s,tot}$ & Maximizing p_{dwn} (Fig. 10)			
	Lower mass estimation				*Upper mass estimation*			
	A	B	C (Orion)	D	E	F	G (Orion)	H
Design Variables	SS θ_s = 75.7° n_2 = 1.31 e = -0.967 α = 26.3°	SS θ_s = 24.0° n_2 = 1.74 e = 0.665 α = -29.6°	SS θ_s = 25.0° n_2 = 2.00 e = 0.0 α = -17.0°	SS θ_s = 5.0° n_2 = 1.98 e = -0.968 α = -19.2°	SS θ_s = 66.0° n_2 = 1.31 e = -0.968 α = 21.1°	SS θ_s = 23.8° n_2 = 1.56 e = 0.654 α = -28.8°	SS θ_s = 25.0° n_2 = 2.00 e = 0.000 α = -17.0°	SS θ_s = 5.0° n_2 = 2.00 e = -0.964 α = -18.7°
γ_E (t_0, $\phi_{b,0}$) (t_1, $\phi_{b,1}$) (t_2, $\phi_{b,2}$) … (t_f, $\phi_{b,f}$)	-6.0° (0 s, 87.1°) (35.6, 143.4°) (67.7, 97.0°) (182.6, 36.6°) (213.4, 42.2°) (287.7, 85.6°) (332.7, 144.9°) (392.6, 155.1°) (563.0, 114.5°) (655.7, 59.7°) (1388.9, 30.4°) (1752.3, 30.4°)	-6.0° (0 s, 88.6°) (27.1, 108.4°) (67.8, 95.8°) (102.0, 91.1°) (132.3, 72.2°) (1284.6, 48.9°) (1600.3, 48.9°)	-6.0° (0 s, 44.1°) (30.1, 126.3°) (66.9, 83.2°) (89.5, 88.8°) (127.5, 52.2°) (1071.4, 65.0°) (1489.7, 65.0°)	-6.0° (0 s, 146.9°) (28.4, 59.0°) (52.0, 83.1°) (93.2, 89.4°) (120.7, 64.4°) (1582.5, 64.4°)	-6.0° (0 s, 173.8°) (44.5, 168.5°) (91.3, 96.9°) (175.1, 71.7°) (299.2, 94.0°) (414.7, 54.7°) (613.4, 118.3°) (744.5, 114.7°) (846.0, 91.7°) (958.7, 77.0°) (3479.8, 113.3°) (3483.8, 113.3°)	-6.0° (0 s, 146.7°) (38.6, 138.9°) (61.8, 108.7°) (98.1, 91.1°) (137.0, 48.8°) (1746.3, 68.2°) (3538.3, 68.2°)	-6.0° (0 s, 39.5°) (21.3, 118.3°) (73.1, 82.2°) (103.0, 104.8°) (119.3, 17.8°) (2764.9, 59.0°) (3514.5, 59.0°)	-6.0° (0 s, 153.7°) (45.0, 91.6°) (68.0, 86.2°) (98.4, 112.5°) (123.7, 6.9°) (1653.1, 59.0°) (3396.8, 58.1°) (3526.8, 58.1°)
Parameters								
$Q_{s,tot}$, kJ/cm^2 ($Q_{s,conv}$, $Q_{s,rad}$)	88.0 (69.3, 18.7)	32.6 (20.8, 11.8)	30.3 (18.9, 11.4)	18.5 (9.6, 8.9)	131.1 (92.6, 38.5)	36.9 (21.0, 15.9)	29.4 (18.0, 11.4)	23.0 (10.7, 12.3)
$q_{s,max}$, W/cm^2 ($q_{s,conv}$, $q_{s,rad}$)	700 (370, 330)	370 (120, 250)	380 (120, 260)	270 (60, 210)	1100 (450, 650)	440 (130, 310)	380 (120, 260)	330 (70, 260)
p_{xrs}, km	3060	1500	710	900	600	370	160	140
p_{dwn}, km	10,790	11,200	10,920	10,580	25,070	25280	25260	25170
C_D	1.04	1.12	1.49	1.52	0.79	1.14	1.49	1.54
L/D	0.95	0.49	0.27	0.32	0.95	0.47	0.27	0.32
BC, kg/m^2	900	450	340	250	1620	570	340	350
D/q_{∞}, m^2	16.8	22.6	29.7	42.7	13.0	23.0	29.7	41.7
m_{EV}, kg	15,100	10,100	10,000	10,500	21,100	13,200	10,000	14,500
$h_{b,HS}$, m	2.65	6.17	5.03	3.01	2.65	6.37	5.03	3.02
S, m^2	16.2	20.2	19.9	28.1	16.4	20.2	19.9	27.1
$\eta_{v,HS}$	65.3%	63.2%	58.3%	32.0%	67.5%	64.0%	58.3%	31.5%

[a]Axial profile SS: spherical segment

Design A, shown in Figure 12.4, is a more slender heat shield with θ_s = 75.7° and a rounded-edge parallelogram base cross section. It is flown at α = 26.3° to produce *L/D* = 0.95 throughout its trajectory, illustrated in Figure 12.5. The high *L/D* requires six bank angle modifications to maintain the trajectory constraints, as shown in Figure 12.5(b). The maximum deceleration limit of 5 *g* is not met but is shown to hover around 4.7 *g* for 100 s. With a trajectory duration of 1752 s, this trajectory design allows the vehicle to generate a cross range of 3000 km. Design B, shown in Figure 12.6, provides *L/D* = 0.49 at α = -29.6°. Its trajectory and bank angle profile is given in Figure 12.7. A close-up of the first 300 s of the trajectory in Figure 12.7(b) indicates that only four bank angle modifications were required to satisfy trajectory constraints, and the peak deceleration load is above 4.7 *g* for less than 40 s. The lower the *L/D* requires fewer bank angle adjustments. This trajectory produces a cross range of 1500 km.

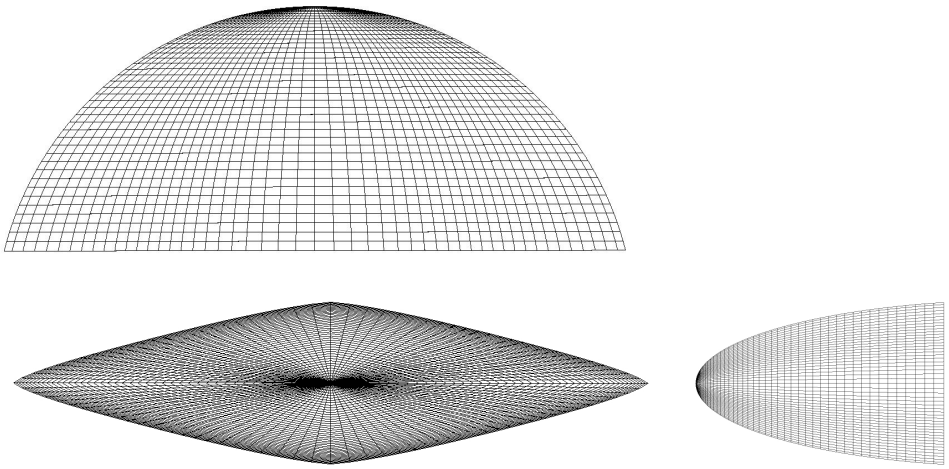

a) Front & top view, parallelogram cross section m_1 = 4 **b) Side view, spherical segment θ_s = 75.7°**

Figure 12.4. Design A from Table 12.1, *e* = -0.967, n_2 = 1.31.

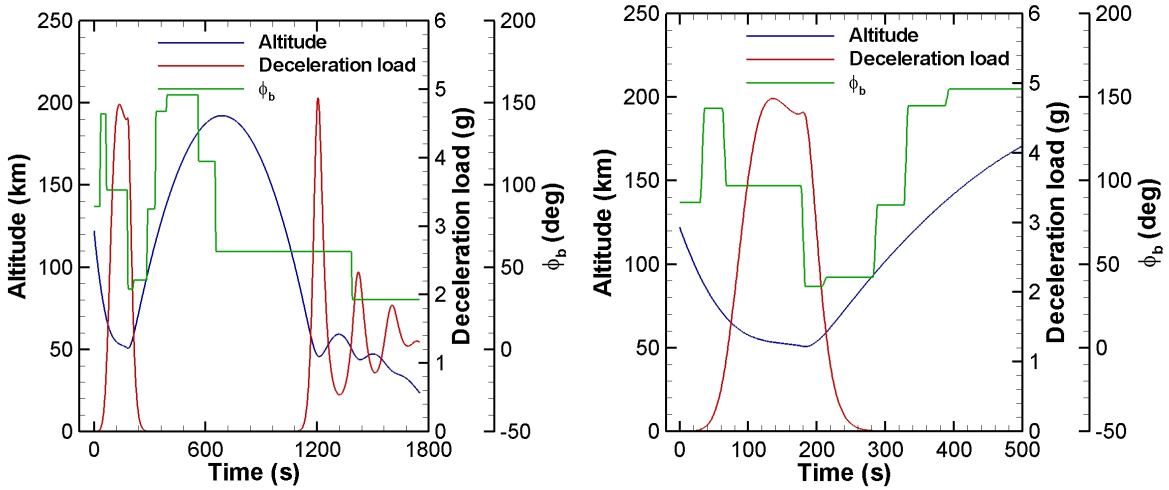

a) Trajectory profiles b) Close-up of first 500 s of trajectory

Figure 12.5. Trajectory of Design A from Table 12.1.

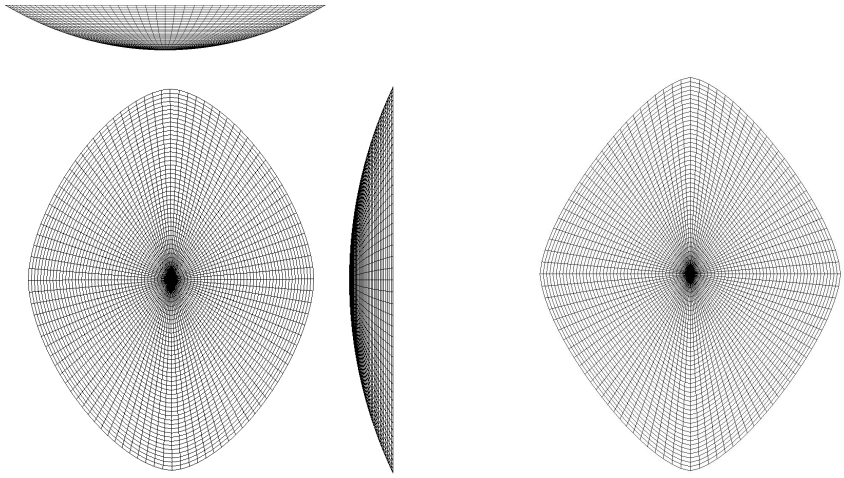

a) Design B, $n_2 = 1.74$ b) Design F base cross section, $n_2 = 1.56$

Figure 12.6. Designs B & F from Table 12.1.

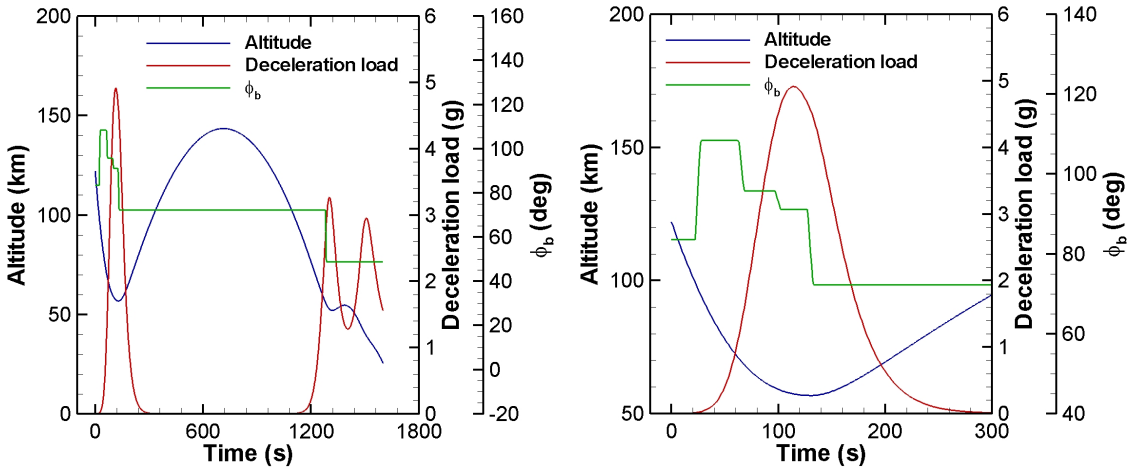

a) Trajectory profiles b) Close-up of first 300 s of trajectory

Figure 12.7. Trajectory of Design B from Table 12.1.

The Pareto frontier with design C in Figure 12.1(b) represents the projected performance of the Orion CEV with L/D = 0.27. The Orion CEV is shown in Figure 12.8. Design D dominates design C since it has both a 27% higher cross range and a 39% lower heat load. Figure 12.3 shows that the Orion CEV can produce a higher cross range when α is not assumed fixed at -17^o to produce L/D = 0.27. Several Pareto frontiers are shown for different cases and initial conditions for $L/D \approx 0.3$. The $\alpha - \varepsilon$ constraint in Table 11.2 has been relaxed to $|\alpha| \leq 1.2\ |\varepsilon + 1^o|$ in order to allow the optimizer to choose among geometries with higher eccentricity as feasible for L/D = 0.3. The L/D = 0.3, SS lower mass, Orion IC, tight constraint case in Figure 12.3 has the original $\alpha - \varepsilon$ constraint. This resulted in a ~10% reduction in $Q_{s,tot}$. The relaxed case with the Orion CEV as the initial condition (IC) is shown in case L/D = 0.3, SS lower mass, Orion IC. Since the two Pareto frontiers are almost completely coincident, this shows the optimizers inability to find more optimal geometric/trajectory designs starting from a random population with a feasible Orion CEV initial condition. Starting the optimization with a feasible geometric/trajectory design with e = -0.968 IC, the heat load of the optimal SS dropped from 27 kJ/cm^2 to 18 kJ/cm^2, 33% reduction, or a 39% reduction from design C to D. The higher e generates Design D, shown in Figure 12.9, produces a base cross section area S increase of 41% and a drag area increase of 43.7%. As a result, the vehicle decelerates higher in the atmosphere. Since the resulting ballistic coefficient is reduced by 36%, the heat load is expected to be reduced significantly. The trajectory and bank angle profile corresponding to design D is given in Figure 12.10. All the bank angle adjustments are produced before the first skip, and the maximum

deceleration load constraint is active only once. Except for the first 28 s, the lift vector for design D is pointing away from the atmosphere for almost the entire trajectory, indicating that the vehicle requires mostly positive lift to produce maximum cross range, rather than the combination as was the case for design A.

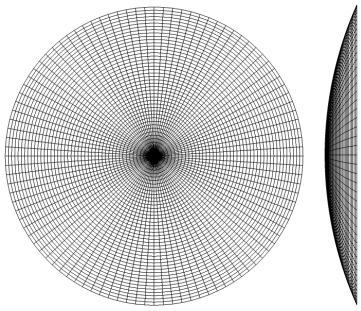

Figure 12.8. Orion CEV Heat Shield, Design C & G without rounded shoulder, $\theta_s = 25^o$, $e = 0$, $n_2 = 2$.

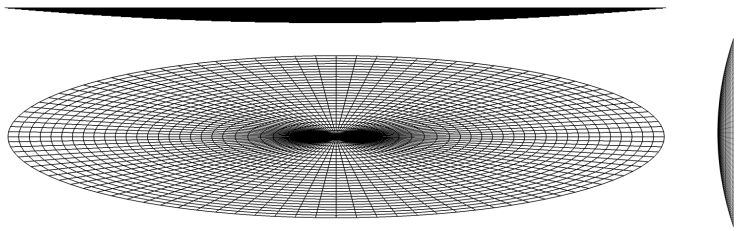

Figure 12.9. Highly oblate and blunt heat shield, approximate Designs D & H, $\theta_s = 5^o$, $e = -0.968$, $n_2 = 2$.

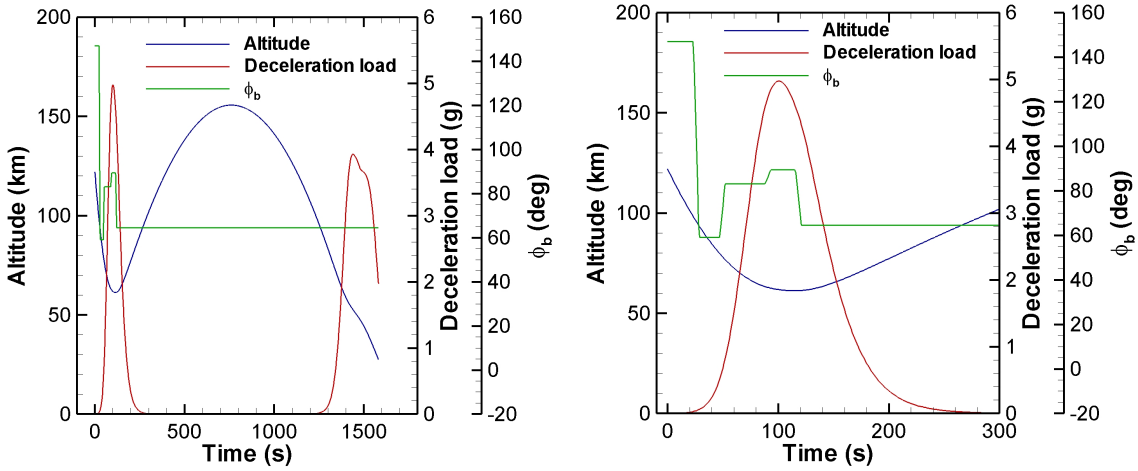

a) Trajectory profiles **b) Close-up of first 300 s of trajectory**

Figure 12.10. Trajectory of Design D from Table 12.1.

The design variable distribution for the $L/D \approx 1.0$, SS lower mass case is given in Figure B.0.1. It shows that the geometry is held constant throughout the Pareto

frontier and the required variances in duration and bank angle variables required to produce the set of cross ranges. For the $L/D \approx 0.5$, SS lower mass case, more variation is shown for the transformation parameter n_2 and eccentricity, as well as $\phi_{b,0}$, $\phi_{b,3}$, $\phi_{b,4}$, and $\phi_{b,6}$. The slight scattering of the time variables along the Pareto frontier indicates that the trajectories are not sensitive to small changes in bank angle ($< 1^o$). Similar trends can be shown in Figure B.0.3 and Figure B.0.4. A more thorough discussion is provided in Chapter 13. Figure 12.11 provides a comparison of the trajectory designs along the Pareto frontier with design D in Figure 12.1(b) at three cross ranges: 240 km, 620 km, and 900 km. The 240 km cross range trajectory is a direct entry while the other two are shown to be skipping trajectories in Figure 12.11(a). A close-up of the first 300 s of the trajectory is given in Figure 12.11(c) and shows the bank angle solutions. Though they follow similar trends, the solutions are composed of different values. The p_{xrs} and p_{dwn} profiles are given in Figure 12.11(e) and indicate that higher cross range trajectories do not necessarily require longer overall durations.

12.2. Maximizing p_{dwn} and minimizing $Q_{s,tot}$

For maximizing down range p_{dwn} and minimizing stagnation-point heat load $Q_{s,tot}$, Pareto frontiers in Figure 12.2 show the maximum $p_{dwn} \approx 26{,}000$ km and does not increase with L/D for the given set of constraints. Note that the constraint that is preventing higher down range is the time constraint. Designs E – H in Table 12.1are based on upper mass estimates. The Pareto frontiers in Figure 12.2 are primarily flat (positive slope << 1) for $4000 < p_{dwn} < 26{,}000$ km. Design E, shown in Figure 12.12, produces $p_{dwn} = 25{,}070$ km with a projected m_{EV} that is 210% greater than the Orion

CEV mass estimate of 10,000 kg, and a 56% decrease in drag area. This results in an increase in BC by a factor of 3.76 and an increase in $Q_{s,tot}$ by a factor of 3.33.

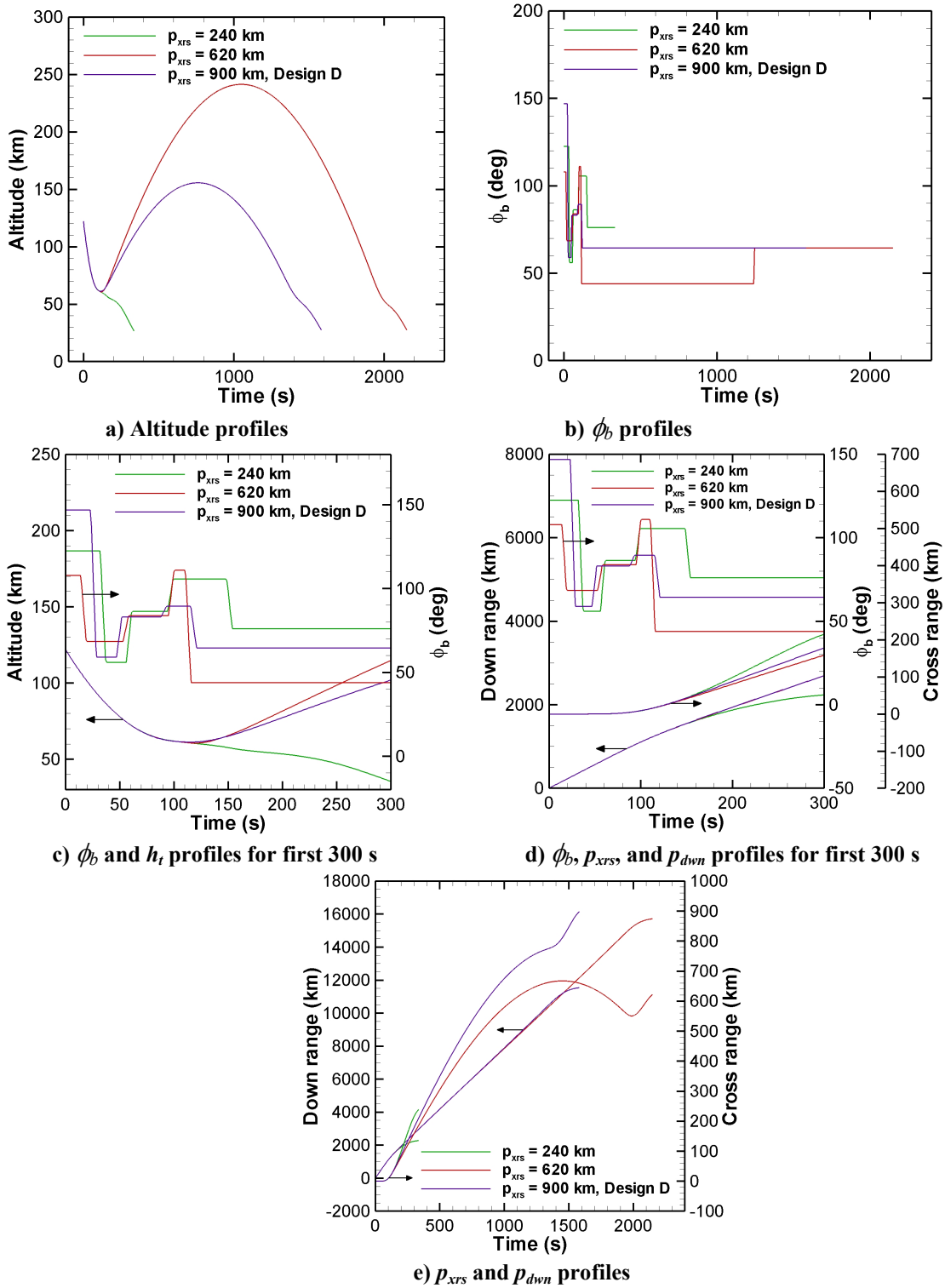

Figure 12.11. Comparisons of trajectories along Pareto frontier with Design D for lunar return, for maximizing p_{xrs} and minimizing $Q_{s,tot}$.

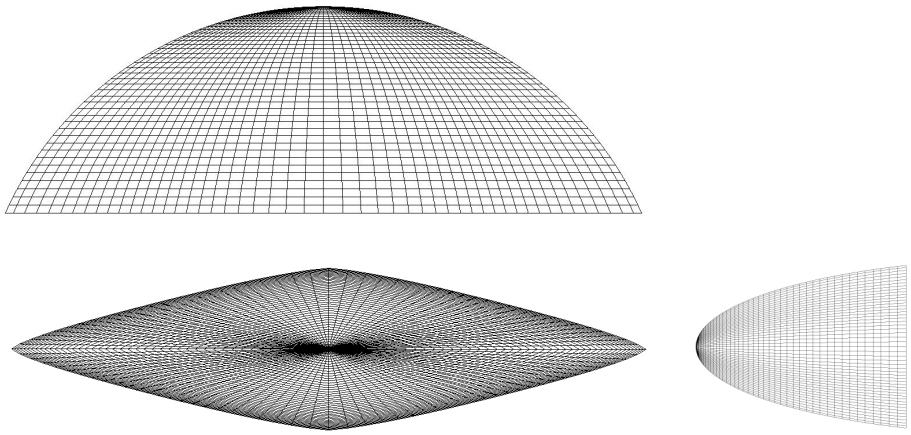

a) Front & top view, parallelogram cross section $m_1 = 4$ b) Side view, spherical segment $\theta_s = 66.0^o$

Figure 12.12. Design E from Table 12.1, $e = -0.968$, $n_2 = 1.31$.

The design variable distributions for the L/D = 1.0 SS upper mass case, given in Figure B.0.5, indicates that the geometry does not vary significantly, but that the time variables t_3 – t_9 vary significantly. The $\phi_{b,4}$ experiences the greatest variance throughout the Pareto frontier. This is the bank angle that is present during the beginning of leaving the trough in the altitude profile, which is when the skipping initiates. The amount of the lift vector pointing away from the atmosphere has a strong effect on how large a skip is generated, though it is a cumulative affect resulting from the entire set of bank angles experienced during the first part of the trajectory (~ first 300 s) rather than one bank angle.

Design F, shown in Figure 12.6, has a 10% reduction in n_2 that indicates a slightly sharper but still rounded-edge parallelogram. This slightly sharper geometry requires a slightly larger $h_{b,HS}$ in order to satisfy scaling requirements, slightly increasing the drag area by 3%. Such small increases are deemed negligible for this analysis. The primary difference in heat load and heat flux compared to design B is due to the 31% greater mass. This combination of mass and drag area requires design F to decelerate lower in the atmosphere than design B. The optimization resulted in

the geometry of design F starting with a random population along with the Orion CEV with a feasible trajectory design in order to start the optimization with at least one design that is feasible. The optimizer determined only reduced θ_s by 5%, while adding an eccentricity of 0.654 and transforming the base cross section to be a rounded edge parallelogram by means of n_2. The design variable distributions in Figure B.0.6 indicate that the geometry throughout the Pareto frontier with design F is relatively constant. As shown in Figure B.0.6(a), α relatively constant in order to keep the *L/D* around 0.50, and thus, the bank angle profile design variables are primarily varied to produce the different overall designs along the Pareto frontier.

Design G, which is located on the Pareto frontier listed as *L/D* = 0.27, SS lower mass, Orion with $\alpha = -17^o$, in Figure 12.2(b), provides a good estimate of what type of heat load would be expected with increasing the down range. The heat load increases by 13% for down ranges between 2000 and 4000 km. For $4000 \leq p_{dwn} \leq$ 26,000 km, the Pareto frontier also shows that the bank angle profile can be adjusted to keep the heat load relatively constant. Additionally, Table 12.1 indicates that the trajectory design can be modified from design C to G to keep $Q_{s,tot}$ relatively constant. Figure 12.13 shows the trajectories for designs C and G. The maximum p_{xrs} trajectory has 42% of the duration of the maximum p_{dwn} trajectory. Additionally, the Orion CEV for this study at *L/D* = 0.27, has a cross capability that is only 2.8% of its down range capability. The bank angle profiles for the first 400 s of their trajectories are given in Figure 12.13(b). The bank angles before the trough of the trajectory (the altitude profile) for both cases vary slightly, and as expected, the down range trajectory uses a lift vector pointing more away from the atmosphere with a 17.8^o bank in order to

produce a larger skip than the maximum cross range trajectory that utilized a 52.2° bank. The corresponding deceleration load profiles closely match and as shown in Figure 12.13(d). The design variables distributions for this Pareto frontier are provided in Figure B.0.7.

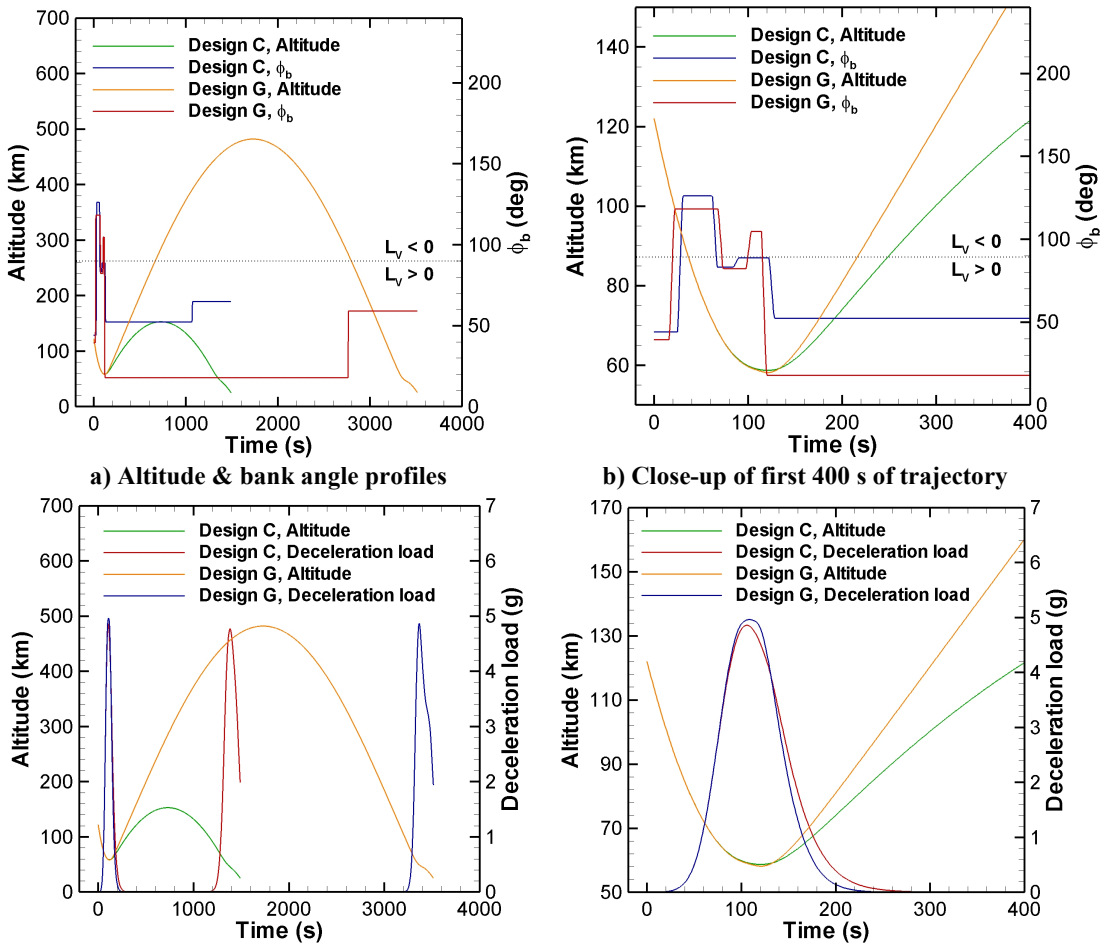

a) Altitude & bank angle profiles

b) Close-up of first 400 s of trajectory

c) Altitude & deceleration load profiles

d) Close-up of first 400 s of profiles

Figure 12.13. Comparison of optimal trajectories of Designs C & G, Orion CEV, from Table 12.1.

For the $L/D \approx 0.3$, SS upper mass with $e = -0.968$ initial condition case, design H is highlighted in Figure 12.2(b) and nearly identical to design D, shown in Figure 12.9. Design H with a L/D of 0.32 provides an example of a case that has a 10% larger m_{EV} than design F, which has $L/D = 0.47$, that is countered by the 81% increase in the drag area that produces a 39% reduction in ballistic coefficient and thus a 38%

decrease in the expected heat load. This demonstrates that, from the standpoint of maximizing down range, a lower *L/D* design could be more massive and still experience a lower heat load due to the heat shield's geometric design that provides a larger drag area. Design H is the only design that experiences a larger radiative heat load than convective heat load. The trajectory for design H is provided in Figure 12.14. The design variable distributions for the Pareto frontier with design H are provided in Figure B.0.8. The minimum down range capability for *L/D* = 0.3 is approximately 2000 km and corresponds to the minimum values reported by Ref. [1]. With an increase in down range to 2700 km, the $\phi_{b,4}$ decreases from 80° to values between 20° and 0°. Figure 12.15 provides trajectories along the Pareto frontier for p_{dwn} = 2280, 10120, and 25170 km. The bank angle profile generates an overall cross range of 140 km for the p_{dwn} = 25,170 km case, and is shown in Figure 12.15(e) to increase to 440 km and decreases to zero, increases, and decreases to 140 km. On this scale, the down range for all three cases increases at similar rates.

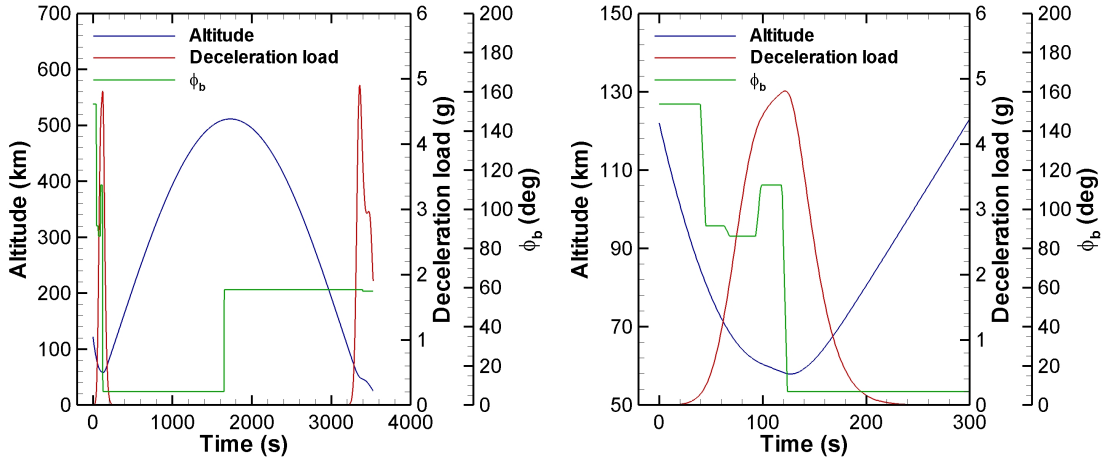

a) Trajectory profiles **b) Close-up of first 300 s of trajectory**

Figure 12.14. Trajectory of Design H from Table 12.1.

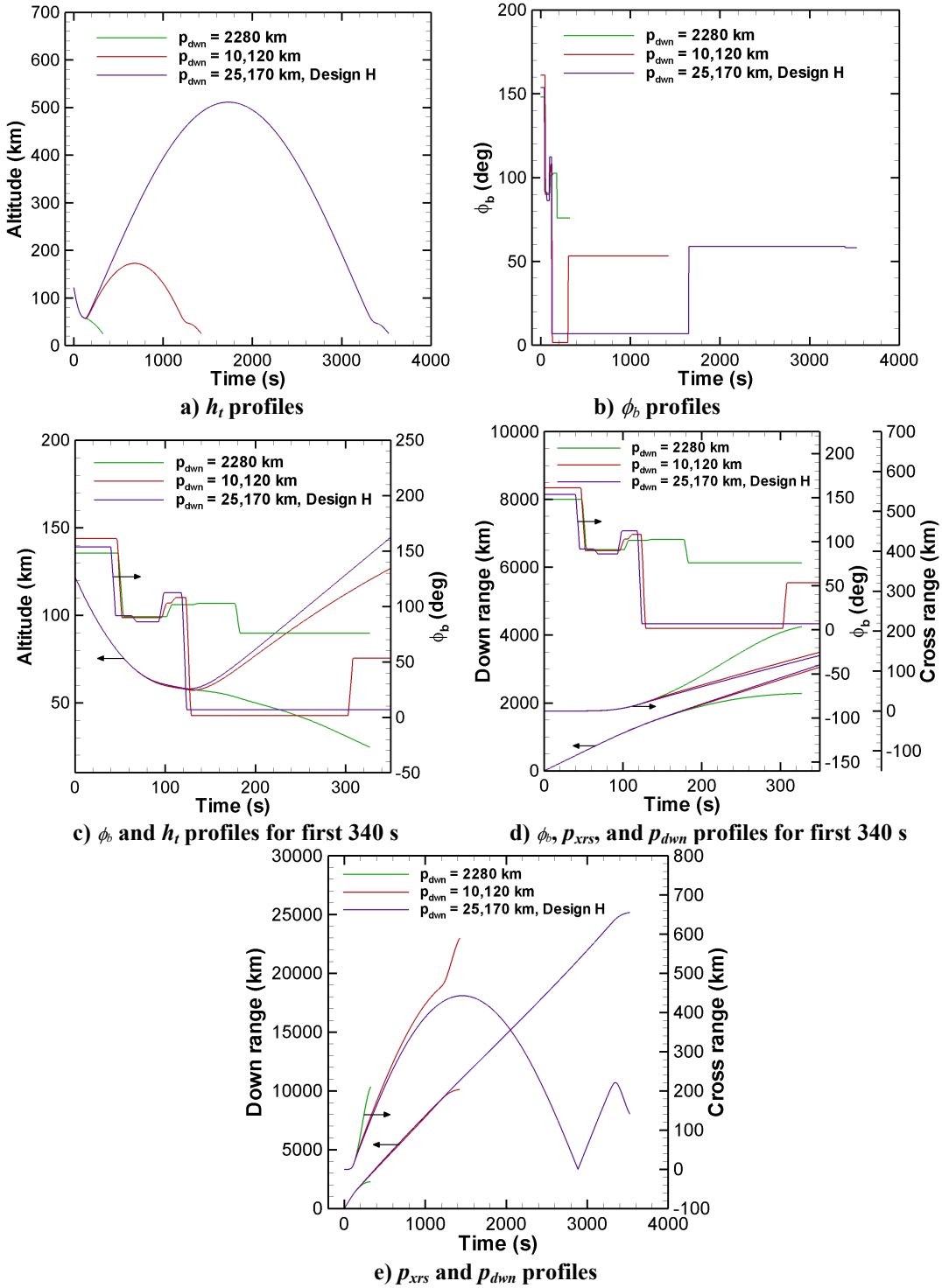

Figure 12.15. Comparisons of trajectories along Pareto frontier with Design H for lunar return, for maximizing p_{dwn} and minimizing $Q_{s,tot}$.

The altitude profiles for the listed designs in Table 12.1are provided in Figure 12.16. Almost all of the maximum p_{dwn} trajectories nearly meet the 3600 s duration

limit while all the maximum p_{xrs} trajectories have durations below 1800 s. Close-ups of the first trough of the trajectory are provided in Figure 12.16(b) and (c). Design E travels the deepest in the atmosphere with $h_t \approx 48$ km, as expected since it has the largest ballistic coefficient at 1620 kg/m^2. Design D decelerates the highest in the atmosphere with the smallest ballistic coefficient at 250 kg/m^2, 26.5% lower BC than the Orion CEV.

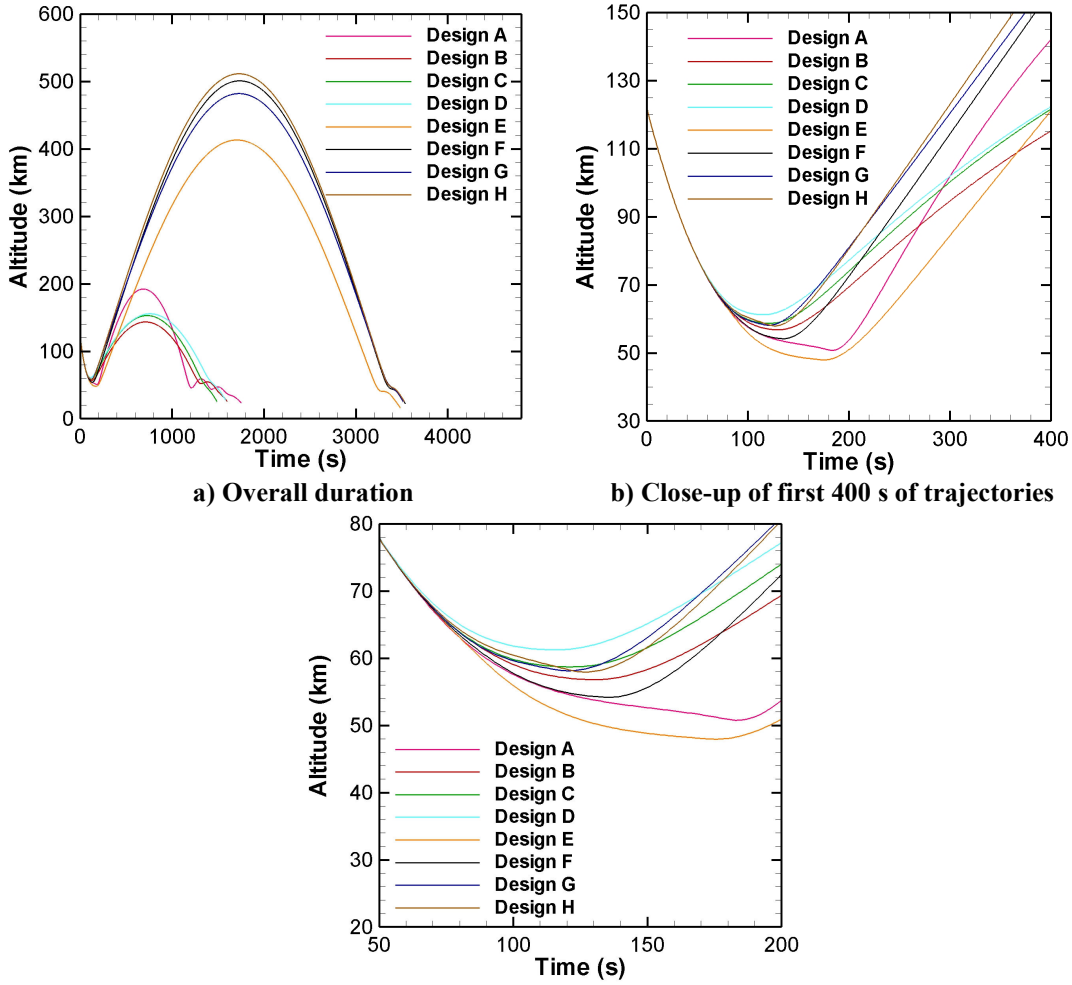

a) Overall duration

b) Close-up of first 400 s of trajectories

c) Close-up of 50 < t < 200 s

Figure 12.16. Altitude profile comparison of trajectories of Designs A – H from Table 12.1.

Chapter 13. Mars Return Results

Optimization has been performed using two types of heat shield axial profiles: the spherical-segment (SS) and the spherically-blunted cone (SC). For V_E = 12.5 km/s and γ_E = -6.4°, Pareto frontiers are provided for two multi-objective function sets: (1) minimizing heat load $Q_{s,tot}$ and maximizing cross range p_{xrs} in Figure 13.1, and (2) minimizing heat load $Q_{s,tot}$ and maximizing down range p_{dwn} in Figure 13.2. Results based on lower and upper mass estimates are given. The aerothermodynamic characteristics of lettered designs in Figure 13.1and Figure 13.2 are listed in Table 13.1. These lettered designs represent one point on the Pareto frontier. Both the geometric and trajectory design variables may vary along the Pareto frontier. Design variable distributions for selected Pareto frontiers are provide in Appendix C in Figure C.0.1– Figure C.0.9. These design variable distributions provide the values of the design variables throughout the Pareto frontier.

13.1. Maximizing p_{xrs} and minimizing $Q_{s,tot}$

The maximum cross range p_{xrs} is shown in Figure 13.1 to increase with *L/D* as expected. Designs A – D are based on lower mass estimates, and their design characteristics are listed in Table 13.1. A *L/D* = 0.3 produces a maximum p_{xrs} = 1100 km, and a *L/D* = 0.5 produces a maximum p_{xrs} = 1600 km before $Q_{s,tot}$ strongly increases. While increasing mass by 30% from 10,000 kg does not affect the maximum possible cross range, it increases $Q_{s,tot}$ by ~24% for both *L/D* = 0.3 and 0.5, spherical segment cases. Projected performance of the Orion CEV indicates a 150 km increase in p_{xrs} capability with the optimal spherical segment case, with a slight

decrease in heat load, but for this low-order heat transfer analysis, the differences between their $Q_{s,tot}$ values are negligible. Increases in p_{xrs} capability are produced by applying slightly eccentric geometries with slightly higher $h_{b,HS}$ to produce a slightly lower *BC*. Design B, shown in Figure 13.3, provides the Orion geometry with p_{xrs} = 910 km and is compared to optimal SS design C in Table 13.1.

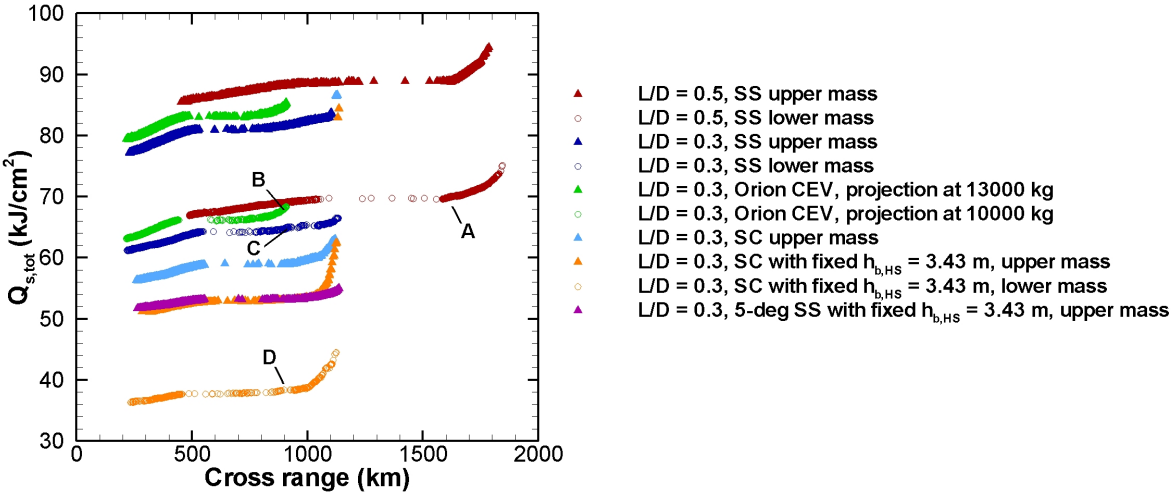

Figure 13.1. Pareto frontiers for maximizing cross range and minimizing stagnation-point heat load, V_E = 12.5 km/s.

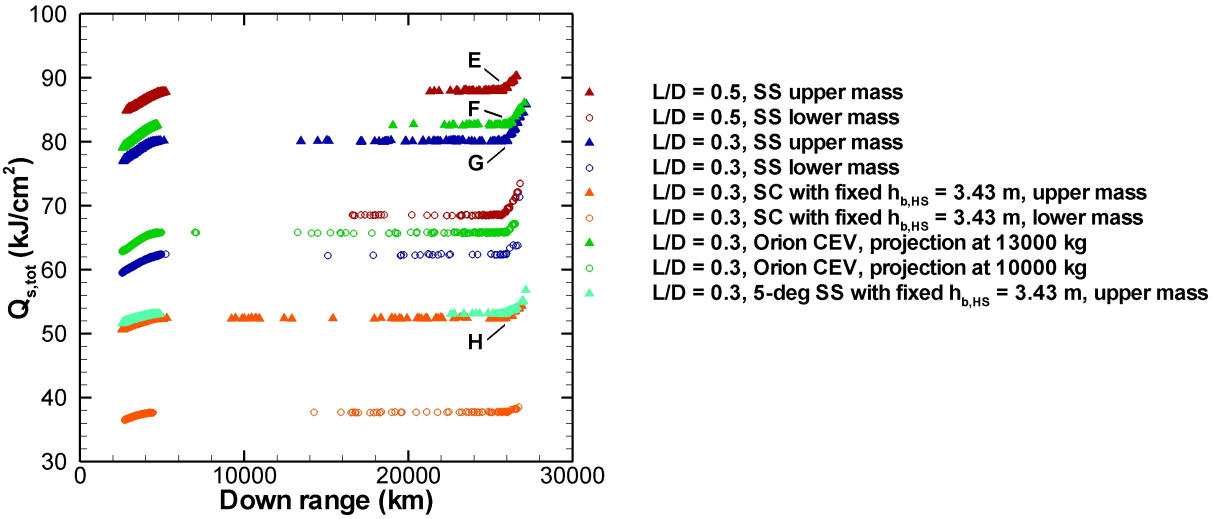

Figure 13.2. Pareto frontiers for maximizing down range and minimizing stagnation-point heat load, V_E = 12.5 km/s.

Table 13.1. Optimal configurations for two multi-objective function sets, V_E = 12.5 km/s, m_1 = 4.[a]

	Minimizing $Q_{s,tot}$ & Maximizing p_{xrs} (Fig. 9)				Minimizing $Q_{s,tot}$ & Maximizing p_{dwn} (Fig. 10)			
	Lower mass estimation				*Upper mass estimation*			
	A	B (Orion)	C	D	E	F (Orion)	G	H
Design Variables	SS θ_s = 23.7° n_2 = 1.66 e = 0.621 α = -28.5°	SS θ_s = 25.0° n_2 = 2.00 e = 0.0 α = -17.0°	SS θ_s = 23.1° n_2 = 1.82 e = -0.341 α = -18.2°	SC θ_c = 88.4° r_n/d =3.95 n_2 = 2.00 e = -0.968 α = -17.7°	SS θ_s = 23.7° n_2 = 1.73 e = 0.537 α = -28.3°	SS θ_s = 25.0° n_2 = 2.00 e = 0.0 α = -17.0°	SS θ_s = 22.5° n_2 = 1.59 e = 0.408 α = -17.4°	SC θ_c = 87.8° r_n/d =3.96 n_2 = 2.00 e = -0.968 α = -17.0°
γ_E (t_0, $\phi_{b,0}$) (t_1, $\phi_{b,1}$) (t_2, $\phi_{b,2}$) … (t_f, $\phi_{b,f}$)	-6.4° (0 s, 110.0°) (46.8, 81.7°) (67.2, 113.8°) (145.1, 66.7°) (752.9, 73.9°) (1525, 73.9°)	-6.4° (0 s, 72.9°) (51.8, 97.0°) (78.2, 124.1°) (127.7, 92.9°) (165.2, 68.0°) (1520, 68.0°)	-6.4° (0 s, 79.9°) (34.4, 85.2°) (73.9, 125.8°) (97.4, 121.7°) (143.6, 48.8°) (1192.3, 65.0°) (1557, 65.0°)	-6.4° (0 s, 48.6°) (32.0, 50.0°) (71.5, 135.8°) (108.9, 109.3°) (135.8, 47.6°) (1557.5, 63.4°) (1788, 63.4°)	-6.4° (0 s, 52.4°) (19.3, 113.7°) (52.1, 108.9°) (102.7, 124.8°) (144.6, 67.8°) (3529.1, 44.4°) (3596.3, 44.4°)	-6.4° (0 s, 177.5°) (40.5, 98.0°) (75.5, 140.2°) (106.3, 121.9°) (144.7, 1.0°) (2832.6, 57.8°) (3589.6, 57.8°)	-6.4° (0 s, 118.0°) (32.6, 103.1°) (76.8, 136.2°) (121.0, 107.4°) (153.0, 153.0°) (823.7, 46.8°) (2719.3, 59.7°) (3597.6, 59.7°)	-6.4° (0 s, 31.8°) (36.5, 80.5°) (79.9, 132.4°) (128.0, 100.8°) (148.5, 11.4°) (1034.7, 96.9°) (1455.5, 63.7°) (3598.0, 63.7°)
Parameters								
$Q_{s,tot,}$, kJ/cm^2 ($Q_{s,conv}$, $Q_{s,rad}$)	69.8 (25.3, 44.5)	68.2 (26.4, 41.8)	64.9 (23.3, 41.6)	38.3 (12.2, 26.1)	89.2 (30.4, 58.8)	82.6 (27.9, 54.7)	81.2 (25.8, 55.4)	52.8 (14.8, 38.1)
$q_{s,max}$, W/cm^2 ($q_{s,conv}$, $q_{s,rad}$)	950 (160, 790)	980 (170, 810)	940 (160, 780)	640 (90, 550)	1200 (180, 1020)	1160 (190, 970)	1140 (160, 980)	860 (110, 750)
p_{xrs}, km	1600	910	900	890	640	210	300	320
p_{dwn}, km	11320	11440	11580	13200	26,150	25,960	26,130	26,080
C_D	1.16	1.49	1.47	1.60	1.17	1.49	1.47	1.61
L/D	0.47	0.27	0.29	0.31	0.47	0.27	0.28	0.30
BC, kg/m^2	430	340	340	190	560	440	450	280
$D/q_{\infty,}$, m^2	23.4	29.7	29.5	58.7	23.6	29.7	29.0	59.1
m_{EV}, kg	10,100	10,000	10,000	11,200	13,200	13,100	13,000	16,580
$h_{b,HS}$, m	6.14	5.03	5.41	3.43	5.83	5.03	5.69	3.43
S, m^2	20.2	19.9	20.1	36.7	20.2	19.9	19.7	36.7
$\eta_{v,HS}$	62.7%	58.3%	57.6%	18.6%	61.0%	58.3%	58.7%	22.4%

[a]Axial profiles SS: spherical segment, SC: spherically-blunted cone

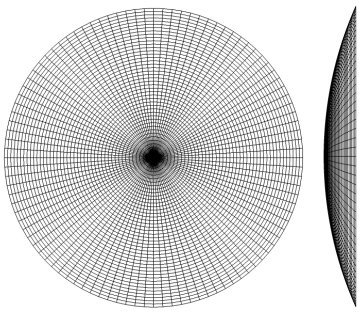

Figure 13.3. Orion CEV, Design B & F without rounded shoulder, θ_s = 25°, e = 0, n_2 = 2.

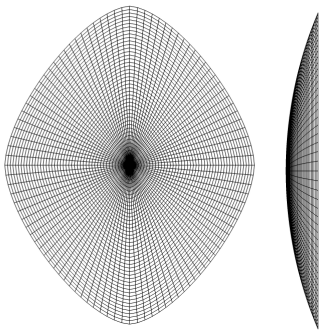

Figure 13.4. Design A, θ_s = 23.7°, e = 0.621, n_2 = 1.66.

For L/D = 0.5, strictly following the $\alpha - \varepsilon$ constraint in Table 11.2 limits the feasible design space to slender blunt bodies similar to Figure 11.3. For this analysis, the L/D = 0.5 cases are run with a relaxed $\alpha - \varepsilon$ constraint: $|\alpha| \leq 1.2\ |\varepsilon + 1^o|$ to allow the optimizer to choose among geometries similar to the Apollo CM or Orion CEV ($\theta_s = 25^o$) flying at higher α. This is a practical constraint since both the Apollo CM and Orion CEV are designed with aft-body cone angles of ~32.5^o, in which flying $|\alpha|$ a few degrees greater than 25^o would still allow the heat shield to be the primary surface determining the hypersonic aerodynamics. Results indicate that with both types of geometries to choose from, a geometry similar in bluntness to the Orion CEV would be more ideal than a slender body. Design A shown in Figure 13.4, consists of a slightly prolate base, a slightly parallelogram base cross section, and a θ_s near Orion's. The main drawback to the slender body geometry is its higher BC, exemplified by the design in Figure 11.3, due to (1) the increased heat shield surface area and mass, and (2) its slenderness that reduces its drag area. Additionally, running the spherically-blunted cone case rendered disguised spherical-segment geometries. Flying these blunter heat shields with α slightly greater than ε allows L/D = 0.5 to be conceivable, though a thorough analysis of the required center-of-gravity to trim at the required α would need to be conducted with a packaged system analysis. As a result, the spherically blunted cone does not produce significantly better results at L/D = 0.5. The trajectory for Design A is given in Figure 13.5.

Optimization of the spherically-blunted cone at L/D = 0.3 was performed with the same relaxed $\alpha - \varepsilon$ constraint, and produced highly oblate elliptical heat shield configurations similar to Figure 13.6(a). With the relaxed constraint, the oblate heat

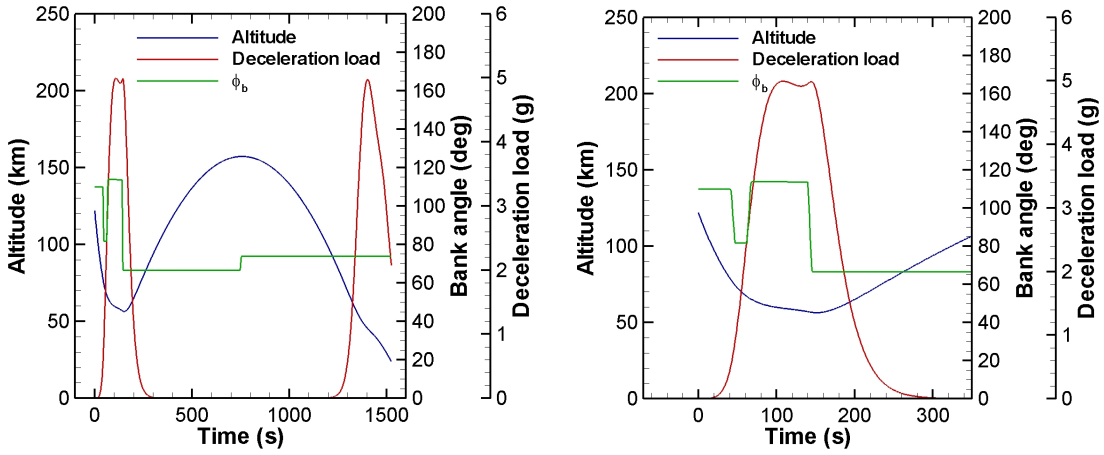

a) Trajectory profiles **b) Close-up of first 340 s of trajectory**

Figure 13.5. Trajectory of design A from Table 13.1.

shields with maximum eccentricity corresponding to $j/k = 4.0$ could be placed at the necessary α to produce $L/D = 0.3$, i.e, design D requires $\alpha = -17.7^{o}$. The scaled down heat shield with $h_{b,HS} = 3.43$ m has nearly $2S$ of Orion with nearly the same perimeter. As a result, the drag area is nearly doubled, allowing the vehicle to decelerate higher in the atmosphere, reducing both $q_{s,max}$ and $Q_{s,tot}$. The SC upper mass Pareto frontier in Figure 13.1 indicates a 20% reduction in $Q_{s,tot}$ from the SS upper mass case. For the applied vehicle scaling method, the optimizer determined that $h_{b,HS} = 3.43$ m is optimal for a base eccentricity of –0.968, and thus, SC optimization was performed for upper and lower mass estimations with fixed $h_{b,HS}$ with results shown in Figure 13.1. An increase of the upper side constraint from $r_n/d \leq 2$ to 4 produced the 6 kJ/cm^2 decrease in heat load from the SC upper mass case.

Design D with the lower mass estimate represents the optimal blunted cone heat shield at $p_{xrs} = 890$ km. Although Design D, displayed in Figure 13.6(a) and (b), has $r_n/d = 4$, it is still a spherically blunted cone due to its high eccentricity. For this case, $d = h_{b,HS}$. The trajectory of design D is shown with its bank angle and

deceleration load profiles in Figure 13.7. The effects of r_n/d on $Q_{s,conv}$ and $Q_{s,rad}$ generated along design D's trajectory are provided in Figure 13.8.

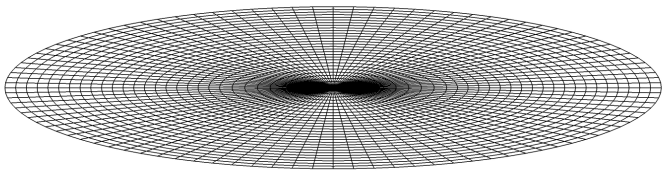

a) Front view, $n_2 = 2.0$

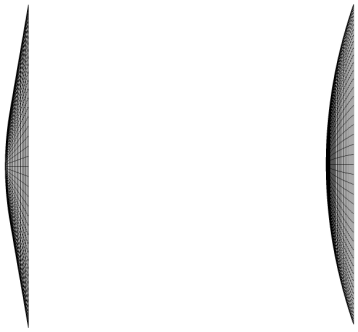

b) Side view, Design D **c) SS with similar performance to design D, $\theta_s = 5^o$**

Figure 13.6. Highly oblate heat shield designs, e = -0.968.

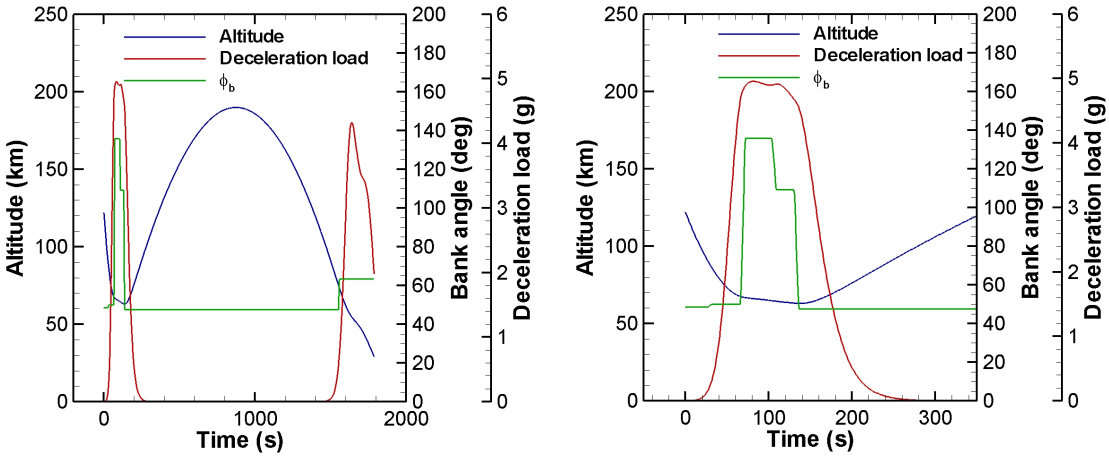

a) Trajectory profiles **b) Close-up of first 340 s of trajectory**

Figure 13.7. Trajectory of design D from Table 13.1.

While $Q_{s,rad}$ slowly increases with r_n/d, $Q_{s,cond}$ strongly decreases, and $Q_{s,tot}$ levels off at $r_n/d \approx 4.0$ for this trajectory. Thus, a spherical segment with an elliptical base and $\theta_s = 5^o$, shown in Figure 13.6(c), produces nearly optimal results in Figure 13.1. Using a spherical segment geometry may alleviate any static longitudinal instabilities produced by sonic line movement on some blunted cone designs. Design D's 97%

increase in drag area over Orion's reduces $Q_{s,tot}$ to 38 kJ/cm^2, which is near Apollo 4's maximum heating listed in Table 7.4. While e = -0.968 for a heat shield may not be presently realistic for first manned Mars return missions, this result indicates the eccentricity of the heat shield for a given mission profile has a strong effect on $Q_{s,tot}$. Eccentricity increases the surface area, and thus, indirectly increases drag area at a higher rate than increasing the heat shield mass, thus reducing BC. Conclusions have not being made concerning whether adding e or increasing the d of a circular base cross section is a better means to increase drag area. Similar effects would be expected by increasing d to produce a larger drag area.

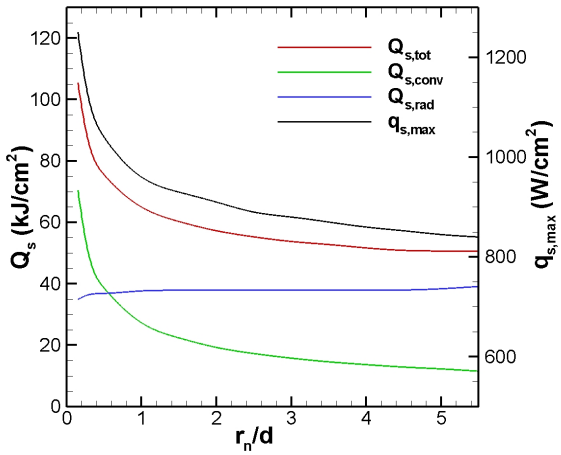

Figure 13.8. Comparison of nose radius on $Q_{s,tot}$ and $q_{s,max}$ generated along the trajectory of design D.

The design variable distributions for the Pareto frontiers that include Designs A – D are given in Figure C.0.1 – Figure C.0.4. For the L/D = 0.5, SS lower mass case, Fig. Figure C.0.1(a) indicates that both θ_s and α are relatively constant. The eccentricity varies between 0.52 and 0.72 and increases with p_{xrs}. The transformation parameter n_2 varies between 1.49 and 1.73 until the Pareto frontier's heat load spikes around p_{xrs} = 1750 km, at which point n_2 increases to 2.0. The time variables in Figure C.0.1(b) and (c) slightly vary in order to increase cross range, but a few of the

bank angles vary dramatically. Figure C.0.1(d) indicates the bank angles that vary the most are $\phi_{b,0}$, $\phi_{b,1}$, $\phi_{b,5}$, and $\phi_{b,6}$. For this case, the trajectory variables were changed more by the optimizer than the geometric variables in order to produce the high cross range. For the $L/D \approx 0.3$, Orion CEV, projection at 10,000 kg case, Figure C.0.2 shows that the time and banks angle design variables vary more dramatically than for the previous case. The $L/D = 0.3$, SS lower mass case varied both more dramatically, as shown in Figure C.0.3. The $\theta_s \approx 23^o$; the other geometric variables are shown to vary, but not to vary the aerothermodynamics dramatically. This explains why the Pareto frontier's heat load $Q_{s,tot}$ does not more than 10% for p_{xrs} from 200 to 1100 km. Figure C.0.4 shows similar for the $L/D = 0.3$, SC with fixed $h_{b,HS} = 3.43$ m, lower mass case. It would make sense for the design variable distributions to the higher mass Pareto frontiers to have similar behavior. As a result, it can be concluded that the flatness of the Pareto frontiers to generated due to the optimizer not changing the geometric features dramatically once it finds a combination of geometry and trajectory that minimize heat load and maximizes cross range. It concurrently varies the geometry slightly while making greater adjustments to α and the trajectory variables.

13.2. Maximizing p_{dwn} and minimizing $Q_{s,tot}$

Pareto frontiers in Figure 13.2 indicate that the maximum down range p_{dwn} is constant at ~26,000 km and does not increase with L/D for the given set of constraints. The main constraint on the down range has been shown to be the time constraint. As a result, Figure 13.2 indicates that there is no advantage to having a

higher *L/D* if only high down range is required. A discussion on the effects of relaxing the $\alpha - \varepsilon$ constraint would be similar to the one above. Designs E – H are based on upper mass estimates and listed in Table 13.1. Each of the Pareto frontiers has nearly constant $Q_{s,tot}$ for 5000 km $\leq p_{dwn} \leq$ 26,000 km. The relatively leveled portion of these Pareto frontiers have $Q_{s,tot}$ that closely match the relatively leveled portions of the Pareto frontiers in Figure 13.1. Since all the optimizations occur at the same V_E and γ_E and the Pareto frontiers' $Q_{s,tot}$ closely match, the contributions of Q_s and $q_{s,max}$ would likely be similar between the two sets of Pareto frontiers. Figure 13.9 shows the base cross sections of designs E and G, and that the higher *L/D* produced a 31.6% more eccentric heat shield.

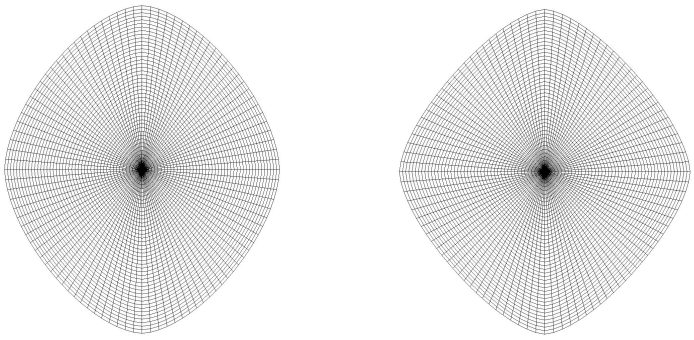

a) Design E, $n_2 = 1.73$, $e = 0.537$ b) Design G, $n_2 = 1.59$, $e = 0.408$

Figure 13.9. Base cross sections for Designs E & G.

Shown in Figure 13.10, the optimal down range trajectories have longer durations than optimal cross range designs. The higher mass Orion CEV case design F is shown in Figure 13.11 to decelerate the deepest in the atmosphere before skipping. The effects of the ballistic coefficient on the minimum altitude of this part of the trajectory for the designs shown in Figure 13.10 and Figure 13.11 can be compared using Table 13.1, and it does follow the established understanding that a lower ballistic coefficient, for a given *L/D*, allows a vehicle to decelerate higher in the

atmosphere. The Orion CEV with a mass of 13,100 kg is listed as Design F and is projected to have nearly the same trajectory as the optimal spherical segment Design G. Prior to the first deceleration peak, each design experiences its peak heat flux. For these cases, $t_d \approx$ 75-85 s. The designs with larger mass experience peak heating at 1.2 km deeper in the atmosphere. This corresponds to an 18% increase in air density and results in a 12% increase in peak $q_{s,conv}$ and a 25% increase in peak $q_{s,rad}$.

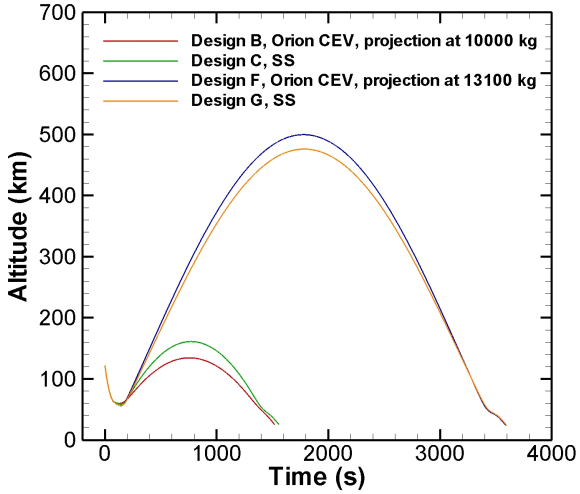

a) Altitude profiles

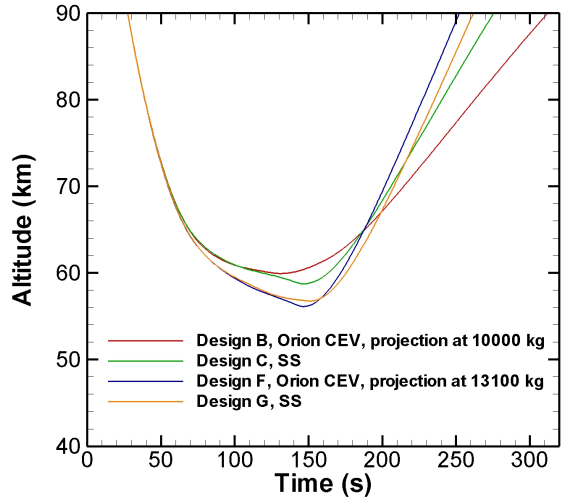

b) Close-up of first 320 s of trajectories

Figure 13.10. Comparison of trajectories of optimal cross range designs B & C and optimal down range designs F & G.

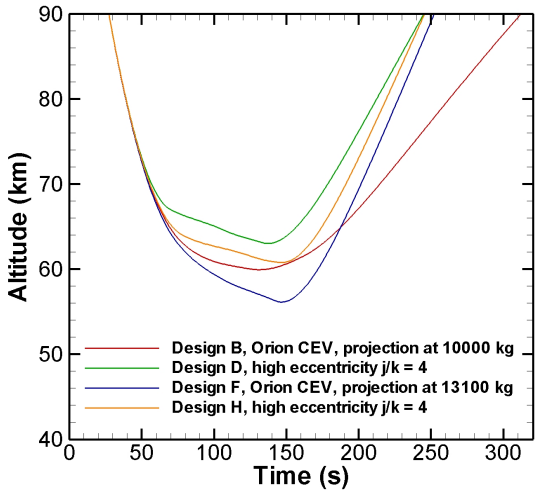

Figure 13.11. Comparison of trajectories of Designs B, D, F, and H for first 320 s.

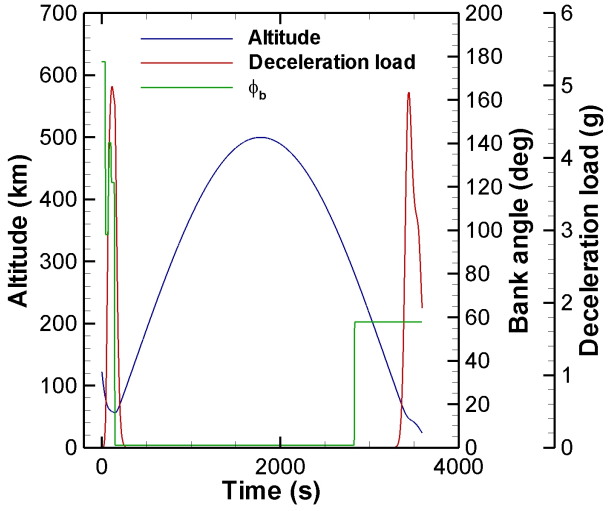

a) Trajectory profiles

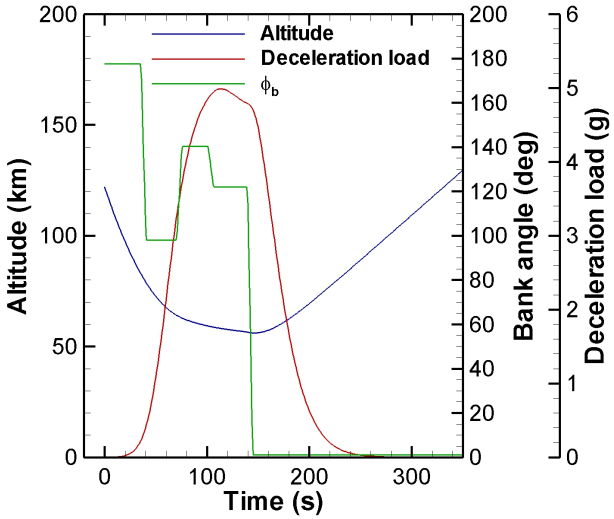

b) Close-up of first 340 s of trajectory

Figure 13.12. Trajectory of design F from Table 13.1, Orion CEV projection at 13100 kg.

Trajectory profiles for design F are provided in Figure 13.12 to give one way to use bank angle control to produce a 25,960 km down range. Six bank angles with different durations were required to produce this trajectory. The deceleration load is shown to meet the 5-*g* upper limit also during the second entry.

The design variable distributions for Pareto frontiers with designs E – H and the L/D = 0.3, 5-deg SS with fixed $h_{b,HS}$ = 3.43 m, upper mass case are provided in Figure C.0.5 – Figure C.0.9. For the L/D = 0.5, SS upper mass case, the geometric variables are relatively constant until the increase in $Q_{s,tot}$ around p_{dwn} > 26,000 km when the designs have either approached or reaching the 1 hr duration constraint. For this Pareto frontier, the time variables are varied more than the bank angles. For 2000 < p_{dwn} < 6000 km, t_4 decreases with increasing down range in order to decelerate the vehicle less by allowing the vehicle to skip sooner. The $\phi_{b,4}$ is shown to have a value near 90^o for this set of down ranges, and the value of $\phi_{b,3}$ is relatively constant at 109^o. As a result, having $\phi_{b,4} \approx 90^o$ rotates the lift vector from pointing significantly into the atmosphere to nearly horizontal. The scatter in values for $t_1 - t_4$ is due to the high scatter in values for $\phi_{b,0}$, and thus the optimizer slightly shifted the time variables and kept the bank angles nearly constant. This shows that the trajectory is not sensitive to $\phi_{b,0}$ for trajectories with down ranges less than 5400 km. For the higher down ranges near 25,000 km, the values of $\phi_{b,0}$ have become stable.

The scatter of a design variable can be derived from at least two possible reasons. The first is that some of the time and bank angles are not within the trajectory. In this case, the variables are randomly varied by the optimizer and don't affect the trajectory, thus showing up as a scatter on the distribution plot. This can be

seen in Figure C.0.5(c) for variable t_6 for 2000 < p_{dwn} < 6000 km in which it varies by > 1000 s. Note that $\phi_{b,6}$ is initiated at t_6 and the amount that $\phi_{b,6}$ varies Figure C.0.5(f) compared to the other bank angles. The final bank angles and times become important for the longer duration trajectories, but are shown to be unnecessary for the lower values of down range. The second cause for scatter is the insensitivity of a vehicle/trajectory design to a given design variable. This is exemplified in the behavior of $\phi_{b,0}$ discussed above.

For the L/D = 0.27, Orion CEV, projection at 13000 kg case, Figure C.0.6(a) shows that $t_2 - t_4$ vary by more than 20 s in varying down range from 2400 km to 4800. The corresponding bank angles are shown in Figure C.0.6(c). For this set of down ranges, some of the designs points t_5 and t_6 are not within the trajectory designs, but they are used in the trajectories with high durations to modify the bank angles for the second entry, allowing the optimizer to produce trajectory designs within g-load limits. For the $L/D \approx 0.3$, SS upper mass case, the design variable distributions show that the combination of bank angles employed for the initial entry period use full lift up with $\phi_{b,4} = 0^o$ for 3400 km < p_{dwn} < 26,000 km. Figure C.0.7(d) shows the transition of $\phi_{b,4}$ as down range is increased from 2600 to 3400 km. The L/D = 0.3, SC with fixed $h_{b,HS}$ = 3.43 m, upper mass case is a good example of a case where geometric variables and α are held constant by the optimizer, as shown in Figure C.0.8(a). As a result, this Pareto frontier that includes design H is produced solely by varying the bank angle profile. Note that not all the trajectory variables vary greatly for 8000 km < p_{dwn} < 24,000 km, but they vary at least slightly. The time t_4 decreases the most dramatically out of all the time variables for this set of down ranges. This

may represent a more sensitive region of the trajectory design space, in which more time and bank angle design variables may be needed. Of the bank angles, $\phi_{b,5}$ varies the most for this set of down ranges, as shown in Figure C.0.8(e). The design variable distributions for the L/D = 0.3, 5-deg SS with fixed $h_{b,HS}$ = 3.43 m, upper mass case are provided in Figure C.0.9. It shows that the time and bank angles vary and have a coherent behavior. Among some of these solutions, the conditions at which $\phi_{b,4}$ is initiated to release the vehicle from the atmosphere (in order to produce a skip) is shown to be directly related to the total down range.

Surface area and volumetric comparisons of the Orion CEV to the Apollo CM indicates scaling is proportional to roughly to surface area. If the Apollo CM's total surface area is approximately 31 m^2 and the Orion CEV's is approximately 51 m^2, then assuming a 5800 kg mass and a surface area ratio of 1.645 renders a projected Orion CEV mass of 9500 kg. The current mass estimated for Orion is assumed to be approximately 10,000 kg, and current unpublished estimates indicate that it's currently between 9000 and 10,000 kg. As a result, this entry vehicle geometry roughly scales with surface area. This means that the ballistic coefficient stays approximately constant at a values of approximately 340 kg/m^2 for α = -17.0^o. A surface area comparison volumetric efficiency for the Orion CEV, using Eq. (2.16), is ~85%, assuming a total volume of 31 m^3 and total surface area of 56 m^3.

As a result, to match the drag area of optimal design D in Table 13.1 with the Orion geometry, the mass would be ~20,300 kg. However, now it has a total volume of 63 m^3, which is 203% larger than the current Orion CEV, having much more volume than required. The resulting benefit gained from having a larger drag area is

completely lost by the higher mass, assuming that scaling the Orion geometry further would exhibit the same behavior as scaling up Apollo.

The optimizer determined that a lower volumetrically efficient geometry design D would be capable of reducing the heat load, indicated by a lower *BC*. Since one of the mission requirements for this research is to match the required pressurized volume for the Orion CEV as much as possible while maintaining the specified minimum size requirements, listed in Chapter 5, the decrease in volumetric efficiency in Eq. (2.16) is accomplished by increasing surface area. If a 57.5^{o} (arbitrarily chosen) elliptical conical frustum is chosen to connect with design D in Figure 12.9(a) and (b) with a length of 1.986 m, then volumetric efficiency is 64%, assuming a total surface area of 100.4 m^2 and a total volume of 48.0 m^3. This tradeoff in geometric features renders a 44% drop in $Q_{s,tot}$ from design B (Orion) to design D for the desired pressurized volume. Additional affects such as the required structure and a chosen crew compartment geometry are not integrated into this analysis and will probably reduce this benefit in heat load, though a high order study would be necessary to determine the reduction. Correlating the mass and shape of one entry vehicle with another of completely different shape probably does not create a direct, linear relationship.

Chapter 14. Comparison of Lunar Return and Mars Return

Comparisons are provided in this chapter regarding the lunar and Mars return results including (1) a discussion of how the results for lunar and Mars return compare, (2) the effects of changing entry velocity and the time constraint on maximizing down range, (3) the effect of a 31% mass increase on trajectory design, and (4) trends showing the effects of ballistic coefficient and drag area on stagnation-point heat load.

For ease of viewing and comparison, the Pareto frontiers for both lunar and Mars return are provided together in Figure 14.1 and Figure 14.2 respectively for maximizing cross range and Figure 14.3 and Figure 14.4 respectively for maximizing down range. First, the L/D = 1 cases are not provided for Mars return, V_E = 12.5 km/s, since the initial designs for the optimization had impractical $Q_{s,tot}$ greater than 190 kJ/cm^2. Even the L/D = 1 cases for lunar return, V_E = 11 km/s, provide heat loads that are so extravagant for lunar return that there may be no advantage from an overall systems perspective to utilize this case in comparison to L/D = 0.3 and 0.5 cases. With its heat loads ranging from 88 to 131 kJ/cm^2, the 40% increase in mass from design A to design E produces an increase in heat load of 43.1 kJ/cm^2 that is greater than the 30 kJ/cm^2 experienced by the manned Apollo CM missions.[41]

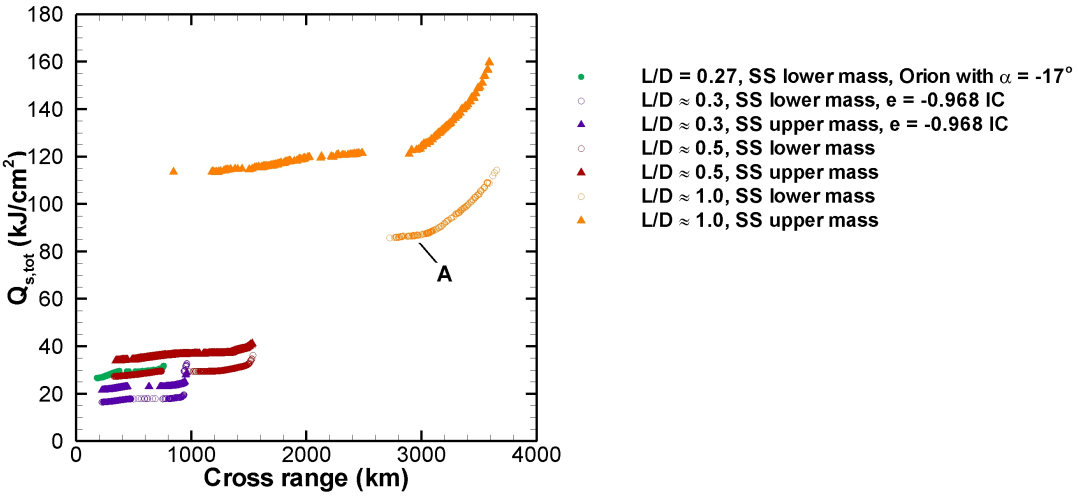

a) *L/D* = 0.3, 0.5, and 1.0 Pareto frontiers

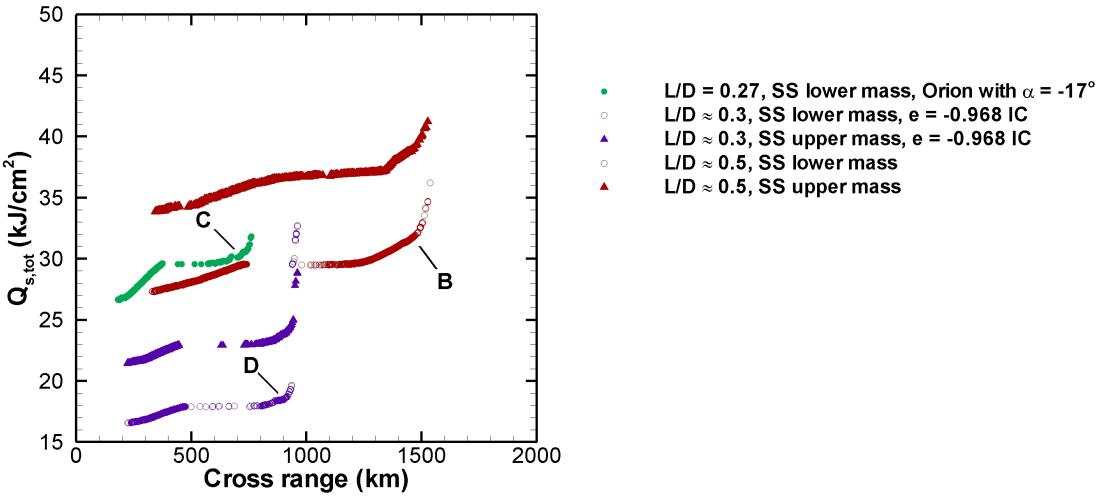

b) Close-up of *L/D* = 0.3 and 0.5 Pareto frontiers

Figure 14.1. Pareto frontiers for maximizing cross range and minimizing stagnation-point heat load, V_E = 11 km/s.

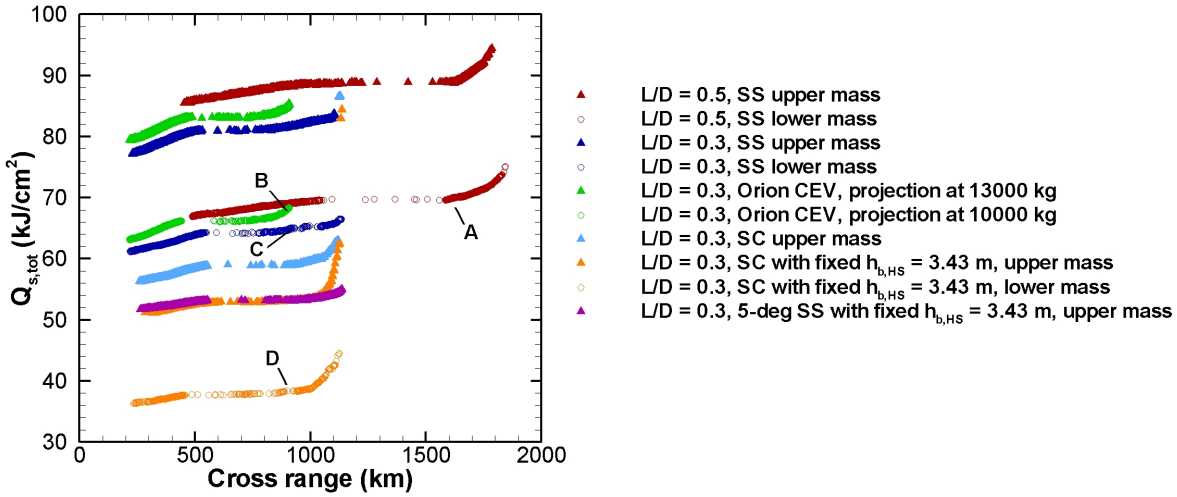

Figure 14.2. Pareto frontiers for maximizing cross range and minimizing stagnation-point heat load, V_E = 12.5 km/s.

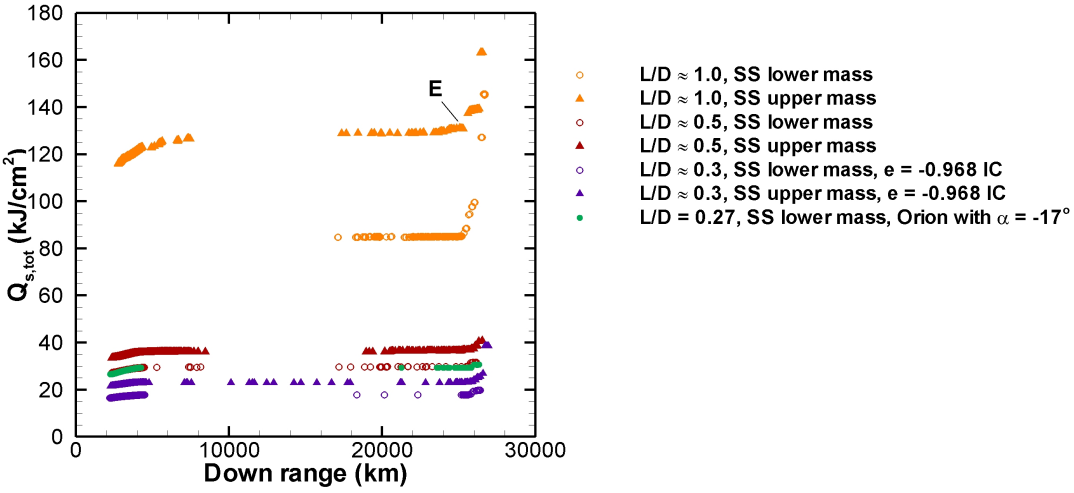

a) L/D = 0.3, 0.5, and 1.0 Pareto frontiers

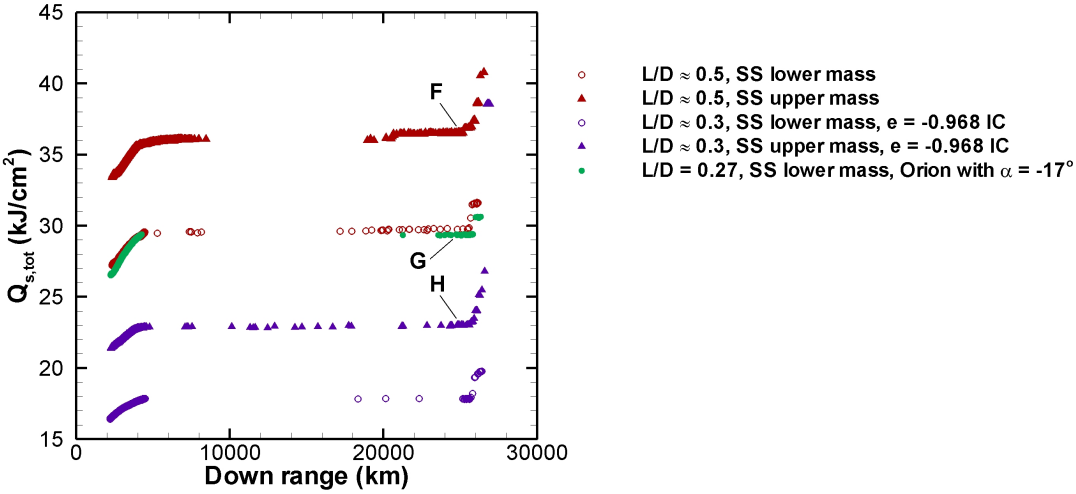

b) Close-up of L/D = 0.3 and 0.5 Pareto frontiers

Figure 14.3. Pareto frontiers for maximizing down range and minimizing stagnation-point heat load, V_E = 11 km/s.

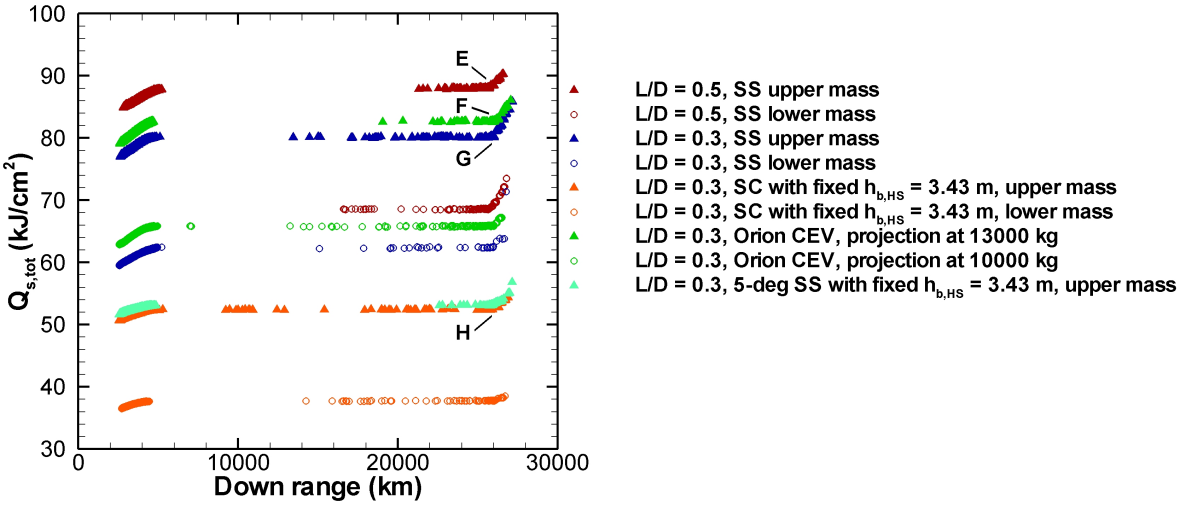

Figure 14.4. Pareto frontiers for maximizing down range and minimizing stagnation-point heat load, V_E = 12.5 km/s.

The maximum cross range for a given case is larger for Mars return than for lunar return. For L/D = 0.5, the Pareto frontier becomes vertical for lunar return at ~1550 km and for Mars return at 1850 km, a 19.4% increase. For L/D = 0.3, there is a 21.0% increase. For the L/D = 0.27 Orion CEV cases, there is a 12.5% increase. The lower percentage increase is probably due to fixing α and thus restricting the optimizer from increasing L/D in order to maximize cross range.

The resulting increase in maximizing down range is subtle when increasing from lunar return to Mars return. As a result, a brief investigation of the effects of changing entry velocity and the time constraint on maximizing down range was conducted. Figure 14.5(a) indicates that for $V_E \geq 9$ km/s, the Pareto frontiers becomes vertical at down ranges of approximately 26,000 km. The V_E = 8.5 and 7.7 km/s cases provided maximum down ranges of 4000 and 2300 km respectively as shown in Figure 14.5(b), for the given set of bank angle controls. Since the Pareto frontiers for $V_E \geq 9$ km/s have relatively identical maximum down ranges and designs E – H for lunar and Mars return all have t_f approaching the limit of 1 hr, the effects of adjusting the time constraint on the optimization has been completed. With the adjustment of the time constraint, the down ranges for both cases are shown in Figure 14.6 to increase and decrease relatively to the same extent. The maximum down range is 12,000 km for $t_f < 1600$ s, 44,000 km for $t_f < 7200$ s, and 50,000 km for $t_f < 10900$ s. While the percentage increase from $t_f < 1600$ s to $t_f < 3600$ s is 117%, it is 69.2% for the increase from $t_f < 3600$ s to $t_f < 7200$ s, and it is 13.6% $t_f < 7200$ s to $t_f < 10900$ s. A final duration t_f constraint between 1600 s and 7200 s provides the greatest variation in down range.

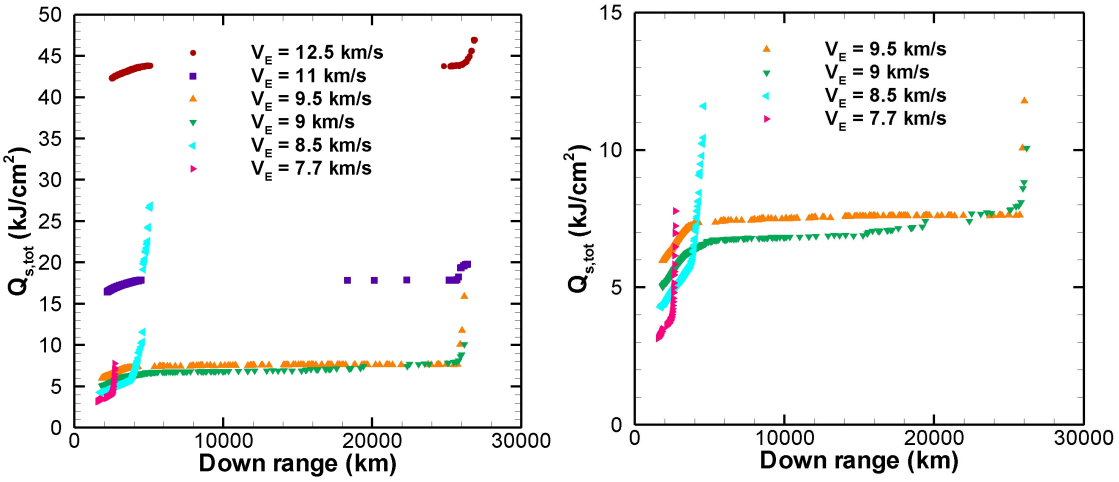

a) Pareto frontiers **b) Close-up of solutions for V_E = 7.7, 8.5, 8, & 9.5 km/s**

Figure 14.5. Comparison of optimal solution sets for V_E from 7.7 to 12.5 km/s for $L/D \approx 0.3$, SS lower mass, e = -0.968 IC case.

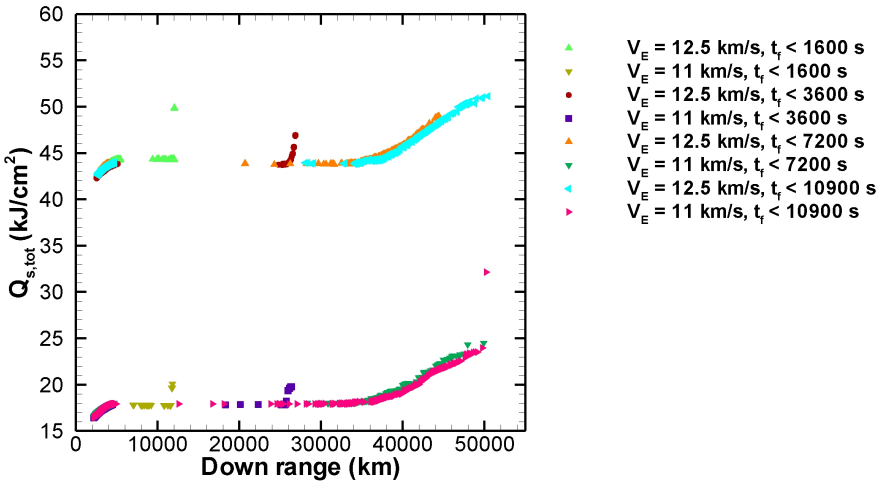

Figure 14.6. Comparison of optimal solution sets with maximum durations from 1600 to 10,900 s for lunar and Mars return for $L/D \approx 0.3$, SS lower mass, e = -0.968 IC case.

A comparison of maximum down range trajectories for the Orion CEV at 10,000 kg is provided in Figure 14.7 for design G from lunar return and trajectory for Mars return that is within 800 km of the down range of design G. The elegance of the bank angle profile solution can be seen in the deceleration of the Mars return case during the initial 200 s to a velocity very similar to the lunar return case, as shown in Figure 14.7(c) using the bank angle controls shown in Figure 14.7(d). As expected,

from that point on in the trajectory, the rates of increase in down range for both cases are relatively the same, as shown in Figure 14.7(a) and (d).

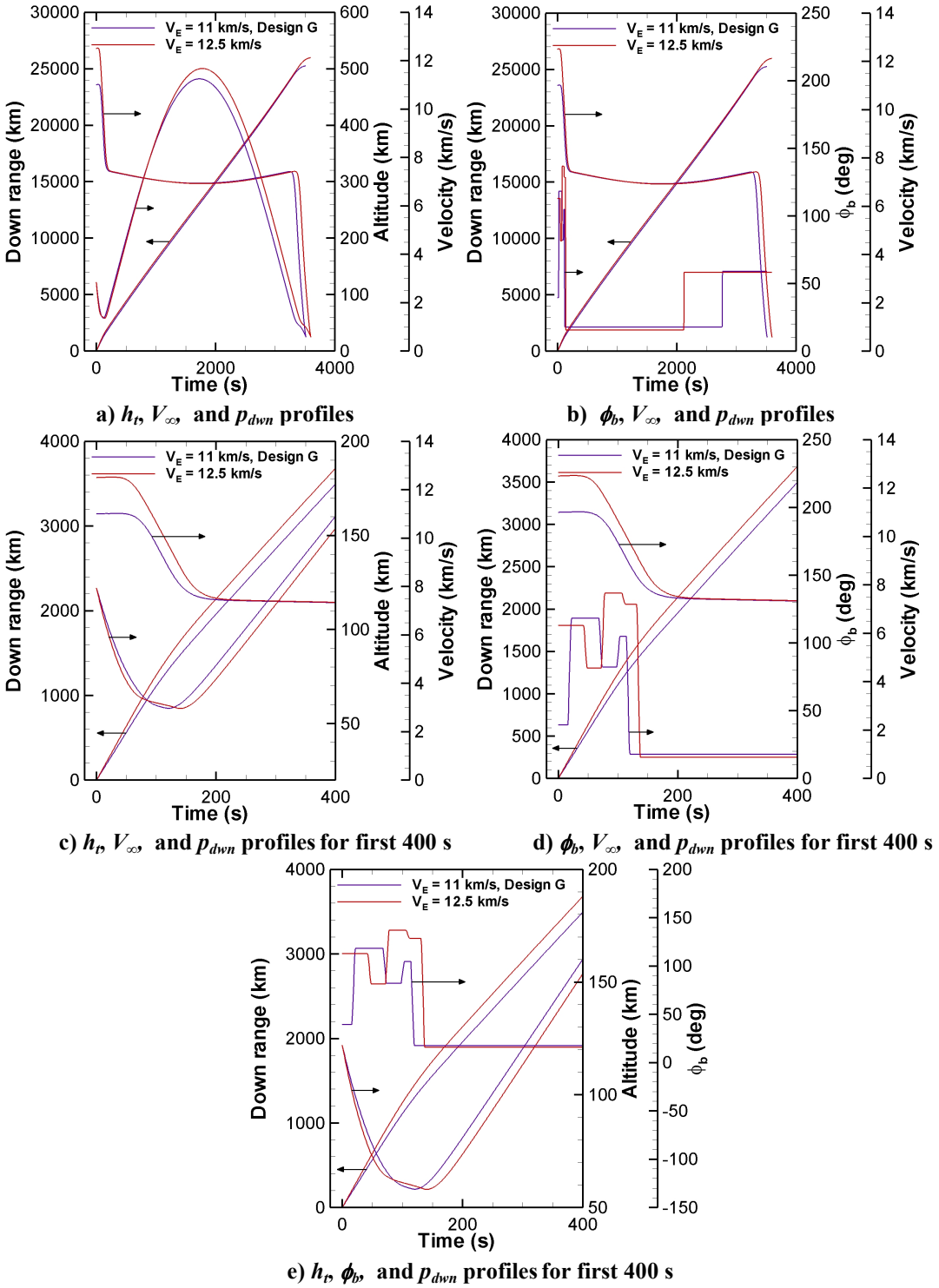

a) h_t, V_∞, and p_{dwn} profiles

b) ϕ_b, V_∞, and p_{dwn} profiles

c) h_t, V_∞, and p_{dwn} profiles for first 400 s

d) ϕ_b, V_∞, and p_{dwn} profiles for first 400 s

e) h_t, ϕ_b, and p_{dwn} profiles for first 400 s

Figure 14.7. Comparisons of lunar and Mars return trajectories for the Orion CEV at 10,000 kg, for $p_{dwn} \approx 25{,}500$ km with lunar Design G and Mars Orion lower mass cases.

Note the variation in bank angle profiles between the two cases in Figure 14.7(d) and that after the initial deceleration, the bank angle profiles almost match in Figure 14.7(b) and (d). The difference in execution time of the final bank in the trajectory, shown in Figure 14.7(b) is irrelevant since both are executed above the sensible atmosphere with altitudes above 250 km. The bank angle profiles are shown in Figure 14.7(e) against the altitude profiles to determine where in the trajectory with respect to the first trough are the primary changes in bank angle produced. For both cases, all bank angles adjustments are completed within the first 150 s and before the end of the first trough. Design G's bank angle profile is listed in Table 12.1, and the last bank angle adjustment from 104.8^{o} to 17.8^{o} represents a rotation of the lift vector to nearly full up, thus allowing the entry vehicle to skip out of the sensible atmosphere.

The effect of a 31% increase in mass of the Orion CEV from 10,000 kg to 13,100 kg for Mars return is provided in Figure 14.8 assuming nearly identical down ranges of ~26,000 km and cross ranges with 100 km of each other. Mars return design F, listed in Table 13.1, is shown to nearly match the 10,000 kg Orion CEV case for velocity and down range profiles in Figure 14.8(a) and (d). The more massive Orion CEV is shown in Figure 14.8(c) to have a minimum altitude of 56.25 km, which is a 3.18% decrease in minimum altitude below the 10,000 kg Orion CEV that has a minimum altitude of 58.10 km. This 1.85 km deeper trajectory produces a 30.9% increase in the radiative heat load and a 15.3% increase in convective heat load, resulting a total increase in heat of 25.2%, with $Q_{s,tot}$ = 66 kJ/cm^2 for the 10,000 kg Orion CEV and $Q_{s,tot}$ = 82.6 kJ/cm^2 for the more massive design F. The effect of the higher density on heat loads for entry at hyperbolic velocities is explained in detail

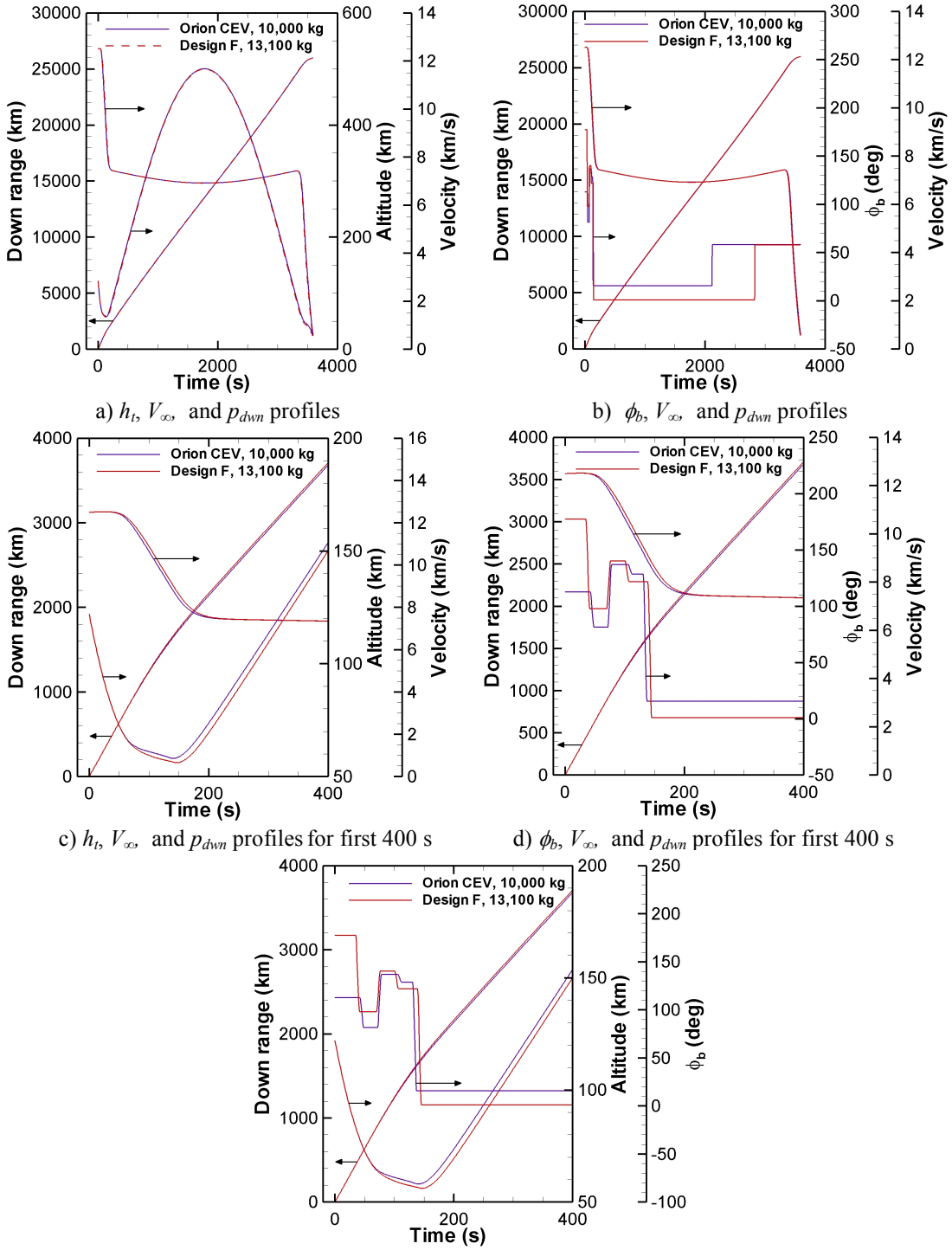

a) h_t, V_∞, and p_{dwn} profiles

b) ϕ_b, V_∞, and p_{dwn} profiles

c) h_t, V_∞, and p_{dwn} profiles for first 400 s

d) ϕ_b, V_∞, and p_{dwn} profiles for first 400 s

e) h_t, ϕ_b, and p_{dwn} profiles for first 400 s

Figure 14.8. Comparisons of optimal Mars return trajectories for the Orion CEV at 10,000 kg and 13,100 kg, for $p_{dwn} \approx 26{,}000$ km.

in Chapter 10. The greatest change between the two trajectory designs, assuming a 31% increase in mass for the production of 26,000 km down range and cross ranges within 100km of each other ($p_{xrs} \approx$ 540 km +/- 50 km) is the bank angle profile. Figure 14.8(d) shows the necessary bank angle controls to keep the velocity profiles of the two geometries to be similar. The final bank angle of 58^o is common to both trajectory designs. The sensitivity of the heat load to the greater mass could be more easily noticed by its 31% larger ballistic coefficient with a value of 440 kg/m^2.

The effects of ballistic coefficient on heat load, which is one of the most sensitive parameters of atmospheric entry, have been correlated in Figure 14.9 for both lunar and Mars return. The data in Figure 14.9 includes the optimal designs from Table 12.1 and Table 13.1 and the non-optimal initial heat shield and trajectory designs from Table 11.3 and Table 11.4. The entire data set is shown in Figure 14.9(a). Disregarding the L/D = 1.0 results for both lunar and Mars return for ballistic coefficient (BC) values greater than 900 kg/m^2, regression curves have been generated, shown in Figure 14.9(b), with R^2 values of at least 86%. This indicates that the heat load increases linearly with ballistic coefficient. Additionally, the rate at which heat load increases with ballistic coefficient at an entry velocity of 12.5 km/s is a factor of 1.59 greater than the rate at 11 km/s. For lunar return, the correlation is

$$Q_{s,tot} = 0.054BC + 7.289, \quad \text{with a } R^2 \text{ value of } 0.860. \tag{14.1}$$

For Mars return, the correlation is

$$Q_{s,tot} = 0.140BC + 15.23, \quad \text{with a } R^2 \text{ value of } 0.944. \tag{14.2}$$

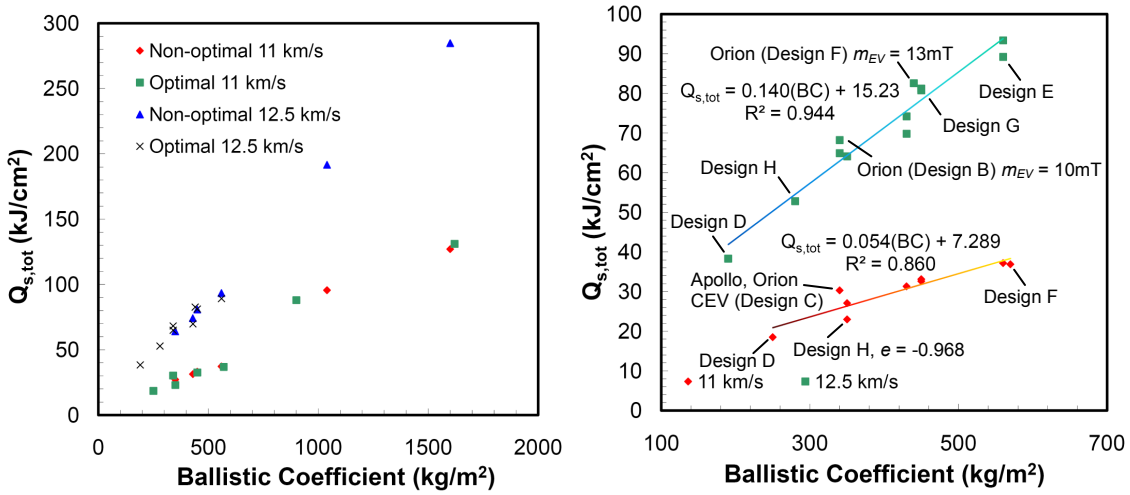

a) Complete data set **b) Correlations for 180 < *BC* < 600 kg/m²**

Figure 14.9. Trends for the effects of *BC* on $Q_{s,tot}$ for lunar and Mars return.

Similar correlations have been made for this data set for heat load against drag area $D/q_\infty = C_D S$ in Figure 14.10. The entire data set is included in Figure 14.10(a), and correlations were generated for $D/q_\infty \geq 16$ m^2 for lower and upper mass estimates in Figure 14.10(b). These also produced linear relations although it would be more logarithmic if the drag areas less than 16 m^2 were included. As expected, the heat load decreases with an increase in drag area since a geometry with a greater drag area for a given mass is able to decelerate in the presence of a lower air density. For lunar return, the correlation for results with the lower mass estimate is

$$Q_{s,tot} = -0.680 D/q_\infty + 48.01, \tag{14.3}$$

with a R^2 value of 0.932.

For lunar return, the correlation for results with the upper mass estimate is

$$Q_{s,tot} = -0.761 D/q_\infty + 54.81, \tag{14.4}$$

with a R^2 value of 0.997.

For Mars return, the correlation for results with the lower mass estimate is

$$Q_{s,tot} = -0.947 D/q_\infty + 93.80, \tag{14.5}$$

with a R^2 value of 0.970.

For Mars return, the correlation for results with the upper mass estimate is

$$Q_{s,tot} = -1.043 D/q_\infty + 113.6, \tag{14.6}$$

with a R^2 value of 0.968.

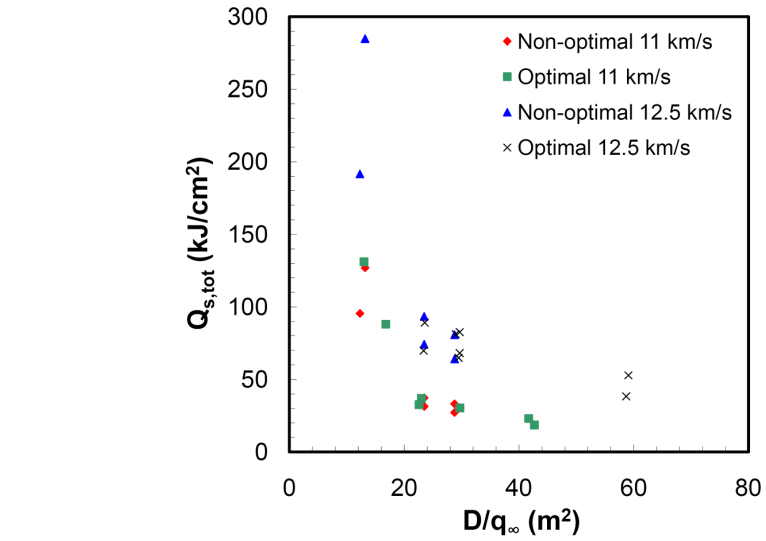

(a) Complete data set

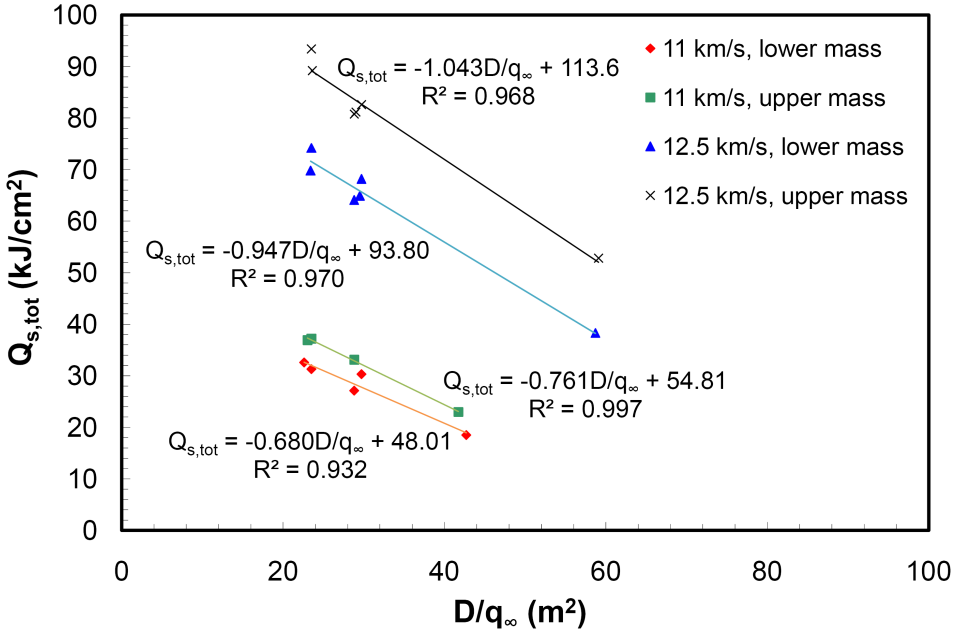

(b) Correlations based on data with $D/q_\infty > 16$ m^2

Figure 14.10. Trends for the effects of drag area on $Q_{s,tot}$ for lunar and Mars return.

Even though these correlations may have fewer number of points per regression curve and thus, may be less accurate than the other correlations, these do provide an initial impression to how heat load varies with drag area for the conditions of this optimization. Due to the few number of data points, extrapolation in either direction is not suggested. The lower and upper mass lunar return cases have a 11.9% difference in slope while it is 9.8% for Mars return. The lower mass Mars return case has a 39.3% increase in slope magnitude over the lower mass lunar return case. The upper mass Mars return case has a 37.1% increase in slope magnitude over the upper mass lunar return case. As a result, the rate of decrease of $Q_{s,tot}$ with D/q_∞ is increased in magnitude by ~11% with the upper mass estimate; and the rate of decrease of $Q_{s,tot}$ with D/q_∞ is increased in magnitude by ~38% with the Mars return case. The correlations in Figure 14.9 and Figure 14.10 can be useful in estimating the expected $Q_{s,tot}$ for a particular entry vehicle once detailed mass and drag area estimates are completed. For the case of design D, applying different crew compartment geometries will produce a range of entry vehicle masses, and thus, the corresponding heat load could be estimated.

14.1. Limitations of the optimization methodology

The methodology that generated these results is limited primarily by the ability of the optimizer to find the global optimum. Part of the optimizer's capability is dictated by its settings, which is the primary reason why the parametric analysis provided in Chapter 9 was conducted: to determine which optimizer settings generated the most optimal results. An evolutionary algorithm does not guarantee that

the determined solution is the global optimum of the entire design space. However, depending on whether the problem is well-posed, the optimizer is capable of finding an engineering optimum that can be categorized a good design. With the initial setup described in Chapter 10, the optimizer could not locate trajectories with acceptable deceleration loads for inhabited Mars return due to at least two reasons: (1) the entry velocity of 15 km/s was not realistic and (2) the trajectory design space was too massive for the optimizer to effectively search. Once it was determined that the heat loads were unrealistic with current and near future material technologies, the entry velocity was reduced to 12.5 km/s; all the specific reasons are mentioned in Chapter 5. Incorporating the entry corridor methodology described in Chapter 11 reduced the trajectory design space and allowed for the optimizer to effectively search the portion of the design space that would be deemed flyable for a given *BC* and *L/D*. These two additions rendered the problem well-posed for the tools available.

One more observation, which may indicate a limitation in the optimizer's capability by itself, is that that the optimizer tends to settle on a particular geometric design for almost an entire Pareto frontier and only modify the trajectory design (ϕ_b – profile). This may result for several reasons. First, the local geometric design space is not significantly sensitive compared to the trajectory design space. Note that the optimizer does not distinguish the geometric from the trajectory design variables; they are all seen simply as design variables. This would suggest that if the objective functions were sensitive with one or two geometric design variables, then the optimizer would change them. Second, when the optimizer greatly changes the geometric design, the trajectory design variables would need to be greatly modified to

produce an overall feasible design. Otherwise, when the optimizer generates a greatly different geometric design with similar trajectory design controls, then new overall design will be infeasible due to trajectory constraints being violated. This was observed to not always occur. There are several cases where the optimizer modified the geometric design successfully. Optimal design A for lunar return listed in Table 12.1 has ~10^{o} increase in θ_s and a great difference in time and bank angle design variables. For Mars return L/D = 0.5 designs, the optimizer modified eccentricity from 0 to -0.621 and also modified the transformation parameter n_2 from 2.00 to 1.66 for design A listed in Table 13.1. It also modified the trajectory design variables successfully. However, for extremely significant changes in geometric design, the optimizer requires assistance with searching other parts of the design space. This is the case for both lunar and Mars return for L/D = 0.3 where the geometric design space is much greater in size than at L/D = 0.5 or 1.0. Shown in Figure 12.3, the L/D = 0.3, SS lower mass, Orion IC case has the Orion geometry with a feasible trajectory design placed within the initial population of the optimization. The optimizer found an optimum geometric design that does not vary much from the original Orion geometry. The L/D = 0.3, SS lower mass, e = -0.968 IC case represents a case starts with a highly oblate eccentricity geometry with a feasible trajectory design in the initial population. The 39% decrease in heat load $Q_{s,tot}$ performance, shown in Figure 12.3, is due to the highly eccentric design having a greater drag area and L/D. This suggests that the optimization setup currently needs assistance to run the global optimization for the case where the performance can be extremely different between geometric designs. The optimizer can only change the geometric design variables to a

certain extent for a given amount of change in the trajectory design for the resulting overall design to be feasible. This makes sense, and intelligently automating the optimization process can only be completed to a certain extent. The background understanding of the researcher directs the optimizer into specific regions of the design space and renders the optimization the most useful. This methodology is applied by utilizing different initial designs in a few of the optimizations, as exemplified earlier with the Orion CEV and high eccentricity $L/D = 0.3$ cases.

With all of this in place, the optimization setup is capable of finding good solutions that improve on the state-of-the-art, if they exist. There is probably more than one ϕ_b – profile that renders a similar heat load and range for a given geometric design, that is, a different combination of bank angles and times at which the bank angles are initiated. Additionally, there is probably more than one combination of geometry and trajectory design that produces the same heat load and range. However, applying the global search capability of the optimizer in this way suggests that only modest improvements if any would be generated, if the evolutionary algorithm is allowed to run the optimization for a longer duration and with a larger population size. The more well-posed a problem is, the higher chance that designs with higher performance can be determined, if they exist. Either way, the current optimization setup is capable of reporting the optimal solutions from all the thousands of feasible solutions it discovers, and these have been analyzed in this work.

Chapter 15. Conclusions

15.1. Contributions to the State of the Art

This research provides the following contributions to the state of the art: (1) broadening the heat shield design space to include new non-spherical, periodic designs, (2) a global design optimization methodology that can be applied to any atmospheric entry, and (3) optimal performance trade-off relationships for several heat shield and trajectory configurations.

First, the design space has been broadened to include new non-spherical, periodic heat shield designs based on three axial profiles and three main types of base cross sections. Axial profiles consist of spherical segments, spherically-blunted cones, and power laws. Base cross sections include rounded-edge polygons, ellipses, rounded-edge concave polygons, and blendings of these. Base cross sections are generated using the superformula of the superellipse, which provides a continuous design space between these three types of cross sections for each polygon type. This research indicates that a highly-blunt, eccentric heat shield design decreases volumetric efficiency but increases drag area to reduce heat loads by more than 35% with an oblate eccentricity of 0.968. Since heating is one of the most sensitive performance characteristics for atmospheric entry vehicles, eccentricity may be a means to enable missions with extremely high heat loads.

Second, a design methodology has been implemented in a global optimization analysis of Earth entry heat shields. An aerothermodynamic code has been developed to quickly estimate the performance of heat shields and filter out impractical designs. Since high-order computational fluid dynamics would render the global optimization

infeasible from a computational time standpoint, the aerothermodynamics code utilizes low-order methods. It is applied with a high-order 3DOF trajectory model to balance the need for fidelity with the desire to have practical computational times. Techniques have been implemented to reduce the runtime of the two codes from 20 min for a 2000 s trajectory to 10 s using interpolation tables and other techniques. An entry corridor methodology has been utilized to focus the global search on that portion of the trajectory design space that would be expected to be applied to an actual mission. With this reduced trajectory space, the global search capability is able to find feasible initial trajectory designs for a given heat shield design; in other words, it is able to find a bank angle profile solution without being given information a priori. This is not possible utilizing the search capabilities of POST, which requires the user to implement an extensive parametric trade study before locating a feasible trajectory design. This work utilizes UPTOP to automate this process with its global search capability. Note that POST has advance capabilities of many types that would not be used in this fundamental research, and that much of those are not present in UPTOP. Additionally, UPTOP is capable of both single and multi-objective function optimizations. The design optimization methodology implemented in this work for Earth entry can be applied to any atmospheric entry, including Mars, Venus, and moons such as Titan.

Third, for lunar and Mars return, this work provides optimal trade-off relationships between performance parameters including down range, cross range, stagnation-point heat flux, and stagnation-point heat load for several heat shield and trajectory configurations. The optimal trade-off curves provide both locations in the

design space that are ideal to take advantage of and those that should be avoided. It also highlights any performance sweet spots and performance walls for the given set of conditions. These optimal trade-off relationships are the resulting Pareto frontiers from the simultaneous optimization of any two performance parameters. Since a Pareto frontier is made up of several heat shield and trajectory designs, this work also provides the design variable distributions for several Pareto frontiers. Together, all three contributions provide a means to determine the geometric features that advance the state of the art in Earth entry heat shield hypersonic aerothermodynamic performance.

15.2. Summary of Results

15.2.1. Initial Lunar Return and Mars Return Results

Optimization has produced optimal heat shield configurations for Earth entry at V_E = 11 and 15 km/s, using two objective function sets: (1) maximizing p_{xrs} and minimizing $Q_{s,tot}$ and (2) minimizing $Q_{s,tot}$ and $q_{s,max}$. For V_E = 11 km/s with a 6 *g*-limit, the spherical segment is the optimal axial profile for maximizing p_{xrs} and minimizing $Q_{s,tot}$. Direct entry trajectories are best for $p_{xrs} \leq 250$ km; then skipping trajectories are utilized. For optimal designs, $Q_{s,tot}$ is 14.7, 22.6, and 29.4 kJ/cm^2 for p_{xrs} of 500, 1000, and 1500 km respectively. The spherically blunted cone and power law solutions are disguised spherical segments for $p_{xrs} > 750$ km. Optimal designs for minimizing $Q_{s,tot}$ and $q_{s,max}$ have direct entry trajectories, and the selected spherical segment and blunted cone geometries are equally optimal.

For V_E = 15 km/s with a 12 *g*-limit, neither the optimal blunted cone nor spherical segment is significantly better. Radiative heat transfer dominates convection in both heat flux and heat load. For the reported designs, the maximum convective heat flux was at most 16.4% of the maximum total heat flux, and the convective heat load was at most 28.4% of the total heat load. For maximizing p_{xrs} and minimizing $Q_{s,tot}$, the $Q_{s,tot}$ slightly increases for $p_{xrs} \leq 1100$ km. For optimal designs, $Q_{s,tot}$ is 64.5, 65.2 and 98.3 kJ/cm^2 for p_{xrs} of 500, 1000, and 1500 km respectively. The significant difference in the blunted cone and spherical segment Pareto frontiers is not caused by differences in axial profile; instead it is caused by the higher sensitivity of radiative heat transfer to air density at hyperbolic speeds (V_∞ greater than escape velocity). The blunted cone's larger drag area allows the vehicle to decelerate with maximum heating at V_∞ = 13.5 km/s and 2 km higher altitude with 40% less air density, thus reducing $q_{s,max}$ and ultimately $Q_{s,tot}$ by 21%. The lower drag area is generated by the vehicle sizing routine that determined the spherical segment can satisfy the mission requirements with a smaller-sized vehicle. If both geometries have the same drag area, the blunted cone would provide only a 4% lower $Q_{s,tot}$ at 1000 km cross range. For minimizing $Q_{s,tot}$ and $q_{s,max}$, the blunted cone produces an 8% lower $q_{s,max}$. Although the optimal spherical segment and blunted cone designs produce nearly the same optimum $Q_{s,tot}$ with two different sets of curvature and shock layer thickness, a proper balance of convective and radiative heat transfer is necessary to minimize $Q_{s,tot}$.

For both entries, highly oblate eccentricity e = -0.968 maximizes drag area, allowing deceleration at higher altitudes, thus lowering both heat flux and heat load.

As more p_{xrs} is required, drag area is traded-off with the need for larger L/D, by decreasing e. This behavior is consistent with the parametric analysis in Ref. [112]. An elliptical cross section rather than a parallelogram-form is optimal for $L/D \leq 0.50$, corresponding to $p_{xrs} \leq 1500$ and 2200 km for $V_E = 11$ and 15 km/s respectively. The parallelogram cross section could be applied to increase L/D beyond the capability of the elliptical cross section, which is expected for higher p_{xrs} and lower peak g-limits.

15.2.2. Final Lunar Return and Mars Return Results

Optimization has produced optimal heat shield configurations for Earth entry from Mars return at $V_E = 12.5$ km/s, using two objective function sets: (1) maximizing p_{xrs} and minimizing $Q_{s,tot}$ and (2) maximizing p_{dwn} and minimizing $Q_{s,tot}$. Conclusions include the following: A hierarchy of three classes of blunt body geometries can be prescribed for reducing stagnation-point heat load: (1) blunt designs with axial profiles consisting of low θ_s or high θ_c and r_n/d, and base cross sections with either oblate e or larger d. The resulting higher drag area allows the entry vehicle to decelerate higher in the atmosphere, (2) similarly blunt designs with circular base cross sections and diameters near the initially prescribed 5 m, and (3) slender designs with axial profiles consisting of high θ_s with highly oblate e base cross sections. Based on L/D requirements, a class may not be available; then the next class would likely be the best option.

For Mars return, the Orion performs nearly optimally compared to spherical-segment geometries with a circular base cross-section. However, an eccentric base cross section reduces heat load significantly. An oblate eccentricity of $j/k = 4$ reduces

the heat load from 65 kJ/cm^2 to 40 kJ/cm^2 by increasing the surface area, and thus, drag area at a higher rate than the increase in heat shield mass, thus allowing the vehicle to decelerate higher in the atmosphere. Although the minimum heat load geometry is the spherically blunted cone with an elliptical base cross section, a low θ_s spherical segment also provides nearly optimal performance since the heat load is nearly constant for $r_n/d > 4.0$.

This work agrees with current literature[1] that $L/D = 0.3$ will produce more than the projected entry corridor width requirement of 0.4^o. L/D = 0.3 produces a maximum cross range of 1100 km. L/D = 0.5 produces a maximum cross range of 1600 km. For the given mission profile, designs with L/D = 1.0 are presently infeasible due to extremely high $Q_{s,tot}$, generated since their ballistic coefficients are twice or thrice that of $L/D = 0.3$ and 0.5 designs.

For both $L/D = 0.3$ and 0.5, a 30% increase in entry vehicle mass from 10,000 kg produces 20-30% increase in $Q_{s,tot}$. There is a tradeoff between volumetric efficiency and drag area that allows for a particular pressurized volume requirement to be maintained and thus keeping the mass increase a lower rate than drag area. As a result, there is a reduction in the stagnation-point heat load. This is indicated by the ballistic coefficient that can be reduced below the expected 340 kg/m^2 value for the Orion CEV for lunar and Mars return.

For lunar return, L/D = 0.3, 0.5, and 1.0 produce maximum cross ranges of 950, 1500, and 3000 km respectively before the Pareto frontiers increase in $Q_{s,tot}$ dramatically. The $L/D = 1.0$ designs have highly oblate, rounded edge parallelogram base cross sections. A spherical segment of $\theta_s = 5^o$ with a highly oblate cross section

e = -0.968 produces both a 27% higher cross range and a 39% lower heat load than the Orion CEV at L/D = 0.27 due to its 41% greater drag area and 18.5% greater L/D. Increasing mass by 30% does not strongly affect the maximum possible cross range or down range, but it increases $Q_{s,tot}$ by at least 23%, 30.3%, and 44% for L/D = 0.3, 0.5, and 1.0 respectively.

There is not any advantage in maximizing down range and minimizing heat load to applying high L/D designs for V_E = 11 and 12.5 km/s. The maximum down range p_{dwn} is ~26,000 km. For both L/D = 0.3 and 0.5, a 30% increase in entry vehicle mass from 10,000 kg produces a 20-30% increase in $Q_{s,tot}$. Maximum cross range increases by ~20% with an increase in entry velocity from 11 to 12.5 km/s. For this optimization setup, the heat load has been determined to increase linearly with ballistic coefficient. The rate at which heat load increases with ballistic coefficient at an entry velocity of 12.5 km/s is a factor of 1.59 greater than the rate at 11 km/s.

15.3. Suggestions for Future Work

A substantial amount of future work in atmospheric entry vehicles can be completed to improve upon both this work and the general understanding of the field. To increase the accuracy of the optimization results, the following additions could be made:

- Account for corner radius. The work of Zoby[47] may also assist in distinguishing heat shields of the same axial shape and cross-section but different corner radii. The corner radius geometry can also be added to the 3D mesh so that the surface pressure distribution accounts for it.

- Improve the method for estimating the shock-standoff distance for angles of attack, especially for the power law axial shape and in accounting for base eccentricity.
- Use a more accurate method to determine the surface pressure distribution. For this work Newtonian Impact Theory was validated, but if the scope of the project were to include analyzing the boundary layer, advanced CFD would need to be applied.
- Utilize a more detailed mass estimation study of manned and unmanned atmospheric entry vehicles.

To increase the scope of the optimization, the following additions could be made:

- Incorporate more axial shapes: the raked, biconic, and bent-biconic cones.
- Include thermal material properties and temperature constraints.
- Include a model for high temperature gas properties at 200000 ft, $M_\infty > 42$. The Tannehill correlations are outside their range for these freestream Mach numbers.
- Develop a method of determining the point of maximum heating for a general 3D body. The velocity gradient could be modeled to determine the point of maximum convective heating for a general 3D body. Zoby[47] provides some results based on the change in the velocity gradient in order to calculate the convection for values of $r_n/d > 2$ more accurately than using the inverse square-root of the nose radius.

Future work concerning atmospheric entry vehicles outside this optimization that would benefit the field:

- Conduct a feasibility study of the static stability of this work's optimal geometries with the estimated required center-of-gravity locations, assuming different types of crew compartment shapes (conical frustum for Apollo CM and Orion CEV). Determine the dynamic stability using a six degree-of-freedom trajectory analysis.
- Analyze raked geometries to reduce cg-offset to generate desire L/D_{trim}. There may be indication that AFE, a raked cone, is dynamically unstable, but this may be fixed by modifying the AFE configuration to have a crew compartment similar in shape to the conical frustum of the Apollo Command Module, which would be a topic for future work.
- Determine whether sonic line movement is present on optimal geometries with higher eccentricity from this work.
- Mitigating sonic line movement on raked cones and raked oblate spherical-segments. Sonic line movement produces static instabilities at geometries at specific M_∞. Raked oblate spherical segment geometries could be generated with similar L/D and C_D to AFE and determine how to make the sonic line stationary on leeward side's shoulder.
- Comparison of $L/D = 1 - 2$ slender body vehicles with both trajectory optimization and aerothermodynamic CFD. A study of their performance at lower entry velocities at which the heat load $Q_{s,tot}$ and heat flux $q_{s,max}$ are deemed feasible.
- Analyze the performance of entry with two trim lift-to-drag ratios with a slender vehicle design. In this way, at high α_{trim}, produce low L/D with high

drag area and at low α_{trim}, produce high *L/D* to provide high cross range. Determine best combination of *L/D* values for minimizing heat load and maximizing cross range simultaneously.

- Determine significance and viability of a two-stage entry vehicle. A blunt heat shield would be used to bleed off most thermal energy, and then a sharp vehicle with propulsion capability could be utilized to transit worldwide.
- Determine possible Mars entry blunt-body geometries for manned missions. Analyze the Mars trajectory design space and recognize current limitations and employ global search capability to assist in locating feasible designs that meet mission requirements.
- Correlating important flow characteristics observed in CFD to low-order methods. This could serve to update the low-order methods to improve accuracy. Feedback high-order analysis into low-order aerothermodynamic models to execute more accurate optimization.
- Perform improved optimization to mitigate aerothermodynamic and boundary layer transition effects.
- Determine wake effects/vehicle interactions for ballute-type heat shields.
- Study laminar, transition, and turbulent boundary layer heat transfer on blunt bodies for $M_\infty > 25$. Wind tunnel analysis of rounded-edge concave heat shields would help in investigating these phenomena. The Apollo Command Module's heat shield experienced laminar heat transfer. Turbulent heat transfer is unknown at $M_\infty > 40$, especially the effects of radiation cooling and convective-radiative coupling that reduce the total heat transfer flux. For a

phenomenon that increases exponentially with Mach number, the radiative heat transfer can easily be miscalculated for $M_\infty > 40$.

- Static and dynamic stability guidelines for inhabited atmospheric entry.
- Flight tests and wind tunnel experiments for $M_\infty > 40$ ranging up to $M_\infty = 55$. This could provide arguably the most useful results concerning planetary entry at $M_\infty > 40$. Current aerothermodynamic understanding of this region of freestream Mach numbers is modest. Since rolling moment experimental and flight data is almost nonexistent, measuring the rolling moment on both axisymmetric and non-axisymmetric heat shields would be beneficial. High temperature correlations, radiation and general heat transfer models could be produced for the first time. Hypersonic aerothermodynamic models can be improved. Some models do exist, but they do not apply well to $M_\infty > 40$.

Appendix A: Curve Fits to Kaattari's Method

A.1 $\theta_* - \theta_{*o}$ as a function of Φ_*

To determine θ_*, Kaattari supplies Figure 6(b) from Ref. [55] that relates the difference $\theta_* - \theta_{*o}$ as a function of Φ_*. This relation varies with the normal-shock density ratio and their corresponding curve-fit equations with Φ_* limits are included

$$
\frac{\theta_* - \theta_{*o}}{(\text{deg})} = \begin{cases}
-7.8164\times10^{-9}\Phi_*^6 + 1.1554\times10^{-6}\Phi_*^5 \\
\quad -6.5557\times10^{-5}\Phi_*^4 + 0.0017384\Phi_*^3 \\
\quad -0.01669\Phi_*^2 - 0.036272\Phi_* + 0.026591, & \frac{\rho_2}{\rho_1} = 3, \quad 1 < \Phi_* \le 40 \\
\quad \text{Norm of residuals: } 0.10637, & \\
-1.3002\times10^{-8}\Phi_*^6 + 1.7632\times10^{-6}\Phi_*^5 \\
\quad -9.1189\times10^{-5}\Phi_*^4 + 0.0021927\Phi_*^3 \\
\quad -0.01933\Phi_*^2 + 0.01135\Phi_* + 0.0031709, & \frac{\rho_2}{\rho_1} = 4, \quad 1 < \Phi_* \le 40 \\
\quad \text{Norm of residuals: } 0.04381, & \\
-6.2549\times10^{-9}\Phi_*^6 + 8.0483\times10^{-7}\Phi_*^5 \\
\quad -3.7688\times10^{-5}\Phi_*^4 + 0.00087115\Phi_*^3 \\
\quad -0.0054599\Phi_*^2 + 0.019362\Phi_* - 0.0085934, & \frac{\rho_2}{\rho_1} = 6, \quad 4 < \Phi_* \le 40 \\
\quad \text{Norm of residuals: } 0.0793, & \\
-6.0809\times10^{-9}\Phi_*^6 + 6.9855\times10^{-7}\Phi_*^5 \\
\quad -2.7801\times10^{-5}\Phi_*^4 + 0.00053225\Phi_*^3 \\
\quad +\ 0.00034058\Phi_*^2 - 0.0016152\Phi_* + 0.0038209, & \frac{\rho_2}{\rho_1} = 8, \quad 4 < \Phi_* \le 40 \\
\quad \text{Norm of residuals: } 0.0583, & \\
-9.8112\times10^{-11}\Phi_*^8 + 1.4038\times10^{-8}\Phi_*^7 \\
\quad -8.0148\times10^{-7}\Phi_*^6 + 2.3289\times10^{-5}\Phi_*^5 \\
\quad -0.00035965\Phi_*^4 + 0.0028275\Phi_*^3 & \frac{\rho_2}{\rho_1} = 12, \quad 0 < \Phi_* \le 40 \\
\quad -0.0034554\Phi_*^2 + 0.0075298\Phi_* - 0.00075942, & \\
\quad \text{Norm of residuals: } 0.067392, & \\
1.5644\times10^{-7}\Phi_*^6 - 3.0006\times10^{-5}\Phi_*^5 \\
\quad +\ 0.0023397\Phi_*^4 - 0.094787\Phi_*^3 \\
\quad +\ 2.1177\Phi_*^2 - 24.509\Phi_* + 115.89, & \frac{\rho_2}{\rho_1} = 16, \quad 17.5 < \Phi_* \le 40 \\
\quad \text{Norm of residuals: } 0.0795, & \\
1.2753\times10^{-8}\Phi_*^6 - 1.4433\times10^{-6}\Phi_*^5 \\
\quad +\ 6.7379\times10^{-5}\Phi_*^4 - 0.0014138\Phi_*^3 \\
\quad +\ 0.020612\Phi_*^2 - 0.040357\Phi_* + 0.012458, & \frac{\rho_2}{\rho_1} = 20, \quad 1 < \Phi_* \le 40. \\
\quad \text{Norm of residuals: } 0.11582, &
\end{cases}
\tag{A.1}
$$

For all equations in this set except $\rho_2/\rho_1 = 12$, for $0 < \Phi_* < 1$ it is assumed that the difference $\theta_* - \theta_{*o}$ is zero. For this region, the equation for $\rho_2/\rho_1 = 12$ is applied for normal-shock density ratios of twelve and greater. The equation for $\rho_2/\rho_1 = 16$ is not applied until $\Phi_* > 17.5$, and if it is used before this, the results could be erroneous since the curve fit was designed only for the noted ranges. Linear interpolation between two of the curves within this range of ρ_2/ρ_1 can be exercised to approximate the values of the difference for normal-shock density ratios that are not listed.

A.2 c_1 as a function of ρ_2/ρ_1 and ε

Figure 9(a) from Ref. [54] shows how the shock correlation coefficient c_1 varies with the normal-shock density ratio and the tangency angle ε and is curve-fitted (input ε in degrees) with indicated limits of applicability

$$c_1 = \begin{cases} -1.93013729\times10^{-7}\varepsilon^3 + 1.16661976\times10^{-5}\varepsilon^2 \\ \quad -7.64482284\times10^{-4}\varepsilon + 0.214380383 & \dfrac{\rho_2}{\rho_1} = 3, \quad 0 < \varepsilon \le 45^o, \\ \quad R^2 = 0.9987, & \\ \\ 9.63317384\times10^{-7}\varepsilon^3 - 8.78810663\times10^{-5}\varepsilon^2 \\ \quad -7.60025063\times10^{-4}\varepsilon + 0.221403281 & \dfrac{\rho_2}{\rho_1} = 4, \quad 0 < \varepsilon \le 45^o, \\ \quad R^2 = 0.9998, & \\ \\ -4.12212802\times10^{-11}\varepsilon^6 + 5.39975415\times10^{-9}\varepsilon^5 \\ \quad -2.31598093\times10^{-7}\varepsilon^4 + 4.78956150\times10^{-6}\varepsilon^3 \\ \quad -1.15717926\times10^{-4}\varepsilon^2 - 2.21715933\times10^{-3}\varepsilon & \dfrac{\rho_2}{\rho_1} = 5, \quad 0 < \varepsilon \le 45^o, \\ \quad +0.230264502 & \\ \quad R^2 = 0.9999, & \end{cases} \tag{A.2}$$

$$
c_1 = \begin{cases}
-2.92464389\times10^{-10}\varepsilon^5 - 2.69993388\times10^{-9}\varepsilon^4 \\
\quad +4.08148122\times10^{-6}\varepsilon^3 - 2.09241117\times10^{-4}\varepsilon^2 \\
\quad -2.50199798\times10^{-3}\varepsilon + 0.232732751 & \dfrac{\rho_2}{\rho_1}=6, \quad 0<\varepsilon\le 42.5^o, \\
\qquad R^2 = 0.9999, & \\
\\
-9.07434828\times10^{-10}\varepsilon^5 + 6.32411067\times10^{-8}\varepsilon^4 \\
\quad +2.18083922\times10^{-6}\varepsilon^3 - 1.56690529\times10^{-4}\varepsilon^2 \\
\quad -4.54631057\times10^{-3}\varepsilon + 0.231841134 & \dfrac{\rho_2}{\rho_1}=8, \quad 0<\varepsilon\le 42.5^o, \\
\qquad R^2 = 0.9999, & \\
\\
2.00439718\times10^{-10}\varepsilon^6 - 2.99995789\times10^{-8}\varepsilon^5 \\
\quad +1.62858238\times10^{-6}\varepsilon^4 - 3.65809838\times10^{-5}\varepsilon^3 \\
\quad +3.31432550\times10^{-4}\varepsilon^2 - 8.40015875\times10^{-3}\varepsilon \\
\quad +0.232406493 & \dfrac{\rho_2}{\rho_1}=10, \quad 0<\varepsilon\le 40^o, \\
\qquad R^2 = 0.9999, & \\
\\
2.56915093\times10^{-10}\varepsilon^6 - 3.32278424\times10^{-8}\varepsilon^5 \\
\quad +1.52078813\times10^{-6}\varepsilon^4 - 2.69805855\times10^{-5}\varepsilon^3 \\
\quad +2.01204775\times10^{-4}\varepsilon^2 - 9.22392526\times10^{-3}\varepsilon \\
\quad +0.232157648 & \dfrac{\rho_2}{\rho_1}=12, \quad 0<\varepsilon\le 40^o, \\
\qquad R^2 = 0.9998, & \\
\\
4.06700008\times10^{-9}\varepsilon^5 - 5.34031912\times10^{-7}\varepsilon^4 \\
\quad +2.54224815\times10^{-5}\varepsilon^3 - 3.58846154\times10^{-4}\varepsilon^2 \\
\quad -8.09283123\times10^{-3}\varepsilon + 0.221551084 & \dfrac{\rho_2}{\rho_1}=16, \quad 0<\varepsilon\le 40^o, \\
\qquad R^2 = 0.9997, & \\
\\
6.06112566\times10^{-9}\varepsilon^5 - 7.49638803\times10^{-7}\varepsilon^4 \\
\quad +3.16638882\times10^{-5}\varepsilon^3 - 3.50334207\times10^{-4}\varepsilon^2 \\
\quad -9.44613956\times10^{-3}\varepsilon + 0.210113003 & \dfrac{\rho_2}{\rho_1}=20, \quad 0<\varepsilon\le 40^o, \\
\qquad R^2 = 0.9991, & \\
\\
4.60808129\times10^{-9}\varepsilon^5 - 6.46122093\times10^{-7}\varepsilon^4 \\
\quad +2.95290942\times10^{-5}\varepsilon^3 - 3.29553862\times10^{-4}\varepsilon^2 \\
\quad -9.52531793\times10^{-3}\varepsilon + 0.200148091 & \dfrac{\rho_2}{\rho_1}=22, \quad 0<\varepsilon\le 40^o. \\
\qquad R^2 = 0.9990, &
\end{cases}
\tag{A.2}
$$

Note that all the digits have to be included in order to maintain accuracy. If digits are removed, it is strongly recommended that the modified curve-fit be plotted to verify that the curve-fit is still valid throughout the entire range and to verify none of the curve-fits intersect each other. Interpolation for cases with normal-shock density ratios in-between the given curve fits has been tested and is completely feasible.

A.3 c_3 as a function of ρ_2/ρ_1 and ε

The correlation constant c_3 is also supplied in Figure 9(b) from Ref. [54], and the curve-fit equations (input ε in degrees) have been generated in this work

$$c_3\left(\frac{r_n \sin(\varepsilon)}{d}\right)^2 = \begin{cases} -3.39744191\times10^{-8}\varepsilon^3 + 3.89964215\times10^{-6}\varepsilon^2 \\ \quad -1.82847314\times10^{-4}\varepsilon + 0.0231888243 & \frac{\rho_2}{\rho_1}=3,\quad 0<\varepsilon\le 45^o, \\ \quad R^2 = 0.9994, & \\ -1.48406667\times10^{-8}\varepsilon^3 + 1.72390334\times10^{-6}\varepsilon^2 \\ \quad -1.35288319\times10^{-4}\varepsilon + 0.0201117430 & \frac{\rho_2}{\rho_1}=4,\quad 0<\varepsilon\le 45^o, \\ \quad R^2 = 0.9995, & \\ -7.15150540\times10^{-12}\varepsilon^6 + 9.54110294\times10^{-10}\varepsilon^5 \\ \quad -4.49628934\times10^{-8}\varepsilon^4 + 8.56040487\times10^{-7}\varepsilon^3 \\ \quad -4.96819914\times10^{-6}\varepsilon^2 - 1.14702612\times10^{-4}\varepsilon & \frac{\rho_2}{\rho_1}=5,\quad 0<\varepsilon\le 45^o, \\ \quad +1.77036651\times10^{-2} & \\ \quad R^2 = 0.9998, & \\ -1.13917530\times10^{-10}\varepsilon^5 + 1.63488703\times10^{-8}\varepsilon^4 \\ \quad -7.24637110\times10^{-7}\varepsilon^3 + 9.92739734\times10^{-6}\varepsilon^2 \\ \quad -1.27550983\times10^{-4}\varepsilon + 0.0159334044 & \frac{\rho_2}{\rho_1}=6,\quad 0<\varepsilon\le 45^o, \\ \quad R^2 = 0.9995, & \\ -3.80921614\times10^{-10}\varepsilon^5 + 4.33744906\times10^{-8}\varepsilon^4 \\ \quad -1.56325253\times10^{-6}\varepsilon^3 + 1.66417857\times10^{-5}\varepsilon^2 \\ \quad -1.21889535\times10^{-4}\varepsilon + 0.0149288590 & \frac{\rho_2}{\rho_1}=7,\quad 0<\varepsilon\le 45^o, \\ \quad R^2 = 0.9995, & \\ -5.69532428\times10^{-10}\varepsilon^5 + 6.22306898\times10^{-8}\varepsilon^4 \\ \quad -2.15386203\times10^{-6}\varepsilon^3 + 2.21510280\times10^{-5}\varepsilon^2 \\ \quad -1.32633841\times10^{-4}\varepsilon + 0.0141488648 & \frac{\rho_2}{\rho_1}=8,\quad 0<\varepsilon\le 40^o, \\ \quad R^2 = 0.9994, & \end{cases} \tag{A.3}$$

$$c_3\left(\frac{r_n \sin(\varepsilon)}{d}\right)^2 = \begin{cases} -7.04675716\times10^{-10}\varepsilon^5 + 7.25696594\times10^{-8}\varepsilon^4 \\ \quad -2.32498214\times10^{-6}\varepsilon^3 + 2.06298722\times10^{-5}\varepsilon^2 \\ \quad -1.27943518\times10^{-4}\varepsilon + 0.0131448916 & \frac{\rho_2}{\rho_1} = 10, \quad 0 < \varepsilon \le 40^o, \\ \qquad R^2 = 0.9995, \\ -7.03151544\times10^{-10}\varepsilon^5 + 6.54759070\times10^{-8}\varepsilon^4 \\ \quad -1.73419068\times10^{-6}\varepsilon^3 + 5.67714535\times10^{-6}\varepsilon^2 \\ \quad -4.76005398\times10^{-5}\varepsilon + 0.0119228070 & \frac{\rho_2}{\rho_1} = 14, \quad 0 < \varepsilon \le 40^o, \\ \qquad R^2 = 0.9993, \\ -6.61739779\times10^{-10}\varepsilon^5 + 6.12012384\times10^{-8}\varepsilon^4 \\ \quad -1.56703453\times10^{-6}\varepsilon^3 + 2.90105343\times10^{-6}\varepsilon^2 \\ \quad -4.37257752\times10^{-5}\varepsilon + 0.0116297874 & \frac{\rho_2}{\rho_1} = 16, \quad 0 < \varepsilon \le 40^o, \\ \qquad R^2 = 0.9996, \\ -6.61739779\times10^{-10}\varepsilon^5 + 6.12012384\times10^{-8}\varepsilon^4 \\ \quad -1.56703453\times10^{-6}\varepsilon^3 + 2.90105343\times10^{-6}\varepsilon^2 \\ \quad -4.37257752\times10^{-5}\varepsilon + 0.0113797874 & \frac{\rho_2}{\rho_1} = 18, \quad 0 < \varepsilon \le 40^o, \\ \qquad R^2 = 0.9996 \\ -6.61739779\times10^{-10}\varepsilon^5 + 6.12012384\times10^{-8}\varepsilon^4 \\ \quad -1.56703453\times10^{-6}\varepsilon^3 + 2.90105343\times10^{-6}\varepsilon^2 \\ \quad -4.37257752\times10^{-5}\varepsilon + 0.0111547874 & \frac{\rho_2}{\rho_1} = 20, \quad 0 < \varepsilon \le 40^o, \\ \qquad R^2 = 0.9996 \\ -6.61739779\times10^{-10}\varepsilon^5 + 6.12012384\times10^{-8}\varepsilon^4 \\ \quad -1.56703453\times10^{-6}\varepsilon^3 + 2.90105343\times10^{-6}\varepsilon^2 \\ \quad -4.37257752\times10^{-5}\varepsilon + 0.0109422874 & \frac{\rho_2}{\rho_1} = 22, \quad 0 < \varepsilon \le 40^o. \\ \qquad R^2 = 0.9996, \end{cases} \tag{A.3}$$

Because density ratios over sixteen may occur in the regions of maximum heat transfer during planetary entry, extrapolation is applied to the curve-fit for $\rho_2/\rho_1 > 16$.

Appendix B: Design Variable Distributions for Lunar Return Results in Chapter 12

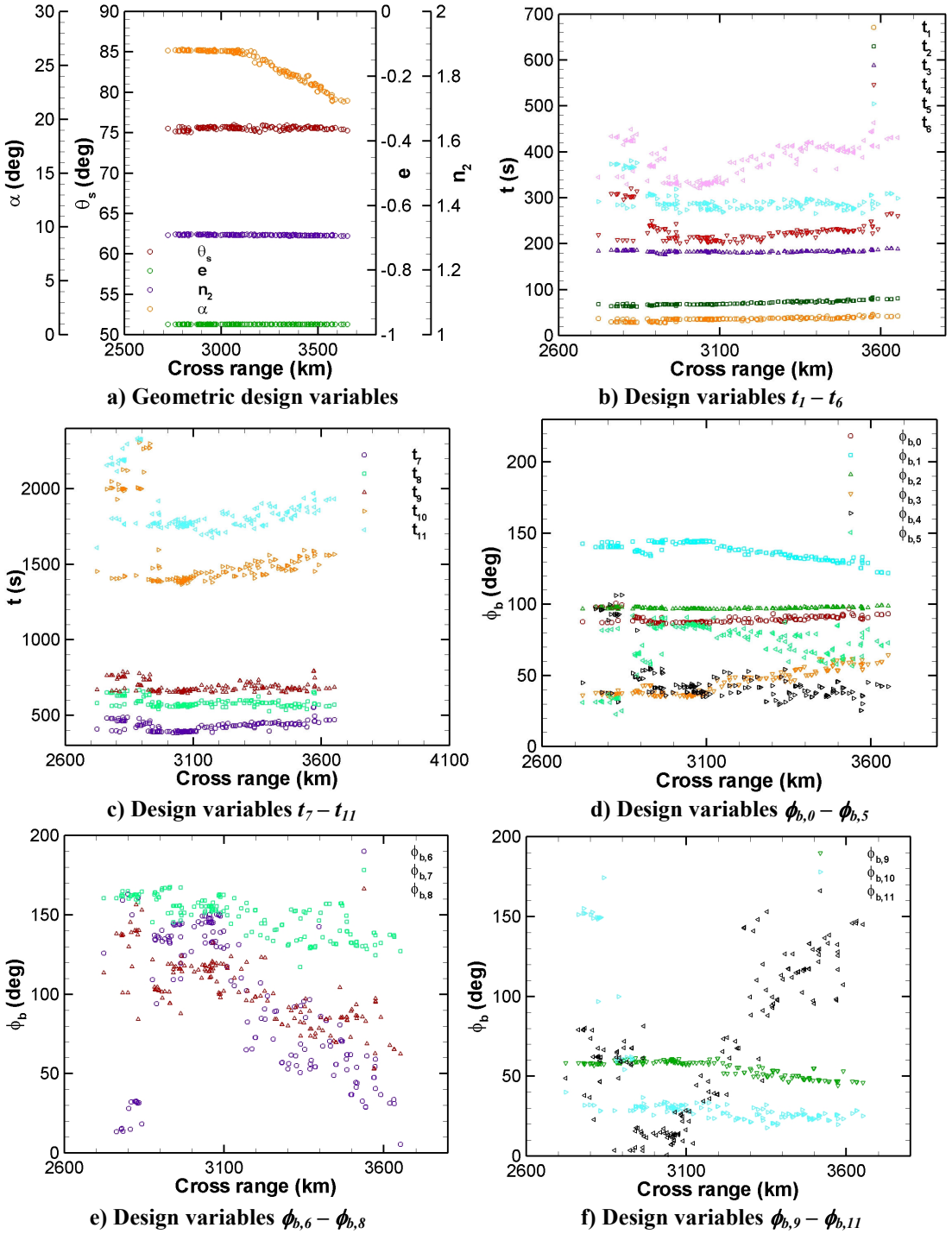

a) Geometric design variables

b) Design variables $t_1 - t_6$

c) Design variables $t_7 - t_{11}$

d) Design variables $\phi_{b,0} - \phi_{b,5}$

e) Design variables $\phi_{b,6} - \phi_{b,8}$

f) Design variables $\phi_{b,9} - \phi_{b,11}$

Figure B.0.1. Design Variable Distributions for Pareto frontier of L/D = 1.0, SS lower mass case from Figure 12.1, for maximizing cross range and minimizing stagnation-point heat load, V_E = 11 km/s.

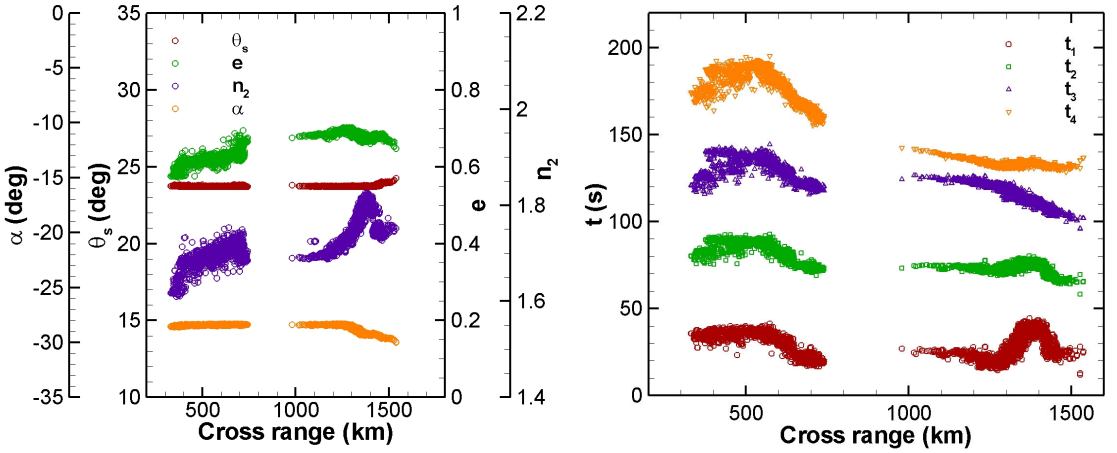

a) Geometric design variables

b) Design variables $t_1 - t_4$

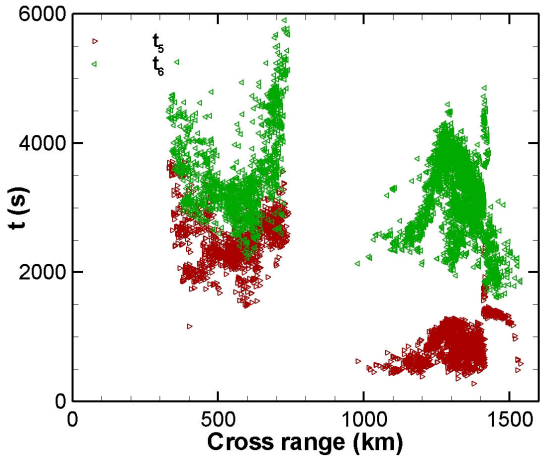

c) Design variables t_5 and t_6

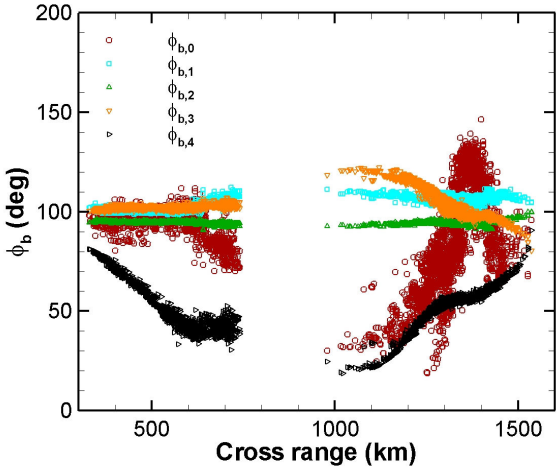

d) Design variables $\phi_{b,0} - \phi_{b,4}$

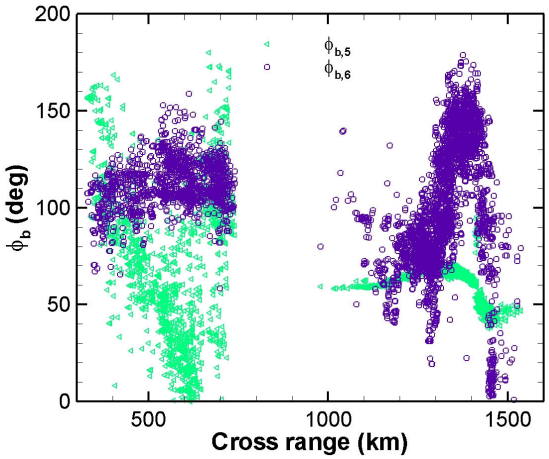

e) Design variables $\phi_{b,5}$ and $\phi_{b,6}$

Figure B.0.2. Design Variable Distributions for Pareto frontier of L/D = 0.5, SS lower mass case from Figure 12.1, for maximizing cross range and minimizing stagnation-point heat load, V_E = 11 km/s.

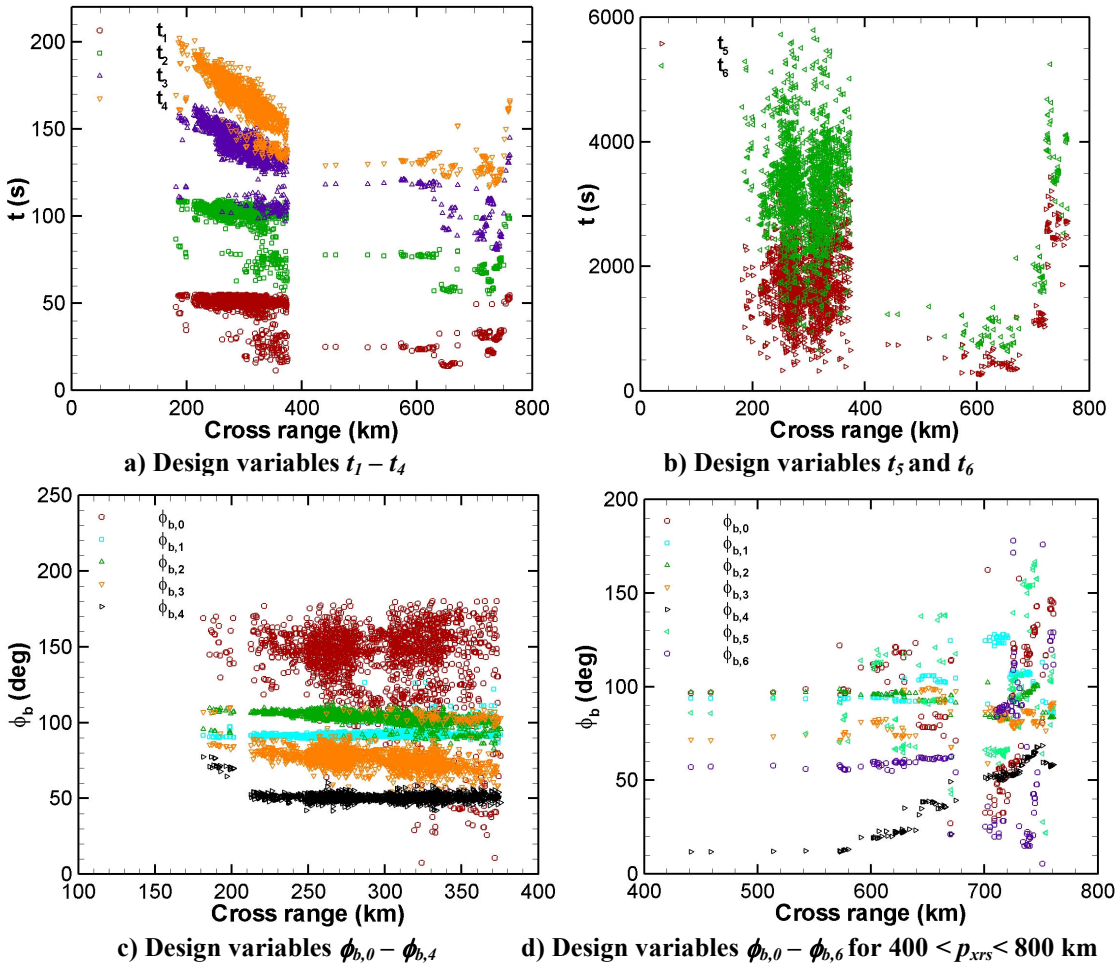

a) Design variables $t_1 - t_4$

b) Design variables t_5 and t_6

c) Design variables $\phi_{b,0} - \phi_{b,4}$

d) Design variables $\phi_{b,0} - \phi_{b,6}$ for $400 < p_{xrs} < 800$ km

Figure B.0.3. Design Variable Distributions for Pareto frontier of $L/D = 0.27$, Orion CEV projection at 10,000 kg from Figure 12.1, for maximizing cross range and minimizing stagnation-point heat load, $V_E = 11$ km/s.

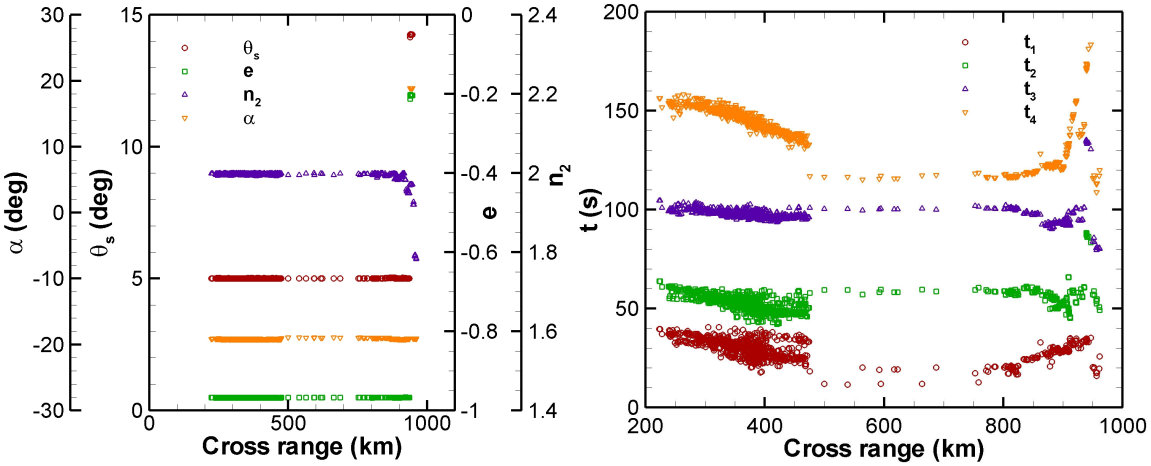

a) Geometric design variables

b) Design variables $t_1 - t_4$

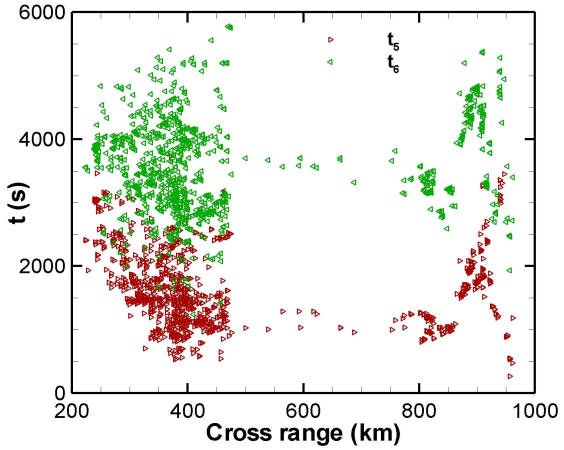

c) Design variables t_5 and t_6

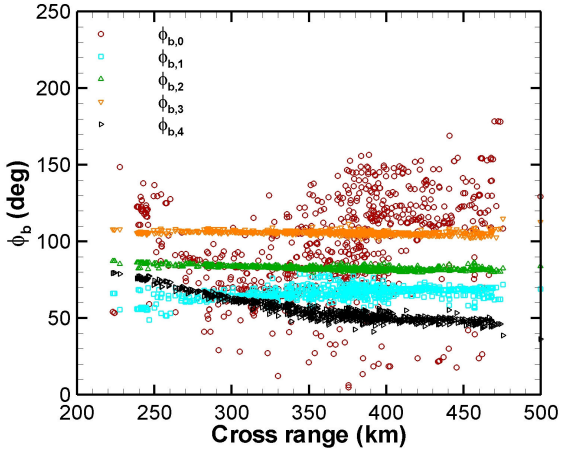

d) Design variables $\phi_{b,0} - \phi_{b,4}$

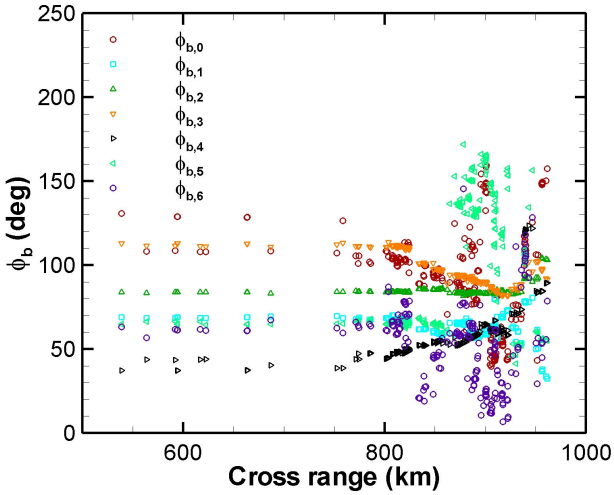

e) Design variables $\phi_{b,0} - \phi_{b,6}$ for $500 < p_{xrs} < 1000$ km

Figure B.0.4. Design Variable Distributions for Pareto frontier of L/D = 0.3, SS lower mass case from Figure 12.1, for maximizing cross range and minimizing stagnation-point heat load, V_E = 11 km/s.

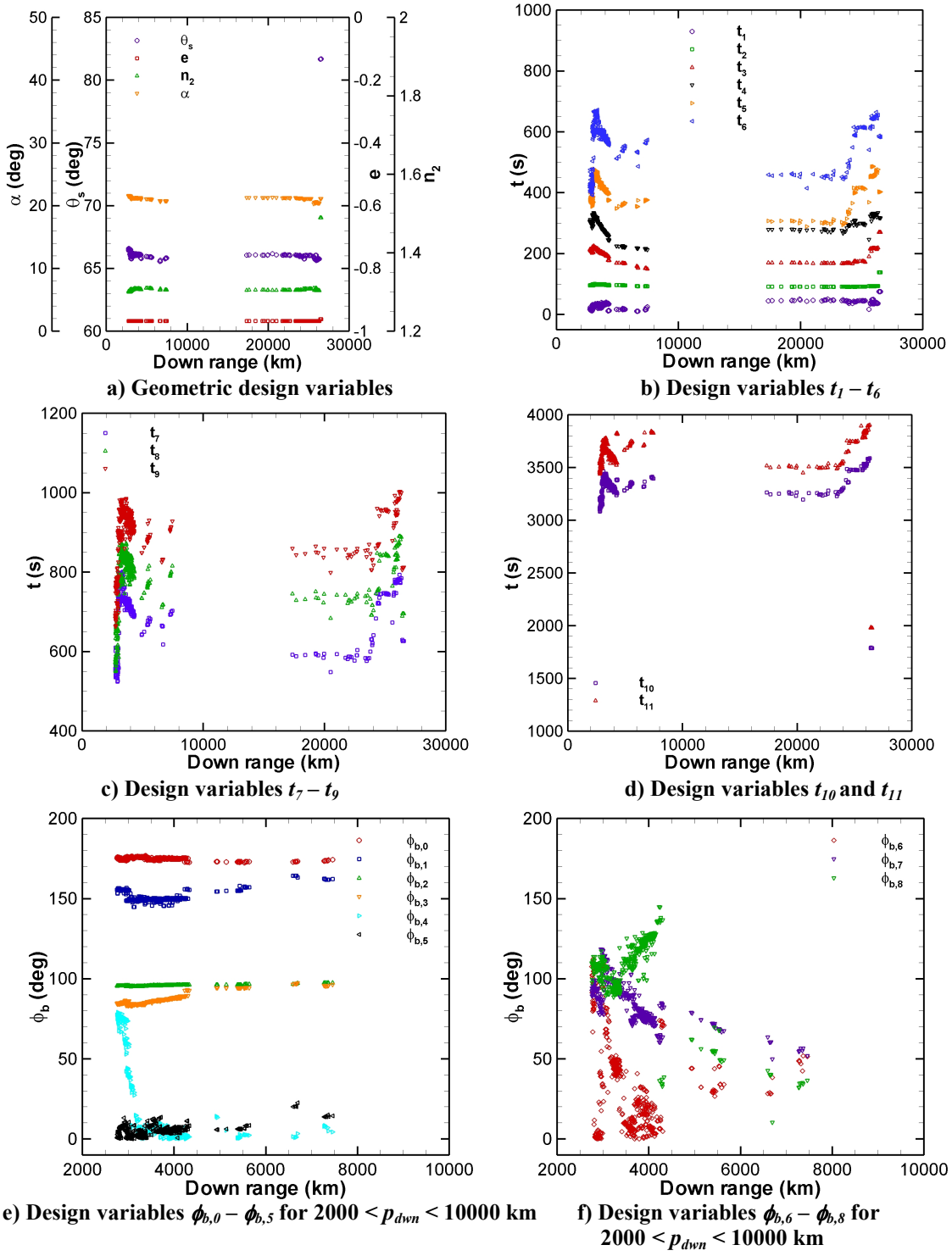

a) Geometric design variables

b) Design variables $t_1 - t_6$

c) Design variables $t_7 - t_9$

d) Design variables t_{10} and t_{11}

e) Design variables $\phi_{b,0} - \phi_{b,5}$ for $2000 < p_{dwn} < 10000$ km

f) Design variables $\phi_{b,6} - \phi_{b,8}$ for $2000 < p_{dwn} < 10000$ km

Figure B.0.5. Design Variable Distributions for Pareto frontier of L/D = 1.0, SS upper mass case from Figure 12.2, for maximizing down range and minimizing stagnation-point heat load, V_E = 11 km/s.

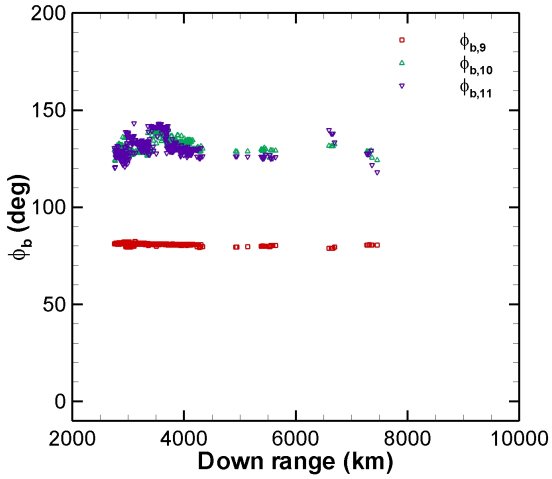

g) Design variables $\phi_{b,9} - \phi_{b,11}$ for $2000 < p_{dwn} < 10000$ km

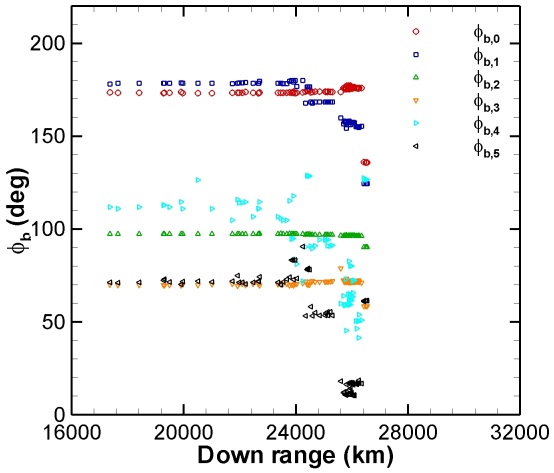

h) Design variables $\phi_{b,0} - \phi_{b,5}$ for $16^{E3} < p_{dwn} < 30^{E3}$ km

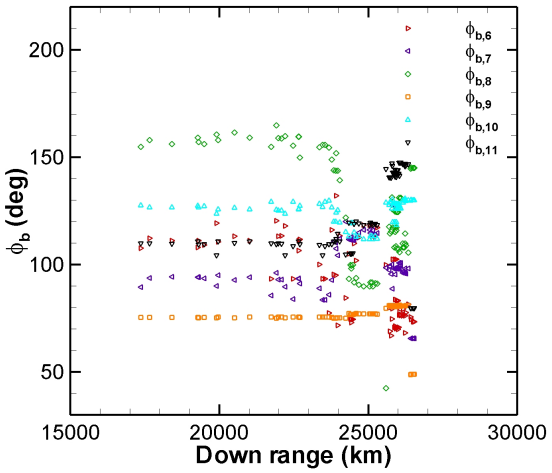

i) Design variables $\phi_{b,6} - \phi_{b,11}$ for $15^{E3} < p_{dwn} < 30^{E3}$ km

Figure B.0.5 (continued) Design Variable Distributions for Pareto frontier of L/D = 1.0, SS upper mass case from Figure 12.2, for maximizing down range and minimizing stagnation-point heat load, V_E = 11 km/s.

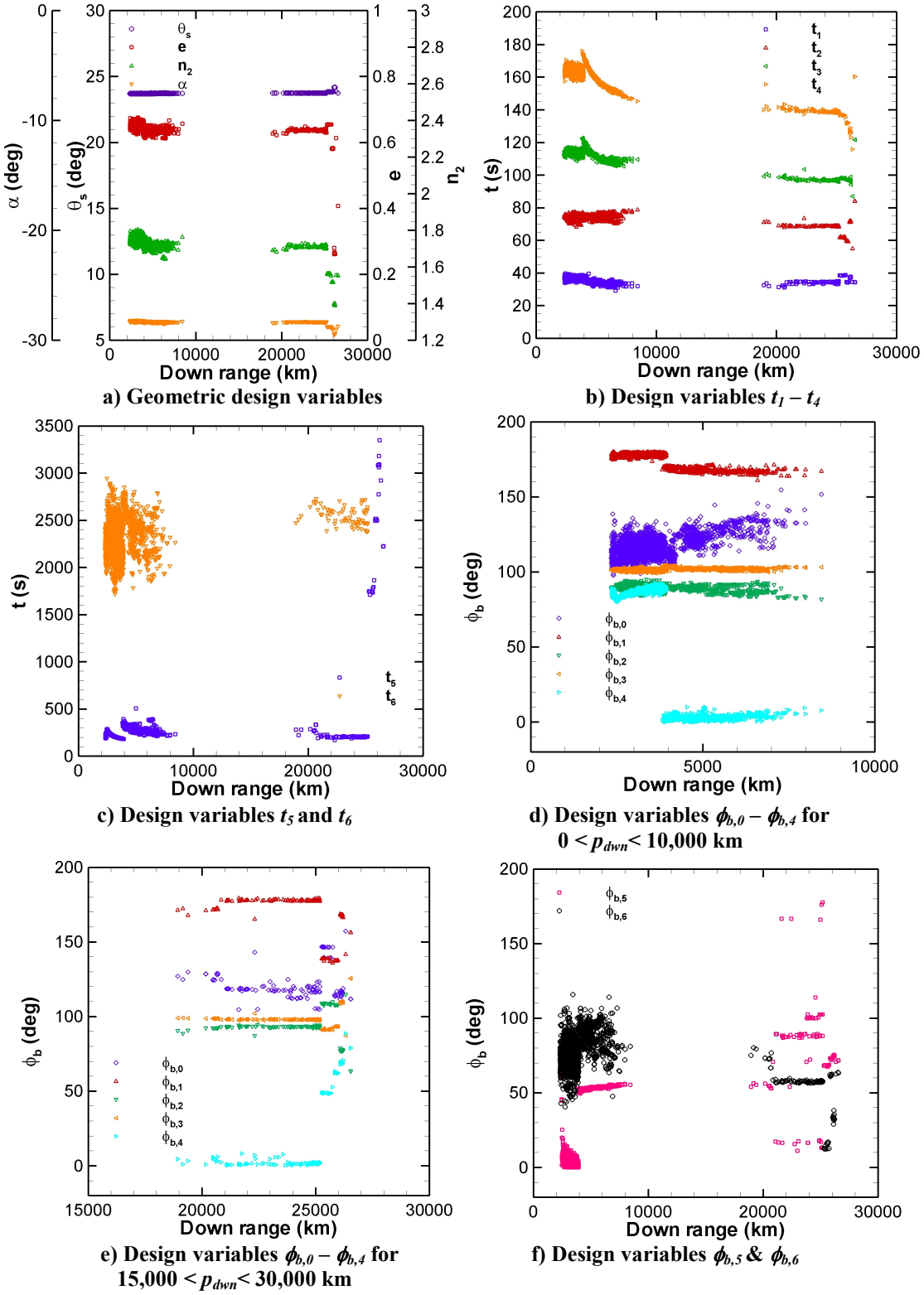

a) Geometric design variables

b) Design variables $t_1 - t_4$

c) Design variables t_5 and t_6

d) Design variables $\phi_{b,0} - \phi_{b,4}$ for $0 < p_{dwn} < 10{,}000$ km

e) Design variables $\phi_{b,0} - \phi_{b,4}$ for $15{,}000 < p_{dwn} < 30{,}000$ km

f) Design variables $\phi_{b,5}$ & $\phi_{b,6}$

Figure B.0.6. Design Variable Distributions for Pareto frontier of L/D = 0.5, SS upper mass case from Figure 12.2, for maximizing down range and minimizing stagnation-point heat load, V_E = 11 km/s.

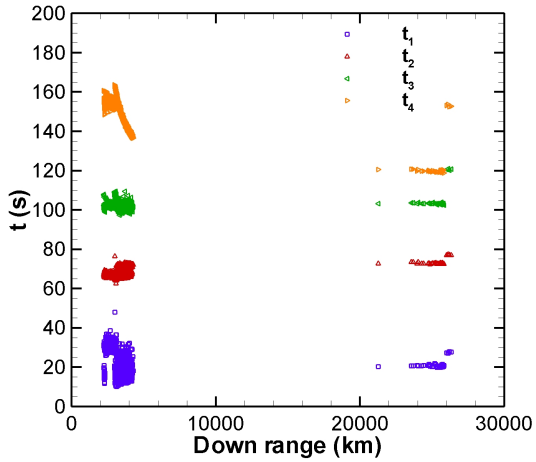

a) Design variables $t_1 - t_4$

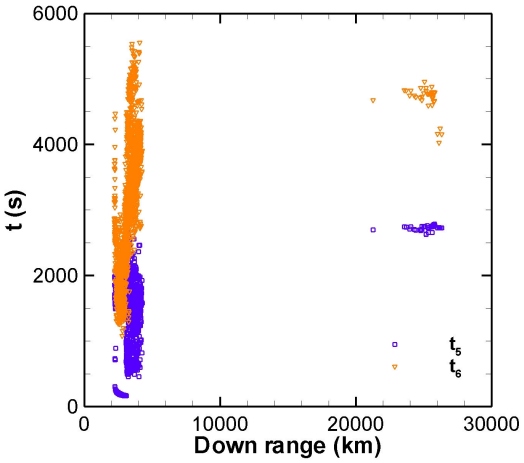

b) Design variables t_5 and t_6

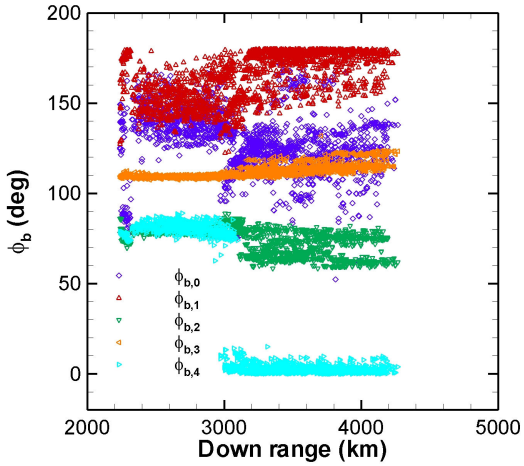

c) Design variables $\phi_{b,0} - \phi_{b,4}$ for $0 < p_{dwn} < 5000$ km

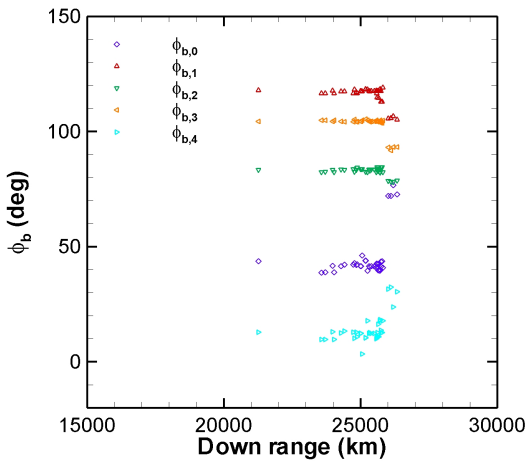

d) Design variables $\phi_{b,0} - \phi_{b,3}$ for $15{,}000 < p_{dwn} < 30{,}000$ km

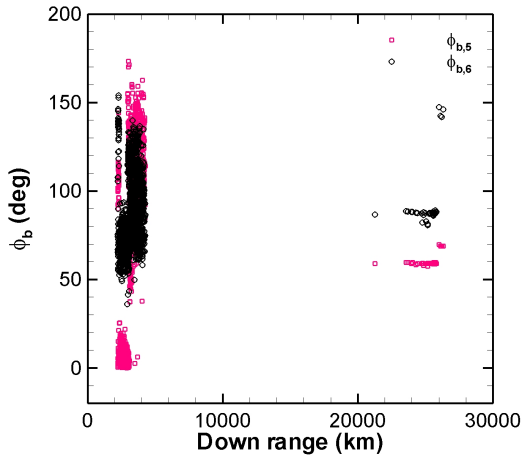

e) Design variables $\phi_{b,5}$ & $\phi_{b,6}$

Figure B.0.7. Design Variable Distributions for Pareto frontier of L/D = 0.3, Orion CEV, projection at 10000 kg case from Figure 12.2, for maximizing down range and minimizing stagnation-point heat load, V_E = 11 km/s.

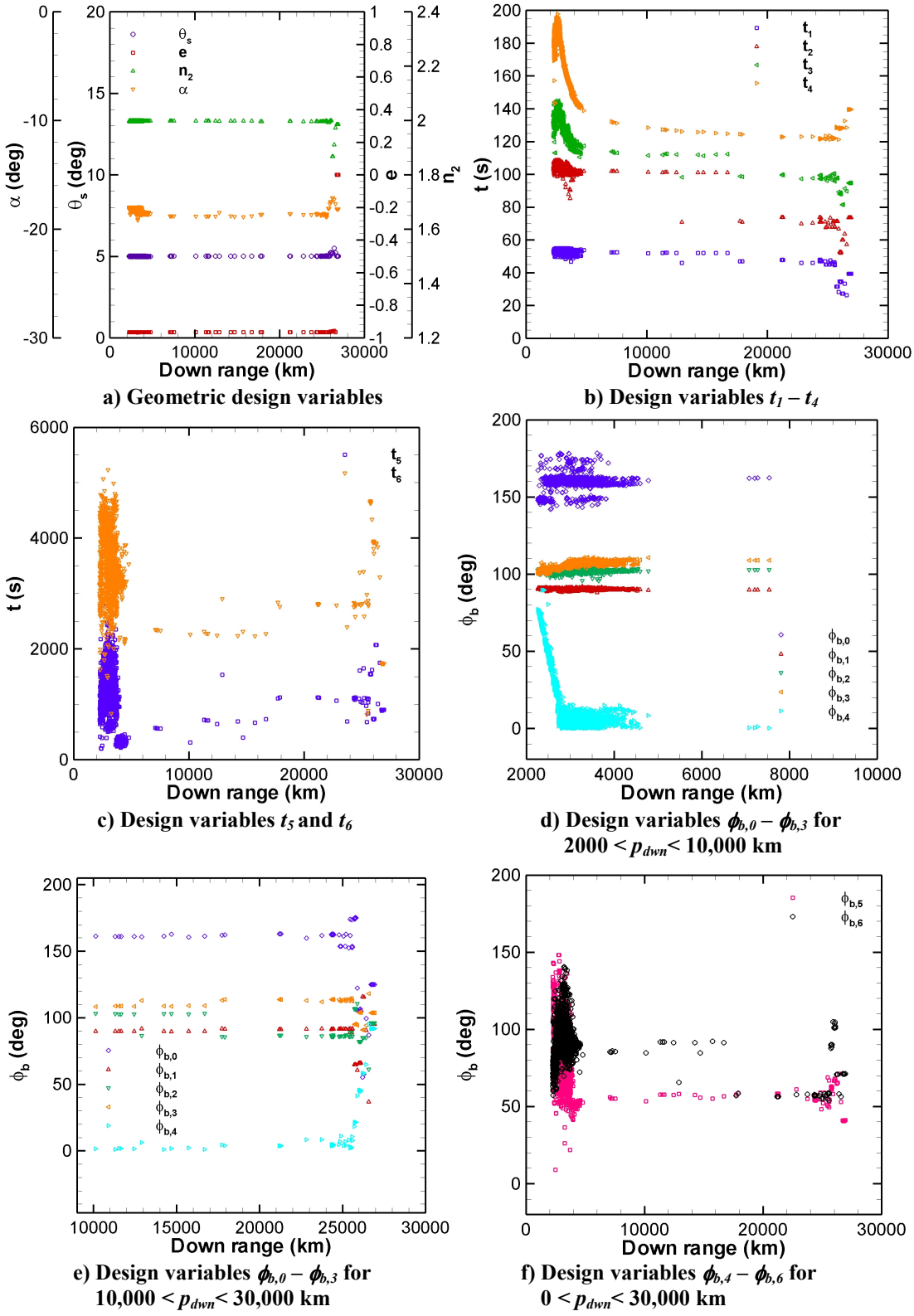

a) Geometric design variables

b) Design variables $t_1 - t_4$

c) Design variables t_5 and t_6

d) Design variables $\phi_{b,0} - \phi_{b,3}$ for $2000 < p_{dwn} < 10{,}000$ km

e) Design variables $\phi_{b,0} - \phi_{b,3}$ for $10{,}000 < p_{dwn} < 30{,}000$ km

f) Design variables $\phi_{b,4} - \phi_{b,6}$ for $0 < p_{dwn} < 30{,}000$ km

Figure B.0.8. Design Variable Distributions for Pareto frontier of L/D = 0.3, SS upper mass, e = -0.968 IC case from Figure 12.2, for maximizing down range and minimizing stagnation-point heat load, V_E = 11 km/s.

Appendix C: Design Variable Distributions for Mars Return Results in Chapter 13

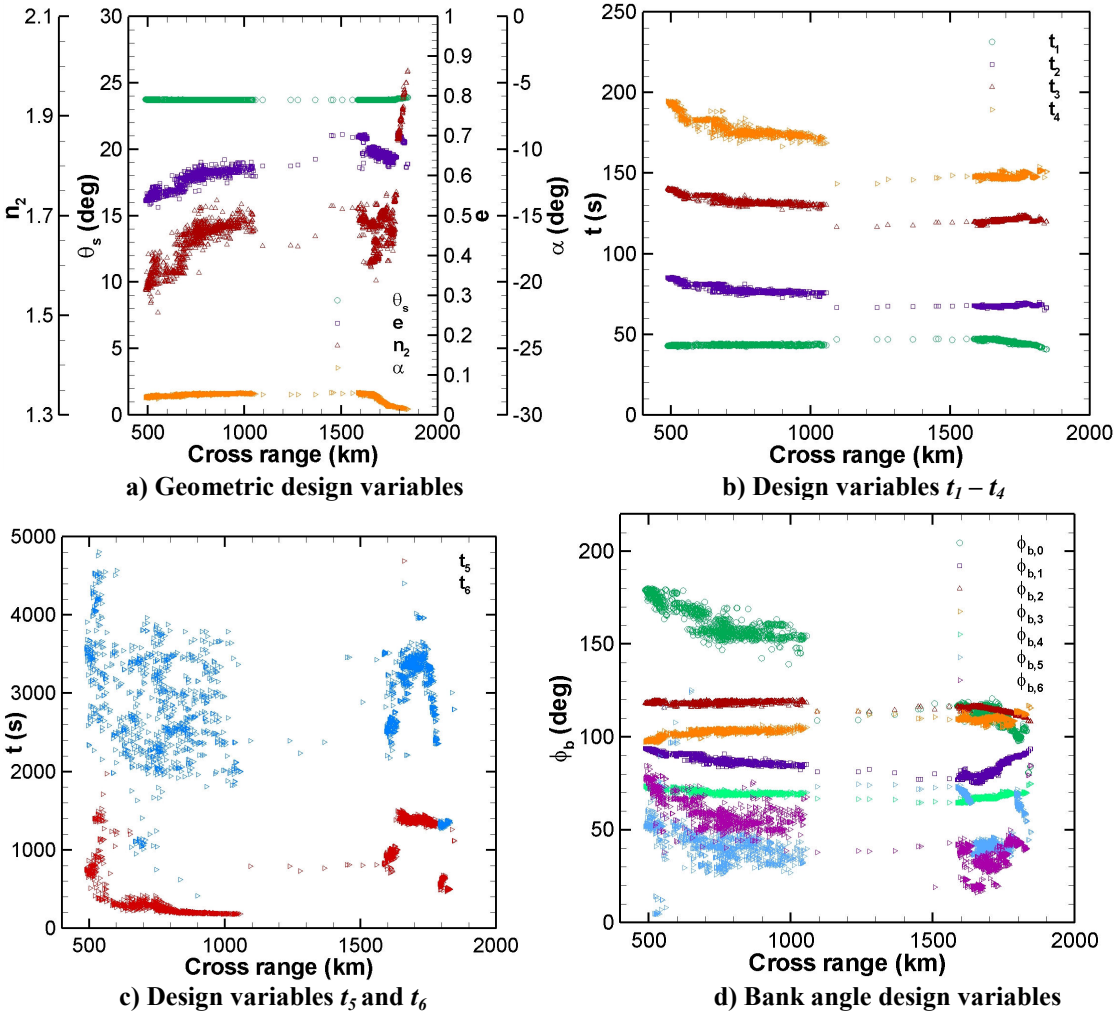

a) Geometric design variables

b) Design variables $t_1 - t_4$

c) Design variables t_5 and t_6

d) Bank angle design variables

Figure C.0.1. Design Variable Distributions for Pareto frontier of L/D = 0.5, SS lower mass case from Figure 13.1, for maximizing cross range and minimizing stagnation-point heat load, V_E = 12.5 km/s.

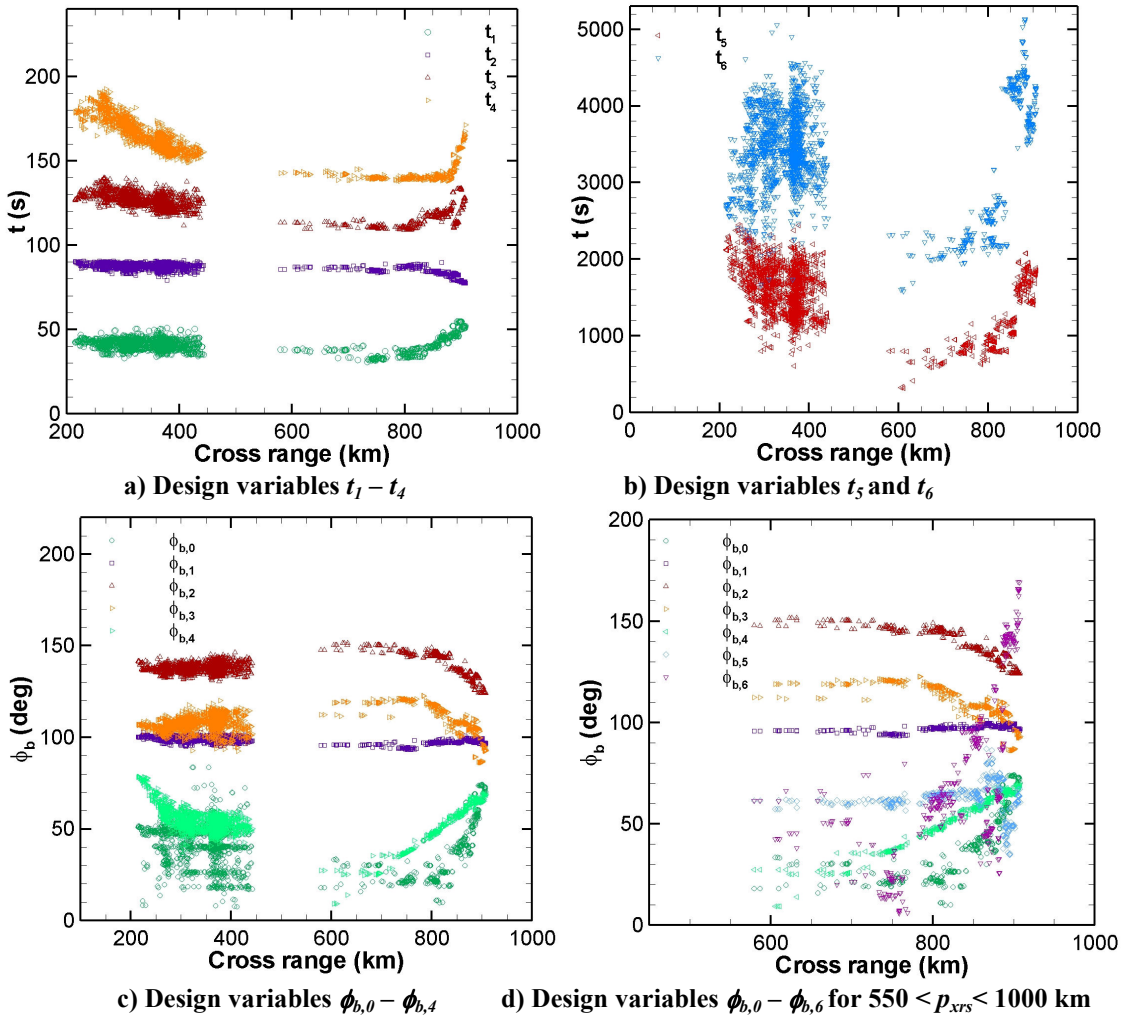

a) Design variables $t_1 - t_4$

b) Design variables t_5 and t_6

c) Design variables $\phi_{b,0} - \phi_{b,4}$

d) Design variables $\phi_{b,0} - \phi_{b,6}$ for $550 < p_{xrs} < 1000$ km

Figure C.0.2. Design Variable Distributions for Pareto frontier of L/D = 0.3, Orion CEV, projection at 10000 kg case from Figure 13.1, for maximizing cross range and minimizing stagnation-point heat load, V_E = 12.5 km/s.

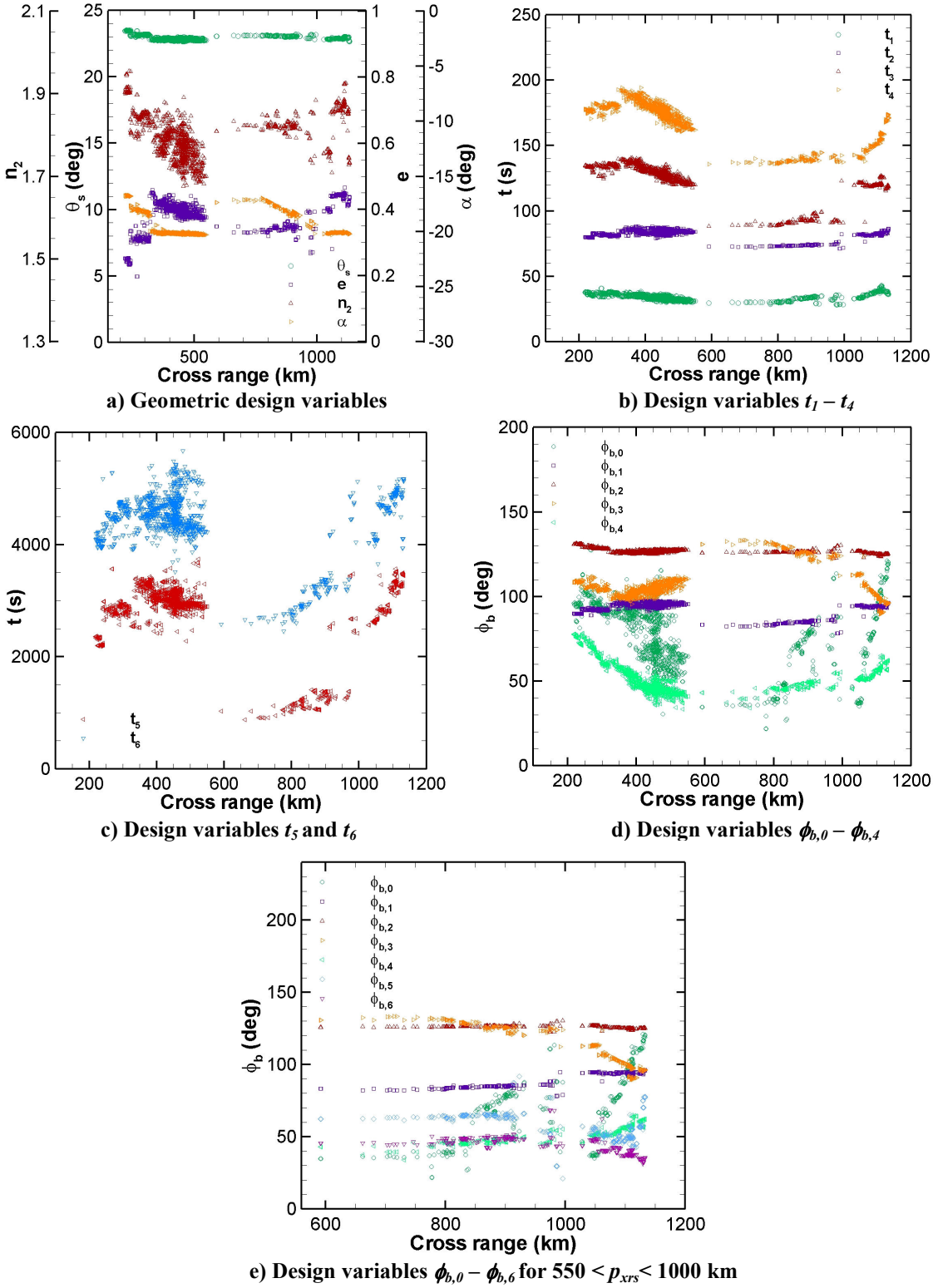

a) Geometric design variables

b) Design variables $t_1 - t_4$

c) Design variables t_5 and t_6

d) Design variables $\phi_{b,0} - \phi_{b,4}$

e) Design variables $\phi_{b,0} - \phi_{b,6}$ for 550 < p_{xrs}< 1000 km

Figure C.0.3. Design Variable Distributions for Pareto frontier of *L/D* = 0.3, SS lower mass case from Figure 13.1, for maximizing cross range and minimizing stagnation-point heat load, V_E = 12.5 km/s.

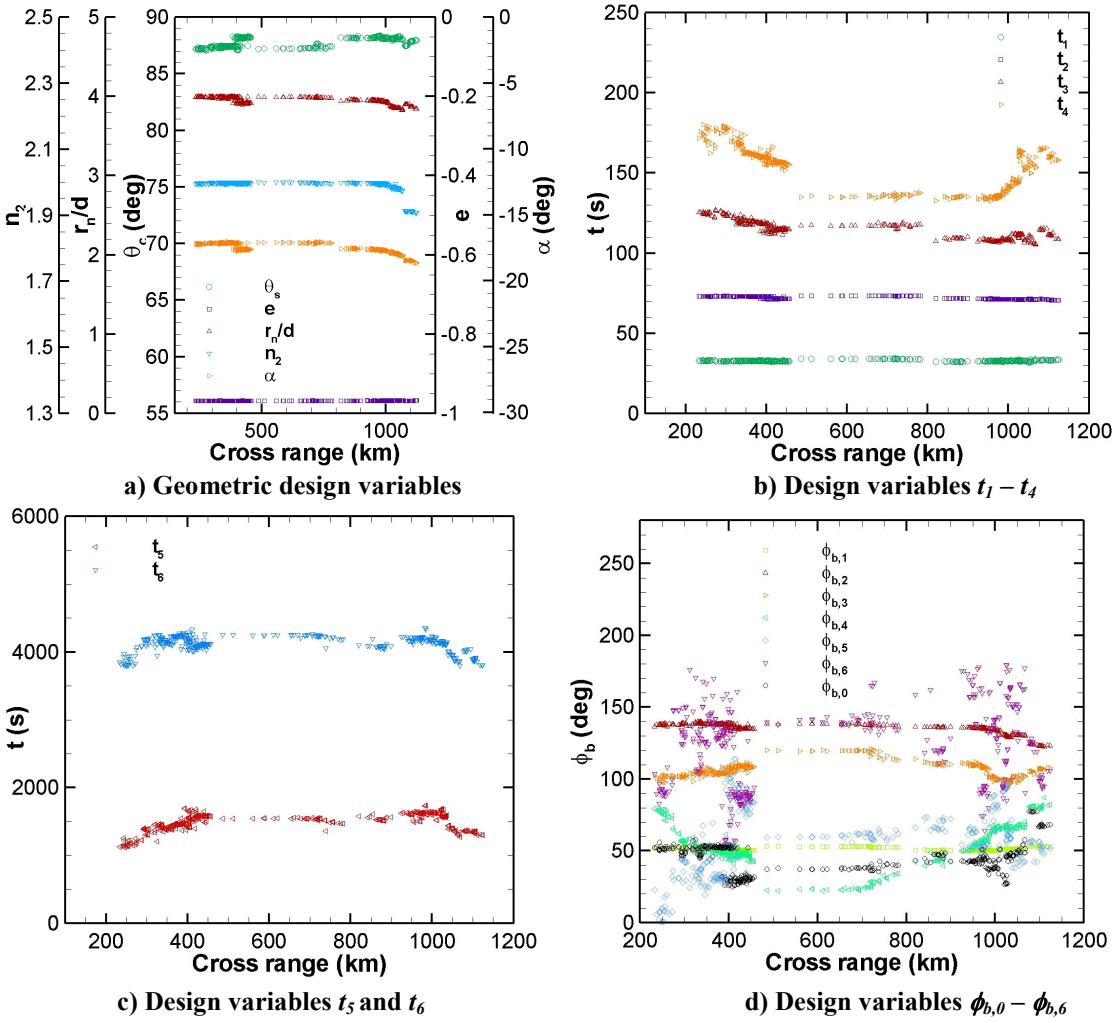

a) Geometric design variables

b) Design variables $t_1 - t_4$

c) Design variables t_5 and t_6

d) Design variables $\phi_{b,0} - \phi_{b,6}$

Figure C.0.4. Design Variable Distributions for Pareto frontier of L/D = 0.3, SC with fixed $h_{b,HS}$ = 3.43 m, lower mass case from Figure 13.1, for maximizing cross range and minimizing stagnation-point heat load, V_E = 12.5 km/s.

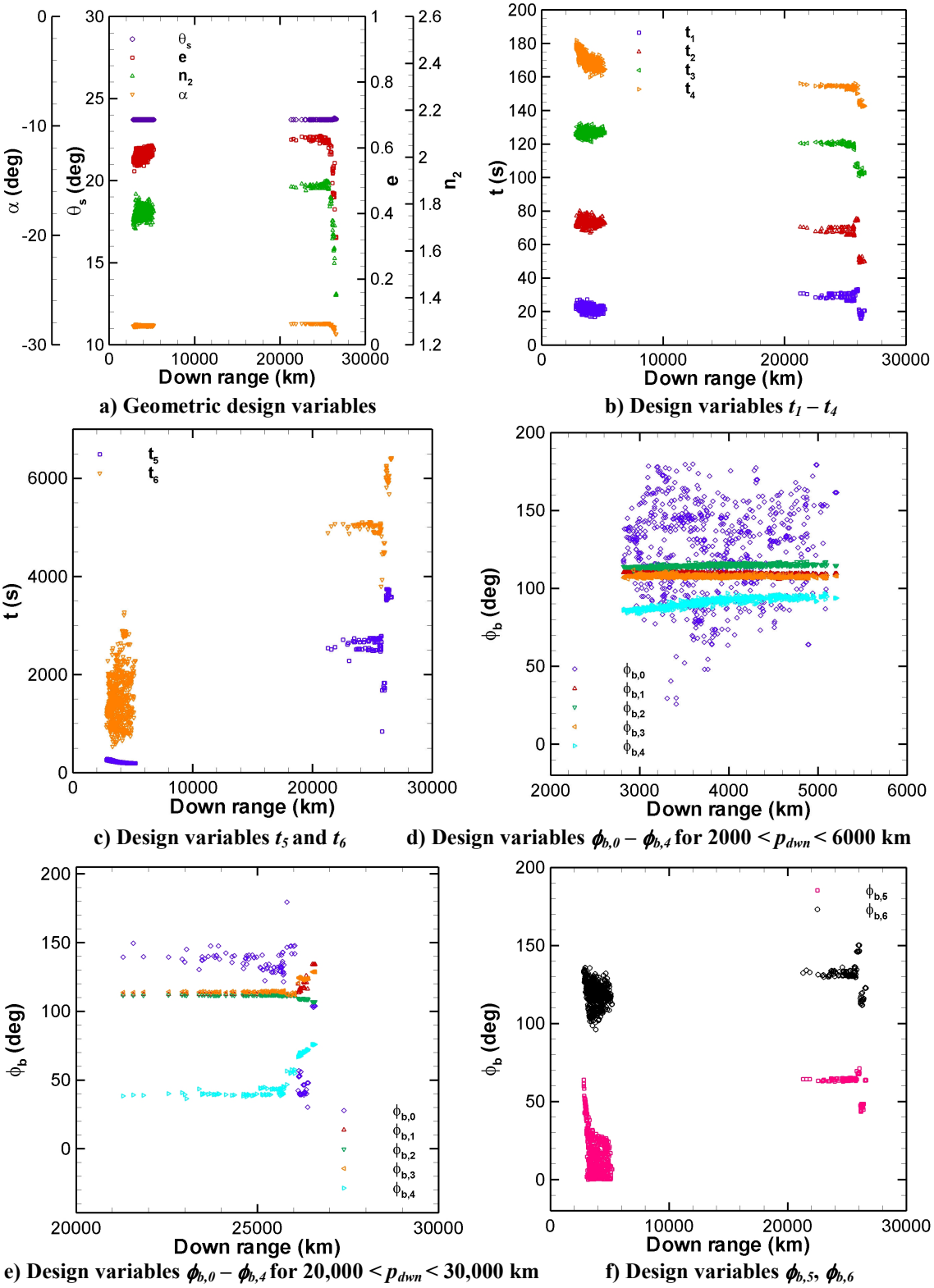

a) Geometric design variables

b) Design variables $t_1 - t_4$

c) Design variables t_5 and t_6

d) Design variables $\phi_{b,0} - \phi_{b,4}$ for $2000 < p_{dwn} < 6000$ km

e) Design variables $\phi_{b,0} - \phi_{b,4}$ for $20{,}000 < p_{dwn} < 30{,}000$ km

f) Design variables $\phi_{b,5}$, $\phi_{b,6}$

Figure C.0.5. Design Variable Distributions for Pareto frontier of $L/D = 0.5$, SS upper mass case from Figure 13.2, for maximizing down range and minimizing stagnation-point heat load, $V_E =$ 12.5 km/s.

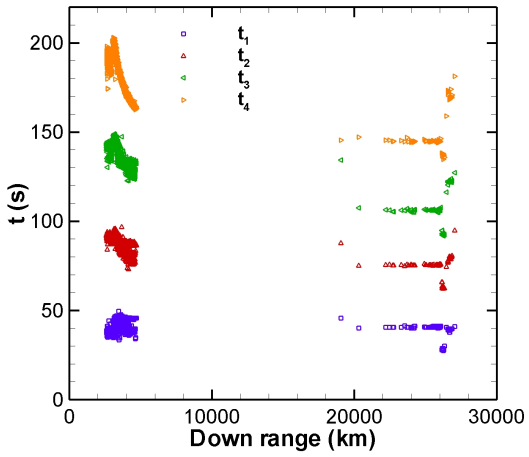

a) Design variables $t_1 - t_4$

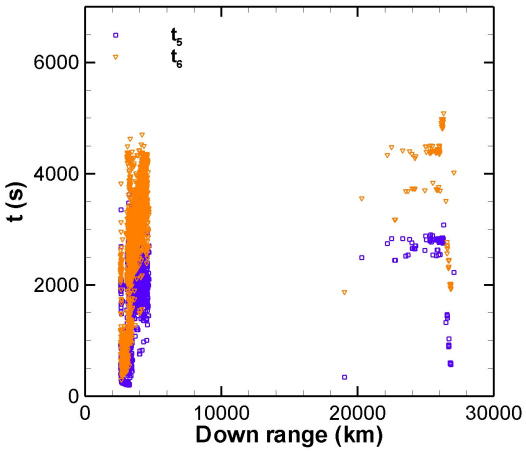

b) Design variables t_5 and t_6

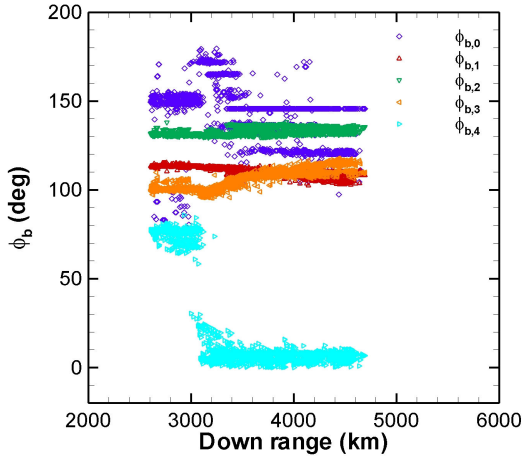

c) Design variables $\phi_{b,0} - \phi_{b,4}$ for $2000 < p_{dwn} < 6000$ km

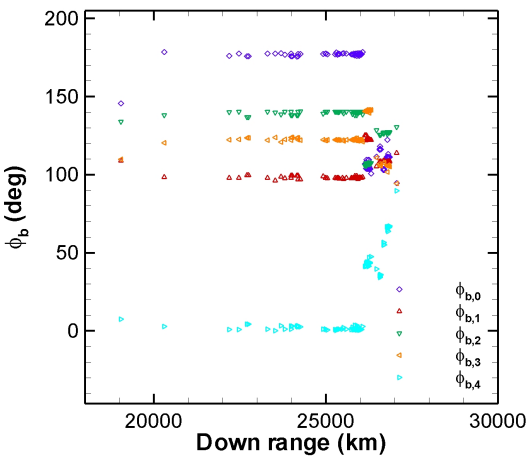

d) Design variables $\phi_{b,0} - \phi_{b,4}$ for $18{,}000 < p_{dwn} < 30{,}000$ km

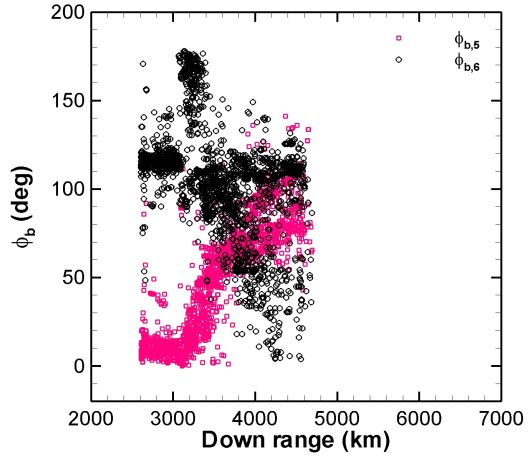

e) Design variables $\phi_{b,5}$, $\phi_{b,6}$ for $2000 < p_{dwn} < 7000$ km

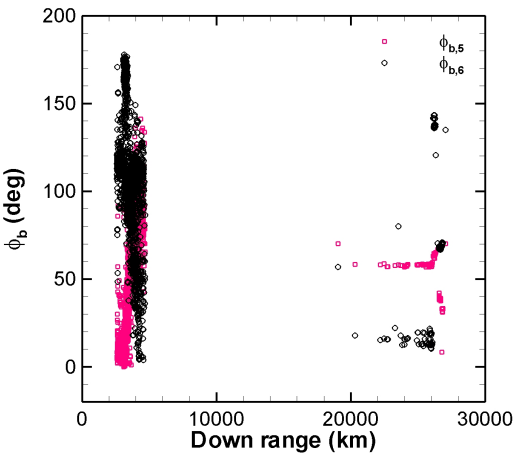

f) Design variables $\phi_{b,5}$, $\phi_{b,6}$ for $0 < p_{dwn} < 30{,}000$ km

Figure C.0.6. Design Variable Distributions for Pareto frontier of $L/D = 0.3$, Orion CEV, projection at 13000 kg case from Figure 13.2, for maximizing down range and minimizing stagnation-point heat load, $V_E = 12.5$ km/s.

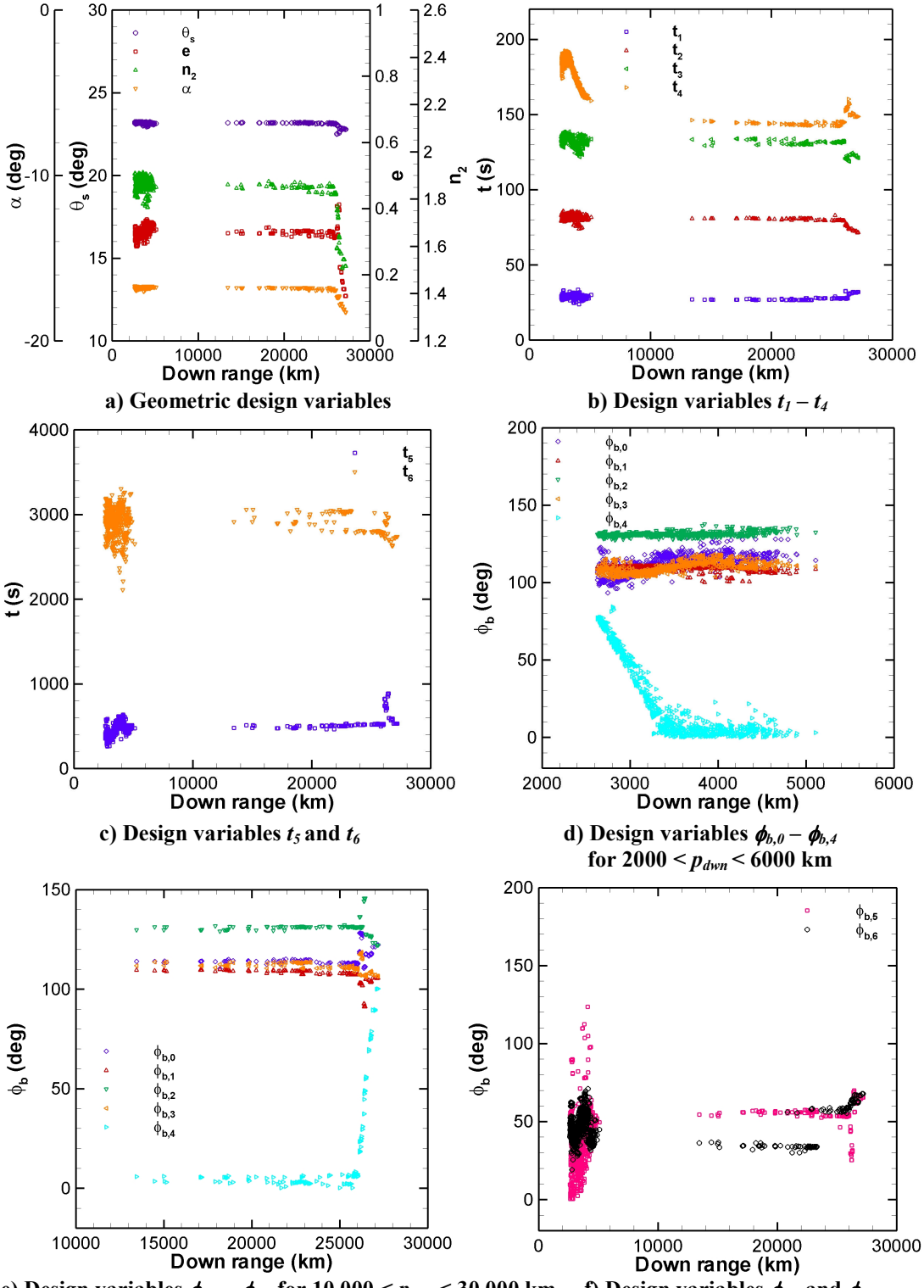

Figure C.0.7. Design Variable Distributions for Pareto frontier of *L/D* = 0.3, SS upper mass case from Figure 13.2, for maximizing down range and minimizing stagnation-point heat load, V_E = 12.5 km/s.

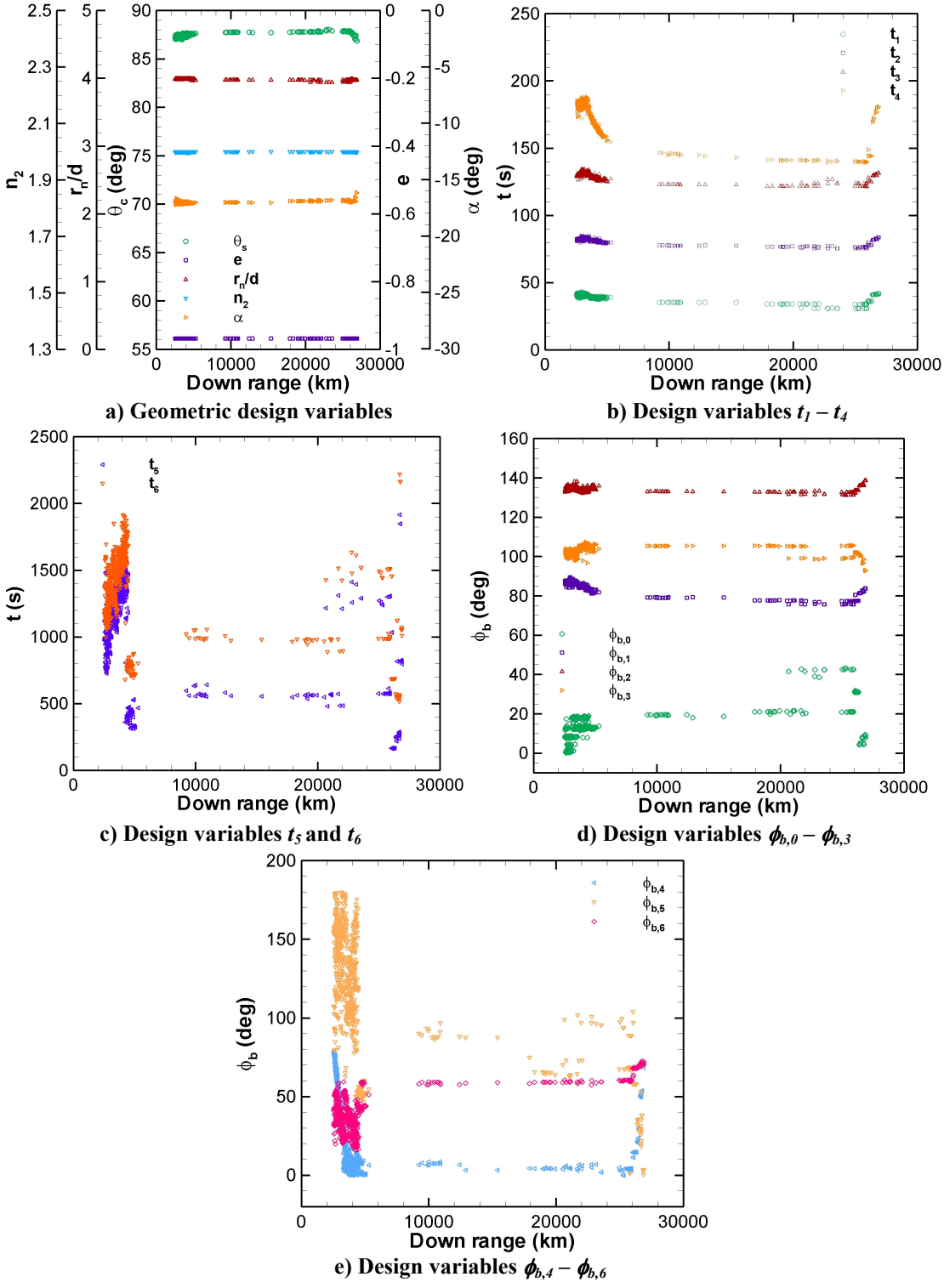

a) Geometric design variables

b) Design variables $t_1 - t_4$

c) Design variables t_5 and t_6

d) Design variables $\phi_{b,0} - \phi_{b,3}$

e) Design variables $\phi_{b,4} - \phi_{b,6}$

Figure C.0.8. Design Variable Distributions for Pareto frontier of L/D = 0.3, SC with fixed $h_{b,HS}$ = 3.43 m, upper mass case from Figure 13.2, for maximizing down range and minimizing stagnation-point heat load, V_E = 12.5 km/s.

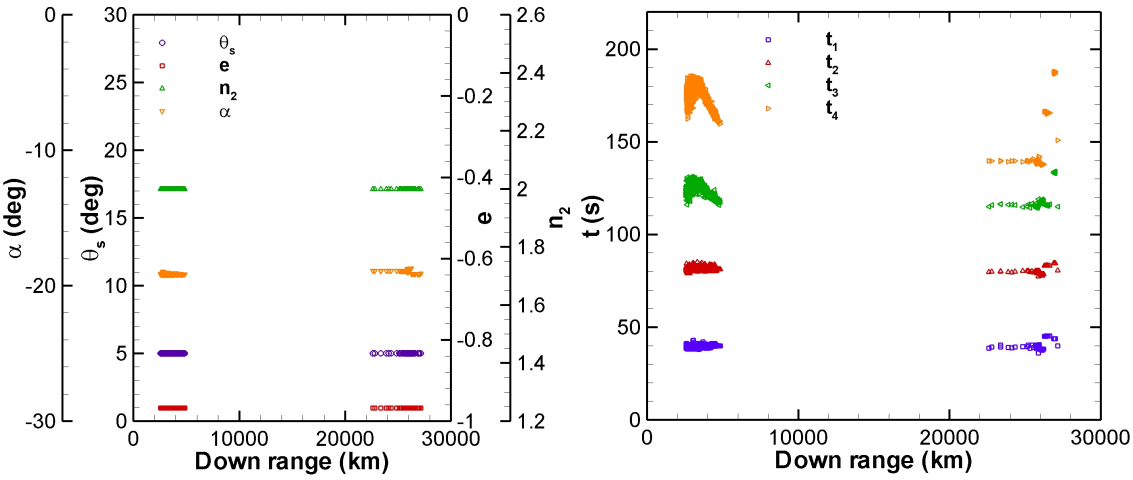

a) Geometric design variables

b) Design variables $t_1 - t_4$

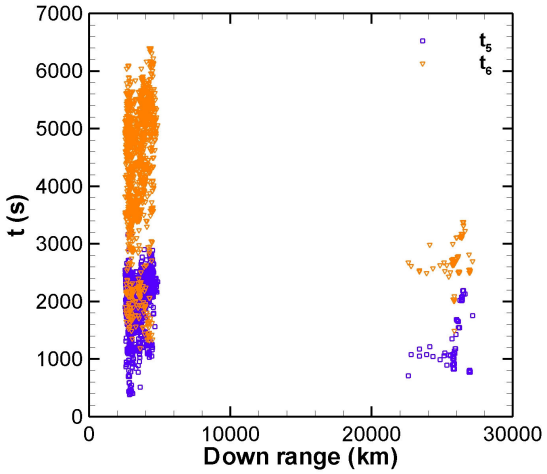

c) Design variables t_5 and t_6

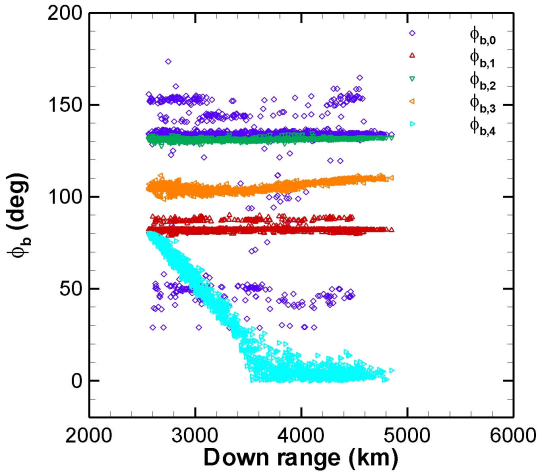

d) Design variables $\phi_{b,0} - \phi_{b,4}$ for $2000 < p_{dwn} < 6000$ km

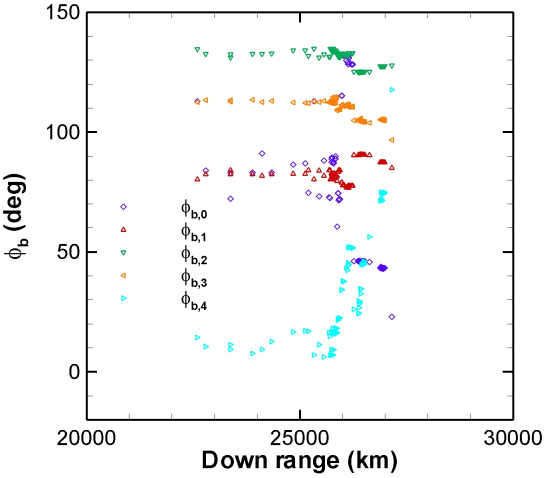

e) Design variables $\phi_{b,4} - \phi_{b,6}$ for $20000 < p_{dwn} < 30000$ km

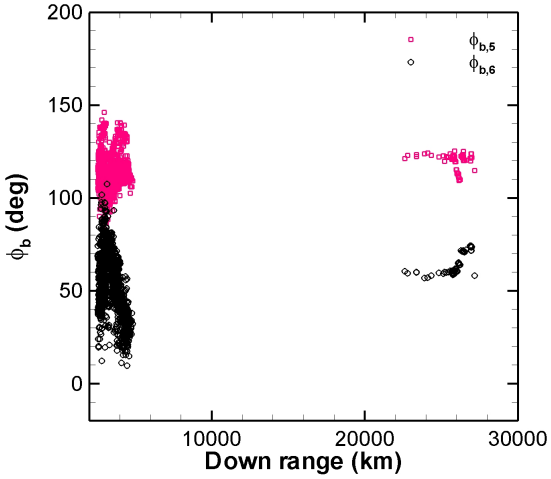

f) Design variables $\phi_{b,5}$ & $\phi_{b,6}$

Figure C.0.9. Design Variable Distributions for Pareto frontier of L/D = 0.3, 5-deg SS with fixed $h_{b,HS}$ = 3.43 m, upper mass case from Figure 13.2, for maximizing down range and minimizing stagnation-point heat load, V_E = 12.5 km/s.

Bibliography

[1] Putnam, Z. R., Braun, R. D., Rohrschneider, R. R., and Dec, J. A., "Entry System Options for Human Return from the Moon and Mars," *Journal of Spacecraft and Rockets,* Vol. 44, No. 1, 2007, pp. 194-202.

[2] Bertin, J., *Hypersonic Aerothermodynamics*, AIAA Education Series, AIAA, New York, 1993.

[3] Anderson, J. D., *Hypersonic and High Temperature Gas Dynamics,* AIAA, Virginia, 2000, Chap. 3, 6.

[4] Crowder, R. S. and Moote, J. D., "Apollo Entry Aerodynamics," *Journal of Spacecraft and Rockets,* Vol. 6, No. 3, 1969, pp. 302-307.

[5] Kirk, D. B., Intrieri, P. F., and Seiff, A., "Aerodynamic Behavior of the Viking Entry Vehicle: Ground Test and Flight Results," Journal of Spacecraft and Rockets, Vol. 15, No. 4, 1978, pp. 208-212.

[6] Chrusciel, G. T. and Hull, L. D., "Theoretical Method for Calculating Aerodynamic Characteristics of Spherically Blunted Cones," AIAA Paper 1968-674, Jun. 1968.

[7] Griffin M. D., and French, J. R., *Space Vehicle Design,* 2nd ed., AIAA Education Series, American Institute of Aeronautics and Astronautics, Inc., Virginia, 2004, Chap. 6.

[8] Faget, M. A., Garland, B. J., and Buglia, J. J., "Preliminary Studies of Manned Satellites, Wingless Configuration: Nonlifting," NACA RM L58E07a, 1958.

[9] Kruse, R. L., Malcolm, G. N., and Short, B. J., "Comparison of Free-Flight Measurement of Stability of the Gemini and Mercury Entry Capsules at Mach Numbers 3 and 9.5," NASA TM-X-957, 1964.

[10] Hillje, Ernest R., "Entry Flight Aerodynamics from Apollo Mission AS-202," NASA TN D-4185, 1967.

[11] Hillje, Ernest R., "Entry Aerodynamics at Lunar Return Conditions Obtained from the Flight of Apollo 4 (AS-501)," NASA TN D-5399, 1969.

[12] Moseley, W. C., Jr., Moore, R. H., Jr., and Hughes, J. E., "Stability Characteristics of the Apollo Command Module," NASA TN D-3890, 1967.

[13] Moseley, W. C., Jr., Graham, R. E., and Hughes, J. E., "Aerodynamic Stability Characteristics of the Apollo Command Module," NASA TN D-4688, 1968.

[14] DeRose, Charles E., "Trim Attitude, Lift and Drag of the Apollo Command Module with Offset Center-of-Gravity Positions at Mach Numbers to 29," NASA TN D-5276, 1969.

[15] Horstman, C. C., and Kussoy, M. I., "Free-flight Measurements of Aerodynamic Viscous Effects on Lifting Re-Entry Bodies," *Journal of Spacecraft and Rockets,* Vol. 4, No. 8, 1967, pp. 1064-1069.

[16] Jones, Robert A., Hunt, James L., "Measured Pressure Distributions on Large-Angle Cones in Hypersonic Flows of Tetrafluoromethane, Air and Helium," NASA TND-7429, Dec 1973.

[17] Tauber, M., Chargin, M., Henline, W., Chiu, A., Yang, L., Hamm, K. R., Jr., Miura, H., "Aerobrake Design Studies for Manned Mars Missions," *Journal of Spacecraft and Rockets,* Vol. 30, No. 6, 1993, pp. 656-664.

[18] Bernot, Peter T., Jordan, Bruce C., "Static Stability Characteristics of Cone and Half-Cone Pyramid Configurations at Mach 6.83," NASA TND-3544, Aug 1966.

[19] Sammonds, R. I. and Kruse, R. L., "Viking Entry Vehicle Aerodynamic at M = 2 in Air and Some Preliminary Test Data for Flight in CO2 at M = 12," NASA TN D-7974, 1975.

[20] Willcockson, W. H., "Mars Pathfinder Heatshield Design and Flight Experience," *Journal of Spacecraft and Rockets,* Vol. 36, No. 3, 1999, pp. 374-379.

[21] Moss, J. N., Blanchard, R. C., Wilmoth, R. G., Braun, R. D., "Mars Pathfinder Rarefied Aerodynamics: Computations and Measurements," AIAA Paper 1998-298, Jan. 1998.

[22] Milos, F. S., Chen, Y. K., "Mars Pathfinder Entry Temperature Data, Aerothermal Heating, and Heatshield Material Response," AIAA Paper 1998-2681, Jun. 1998.

[23] Ezell, Edward Clinton, and Linda Neuman Ezell. *On Mars: Exploration of the Red Planet, 1958-1978.* NASA SP-4212, 1984.

[24] Shapland, D. J., Price, D. A., Hearne, L. F., "A Configuration for Re-Entry from Mars Missions Using Aerobraking," *Journal of Spacecraft and Rockets,* Vol. 2, No. 4, 1965, pp. 501-507.

[25] Micol, J. R. and Wells, W. L., "Hypersonic Lateral and Directional Stability Characteristics of Aeroassist Flight Experiment Configuration in Air and CF_4," NASA TM 4435, 1993.

[26] Wells, William L., "Measured and Predicted Aerodynamic Coefficients and Shock Shapes for Aeroassist Flight Experiment (AFE) Configuration," NASA TP-2956, 1990.

[27] Micol, John R., "Simulation of Real-Gas Effects on Pressure Distributions for Aeroassist Flight Experiment Vehicle and Comparison With Prediction," NASA TP-3157, Apr 1992.

[28] Davies, Carol B., Park, Chul, "Aerodynamic Characteristics of Generalized Bent Biconic Bodies for Aero-Assisted Orbital-Transfer Vehicles," NASA TM 84362, May 1983.

[29] Davies, Carol B., Park, Chul, "Optimum Configuration of High-Lift Aeromaneuvering Orbital Transfer Vehicles in Viscous Flow," *Journal of Spacecraft and Rockets,* Vol. 25, No. 3, Jun 1988, pp. 193-201.

[30] Magazu, Harry K., Lewis, Mark J., and Akin, David L., "Aerothermodynamics of a Parashield Re-Entry Vehicle," *Journal of Spacecraft and Rockets,* Vol. 35, No. 4, 1998, pp. 434-441.

[31] Murbach, Marcus S., "SCRAMP: The Development of an Advanced Planetary Probe from CFD to Re-entry Test Flight," 3rd International Planetary Probe Workshop, Athens, Greece, June 27-July 1, 2005.

[32] Whitmore, Stephen A., Banks, D., Andersen, B., and Jolley, P., "Direct-Entry, Aerobraking, and Lifting Aerocapture for Human-Rated Lunar Return Vehicles," AIAA Paper 2006-1033, AIAA Aerospace Sciences Meeting, Jan 2006.

[33] Rasmussen, M., *Hypersonic Flow*, John Wiley & Sons, Inc. New York, 1994.

[34] Park, C., Davies, C. B., "Aerothermodynamics of Manned Mars Missions," AIAA Paper 1989-0313, Jan. 1989.

[35] Rochelle, W. C., Bouslog, S. A., and Ting, P. C., "Aerothermodynamic Environments for Mars Entry, Mars Return, and Lunar Return Aerobraking Missions," AIAA Paper 1990-1791, Jun 1990.

[36] Rose, P. H., Stark, W. I., "Stagnation Point Heat-Transfer Measurements in Dissociated Air," *Journal of the Aeronautical Sciences,* Vol. 25, No. 1, Feb 1958.

[37] Kemp, Nelson H., Rose, P. H., Detra, R. W., "Laminar Heat Transfer Around Blunt Bodies in Dissociated Air," *Journal of the Aero/space Sciences,* Vol. 26, No. 7, Jul 1959, pp 421-430.

[38] Lee, D. B., Bertin, J. J., Ried, R. C., "Apollo Reentry Heating," NASA TM X-66780, Sept 1963.

[39] Lee, D. B., Goodrich, W. D., "The Aerothermodynamic Environment of the Apollo Command Module During Superorbital Entry," NASA TN D-6792, Apr 1972.

[40] Lee, D. B., "Apollo Experience Report – Aerothermodynamics Evaluation," NASA TN D-6843, Jun 1972.

[41] Pavlosky, J. E., Leger, L. G. St., "Apollo Experience Report – Thermal Protection Subsytem," NASA TN D-7564.

[42] Park, C., Tauber, M. E., "Heatshielding Problems of Planetary Entry, A Review," AIAA Paper 1999-3415, Jun 1999.

[43] Scotti, S. J., "Current Technology for Thermal Protection Systems," NASA CP-3157, Feb 1992.

[44] Lovelace, Uriel M., "Charts Depicting Kinematic and Heating Parameters for a Ballistic Reentry at Speeds of 26,000 to 45,000 Feet Per Second," NASA TN D-968, Oct 1961.

[45] Tauber, M. E., and G. P. Menees, "Aerothermodynamics of Transatmospheric Vehicles," *AIAA Journal of Aircraft,* Vol. 24, No. 9, 1987, pp. 594-602.

[46] Fay, J. A., Riddell, F. R., "Theory of Stagnation Point Heat Transfer in Dissociated Air," *Journal of Aeronautical Sciences,* Vol. 25, No. 2, Feb 1958, pp. 73-85.

[47] Zoby, E. V., Sullivan, E. M., "Effects of Corner Radius on Stagnation-Point Velocity Gradients on Blunt Axisymmetric Bodies," NASA TM X-1067, Mar 1965.

[48] Tauber, M. E., Sutton, K., "Stagnation-Point Radiative Heating Relations for Earth and Mars Entries," *AIAA Journal of Spacecraft & Rockets,* Vol. 28, No. 1, 1991, pp. 40-42.

[49] Park, C., "Stagnation-Point Radiation for Apollo 4 – A Review and Current Status," AIAA Paper 2001-3070, Jun 2001.

[50] Cauchon, D. L., "Radiative Heating Results form the FIRE II Flight Experiment at a Reentry Velocity of 11.4 Kilometers per Second," NASA TM X-1402, Jul 1967.

[51] Ried, Jr., R. C., Rochelle, W. C., Milhoan, J. D., "Radiative Heating to the Apollo Command Module: Engineering Prediction and Flight Measurement," NASA TM X-58091, Apr 1972.

[52] Suttles, J. T., Sullivan, E. M., Margolis, S. B., "Curve Fits of Predicted Inviscid Stagnation-Point Radiative Heating Rates, Cooling Factors, and Shock Standoff Distances for Hyperbolic Earth Entry," NASA TN D-7622, Jul 1974.

[53] Walters, Edward E., "Free-Flight Measurements of Radiative Heating to the Front Face of the Apollo Reentry Capsule as a Function of Angle of Attack," NASA TM X-851, Feb 1964.

[54] Kaattari, George E., "Shock Envelopes of Blunt Bodies at Large Angles of Attack," NASA TN D-1980, Dec 1963.

[55] Kaattari, George E., "A Method for Predicting Shock Shapes and Pressure Distributions for a Wide Variety of Blunt Bodies at Zero Angle of Attack," NASA TN D-4539, Apr 1968.

[56] Srinivasan, S., Tannehill, J. C., Weilmuenster, K. J., "Simplified Curve Fits for the Thermodynamic Properties of Equilibrium Air," NASA-CR-181245, Jun 1986.

[57] Tannehill, J. C., and P. H. Mugge, "Improved Curve Fits for the Thermodynamic Properties of Equilibrium Air Suitable for Numerical Computation Using Time-Dependent or Shock-Capturing Methods," NASA CR-2470, Oct 1974.

[58] Brauer, G. L.; Cornick, D. E.; Habeger, A. R.; Petersen, F. M.; Stevenson, R., "Program to Optimize Simulated Trajectories (POST). Volume 1 Formulation manual," NASA-CR-132689, Apr 1975.

[59] Powell, R. W., Striepe, S. A., Desai, P. N., Braun, R. D., "Program to Optimize Simulated Trajectories (POST). Volume 2 Utilization manual, Version 5.2" NASA Langley Research Center, Oct 1997.

[60] Hargraves, C.R., Paris, S.W., and Gailey, J.W., Optimal Trajectories by Implicit Simulation Manual, Vol. I-IV, 1988, AFWAL TR-88-3057.

[61] Braun, R. D., Powell, R. W., "Aerodynamic Requirements of a Manned Mars Aerobraking Transfer Vehicle," *Journal of Spacecraft and Rockets,* Vol. 28, No. 4, 1991, pp. 361-367

[62] Braun, R. D., Powell, R. W., Lyne, J. E., "Earth Aerobraking Strategies for Manned Return from Mars," *Journal of Spacecraft and Rockets,* Vol. 29, No. 3, 1992, pp. 297-304.

[63] Putnam, Z. R., Braun, R. D., Rohrschneider, R. R., Dec, J. A., "Entry System Options for Human Return from the Moon and Mars," *Journal of Spacecraft and Rockets,* Vol. 44, No. 1, 2007, pp. 194-202.

[64] Regan, F., *Re-Entry Vehicle Dynamics*, 1st ed., AIAA Education Series. AIAA, New York, 1994, Chap. 9.

[65] Levine, P., Ellis, T.R., Georgiev, S., "Factors Influencing the Design and Performance of Mars Entry Vehicles," *Journal of Spacecraft and Rockets,* Vol. 2, No. 2, 1965, pp. 130-146.

[66] Arora, R. K., Kumar, P., "Aerodynamic Shape Optimization of a Re-entry Capsule," AIAA Paper 2003-5394, AIAA Atmospheric Flight Mechanics Conference, Aug 2003.

[67] Papadopoulos, Periklis and Prabhakar Subrahmanyam, "Computational Investigation and Simulation of the Aerothermodynamics of Reentry Vehicles," AIAA 2005-3206, AIAA/CIRA 13th International Space Planes and Hypersonics Systems and Technologies, May 2005.

[68] Papadopoulos, Periklis and Prabhakar Subrahmanyam, "Trajectory Coupled Aerothermodynamics Modeling for Atmospheric Entry Probes at Hypersonic Velocities," AIAA 2006-1034, 44th AIAA Aerospace Sciences Meeting and Exhibit, Jan 2006.

[69] Barter, Neville J., *Space Data,* Northrop Grumman Space Technology, 5th ed, Mar 2003, Section 7.

[70] Gupta, R. N., Jones, J. J., Rochelle, W. C., "Stagnation-Point Heat-Transfer Rate Predictions at Aeroassist Flight Conditions," NASA TP-3208, Sept 1992.

[71] Johnson, J. E., "Multidisciplinary Optimization of Non-Spherical, Blunt-Body Heat Shields for a Planetary Entry Vehicle," M.S. Thesis, Univ. of Maryland, College Park, MD, 2006.

[72] Sabean, John W., "Optimization of a Hypersonic Inlet with a Rectangular to Circular Transition Duct," Ph.D. Dissertation UM-AERO 99-09, Department of Aerospace Engineering, University of Maryland, College Park, MD, 1999.

[73] Gielis, J., "A Generic Geometric Transformation that Unifies a Wide Range of Natural and Abstract Shapes," *American Journal of Botany,* Vol. 90, No. 3, 2003, pp. 333-338.

[74] Eric W. Weisstein. "Simpson's Rule." From *MathWorld*--A Wolfram Web Resource. http://mathworld.wolfram.com/SimpsonsRule.html.

[75] Anderson, J. D., *Fundamentals of Aerodynamics,* 3rd ed., McGraw-Hill Book Co., New York, 2001, Chap. 8.

[76] Nelson, Robert. C., *Flight Stability and Automatic Control,* 2nd Ed., McGraw-Hill Book Co., New York, 1997, Chap. 1, 2.

[77] Phillips, W. F., *Mechanics of Flight,* John Wiley & Sons, Inc., Hoboken, NJ, 2004.

[78] Anderson, J. D., *Introduction to Flight,* 4rd ed., McGraw-Hill Book Co., New York, 2000, Chap. 3.

[79] NOAA, NASA, USAF, "U.S. Standard Atmosphere, 1976," NASA-TM-X-74335, NOAA-S/T-76-1562, Oct 1976.

[80] Wooster, P. D., Braun, R. D., Ahn, J., Putnam, Z. R., "Trajectory Options for Human Mars Missions," AIAA Paper 2006-6308, Aug. 2006.

[81] "Constellation Program: The Orion Crew Exploration Vehicle," NASA Facts, Johnson Space Center, FS-2006-08-022-JSC, 2006.

[82] Larson, W. J., and Pranke, L. K. (eds.), *Human Spaceflight Mission Analysis and Design,* Space Technology Series, The McGraw-Hill Companies, Inc., New York, 1999, Chap. 10, 12.

[83] Braun, R. D., Powell, R. W., and Lyne, J. E., "Earth Aerobraking Strategies for Manned Return from Mars," *Journal of Spacecraft and Rockets,* Vol. 29, No. 3, 1992, pp. 297-304.

[84] "Spacecraft – Mercury," *Rocket & Space Technology* [online database], URL: http://www.braeunig.us/space/specs/mercury.htm [modified 15 June 2007], [cited 22 April 2009].

[85] "Project Gemini," *Wikipedia, the free encyclopedia,* URL: http://en.wikipedia.org/wiki/Project_Gemini [cited 24 January 2009].

[86] "Apollo Command/Service Module," *Wikipedia, the free encyclopedia,* URL: http://en.wikipedia.org/wiki/Apollo_Command_Module [cited 24 January 2009].

[87] "Final Environment Assessment for the Development of the Crew Exploration Vehicle," NASA Headquarters, NP-2006-08-444-HQ, 2006.

[88] "Orion," *Encyclopedia Astronautica,* URL: http://www.astronautix.com/craft/orion.htm [modified 5 August 2008], [cited 22 April 2009].

[89] "Dyna-soar," *Encyclopedia Astronautica,* URL: http://www.astronautix.com/craft/dynasoar.htm [modified 31 July 2008], [cited 24 April 2009].

[90] "X-20 Dyna-Soar," *Wikipedia, the free encyclopedia,* URL: http://en.wikipedia.org/wiki/X-20_Dyna-Soar [modified 21 April 2009], [cited 24 April 2009].

[91] "ASSET," *Encyclopedia Astronautica,* URL: http://www.astronautix.com/craft/asset.htm [modified 31 July 2008], [cited 24 April 2009].

[92] "ASSET (spaceplane)," *Wikipedia, the free encyclopedia,* URL: http://en.wikipedia.org/wiki/ASSET_(spaceplane) [modified 10 April 2009], [cited 24 April 2009].

[93] Starkey, R. P., Rankins, F., and Pines, D. J., "Effects of Hypersonic Cruise Trajectory Optimization Coupled with Airbreathing Vehicle Design," AIAA Paper 2006-1036, Jan. 2006.

[94] Rankins, F., "The University of Maryland Parallel Trajectory Optimization Program User's Manual," University of Maryland, College Park, 2007.

[95] Stevens, B. L., and Lewis, F. L., *Aircraft Control and Simulation,* John Wiley & Sons, Ltd., New York, 1992.

[96] Minzner, R. A., K. S. W. Champion, and H. L. Pond: *The ARDC Model Atmosphere, 1959,* Air Force Cambridge Research Center Report No. TR-59-267, U.S. Air Force, Bedford, MA, 1959.

[97] Anderson, J. A., *Introduction to Flight,* 4th ed, McGraw Hill, Boston, 2000, Chap. 3.

[98] "US Standard Atmosphere, 1976," NASA-TM-X-74335, Oct 1976.

[99] Scott, C. D., Ried, R. C., Maraia, R. J., Li, C. P., and Derry, S. M., "An AOTV Aeroheating and Thermal Protection Study," H. F. Nelson (ed.), *Thermal Design of Aeroassisted Orbital Transfer Vehicles*, Vol. 96 of Progress in Astronautics and Aeronautics, AIAA, New York, 1995, pp. 309-337.

[100] "Department of Defense World Geodetic System 1984, Its Definition and Relationships With Local Geodetic Systems," NIMA TR8350.2, Third Edition, Jul 1997.

[101] Picone, J. M., Hedin, A. E. Drob, D. P., and Aikin, A. C., "NRLMSISE-00 empirical model of the atmosphere: Statistical comparisons and scientific issues,"

Journal of Geophysical Research, Vol. 107, No. A12, Dec 2002, pp. SIA15.1-SIA15.16.

[102] "Design Optimization Tools Version 4.20, User's Manual," Vanderplaats Research & Development, Inc., Colorado Springs, CO, 1995.

[103] Brauer, G. L.; Cornick, D. E.; Habeger, A. R.; Petersen, F. M.; Stevenson, R., "Program to Optimize Simulated Trajectories (POST). Volume 1 Formulation manual," NASA-CR-132689, Apr 1975.

[104] Powell, R. W., Striepe, S. A., Desai, P. N., Braun, R. D., "Program to Optimize Simulated Trajectories (POST). Volume 2 Utilization manual, Version 5.2" NASA Langley Research Center, Oct 1997.

[105] Johnson, J. E., Starkey, R. P., and Lewis, M. J., "Aerothermodynamic Optimization of Reentry Heat Shield Shapes for a Crew Exploration Vehicle," *AIAA Journal of Spacecraft & Rockets*, Vol. 44, No. 4, July/Aug 2007, pp. 849-859. Presented earlier version at the AIAA Atmospheric Flight Mechanics Conf. as AIAA Paper 2006-6273, Aug 2006.

[106] Madavan, N. K., "On Improving Efficiency of Differential Evolution for Aerodynamic Shape Optimization Applications," AIAA Paper 2004-4622, Aug. 2004.

[107] Deb, K., *Multi-Objective Optimization Using Evolutionary Algorithms,* John Wiley & Sons, Ltd., Chichester, 2001.

[108] Rai, M. M., "Robust Optimal Aerodynamic Design Using Evolutionary Methods and Neural Networks," AIAA Paper 2004-778, Jan. 2004.

[109] Rai, M., "Towards a Hybrid Aerodynamic Design Procedure Based on Neural Networks and Evolutionary Methods," AIAA Paper 2002-3143, 20th AIAA Applied Aerodynamics Conference, 24-26 Jun 2002.

[110] Johnson, J. E., Starkey, R. P., and Lewis, M. J., "Multi-Objective Optimization of Entry Vehicle Heat Shields with Reentry Trajectory Analysis," 58th International Astronautical Congress, Hyderabad, India, IAC-07-C2.7.09, Sept 2007.

[111] Johnson, J. E., Lewis, M. J., and Starkey, R. P., "Analysis of Optimal Earth Entry Heat Shield/Trajectory Configurations," AIAA Paper 2008-2594, April 2008.

[112] Johnson, J. E., Starkey, R. P., and Lewis, M. J., "Aerodynamic Stability of Reentry Heat Shield Shapes for a Crew Exploration Vehicle," *AIAA Journal of Spacecraft &*

Rockets, Vol. 43, No. 4, July/Aug 2006, pp. 721-730. Presented earlier version at the AIAA Joint Propulsion Conf. as AIAA Paper 2005-4112, Jul 2005.

[113] Graves, C. A., and Harpold, J. C., "Re-Entry Targeting Philosophy and Flight Results from Apollo 10 and 11," AIAA Paper 1970-28, Jan. 1970.

[114] Young, J. W., and Smith, R. E., "Trajectory Optimization for An Apollo-Type Vehicle Under Entry Conditions Encountered During Lunar Return," NASA TR- R-258, May 1967.

[115] Johnson, J. E., Lewis, M. J., and Starkey, R. P., "Coupled Entry Heat Shield/Trajectory Optimization for Lunar Return," AIAA Paper 2008-6557, AIAA Atmospheric Flight Mechanics Conf., 18 – 21 Aug 2008.

[116] Rea, J. R., "Orion Entry Flight Corridor Analysis," AIAA Paper 2008-7153, AIAA Guidance, Navigation, and Control Conf., 18 – 21 Aug, 2008.